NASA CONTRACTOR REPORT

NASA CR-2324

NASA CR-2324

AIR POLLUTION MEASUREMENTS FROM SATELLITES

by C. B. Ludwig, M. Griggs, W. Malkmus,
and E. R. Bartle

Prepared by
CONVAIR AEROSPACE DIVISION
GENERAL DYNAMICS CORPORATION
San Diego, Calif.
for Langley Research Center

NATIONAL AERONAUTICS AND SPACE ADMINISTRATION • WASHINGTON, D. C. • NOVEMBER 1973

1. Report No. NASA CR-2324	2. Government Accession No.	3. Recipient's Catalog No.
4. Title and Subtitle AIR POLLUTION MEASUREMENTS FROM SATELLITES		5. Report Date November 1973 6. Performing Organization Code
7. Author(s) C. B. Ludwig, M. Griggs, W. Malkmus, and E. R. Bartle		8. Performing Organization Report No. GDCA-HAB-73-011
9. Performing Organization Name and Address Convair Aerospace Division General Dynamics Corporation San Diego, CA		10. Work Unit No. 160-44-64-01 11. Contract or Grant No. NAS1-10466
12. Sponsoring Agency Name and Address National Aeronautics and Space Administration Washington, D.C. 20546		13. Type of Report and Period Covered Contractor Report 14. Sponsoring Agency Code

15. Supplementary Notes

This is a topical report.

16. Abstract

This report is a continuation of a study on the remote sensing of gaseous and particulate air pollutants and is an extension of the previous NASA report "Study of Air Pollutant Detection by Remote Sensors" (CR 1380, July 1969). Pollutants can be observed by either active or passive remote sensing systems. Calculations discussed herein indicate that tropospheric CO, CO_2, SO_2, NO_2, NH_3, HCHO, and CH_4 can be measured by means of nadir looking passive systems. Additional species such as NO, HNO_3, O_3, and H_2O may be measured in the stratosphere through a horizon experiment. In the discussion of active systems for measurement of gases, a brief theoretical overview of resonance Raman scattering and resonance fluorescence is given. Several techniques for measuring aerosol in a nadir looking experiment are examined and it is found that radiance measurements are most promising for general global applications. It is also found that stratospheric aerosol may be measured using a sun occultation technique. The instrumentation requirements for both active and passive systems are examined and various instruments now under development are described.

17. Key Words (Suggested by Author(s)) Pollution Aerosols Satellite Infrared Spectroscopy	18. Distribution Statement Unclassified - Unlimited

19. Security Classif. (of this report) Unclassified	20. Security Classif. (of this page) Unclassified	21. No. of Pages 222	22. Price* Domestic, \$5.50 Foreign, \$8.00

*For sale by the National Technical Information Service, Springfield, Virginia 22151

TABLE OF CONTENTS

TABLE OF CONTENTS (Continued)

4 (Continued) Page

TABLE OF CONTENTS (Continued)

AIR POLLUTION MEASUREMENTS FROM SATELLITES

By C. B. Ludwig, M. Griggs, W. Malkmus and E. R. Bartle*
General Dynamics Corporation
Convair Aerospace Division

SUMMARY

This work is the continuation of a study on remote sensing of air pollutants from satellites and the present report is an update of the previous NASA report "Study of Air Pollutant Detection by Remote Sensors" (CR 1380, July 1969), in which the feasibility of detecting certain gaseous pollutants from earth-oriented sensors was tentatively established. The present report is written in cognizance of the studies of several working groups whose results were published in "Study of Critical Environmental Problems (SCEP)" (MIT Press 1970), "Study of Man's Impact on Climate (SMIC)" (MIT Press 1971), and "Remote Measurement of Pollution" (NASA SP-285, 1971). Those studies were concerned with the need for global monitoring of pollution and with various aspects of the potential and established feasibility of remote sensing; the present work is concerned with the detailed analysis of the actual task.

The pollutants are grouped according to the atmospheric regions in which they are of concern, because the techniques for measuring trace gases in the troposphere and stratosphere are distinctly different. Man's understanding of the impact of the pollutants on the global environment has evolved over the past few years and is summarized in this report. The present status of knowledge about the fate of the relevant pollutants in the atmosphere--their sources, sinks, and reaction mechanisms--is briefly reviewed.

The pollutants can conceptually be observed from satellites by passive and active systems. An overview of the different contributions to the radiance emerging at the top of the atmosphere in the spectral interval from the ultraviolet to the microwave is presented. Although pollutants can have spectral signatures throughout this interval, it is found that only the infrared region from 2 to 13 μm is useful for the measurement of pollutants by passive systems. Detailed line-by-line calculations are performed to determine the signal change, i.e., the radiance difference between "clean" and "polluted" atmospheres, choosing pollutant concentrations at levels close to "established" global background values. The results show that the

---

* All authors are now with Science Applications, Inc., La Jolla, California.

measurement of tropospheric CO, CO_2, SO_2, NO_2, NH_3, HCHO and CH_4 appears feasible. Additional species, such as NO, HNO_3, NH_3, O_3 and H_2O may be measured in the stratosphere through a horizon experiment. In the discussion of active systems, a brief theoretical overview of the two most promising methods, resonance Raman scattering and resonance fluorescence, is given.

For the observation of particulate matter in a nadir experiment, the techniques of contrast reduction, polarization and radiance measurement are analyzed. It is found that the latter technique appears most promising for general global applications. An analysis of the sun occultation measurement indicates that the stratospheric aerosol content may be readily measured from a satellite with an accuracy sufficient to monitor the anticipated effects of high-flying aircraft.

Instruments to be used in the passive earth-oriented mode (where the interference problem by the "normal" atmosphere is severe) must be sensitive, specific and fast in time response. Theoretically, instruments with a large throughput and the multiplex advantage fulfill these requirements. Examples are electro-optical correlation instruments and interferometer-spectrometers. These two types are discussed in detail. Instruments used in the horizon-oriented mode do not require high specificity for many trace gases because interference from water vapor is greatly reduced. Thus, low resolution, sensitive radiometers can be used. Applications of active laser systems for the absorption, resonant Raman and fluorescence backscattering schemes are briefly discussed. It is found that these systems require high power, making the employment of large (manned) space stations necessary.

1

INTRODUCTION

The steady increase of industrialization and urbanization magnifies the problem of air pollution in an accelerating degree. The injection of man-made gaseous and particulate matter into the atmosphere has many observable adverse effects on all aspects of human, animal, and plant organisms. In a larger sense, it affects our "quality of life." At the present time, several monitoring and controlling programs are in progress to combat the danger of air pollution on a local basis.

Recently, studies were undertaken to assess the problem of air pollution on a global scale (ref. 1, 2). Answers to questions such as the accumulation of air pollutants, the effects on the global heat balance and, thus, on the global meteorology, the effects of high-flying aircraft, the relationships between sources, routes, and reservoirs and the role of air chemistry were sought. The conclusions were that no definite answers can be given because too little is known about the complex interaction of man-made and naturally produced air pollution with the "normal" atmosphere. Therefore, an intensification of measurement programs (together with research programs on reaction rates) has been recommended to overcome this lack of knowledge.

In the global problem, measurements must be made over the entire surface of the earth. Satellites offer the unique opportunity to conduct global measurements, covering regions where it is impractical to employ ground stations. It appears that satellites would also be economical because remote sensing of air pollution would be but one of several observations from the same platform. On the other hand, satellite observations are limited to a certain number of pollutants and to a certain accuracy, which is not only given by the sensitivity of the sensor, but also by certain assumptions which must be made in the data interpretation procedure. It is thus important to emphasize that satellite observations are just one portion of the overall task of providing complete global coverage and that they will serve to complement (and not supplant) ground-based observations. For the future, one may envision a systems concept of measuring atmospheric pollution which employs ground observations in urban, rural and remote locations (including ocean buoys) for localized coverage (see Table 1-1). The information collected from these different platforms is then fed into a centralized data collection center (see fig. 1-1).

It must be pointed out that many changes in surface features also affect the global climate, such as eutrophication, changes in estuaries, oil slicks on oceans, changes in vegetation, etc. Some of these changes can routinely be observed from satellites. However, these tasks were not considered in the present study.

TABLE 1-1. OVERVIEW OF APPLICATION

		Satellite	Aircraft	Ground	
				Remote	Point
Global	Pollutant Distribution	X			
	Dispersal Rates	X			
	Pollutant Build-Up	X			
	Global Air Quality	X			
	Pollution Forecasting	X			
	Interaction W/Global Meteorology	X			
	Upper Atmosphere Chemistry	X			
Regional	Pollutant Distribution	X	X		
	Dispersal Rates	X	X		
	Regional Air Quality	X	X		
	Pollution Forecasting	X	X		
	Interaction with Meteorology	X	X		
Local	Concentration Distribution		X	X	X
	Tactical Air Quality		X	X	X
	Forecasting			X	X
	Law Enforcement			X	X
	Control Assist				X

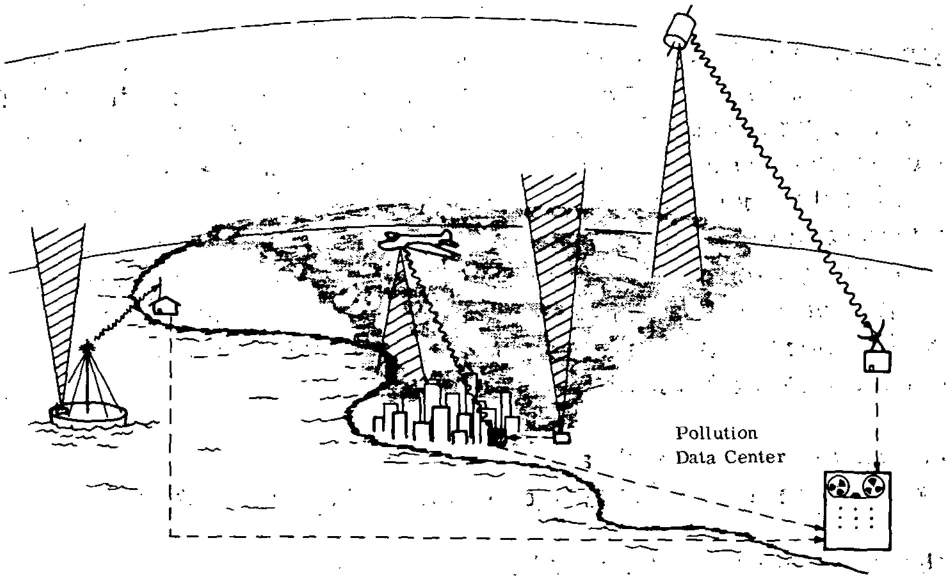

Figure 1-1. Systems Concept for Remote Sensing of Air Pollution on a Global Basis

The first feasibility study of satellite observations of pollutants was conducted in 1968/69 (ref. 3). In that study, the chemistry, concentration and distribution of the major pollutant species, the radiative transfer problem in the ultraviolet, visible, infrared and microwave portions of the electromagnetic spectrum and the performance of different spectroscopic instruments for the remote detection of pollutants were discussed. The major pollutants considered were carbon monoxide, sulfur dioxide, ozone, ammonia, nitrogen dioxide, typical hydrocarbons, peroxy acetyl nitrate (PAN) and aerosols. Their global concentrations were deduced from data taken at many monitoring stations in urban, rural and remote areas. Then, the utility of the different portions of the spectrum was analyzed and it was found that the infrared region extending from 3.5 to 13 μm is the most useful one because the problems of atmospheric scattering at the shorter wave lengths and of poor specificity at the longer wave lengths are avoided. The major requirement in the use of the thermal infrared region is the knowledge of the atmospheric temperature profile, which must be obtained independently. The "signal changes," i.e., the percentage change in radiance at orbital altitudes between a "clean" and "polluted" atmosphere, were calculated with band models, using low-resolution spectral characteristics of the pollutants and normal atmospheric constituents. It was found that under most atmospheric conditions, pollutant layers can give rise to 1 percent signal changes. The different spectroscopic instruments considered included radiometers, grating spectrometers, interferometer-spectrometers, correlation instruments and one active laser system. It was found that interferometer-spectrometers and instruments using correlation methods appeared to fulfill best the requirements of high sensitivity, high specificity and short observation time for earth-oriented observations of air pollutants. However, the practical realization of a fast-scanning, high-resolution (better than 0.1 cm^{-1}) interferometer-spectrometer for satellite application seemed unlikely in the near future.

In the present report, these findings and conclusions are re-examined in light of new discoveries in terms of global pollutant concentrations, the introduction of line-by-line calculations and advances in instrument developments. In Section 2, the pollutants which appear to be important on a global scale and which can be observed from satellites are discussed. These include pollutants (trace contaminants) from both natural and anthropogenic sources. In Sections 3 and 4, the principles of observation for the gaseous and particulate trace contaminants are discussed, i.e., the observation of electromagnetic energy received at the entrance pupil of the instrument and its interpretation in terms of pollutant concentration. In Section 5, a description of the various instruments is given.

In the appendices, selected details on pollutant spectra in the infrared, on scattering theory, on optical correlation and on band modeling are given.

The authors wish to thank C. N. Abeyta and R. M. Smith for the programming, Dr. J. Wang for calculating some of the molecular spectra, W. Marggraf for the investigations of the meteorological influence on the data, and L. Acton and G. Hall for helpful discussions.

2

GLOBAL DISTRIBUTION OF AIR POLLUTANTS

2.1 Introduction

It is convenient to define all minor constituents of the atmosphere, which may be gaseous or particulate, as air pollutants except the noble gases. Thus, this definition does not distinguish between man-made and natural-made pollutants.

There are many pollutants which are a problem on the local scale. These include the aerosols, carbon monoxide, sulfur dioxide, the oxides of nitrogen, ozone, the halogens, the reactive hydrocarbons and the products of photochemical smog, such as the aldehydes, the aromatics and PAN.

In this study, we are interested in the global effect of these locally produced pollutants, as well as the future trends of emissions on a global scale due to the increasing industrial development of all nations.

At the present time, several pollutants are implicated to have a global impact. The observed increase of carbon dioxide concentration may increase the global mean air temperature due to the greenhouse effect; the potential increase of aerosols may decrease the global mean air temperature. Gaseous pollutants such as hydrocarbons, sulfur and nitrogen dioxides and possibly carbon monoxide contribute to the formation of the aerosols. Thus, it is important that these air pollutants be considered on a global scale.

In the following sections, we discuss briefly the present status of knowledge about the fate of the different pollutants in the atmosphere, their sources, sinks, and reaction mechanisms which are summarized in Table 2-1 on page 18. These discussions are by no means exhaustive but serve mainly to indicate the uncertainties in the existing state of knowledge.

2.2 Gaseous Pollutants

2.2.1 Carbon Dioxide

On a local basis, CO_2 is not considered to be a pollutant, but it is one of the most important species globally, because of its influence on the world's climate.

This was pointed out as early as the beginning of this century by Chamberlain (ref. 4). By 1950, evidence was accumulating that the mean concentration of CO_2 had increased by 10% from the value of 290 ppm determined in the 19th century. Since the local CO_2 concentration is heavily influenced by nearby combustion sources, trends in the global atmosphere can only be established in relatively undisturbed areas. One such area is the Mauna Loa Observatory in Hawaii. There are very few other stations around the globe and our knowledge about the global distribution is at best limited.

The major source of CO_2 is the oxidation of carbonaceous materials in the combustion of organic fuel and in the decay of organic materials. The major sink is the biosphere (photosynthesis). It is believed that the balance in this cycle is being disturbed by the increased emission of CO_2 into the atmosphere from the ever-increasing industrialization. This rate of increase is shown in fig. 2-1, which is based upon the estimates by Revelle (ref. 6) for commercial fuels from 1860 to 1960. Robinson and Robbins (ref. 5) have estimated the CO_2 emissions up to the year 2000, which is also shown in the same figure. If half the emitted amount remains in the atmosphere, the total CO_2 would increase from the present concentration of 320 ppm to about 370 ppm by the year 2000.

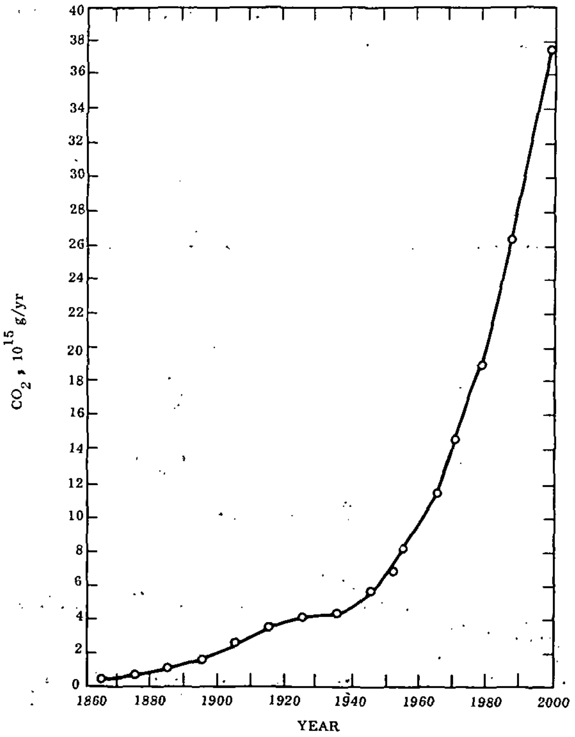

Figure 2-1. Estimated Historical and Projected CO_2 Emissions From Fuel Combustion (based on references 5 and 6)

There have been a number of theoretical models developed in which the effect of the CO_2 increase is linked with a mean global temperature increase. In general, these models have not been too successful because the end results were unreasonably sensitive to minor changes in some critical assumptions. For example, Manabe and Wetherald (ref. 7) calculate that the estimated increase in CO_2 concentration by the year 2000 would raise the average atmospheric temperature by 0.5° C. Whether this temperature increase would really occur is open to question, since it could be counterbalanced by a 1% change in total average cloudiness (ref. 8). In addition, the apparent increase of global aerosol concentration (ref. 9) could have a similar counterbalancing effect.

Measurements of the CO_2 concentration at isolated ground stations show great fluctuations. The results of Callendar (ref. 10) who analyzed historical and new CO_2 measurements for the time period from 1870 to 1955 are presented in fig. 2-2. More recent data for a twelve-month running mean at Mauna Loa between 1959 and 1963 indicate an increase of 0.68 ppm/yr (see fig. 2-3). The monthly averages show greater fluctuations and this is indicated in fig. 2-4 for the years between 1959 and 1970 (ref. 11). These fluctuations are caused by the seasonal assimilation and respiration exchanges in the biosphere. Since about 1968, even greater fluctuations and a greater than 0.68 ppm/yr increase is indicated in fig. 2-4.

In addition to the biosphere, the ocean is a major sink for CO_2 in the form of intake by biological matter. When these organisms die and settle onto the bottom, they are removed from the exchange cycle.

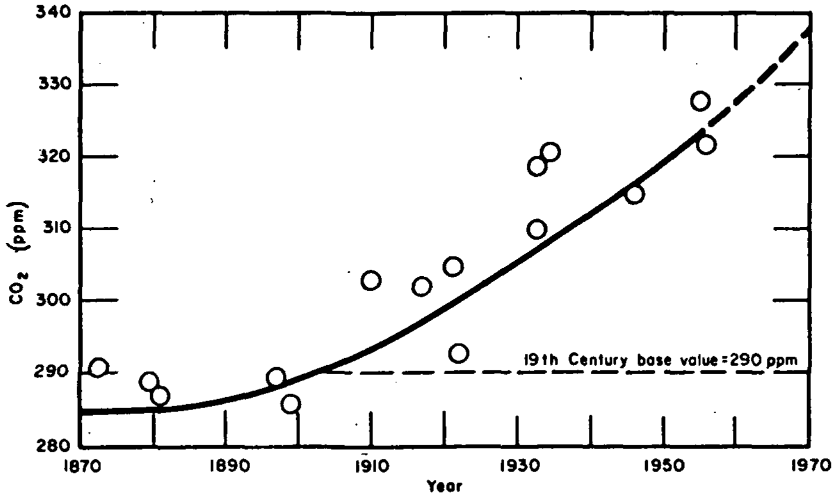

Figure 2-2. Average CO_2 Concentration in North Atlantic Region (from ref. 10)

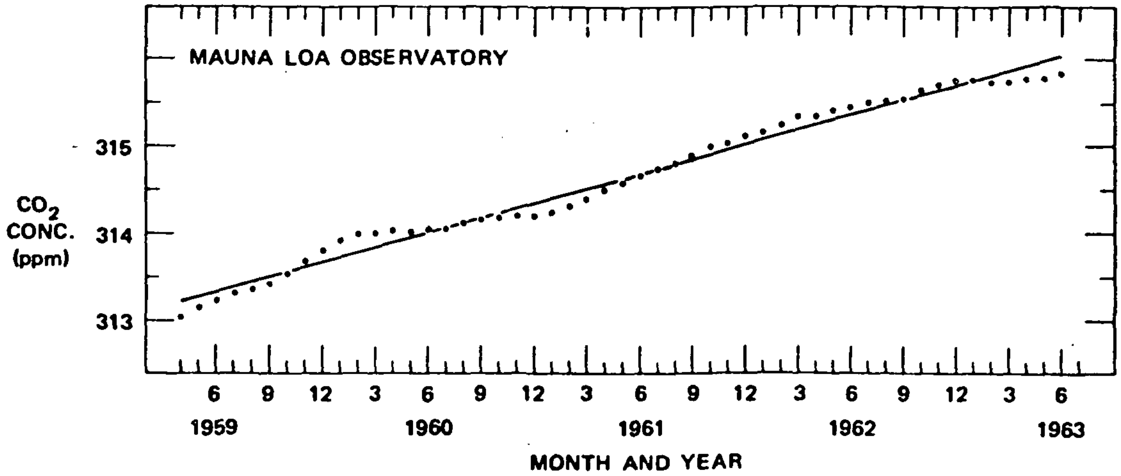

Figure 2-3. Twelve-Month Running Mean of the Concentration of Atmospheric CO_2 at Mauna Loa Observatory

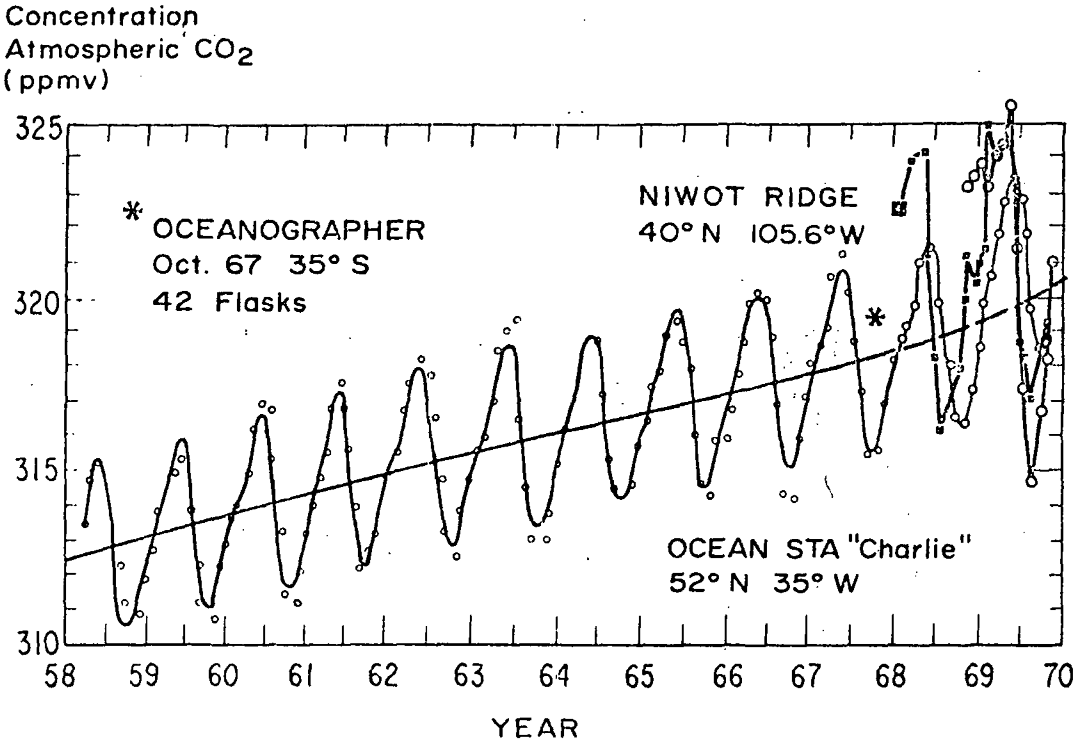

Figure 2-4. Atmospheric CO_2 concentrations at Mauna Loa Observatory (small open circles), Niwot Ridge, Colorado (solid squares), and Weather Ship "Charlie" (large open circles), plotted as functions of time. Also shown by the asterisk is the mean of 42 observations at Lat. 35^oS in the South Pacific, taken aboard the research vessel "Oceanographer." (from ref. 11)

2.2.2 Carbon Monoxide

The present knowledge of CO concentration, global distribution, sources and sinks is limited. CO was detected spectroscopically in the atmosphere by Migeotte (ref. 12) in 1949 through the observation of the 4.6-μm band in the solar spectrum at the Jungfraujoch Observatory. In the following decade, more spectroscopic data were obtained by Benesch et al. (ref. 13), Locke and Herzberg (ref. 14), and Shaw (ref. 15) at Jungfraujoch, Ottawa, Mt. Wilson and Columbus, Ohio. The mixing ratios obtained through these observations range from 0.031 to 2.2 ppm. It is clear that these measurements were too sporadic to permit firm conclusions about overall atmospheric concentration and long-term trends.

Even later data, taken more systematically, exhibit a similar scatter. Robbins et al. (ref. 16) report data taken at Camp Century in Greenland, North Coast of California, Crater Lake in Oregon and Patrick Point in California, which range from 0.03 to 0.9 ppm. The data seem to suggest that air masses originating over the Pacific Ocean contain lower amounts of CO (<0.06 ppm) than the continental air masses. Diurnal variations of a factor of 10 were also recorded. Subsequent measurements were made by Robinson and Robbins (ref. 17) in 1967 and 1968 in the North Pacific, Greenland and the South Pacific, with a range of 0.03 to 0.8 ppm.

All of these data seem to indicate large diurnal variations over the Pacific Ocean, with peak values at night. There is also a difference between the northern and southern hemispheres, with lower values in the southern hemisphere. In the past, large natural sources have been ruled out. The total man-made emission is estimated to be over 200 million tons, 85% of which comes from auto exhaust, the rest from industrial processes, domestic heating, power plants and forest fires. The total amount of CO in the atmosphere is estimated to be 560 million tons (corresponding to a 0.1 ppm mixing ratio), implying a lifetime of about 3 years. Robinson and Robbins (ref. 5) point out, though, that the observed short-term variations of CO in clean air suggest lower values. This would imply a higher production rate or a lower than 0.1 ppm average CO concentration in the atmosphere, or both. Since the estimate of the production rate is fairly reliable, they suggest a lower average mixing ratio (~.05 ppm). This is in agreement with the measurements in the South Pacific, but not in the North Pacific. They also claim that no sink exists in the atmosphere.

The theoretical study by Pressman et al. (ref. 18) indicates that the stratosphere provides a significant sink for CO through the reaction

$$OH + CO \rightarrow CO_2 + H.$$

The radical OH is produced in a moist ozonosphere with a rate several orders of magnitude faster than that of the CO oxidation reaction so that almost all the CO entering the stratosphere is destroyed. The rate-limiting factor is the transport of CO-rich air through the tropopause. The important conclusion reached by Pressman et al. is that the stratosphere is a sufficient sink for the present emission of CO into the troposphere by anthropogenic sources. Should this emission increase during the next 10 years, the stratospheric sink would not be sufficient to remove the additional CO because of the limitation in the diffusion rate. If this increase is not detected, it is argued that the man-made production is minor compared with the natural production and that sinks much larger than that provided by the stratosphere must be operative.

Recently, Seiler and Junge (ref. 19) and Junge et al. (ref. 20) have come to different conclusions. There is mounting evidence that the oceans provide a major source (see ref. 21 and fig. 2-5) and the lower stratosphere a major sink of CO. An additional tropospheric sink of unknown nature is also postulated. Using the natural production of the isotope $C^{14}O$ and its flux across the tropopause, model calculations were performed (ref. 20) to arrive at the magnitude of the tropospheric sink and residence time as a function of the tropospheric $C^{14}O$ concentration. It is argued that the residence time of $C^{14}O$ is about 0.2 yr. and that of $C^{12}O$ is about 1 yr. In fig. 2-6 the essential data on the global distribution of CO as a function of latitude is shown.

The importance of CO in the atmosphere has recently been demonstrated by Westberg et al. (ref. 22), who have shown that CO may play a role in the formation of photochemical smog. However, the concentrations of hydrocarbons, NO and CO used in the laboratory experiments were about an order of magnitude larger than those found in polluted atmospheres.

An additional source of CO was discovered by Swinnerton et al. (ref. 23). Concentrations of CO in rainwater collected at widely diverse locations are found to be 200 times super-saturated relative to the partial pressure of the gas in the atmosphere. The production of CO in clouds was tentatively attributed to the photochemical oxidation of organic matter and/or the slight dissociation of CO_2 induced by electrical discharges.

The activity by micro-organisms in the soil was first postulated (ref. 24) to play a role in the CO cycle in 1968. Recently (ref. 25) tests with a potting soil mixture indicated that CO in a test atmosphere was depleted from 120 ppm to near zero in 3 hours. Maximum activity occurred at 30° C in acidic soils with high content of organic matter.

Hays and Olivero (ref. 26) have postulated a reaction scheme that indicates a decreasing mixing ratio of CO_2 in the stratosphere due to photo-dissociation and a significant increase of CO.

Levy (ref. 27) has suggested in a steady-state model of the "normal" (unpolluted) lower troposphere that radicals and formaldehyde are formed, which in turn may be responsible for the rapid removal of CO, leading to a lifetime as

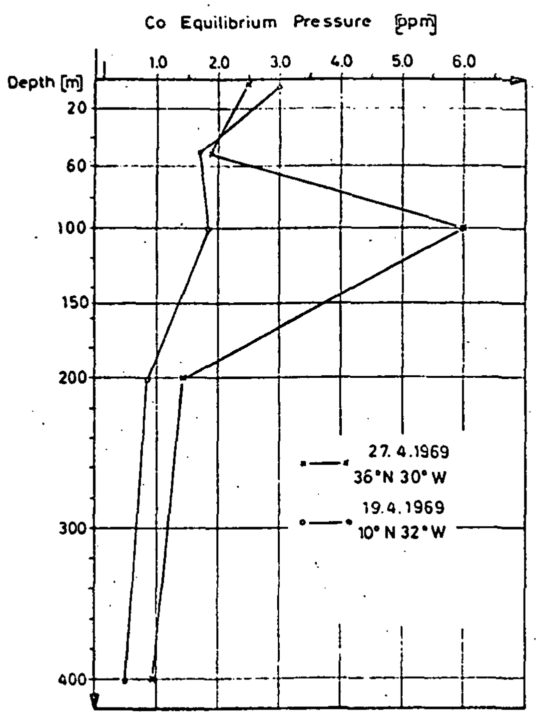

Figure 2-5. Typical profiles of dissolved carbon monoxide in Atlantic Ocean water. (From ref. 19.)

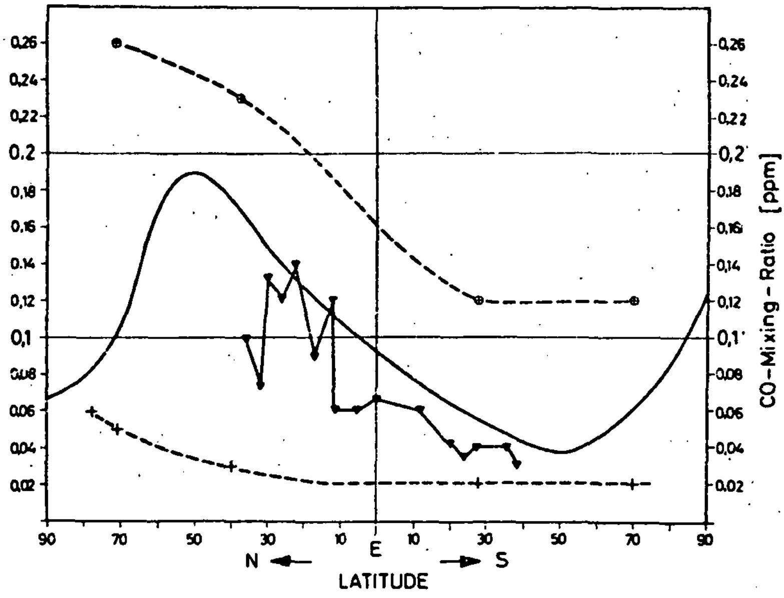

Figure 2-6. CO distribution as function of latitude. Measurements by Robinson and Robbins (ref. 17): full triangles represent Eltanin cruise (Nov.-Dec. 1967) from San Francisco to New Zealand; crosses represent the lowest CO-concentrations; circled crosses represent the highest CO concentrations; solid line represents the estimated mean CO distribution of CO as a function of latitude. (From ref. 20.)

low as 0.2 year. A similar mechanism, involving the hydroxyl radical and methane, has been proposed by Weinstock and Niki (ref. 28). The major removal mechanism for CO is the oxidation by OH and the major source is the oxidation of CH_4 by OH. The natural production of CO is estimated to be 25 times greater than the anthropogenic production. This scheme leads to a residence time of CO in the troposphere of about 0.1 year. Stevens et al. (ref. 29) reached similar conclusions after a three-year study of the CO distribution and temporal changes in Illinois. These workers estimate a yearly production of 3.9×10^9 tons/year for the entire globe, 0.4×10^9 tons/year of which is man-made.

2.2.3 Nitrogen Compounds

The primary emissions of nitrogen compounds are the naturally produced N_2O, NH_3 and the oxides of nitrogen, NO and NO_2, abbreviated to NO_x. Anthropogenic sources exist for the oxides of nitrogen, but their contribution is only about 10% of that of the natural sources (ref. 5). Thus, it would appear that the atmospheric nitrogen cycle on a global scale is little influenced by the man-made NO_x pollution. However, the established steady-state condition may be affected by the increased hydrocarbon and SO_2 emissions from anthropogenic sources, both of which form aerosols with the oxides of nitrogen and with ammonia.

The formation of aerosols, then, is the main reason why a study of the nitrogen cycle and measurements on a global scale are mandatory. On a local scale, NO_x in automobile exhaust has long been recognized as the main contributor to the formation of photochemical smog, with the subsequent reactions involving NO_2, O_3 and olefins to form the eye irritants PAN and PBZN (ref. 30, 31). It should be noted that similar reactions may occur above forests, which produce terpenes, which in turn react with atmospheric NO_2 and O_3 to form photochemical smog.

Robinson and Robbins (ref. 5) have formulated the schematics of the environmental circulation of nitrogen compounds. Essentially, three separate cycles, which do not interact with each other, have been postulated. One cycle involves the emission of N_2O from the biosphere (592×10^6 tons/yr) and the return to it, minus a small portion which entered the stratosphere to undergo photochemical reactions. The second cycle is the emission of ammonia gas (1160×10^6 tons/yr) from decay processes in the biosphere. About 75% is returned as NH_3 and 25% is converted into NH_4 to form with SO_2 the aerosol $(NH4)2\ SO4$, which either settles out or is washed out. The third cycle is the emission of NO_x, 769×10^6 tons/yr from the biosphere, and 53×10^6 tons/yr from anthropogenic sources. Of the total amount in the atmosphere, about 60% is returned as gas, 40% is oxidized to NO_3, which then forms nitrate aerosols.

Some measurements of the NO_x concentrations at different locations have been made since 1956. The results for NO_2 are plotted (from a table presented in ref. 5) in fig. 2-7 as a function of latitude in the northern and southern hemisphere for land

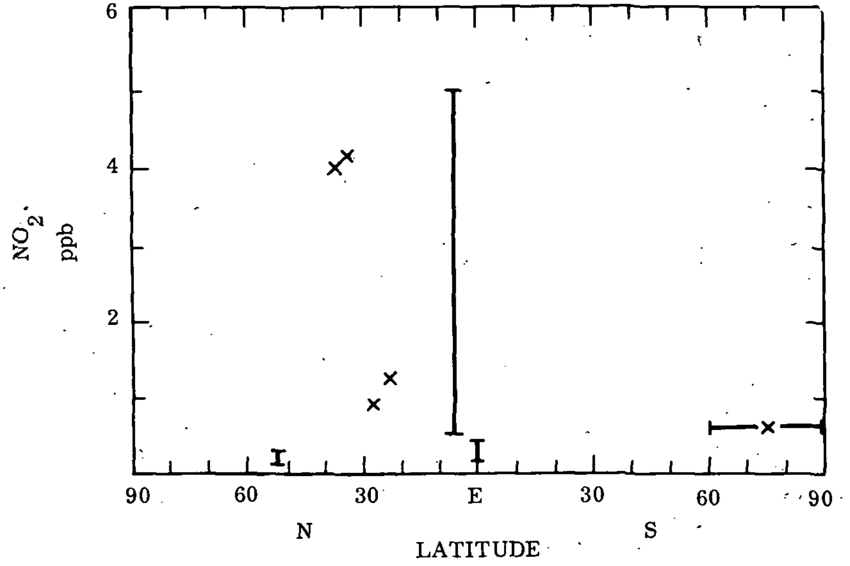

Figure 2-7. Measured Concentrations of Nitrogen Dioxide as a Function of Latitude. Data taken from ref. 5.

areas, together with mean concentrations assumed by Robinson and Robbins. Values for all ocean areas were assumed to be smaller by a factor of 8. Very few data are available for NO concentrations. Measurements by Lodge and Pate (ref. 32) in the Panama forest indicate a range from 0 to 6 ppb of NO. The only other available measurement for NO is from Pike's Peak, which gives a concentration of 2.7 ppb (ref. 33). A secondary nitrogen compound is nitric acid, which may also play a role in the formation of aerosols. This gas was discovered in the atmosphere by Murcray et al. (ref. 34), using sun occultation observations made from a balloon at 30 km. It appears that HNO_3 is layered much like ozone and is located primarily in the stratosphere from 10 to 50 km with a maximum mixing ratio of about 10 ppb. The background values of NH_3 are estimated to be from 6 to 20 ppb (ref. 5).

2.2.4 Sulfur Compounds

The major sulfur compounds in the atmosphere are SO_2, H_2S and sulfates. Of these, primary SO_2 emission is exclusively man-made, while up to 97% of H_2S is estimated to be naturally produced. The global importance of SO_2 lies in the fact that it reacts photochemically with NO_2 and hydrocarbons and also oxidizes to sulfates which react with NH_3 to form the ammonium sulfate aerosol. According to estimates made by Robinson and Robbins (ref. 5) the man-made SO_2 emission in 1965 is about as high as the natural production of H_2S (140×10^6 tons/yr). In terms of sulfur alone, man emitted about half of the amount produced by nature. These authors have also tabulated the SO_2 emission from 1860 to 1965 and have estimated further emission up to the year 2000, based upon estimates of production increases in the coal, petroleum, copper, lead and zinc industries. These estimates will change as more worldwide emission controls become effective. The results for no emission control are shown in fig. 2-8. It appears that by the year 1995, the man-made sulfur emission (one-half of 280 × 10^6 ton/yr) will exceed the natural sulfur emission.

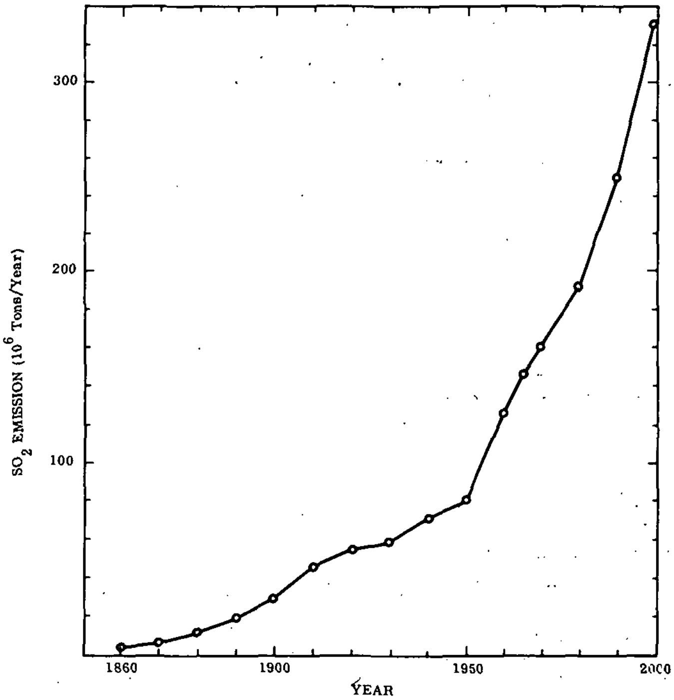

Figure 2-8. Estimated Historical and Projected SO_2 Emissions (based on ref. 5)

Since most industries are located in the northern hemisphere, it is estimated that over 90% of the total SO_2 emissions occur north of the equator. The corresponding values for the natural sources from land, marine life and sea spray are estimated to be about 60% for the northern, and 40% for the southern hemisphere. This would mean that the man-made emission of sulfur will exceed the natural production by 1975 in the northern hemisphere (see fig. 2-9).

The background values for SO_2 and H_2S are estimated to be 0.2 ppb with a residence time of 4 and 2 days, respectively. However, earlier estimates place the background values higher by a factor of 10 (ref. 35).

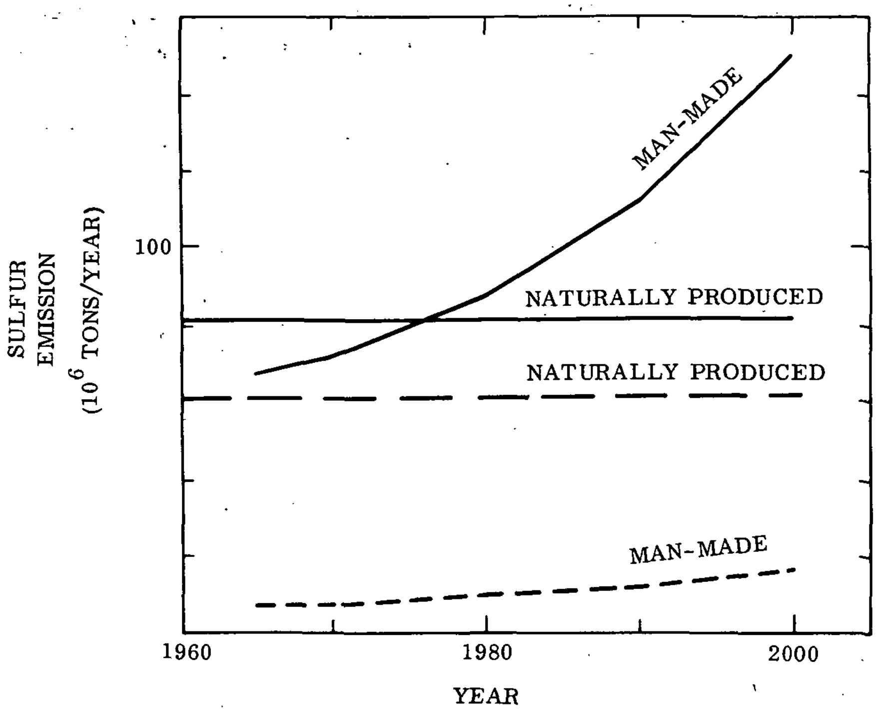

Figure 2-9. Estimated Sulfur Emission by Anthropogenic and Natural Sources for Northern (Solid Line) and Southern (Dashed Line) Hemispheres (Based on ref. 5)

2.2.5 Hydrocarbons

Hydrocarbons play an important rôle in the formation of smog and of aerosols. Except for methane, which is produced mainly in natural processes, the background levels and global distribution of the HC's are not known.

Methane is formed mainly through biological decay (ref. 36) and appears to have a constant mixing ratio of 1.4 ppm up to 20 km (ref. 37). In the stratosphere, the mixing ratio decreases (ref. 38), and it is believed that CH_4 is oxidized to H_2O and CO_2 (ref. 39) and may be involved in the ozone photochemical reactions. In the troposphere, methane does not appear to be of importance because of its low reactivity nor does it play a significant role in the heat balance of the atmosphere. However, this statement may not be true in view of the reaction with OH, according to references 28 and 29. All the other paraffins are believed to be less abundant and, thus, even less significant than CH_4 on a global scale; however, high concentrations due to automobile exhaust emissions may have some influence on the photochemistry of smog (ref. 40). Olefins and aromatics are more reactive than the paraffins and are thus more important in the photochemistry of smog. But because of their greater reactivity, their background levels are very low.

One of the end products in photochemical smog is formaldehyde, which is rather stable. On a global scale, its formation in the "unpolluted" atmosphere has been postulated by Levy (ref. 27) to occur due to reactions involving the radicals OH, HO_2, and CH_3O, with prevailing daytime concentrations up to 2 ppb.

Another class of HC's are the nitrogen-hydrocarbons, i.e., peroxyacetylnitrate (PAN) and peroxybenzoylnitrate (PBZN), which are formed in photochemical smog and which cause respiratory diseases, eye irritation and plant damage. These compounds are assumed to have a life time of 12 to 24 hours, thus they may spread during nighttime from urban centers into rural areas.

2.2.6 Stratospheric Water Vapor

The concentration profile of water vapor in the stratosphere is variable and should be measured on a routine basis. Its significance lies in the fact that stratospheric water vapor is important in the photochemical reactions involving ozone and may play a role in the formation of stratospheric aerosols; the importance of these processes on the heat balance is not clear. The direct influence of water vapor on the ozone layer concentrations has been a subject of several studies (ref. 41, 42). It was concluded that the reduction in ozone and thus the increase of transmitted solar ultraviolet radiation was not significant. The same conclusion was reached during the Survey Conference on the Climatic Impact Assessment Program, held February 15-16, 1972, in Boston under DOT sponsorship (see ref. 43).

2.2.7 Ozone

Ozone is found throughout the atmosphere with the highest concentrations ($\sim 20 \times 10^{-3}$ cm/km) near 25 km, and normally low concentrations ($\sim 2 \times 10^{-3}$ cm/km) in the troposphere. The ozone in the troposphere mostly diffuses from the stratosphere (ref. 44). However, in areas with large numbers of automobiles, such as Los Angeles, significant ozone concentrations (up to 50 times normal) may be formed by photochemical reactions involving the oxides of nitrogen and hydrocarbons from car exhausts.

The ozone in the upper stratosphere is in photochemical equilibrium. However, this equilibrium may be disturbed by interaction of the ozone with the exhaust gases of large numbers of SST's. Since the stratospheric ozone shields the surface of the earth from the harmful short wavelength solar radiation between 2000Å and 3000Å, it is important that these equilibrium concentrations not be significantly reduced. A recent investigation by Johnston (ref. 45) indicates that the projected increase in stratospheric oxides of nitrogen could reduce the ozone shield by a factor of 2. Scientists at the Survey Conference (ref. 43) agreed that the nitrogen oxides emitted by conventionally fueled engines can possibly reduce stratospheric ozone. (However, A. Ferri (ref. 43) points out that by redesigning the engines, the production of oxides of nitrogen can be minimized.)

2.2.8 Others

The hydrogen halides are only of local concern as effluents of certain industries and incinerators where plastic refuse is burned.

Volatile fluorocarbons are also only of local concern. Their present global background values are believed to be very low.

Many elements are emitted into the atmosphere due to man's activities. They are being measured by local agencies and no remote sensing techniques have been identified as being feasible.

2.3 Aerosols

The scientific community has become increasingly aware in recent years of the importance of atmospheric aerosols and their optical properties in possible climate modification. The aerosols in the atmosphere consist of man-made and natural particles, and it is the man-made contribution due to combustion added to the natural (dust, sea spray, forest fires and volcanic dust) background that is generally considered to be important in determining climatic changes. However, the man-made contribution on a global scale is quite small; estimates range from a negligible amount (ref. 46) to about 6% of the natural background (ref. 47). (Of course, on a local scale, e.g., the Los Angeles basin, man-made particles can far exceed the natural concentration.) It may well be that global changes in the natural background are more important than man-made particles. With the increased cultivation of land and activities of man in arid areas, the background level of aerosols is likely to increase.

McCormick and Ludwig (ref. 48) presented evidence of a worldwide buildup of atmospheric aerosols which could increase the earth albedo resulting in a cooling of the earth-atmosphere system. This effect would counteract the postulated increase of temperature in the lower atmosphere due to the "greenhouse effect" of the increased CO_2 emissions by human activities. In fact, there has been a decrease in the mean annual air temperature since about 1945 at mid latitudes, suggesting that the aerosol pollution effect is greater than that of CO_2 increase. However, the effects of aerosols and CO_2 are more complex than suggested above, so that their effects on climate are not readily predicted. For instance, Robinson (ref. 49) points out that the earth may self-regulate its temperature by the variation of cloud amount: the higher temperatures, due to the CO_2 "greenhouse effect", lead to a higher water content in the lower atmosphere, which may increase the cloud amount; this increases the albedo, thereby decreasing the temperature. Robinson concludes there is no justification for forecasting a final equilibrium temperature due to an increase in CO_2 content, until atmospheric models are significantly improved to include the cloud cover as a variable.

In addition to the uncertainties in the climatic effects of CO_2, the cooling effect of aerosols suggested by McCormick and Ludwig may not be correct. Charlson and Pilat (ref. 50), Atwater (ref. 51) and Mitchell (ref. 52) have shown that since aerosols absorb and scatter, they may produce warming or cooling, depending on the ratio of absorption to scattering.

Thus, it is clear that considerably more work on the complex problem of modelling the atmosphere and on the optical properties of aerosols is needed before the long term effects of man-made pollution can be predicted. Since these problems will not be solved in the near future, it is desirable to initiate global measurements of aerosols on a continuous basis to monitor any changes. At the same time the earth albedo should be monitored and related to the aerosol changes and mean air temperature variations.

TABLE 2-1. SOURCES, SINKS AND DISTRIBUTION OF POLLUTANTS

Yearly Total Emission 10^6 Tons		Sources		Concentration (ppm) Troposphere			(ppm) Lower Stratosphere	Residence Time in Troposphere	Removal Mechanism
		Natural	Anthropogenic	Global	Regional	Local			
CO	231	Fires, Ocean	Combustion	~.1 (?)	>.1	< 100	.003	0.1 - 3 yr.	Sink in stratosphere and biosphere
CO_2	1012	Decay, Ocean	Combustion	320	>320	Up to 500	320	4 yr.	Absorption by oceans; photosynthesis
SO_2	146	Volcanoes	Combustion, Chem. Process	.002	.05-.1	< 3	Trace ?	4 day	Oxidation; absorption by aerosols
H_2S	103	Volcanoes, biol. action	Chem. Process			.002 - 1	Trace ?	2 day	Oxidation to SO_2
HF			Incineration			.001 - .08			
HCl			Incineration			< 30			
NO			Combustion	.0001		< 1.4	.1 (60 km)		
	553	Bacterial Action in Soil (?)			.03-.06			5 day	Oxidation
NO_2			Combustion Photochem.	.001		<.8	Some		
N_2O	1000	Biological	None	.25		.25	~.02	1-3 yr.	Sink in stratosphere and biosphere
HNO_3		Stratosphere Photochem.	Chemical Process			?	~.006 (max)		
NH_3	5904	Biological	Waste Treatment	.006-.02		.02-3		2 days	Reaction with SO_2; oxidation
O_3		Photochemistry	Photochemistry			.009-1	1-10		
H_2O		Evaporation	Combustion	Variable			3-200		
CH_4		Biological	Combustion	1.5		2-3	<.1	16 yr.	
PAN		None	Photochemistry			< .1			
< HC >	568	Biological	Combustion	?		< 20			
Aerosols	3900	Sea Spray, Vegetation	Combustion	$\sim 70 \mu g/m^3$		Variable	$-0.7 \mu g/m^3$	3-5 days	Washout; sedimentation

3

OBSERVATIONS OF GASEOUS POLLUTANTS

In remote sensing of gaseous pollutants, the phenomenon to be observed is the modulation of radiation in specific regions of the electromagnetic spectrum arising from the presence of trace contaminants in the atmosphere. Each pollutant has a unique spectral signature, whose observed intensity is a measure of the optical thickness.

For convenience, we distinguish three separate operational modes from satellites: passive earth-oriented (nadir experiment), passive horizon-oriented (limb experiment), and modes utilizing active sensors.

The information obtained in the nadir experiment relates directly to the measurement of the concentration of the pollutants in the troposphere, where the bulk of the global pollution is found. However, this observational model suffers from the fact that in the thermal region the large contribution of the earth background radiation has to be taken into account, requiring additional information about surface parameters, and that in the sun-reflected region, uncertainties due to the atmospheric back-scattering are introduced.

These limitations are reduced in the limb experiment, where the cold space background does not contribute. However, the information obtained in the limb experiment is restricted to the stratosphere because of clouds extending throughout the troposphere.

In the active double-ended mode, where the source is located on the ground or on a cooperating platform, the overall systems complexity is greatly increased because of the requirement of aligning the source and receiver precisely.

The active single-ended mode (Raman, fluorescence) appears to offer many advantages from the systems standpoint. It suffers, however, from the larger power requirements of the laser source to assure an adequate return signal from the scattering pollutants.

3.1 Passive Mode

Passive observations of trace contaminants from satellites can be conducted through a nadir experiment, in which the sensor is earth-oriented, and through a limb experiment, in which the sensor is oriented toward the horizon. In both experiments, the sun radiation and/or the thermal radiation may be the energy source. In principle, the electromagnetic spectrum from the ultraviolet to the microwave region is available. However, we found that the infrared region from 2 to 20 μm is the most suitable one for observing gaseous pollutants in the troposphere and lower stratosphere. Measurements in the visible and ultraviolet region are extremely difficult to interpret because of the Rayleigh and Mie scattering. Measurements in the far infrared between 20 μm and the microwave region, are not possible because of the strong rotational band of water vapor. Measurements in the microwave region are hampered by the poor specificity due to the line broadening. Although we had over-estimated the line half-widths in our previous report (ref. 3), the conclusion reached at that time remains unchanged. Most air-broadened molecular absorption lines have half-widths of the order of 0.1 $\text{cm}^{-1}\,\text{atm}^{-1}$ ($\sim$3 GHz atm^{-1}). This value, in frequency units, is largely independent of frequency, depending primarily on the mean time between collisions. For microwave frequencies of the order of 30-100 GHz, a line half-width of 3 GHz is quite large compared with the width of the atmospheric windows, and if several species, each with several lines, are present, considerable overlapping of lines must be expected. The lines indicated schematically in Figure 3-27 of Ref. 3 are the most prominent ones in the microwave spectrum. For nonlinear molecules, such as NO_2, SO_2, NH_3, etc., many other less prominent lines appear in the spectrum. Microwave spectroscopy has proved extremely valuable in providing unambiguous species identification, but at pressures of the order of 10^{-6} to 10^{-3} atm (equivalent to altitudes above 50 km) under which conditions the lines are extremely narrow. It appears that the use of microwave methods would be of value only for lines of sight which are restricted to pressures much lower than exist in the troposphere.

3.1.1 Nadir Experiment

3.1.1.1 Upward radiance at the top of the atmosphere. The radiation at the entrance pupil of the sensor designated here as $E(\omega)$ is in general composed of the solar energy reflected from the earth surface and scattered from the atmosphere, and the thermal emission from the ground and the atmosphere.

The actual calculation of $E(\omega)$ is an extremely formidable task. The major complexities arise from the presence of the scattering processes, which alter the direction of propagation of individual photons in a manner which can only be predicted statistically. It is thus desirable to separate $E(\omega)$ into its components as

C2324

far as possible in order to obtain an overview of the problem. The quantity $E(\omega)$ may be written as a sum of component terms in the following form:

$$E(\omega) = E_G(\omega) + E_R(\omega) + E_\phi(\omega) + E_{\phi R}(\omega) \tag{3-1}$$

in which $E_G(\omega)$ represents the thermal radiation emitted by the underlying surface and the atmosphere, $E_R(\omega)$ represents the incident solar radiation reflected by the surface, $E_\phi(\omega)$ represents the radiation scattered by single or multiple-scattering processes in the atmosphere without having been reflected from the surface, and $E_{\phi R}(\omega)$, another atmospheric scattering term similar to $E_\phi(\omega)$, but for radiation which has undergone a reflection from the surface having a different reflectivity than the term $E_R(\omega)$. A schematic representation of these radiation terms is shown in fig. 3-1.

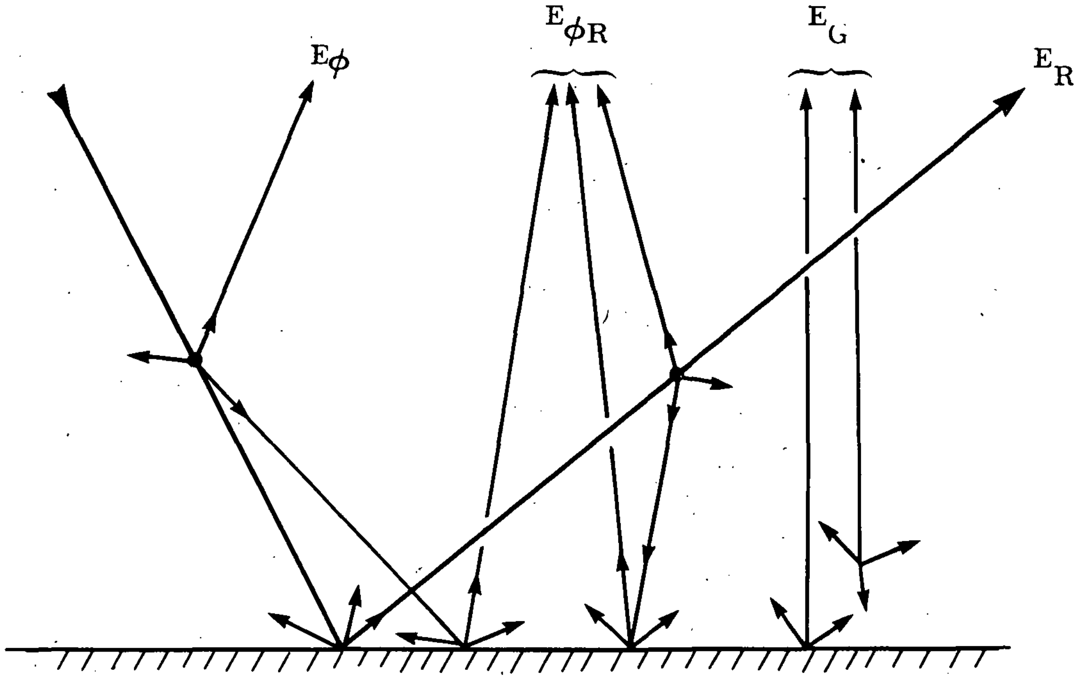

Figure 3-1. Schematic Representation of Terms Contributing to the Radiation Emerging from the Top of the Atmosphere

The functional dependence of these components of $E(\omega)$ is indicated as follows:

$$\left.\begin{aligned} E_G(\omega) &= E_G\left(\omega;\ \epsilon,\ \tau,\ T_S,\ T_A\right) \\ E_R(\omega) &= E_R\left(\omega;\ \rho,\ \theta,\ \tau\right) \\ E_\phi(\omega) &= E_\phi\left(\omega;\ \theta,\ n\sigma,\ \tau\right) \\ E_{\phi R}(\omega) &= E_{R\phi}\left(\omega;\ \rho,\ \theta,\ n\sigma,\ \tau\right) \end{aligned}\right\} \tag{3-2}$$

where T_S, T_A are the surface and atmospheric temperatures, ϵ, ρ are the surface emissivity and reflectivity, θ is the sun zenith angle, $(n\sigma)$ is the product of number of scattering centers (n) and scattering cross section (σ), τ is the transmissivity of atmosphere, referring generically to all sources of attenuation: molecular and particulate absorption and molecular and particulate scattering.

The equation of radiative transfer, without scattering and without solar radiation, for thermal radiation emerging from a plane-parallel atmosphere with an underlying surface of emissivity $\tau(\omega)$ can be written as

$$\begin{aligned} E(\omega) &= E_G(\omega) \\ &= \epsilon(\omega)\, N^0\left(\omega, T_S\right) \tau(\omega, 0) + \int_0^h N^0\left(\omega, T(z)\right) \frac{d\tau(\omega, z)}{dz}\, dz \qquad (3\text{-}3) \end{aligned}$$

in which $N^0(\omega, T)$ is the Planck blackbody function, T_S is the surface temperature, h is altitude at top of atmosphere, $\tau(\omega, z)$ is the monochromatic transmissivity of the atmosphere at wavenumber ω between altitude z and top of atmosphere, T(z) is the temperature of the atmosphere at altitude z.

The general expression for the transmissivity is given by

$$\tau(\omega) = \Pi_i\, \tau_i(\omega) = \exp\left[-\int \sum_i \kappa_i(\omega)\, c_i(z)\, p_t(z)\, dz\right] \qquad (3\text{-}4)$$

where $\kappa_i(\omega)$ is the extinction coefficient for species i which is given by the sum of the scattering and absorption coefficients, $c_i(z)$ is the concentration of species i at z, $p_t(z)$ is the total pressure, and z is the path length.

The contribution from the direct beam of the sunlight reflected from the surface becomes significant at the shorter wavelengths and is given by

$$E_R(\omega) = \frac{1}{\pi}\left[1 - \epsilon(\omega)\right] \cos\theta\, H_s(\omega) \left(\tau(\omega)\right)^{\alpha} \qquad (3\text{-}5)$$

where $[1 - \epsilon(\omega)]$ is the ground reflectance of a diffuse surface, θ is the sun zenith angle, $H_s(\omega)$ is the sun irradiance on top of the atmosphere, $\tau(\omega) = \tau(\omega, 0)$ is the transmission vertically through the atmosphere, and $\alpha = 1 + f(\theta)$ with $f(\theta) = \sec\theta$ for $0 \leq \theta \leq 60°$ and Ch θ for $\theta > 60°$. (Ch θ is the Chapman function.)

The terms $E_\phi(\omega)$ and $E_{\phi R}(\omega)$ cannot be expressed in a simple form like $E_G(\omega)$ and $E_R(\omega)$, due to the complexities of multiple scattering, particularly when Mie scattering is involved. However, both terms may be estimated in particular cases where calculations have been performed for zero albedo and other albedos, as described below.

Figure 3-2 shows the magnitude of the various terms in Eq. 3-1 for typical conditions over land and over oceans. The observer is looking vertically down and the sun zenith angle is 45°; both the land and the ocean are assumed to be Lambertian reflectors with albedos of 0.2 and 0.02 respectively, and hence emissivities of 0.8 and 0.98 respectively, at all wavelengths. The surface temperature is assumed to be 300K. For simplicity in the figure, the effects of atmospheric absorption and emission in the infrared are not included; in general, the radiance level would be lower in atmospheric absorption bands. The term $E_G(\omega)$ is thus given by only the first term on the right hand side of Eq. 3-3, with $\tau(\omega, 0) = 1$.

The direct solar beam term $E_R(\omega)$ is given by Eq. 3-5, with the atmospheric transmission in the UV and visible based on the 1964 model of Elterman (ref. 53), who included molecular and particulate extinction by scattering, and ozone absorption.

The first scattering term $E_\phi(\omega)$ is the radiance calculated for a model atmosphere with an underlying zero albedo. Plass and Kattawar (ref. 54) have made such calculations, using Monte Carlo techniques, for Elterman's 1964 model atmosphere at wavelengths ranging from $0.3\,\mu$ to $1.67\,\mu$. The values were extrapolated to the longer wavelengths assuming a smooth variation of scattering extinction (ref. 55). This term $E_\phi(\omega)$ is independent of the underlying albedo.

The second scattering term $E_{\phi R}(\omega)$ depends on the albedo. This term has not been determined explicitly in any of the model calculations. However, it is contained implicitly in calculations for surfaces with non-zero albedo and may be extracted by consideration of Eq. 3-1. The terms $E_R(\omega)$ and $E_\phi(\omega)$ have been calculated as explained above, so that at the shorter wavelengths where $E_G(\omega)$ is negligible,

$$E_{\phi R}(\omega) = E(\omega) - E_R(\omega) - E_\phi(\omega)$$

The results of Plass and Kattawar were used to determine $E_{\phi R}(\omega)$ for an albedo of 0.2. The values for an albedo of 0.02 were obtained by assuming that $E_{\phi R}(\omega)$ is proportional to the albedo. This assumption was verified to be reasonable from the calculations of Dave and Furukawa (ref. 56) for a pure Rayleigh atmosphere.

The values of the reflected sunlight terms in fig. 3-2 are for a normal amount of aerosols, as defined by Elterman (ref. 57) for a ground level visibility of 25 km. As the number of aerosols increases, so $E_R(\omega)$ decreases and $E_\phi(\omega)$ increases; the value of $E_{\phi R}(\omega)$ will initially increase and then decrease as the particulate optical thickness becomes very large (in the limit of infinite optical thickness, $E_{\phi R}(\omega)$ is zero since no radiation reaches the surface).

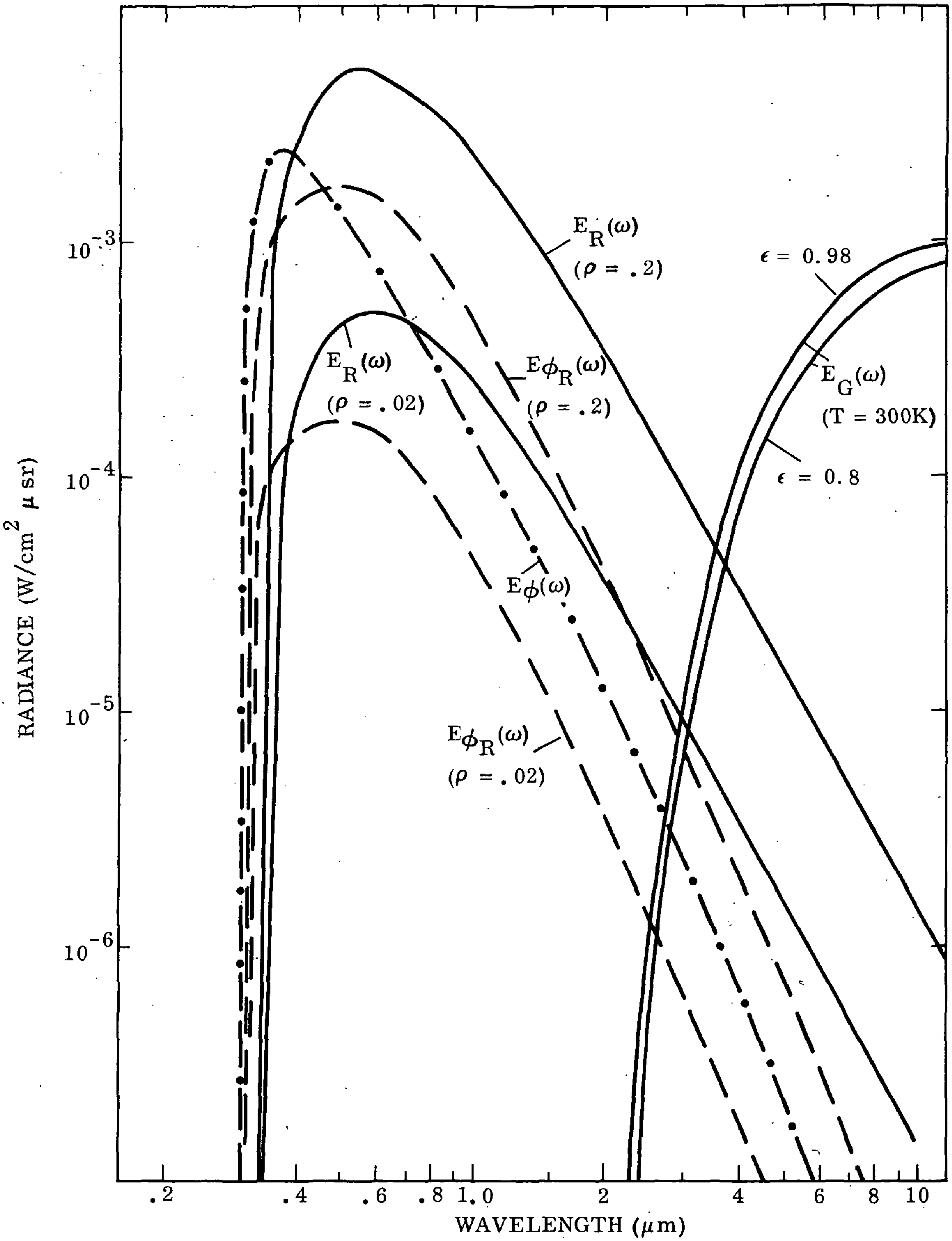

Figure 3-2. Upwelling radiation at the top of the atmosphere. Contributions from reflected sun radiation $E_R(\omega)$, atmospheric scattering $E_\phi(\omega)$ and $E_{\phi R}(\omega)$, and thermal radiation $E_G(\omega)$. Ground temperature = 300° K, sun zenith angle = 45°; particulate distribution according to Elterman 1964 (ref. 53).

Figure 3-2 shows that the sunlight scattered by the atmosphere contributes significantly to the upward radiation. It is much greater than the direct beam reflected from the surface in the ultraviolet, but becomes less at longer wavelengths. However, even at 2 μm, the scattered radiation amounts to about 35% of the reflected radiation for an albedo of 0.02, and about 12% for an albedo of 0.2. At longer wavelengths, where thermal emission dominates, the scattered sunlight term is negligible. There is, of course, some scattering of the thermal radiation. However, since the optical thickness is less than 0.1 beyond 4 μm (in Elterman's model), only single scattering is important (ref. 58), and the contribution to the total upward radiation is very small. In addition, the scattering coefficient decreases rapidly with increasing wavelength (by a factor of about 20 between 4 and 10 μm) (ref. 59).

Although the problem of atmospheric scattering is very much reduced in the thermal region, a different type of problem must be solved. Since the emission from the ground and the atmosphere depends upon the ground brightness temperature and the temperature profile of the atmosphere, an independent knowledge of these parameters is required for the data interpretation. (Since the signal in this region depends on the pollutant density and on the temperature difference between the pollutant and the underlying surface, the technique shows a signal weighting function with a broad peak in the lower troposphere.) Fortunately the atmospheric temperature profile and the ground brightness temperature can be determined to a degree of accuracy sufficient for the data analysis of pollutant concentrations.

Since every spectroscopic instrument integrates over a spectral interval ($\Delta\omega$), the observable radiance (neglecting instrument parameters) becomes

$$E_{\Delta\omega} = \int_{\Delta\omega} E(\omega)\, d\omega \qquad (3\text{-}6)$$

where $E(\omega)$ is given by Eq. (3-1). The unknown quantity for which Eq. (3-6) must be solved is the pollutant concentration. This is indicated by identifying one of the species i which contributes to the spectral interval $\Delta\lambda$, as species p. Thus, from Eq. (3-2)

$$\tau = \tau_1 \tau_2 \ldots \tau_p \ldots$$

where τ_1, τ_2 ... are the transmissivities of the normal atmospheric constituents, and τ_p is that of the pollutant species. The expression of τ_i for gaseous constituents is given by

$$\tau_i(\omega) = \exp\left[- \int_{z'} k_i\big(\omega, p_t(z), T(z)\big)\, c_i(z)\, p_t(z)\, dz \right] \qquad (3\text{-}7)$$

where $k_i(\omega, p_t(z), T(z))$ is the monochromatic absorption coefficient as a function of wavenumber ω, total pressure p_t, and altitude dependent temperature $T(z)$, $c_i(z)$ is the altitude dependent concentration, and dz is the incremental geometrical pathlength in the vertical direction.

The corresponding expression for particulate matter is given by

$$\tau_i(\omega) = \exp\left[-\int_{z'} \sigma_i(\omega)\, n_i(z)\, dz\right] \tag{3-8}$$

where $\sigma_i(\omega)$ is the extinction cross section and $n_i(z)$ is the particulate number density.

If in a given spectral interval, in which the pollutant absorbs, n independent measurements could be taken, namely $E_{\Delta\omega 1}$, $E_{\Delta\omega 2}$, . . . , $E_{\Delta\omega n}$, it would be possible to obtain the pollutant concentration in n layers. However, for the low concentrations of pollutants existing in the atmosphere, n such independent measurements are not feasible. Thus, only one independent measurement can be made which permits the determination of one average value of pollutant concentration throughout the atmosphere - in other words, $c_p(z) = \text{constant}$.

In order to establish the feasibility of measuring the average concentrations of pollutants from satellites, computations of $E(\omega)$ and $E_{\Delta\omega}$ have been made under realistic physical conditions. These computations require that the monochromatic absorption coefficients for all species (pollutant as well as normal atmospheric constituents) be known.

Until the present study, the line parameters (position, strength, width, and lower energy level) of only a few molecules of interest have been published in the open literature. Thus, most feasibility calculations conducted so far use either the total band strength (ref. 60) or band model parameters. In our previous study (ref. 3) we used band model parameters for the pollutant and atmospheric species and the Curtis-Godson approximation for the radiative transfer in a non-homogeneous atmosphere (see also Appendix D). As we had pointed out, these calculations serve only to obtain an approximate value of the signal change due to the presence of a postulated pollutant concentration. For the purpose of evaluating the influence of interfering lines from other species, band model calculations are not sufficient.

3.1.1.2 Pollutant spectra in the infrared. In this section, we discuss the major absorption bands of the pollutants in the infrared region between 2 and 20μ. Figure 3-3 shows the spectral location of the pollutants in relationship to the major absorption bands of water vapor and carbon dioxide. The two blackbody curves represent the thermal emission and are given for typical values of ground temperatures and atmospheric temperatures. Besides the interference by H_2O and CO_2,

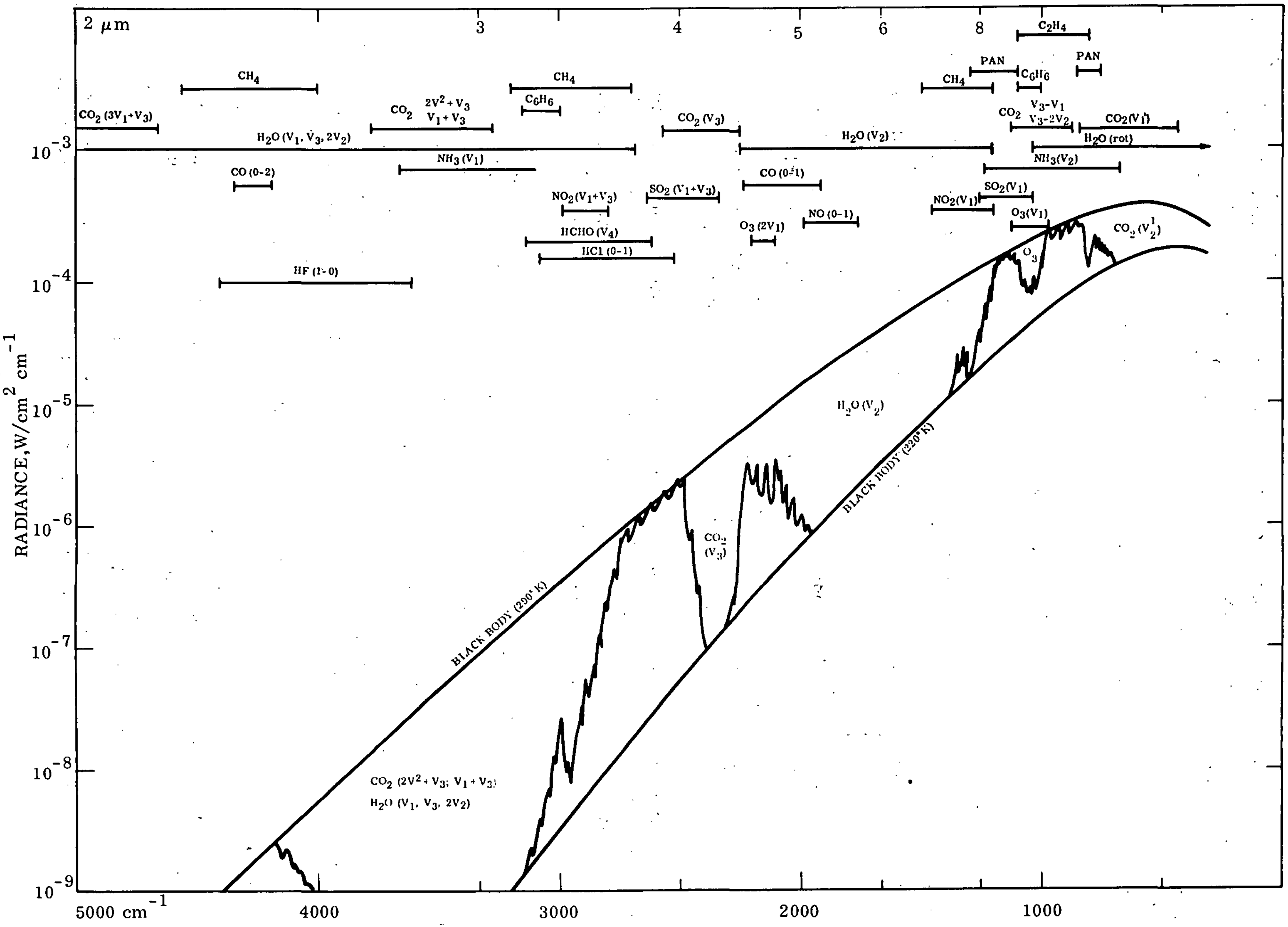

Figure 3-3. Overview of Atmospheric and Pollutant Absorption Bands

many other atmospheric constituents are also interfering, as is shown in Table 3-1. On the left hand side of this table, seven pollutants are listed. Across the top, these pollutants together with interfering atmospheric species are listed. The entries under "Solar Lines" refer to the Fraunhofer lines contained in the sun spectra, for which a correction must be made when the reflected sun light is observed.

Under a separate NASA-sponsored program (ref. 61) we have generated the line parameters for most of the transitions listed in the table. A brief description of the approach using a symmetric top model is given in the Appendices. A summary of the molecules we have investigated, their respective transitions, the number of lines calculated and their overall agreement with experimental data are shown in Table 3-2. From the schematic representation in fig. 3-3 and from Table 3-1, it is clear that no single pollutant can be observed without interference by one or more other species. "Interference" means that spectral lines of other species are located within the pollutant rotation-vibration band. Since the total strength of the interfering lines may be stronger than the total strength of the pollutant lines, measurements taken at low spectral resolution require large corrections.

The requirement of large corrections is reduced for measurements taken at a high spectral resolution. In that case, single lines can be distinguished and the equivalent width can be estimated after judiciously choosing the baseline, from which the area under the line contour is to be determined.

In Appendix A, details about the spectra of the major pollutants and interfering species are discussed.

3.1.1.3 Calculated signal change due to pollutants. In this section we discuss the results obtained from the line-by-line radiative transfer computations, made for various atmospheric conditions.

First we present the results of the calculated radiance at the top of the atmosphere for a spectral region where both the reflected sunlight and thermal radiation contribute (4-6μm). The function $E(\omega)$ in Eq. (3-6) is given by the sum of Eqs. (3-3) and (3-5) and the integration limits are from 2070 to 2220 cm^{-1}. For these calculations, the contribution of the scattering terms E_ϕ and $E_{\phi R}$ have not been included, because the required Monte Carlo calculations, which include the absorption by the pollutant molecules, have not been performed as yet. The estimated contributions of these terms amount to less than 10% of the ground reflected sun radiation E_R, when the reflectivity is 0.2 and the sun angle is 45° (see fig. 3-2). For these conditions, the reflected sun radiation E_R amounts only to about 10% of the thermal radiation.

In the calculation, the troposphere is divided into 8 layers and the stratosphere into 12 layers. The U.S. Standard Atmosphere (ref. 62) is assumed, with the temperature and pressure profiles as shown in fig. 3-4, and the Gutnick water vapor profile (ref. 63) as shown in fig. 3-5.

TABLE 3-1. INFRARED BANDS OF POLLUTANTS AND INTERFERING GASES

Pollutants \ All Species	λ (μm)	CO_2	CO	SO_2	NO_2	NH_3	NO	CH_2O	N_2O	CH_4	H_2O	HDO	H_2O^{18}	O_3	Solar Lines
CO_2	1.6	$3\nu_1 + \nu_3$								$2\nu_3$	$2\nu_2 + \nu_3$				Fe, C, Ni, S, Si, Ti, Na, P, Mg
	2.1	$2\nu_1 + \nu_3$									$\nu_1 + \nu_2$ $\nu_2 + \nu_3$ $3\nu_2$				Fe, Ca, Ni, Si
CO	4.6	$\nu_1 + \nu_2$ $2\nu_1 - \nu_2$	0-1						ν_3		ν_2 $\nu_3 - \nu_2$ $\nu_1 - \nu_2$			$2\nu_1$	Co
	2.3		0-2							$\nu_3 + \nu_4$ (?)	ν_1, ν_3	$3\nu_2$ (?) $\nu_1 + \nu_2$			Fe, Ti, Na, P, Mg, C, Ni, S, Si
SO_2	8.6			ν_1					$2\nu_2$	(?)	ν_2	ν_2	ν_2	ν_3	
	4			$\nu_1 + \nu_3$					$\nu_1 + 2\nu_2$ $2\nu_1$	few lines					Si, Ca, Na
NO_2	7.6				ν_1				ν_1	ν_4	ν_2	ν_2	ν_2		
	3.4				$\nu_1 + \nu_3$					ν_3	$2\nu_2$	$\nu_1, 2\nu_2$			Ca
NH_3	10.5	$\nu_3 - 2\nu_2$ $\nu_3 - \nu_1$				ν_2			$2\nu_2, \nu_1$	(?)	ν_2	ν_2	ν_2	ν_3	
	3.0	$3\nu_2 + \nu_3$ $- \nu_2$				ν_1			$\nu_1 + \nu_3$ $2\nu_2 + \nu_3$	ν_3	$\nu_1, \nu_3,$ $2\nu_2$				Si, Fe, Ca, Ti, C
NO	5.3	$3\nu_2^1$	0-1				0-1				ν_2				
HCHO	3.5							ν_4	$2\nu_2 + \nu_3$	$2\nu_4, \nu_3$	$2\nu_2$	$\nu_1, 2\nu_2$			Mg, Si, Ti, Fe

TABLE 3-2. LINE PARAMETERS GENERATED FOR POLLUTANTS AND INTERFERING GASES

Species	λ (μm)	Transition	# Lines	Comparison
CO	4.6	0-1	145	Excellent
	2.3	0-2	160	Excellent
CO_2	1.6	$3\nu_1 + \nu_3$	1634	Excellent
	2.1	$2\nu_1 + \nu_3$	924	Excellent
	2.7	$3\nu_2^1 - \nu_2^1 + \nu_3$ $2\nu_2 - \nu_3$	130	Excellent
	5.0	$2\nu_1 - \nu_2$ $\nu_1 + \nu_2$	585	Excellent
	10.5	$\nu_3 - \nu_1$ $\nu_3 - 2\nu_2$	427	Excellent
SO_2	4.0	$\nu_1 + \nu_3$	3079	Fair
	8.6	ν_1	6311	Fair
NO_2	3.3	$\nu_1 + \nu_3$	1420	Not Available
	7.6	ν_1	2583	Not Available
NO	5.3	0-1	484	Excellent
N_2O	3.0	$\nu_1 + \nu_3$ $2\nu_2 + \nu_3$	303	Excellent
	4.0	$2\nu_1$ $\nu_1 + 2\nu_2$	688	Excellent
	4.5	ν_3	976	Excellent
	7.8	ν_1	161	Excellent
	8.6	$2\nu_2$	156	Excellent
NH_3	2.3	$\nu_1 + \nu_2$ $\nu_2 + \nu_3$	3007	Excellent
	3.0	ν_1	1015	Good
	10.5	ν_2	1015	Very Good
CH_4	2.3	$\nu_3 + \nu_4$		—
	3.3	ν_3		Fair
	3.5	$\nu_2 + \nu_4$		
	3.8	$2\nu_4$		
	7.7	ν_4		
HCHO	3.5	ν_4	1861	Very Good
H_2O	2.7, 6.3	ν_3, ν_2	~1000	Excellent
O_3	4.7	$2\nu_1$		

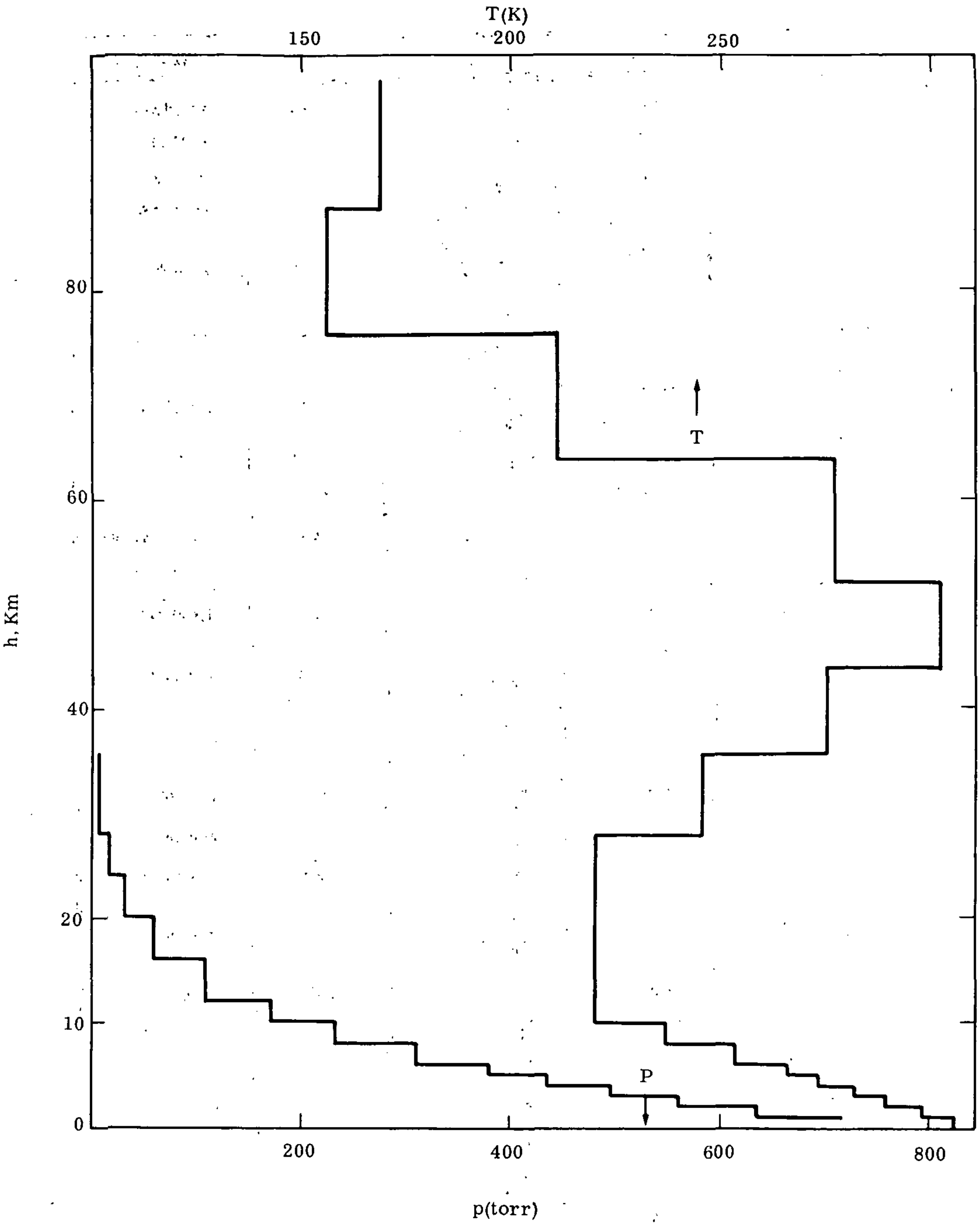

Figure 3-4. Temperature and Pressure Profiles Used in the Model Calculations (from ref. 62)

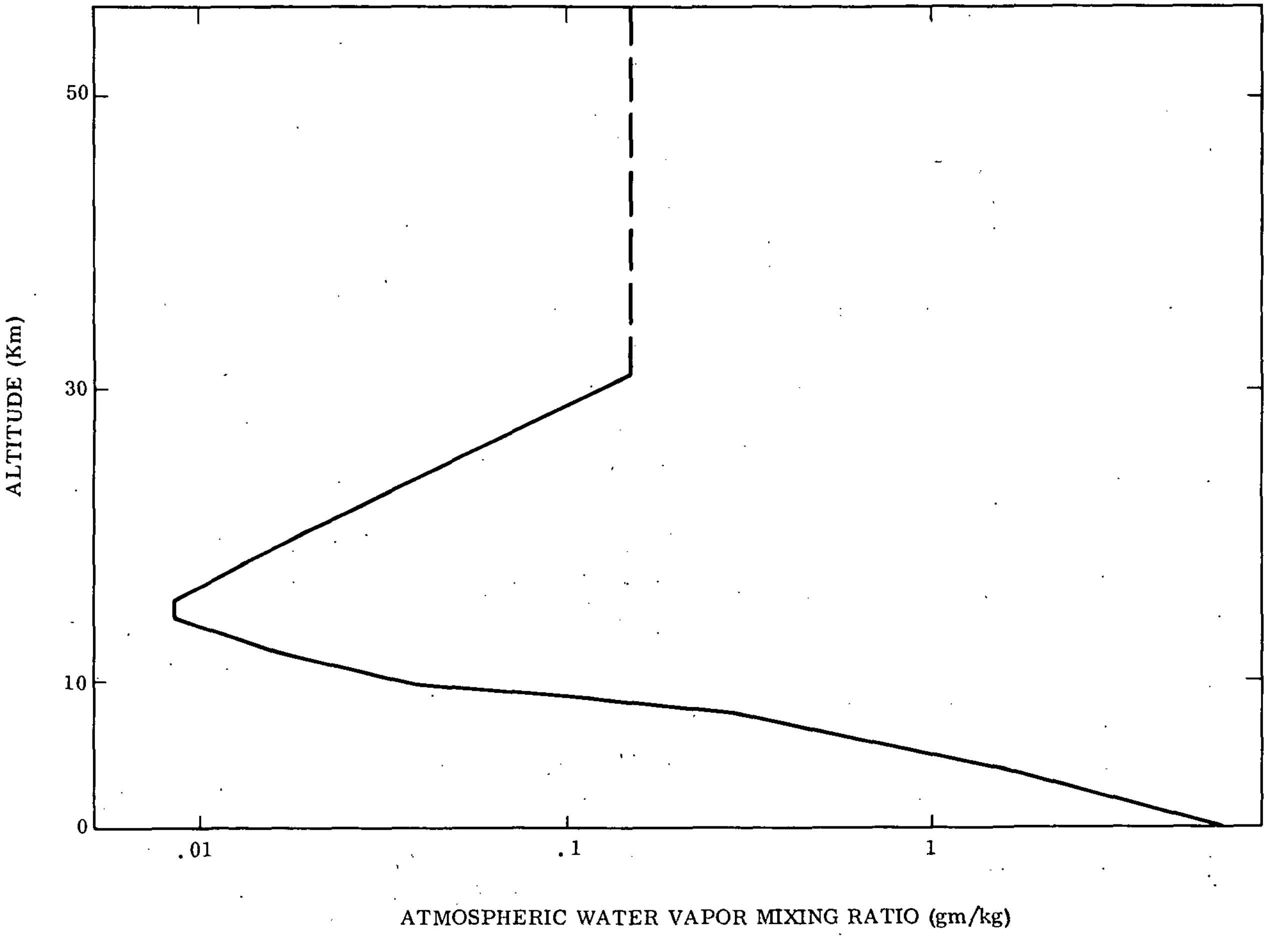

Figure 3-5. Water Vapor Distribution According to Gutnick (from ref. 63)

The results of the radiance calculations as a function of ground emissivity ϵ for two ground temperatures and four sun angles are shown in fig. 3-6. This graph is readily constructed since the radiance is a linear function of ϵ and hence, only one calculation for each ground temperature at $\epsilon = 1.0$, and one calculation for each sun zenith angle at $\epsilon = 0$ need be made and the points connected. The line for $\theta = 90°$ corresponds to the case of pure thermal radiation (nighttime observation). The difference between the lines at $\theta = 90°$ and $\theta < 90°$ is the addition of the reflected sun radiation to the thermal emission. In general, the ground emissivities vary between 1 and 0.8. In these calculations, the ground emissivity was assumed to be constant over the wavenumber interval from 2070 to 2220 cm^{-1}.

The effect of a variable ground emissivity versus an averaged (ω independent) emissivity on the signal change was investigated. The emissivities were taken from the measurements by Hovis (ref. 64) for two surfaces, silica sand and Pawnee Grassland soil. In the case of the silica sand, the spectral emissivity varies from 0.98 at 5 to 0.78 at 4.6 μm and the average emissivity is found to be 0.84. The results show that the radiance is not influenced by a significant amount when the wavenumber-dependent emissivity is replaced by the averaged one (ref. 61). This is an important result because it means that an average ground emissivity can be assumed for interpreting spectral data measured over a finite wavenumber interval.

In the following, we present the results of the calculated signal changes due to pollutant concentrations in the atmosphere. The signal change is an important parameter in the determination of the signal-to-noise ratio (SNR) for a given sensor system. The calculations were performed over wavelength intervals which encompass the majority of rotational lines in a given rotation-vibration band of a given pollutant. Thus the signal change is essentially the integration of changes in the intensity of individual lines. This may be measured by instruments with low spectral resolution, whose response function encompasses the entire wavelength interval, or by instruments with high spectral resolution, which have the multiplex feature. The application of these two types of instruments will be discussed in Section 5.

An overview of calculations performed (ref. 61) for different pollutants is presented in Table 3-3. In general, only one representative ground temperature, one atmospheric temperature profile, one sun angle, one ground emissivity and one reflectivity have been chosen for these calculations because of cost limitations. Only for the pollutant CO were additional calculations made, varying the ground and atmospheric parameters and sun angle. The results of the calculations are presented below.

The signal change SC in $w/cm^2 sr$ is calculated through

$$SC = \int_{\Delta\omega} \left[E(\omega;\ r_0) - E(\omega;\ r_p) \right] d\omega \qquad (3\text{-}9)$$

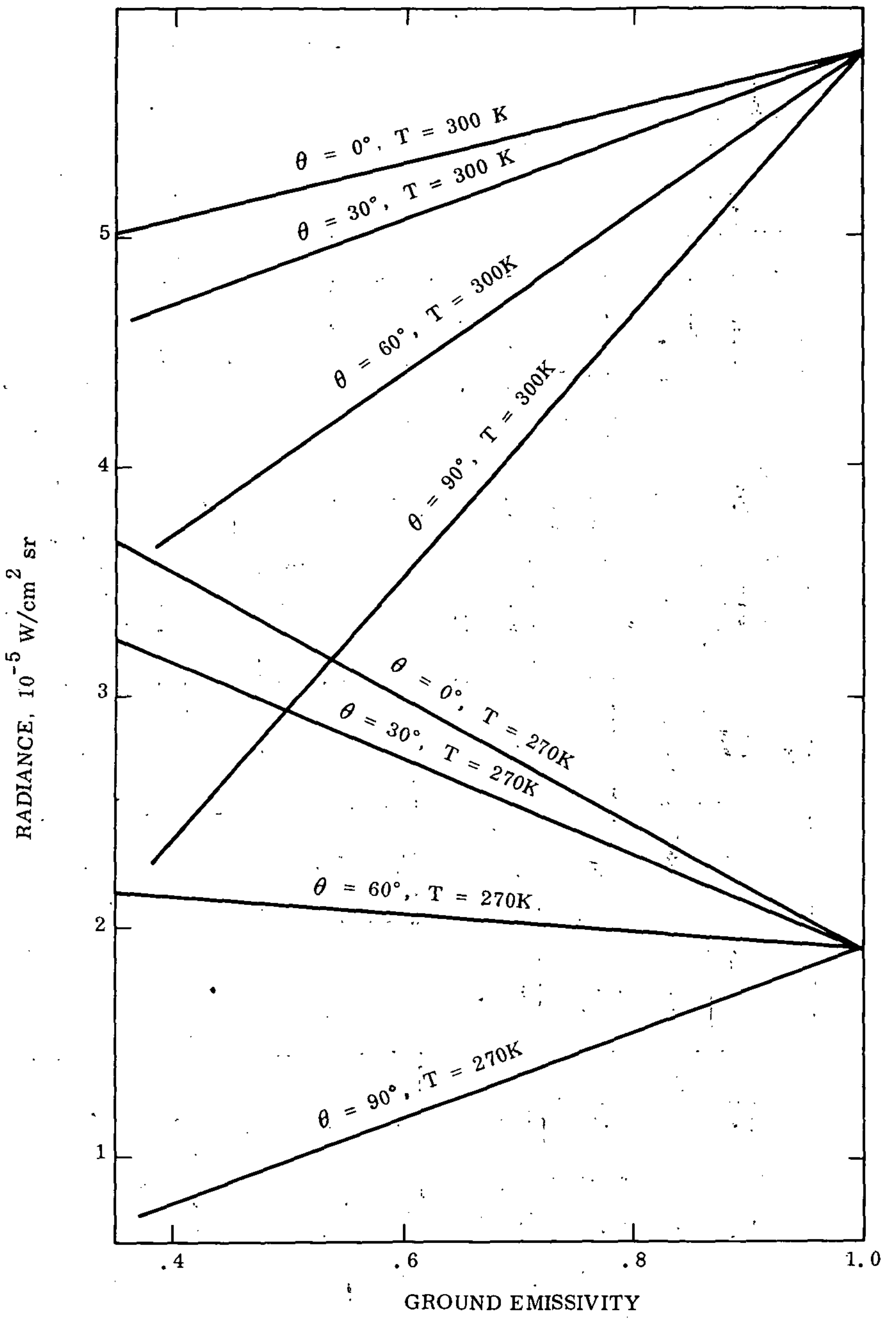

Figure 3-6. Radiance at the Top of Atmosphere for Different Sun Zenith Angles and Ground Temperatures at 4.6 μm

TABLE 3-3. OVERVIEW OF MODEL CALCULATIONS

	λ (μm)	T_{Ground} (°K)	ϵ_{Ground}	θ	No. of Atm. Temp. Prof.	Interf. Species Incl.	Interf. Species Not Incl.	Poll. Conc. (ppm)	No. of Poll. Conc. Prof.	No. of H_2O Conc. & Prof.
CO	4.6	270-330	0.0-1.0	0°-90°	Several	H_2O N_2O	CO_2 O_3	0-0.4	3	4
CO_2	1.6	300	.98	30°	1		H_2O CH_4	320	1	
	2.1	300	.98	30°	1	H_2O	NH_3	300-400	1	1
SO_2	8.6	300	1.00	0°	1	H_2O	N_2O O_3	.002	1	1
	4.0	300	.8	30°	1		N_2O CH_4	.002	1	
NO_2	7.6	300	1.0	0°	1	H_2O N_2O	CH_4	.002	1	1
	3.3	300	.8	30°	1		CH_4 H_2O	.002	1	
NO	5.3	300	.8	30°	1	H_2O CO_2		.0002-.02	1	1
NH_3	10.5	300	1.00	0°	1		H_2O O_3, CO_2	.02	1	
	3	300	.8	30°	1		CO_2, N_2O CH_4, H_2O	.02	1	
HCHO	3.5	300	.8	30°	1		H_2O	.002	1	

where, as before, $E(\omega; \tau)$ is given by the sum of Eqs. (3-3) and (3-5). The transmissivities τ_0 and τ_p in Eq. (3-9) refer to two different pollutant conditions; unless otherwise noted, τ_0 refers to the "clean" atmosphere, for which the pollutant concentration is zero.

The signal change for different carbon monoxide concentrations uniformly distributed through the troposphere has been calculated for the wavenumber interval between 2070 and 2220 cm^{-1} in the presence of 0.25 ppm of N_2O, using the standard U.S. wet atmosphere (Gutnick (ref. 63) water vapor distribution). The results are shown in fig. 3-7. The influence of different amounts of water vapor on the signal change* is shown in fig. 3-8. The influence of the stratospheric water vapor on the signal change, using the mixing ratio shown in fig. 3-5, is found to be negligible (ref. 61). It should be noted that the mixing ratio in the stratosphere is reported to be less than one to two orders of magnitude (ref. 65 and 66).

---

* The 2x Gutnick distribution would imply that the atmosphere is slightly supersaturated below 10 km, but is used for convenience in illustrating the water vapor effects.

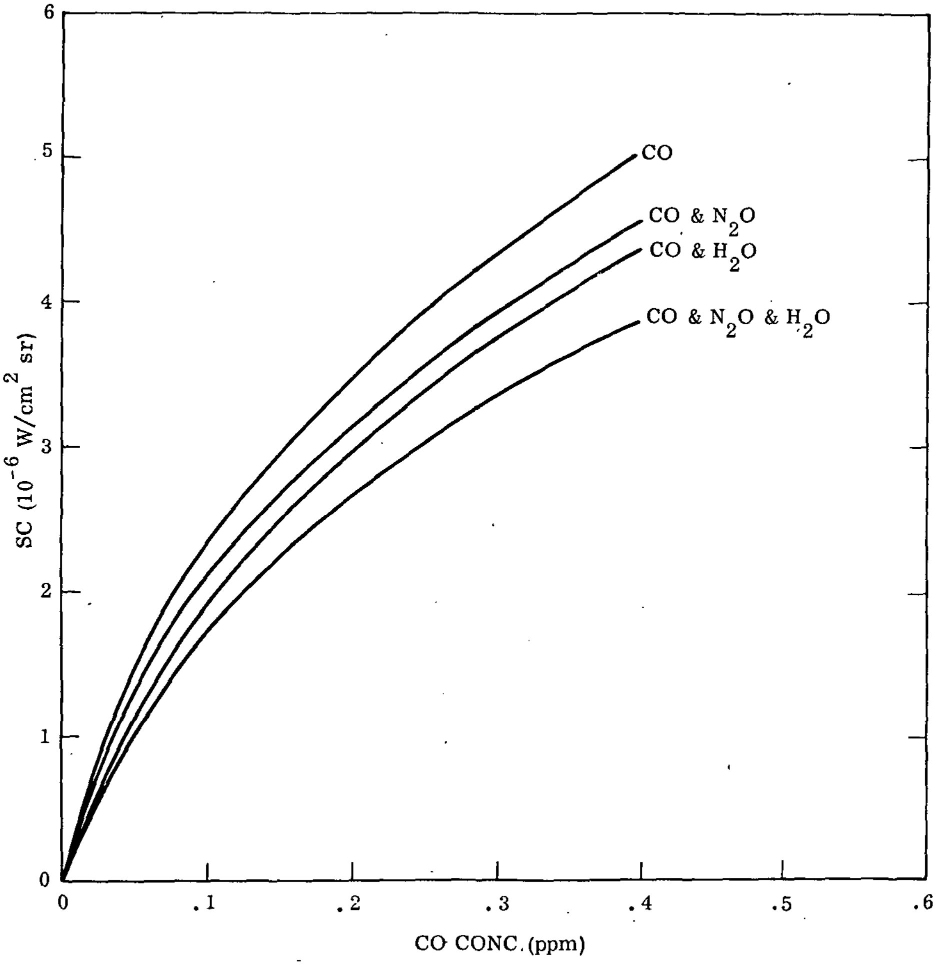

Figure 3-7. Signal Change as a Function of CO Concentration for Different Interfering Species. Ground Brightness Temperature = 300K.

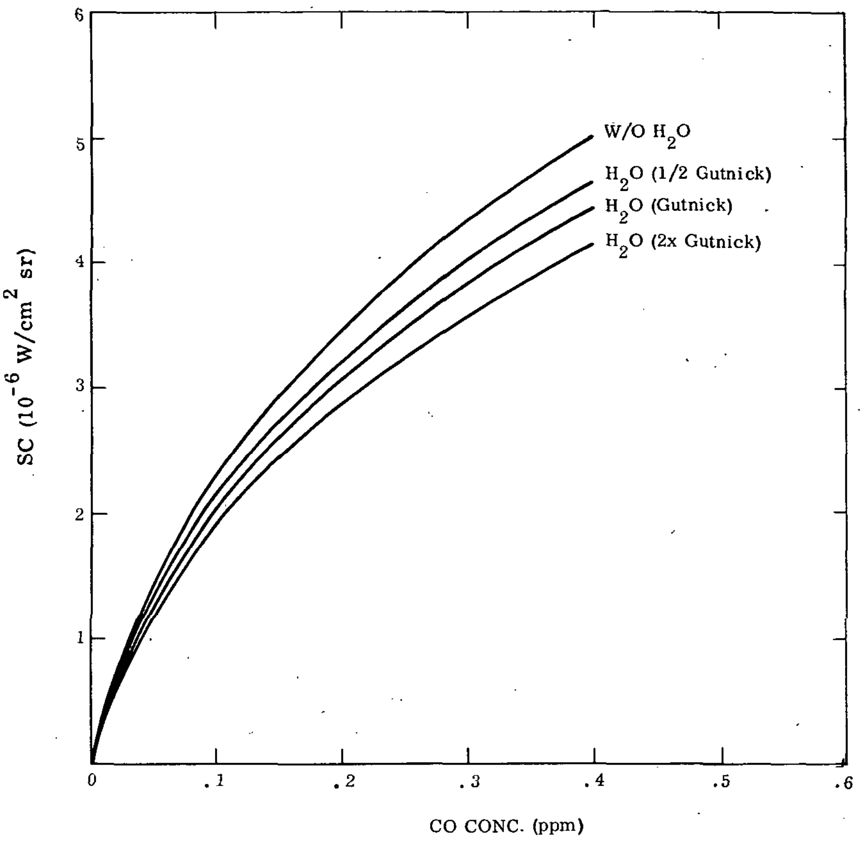

Figure 3-8. Signal Change as a Function of CO Concentration for Different Amounts of Water Vapor. Ground Brightness Temperature = 300K.

Figure 3-9 shows the signal changes for surface temperatures of 270, 300 and 330 K and a ground emissivity of 0. 8, representing a typical value for land surfaces, and for two sun zenith angles. The nighttime observations are represented by the $\theta = 90°$ curves, which are always lower.

The results of the calculations for the CO_2 molecule in the 2.1 μm range are shown in fig. 3-10 in terms of signal change versus concentration between 300 and 400 ppm. The calculations were performed over the band pass from 4892 to 5016 cm^{-1}. The only interfering species considered was water vapor, whose average absorption in this spectral region is about 15%, using the Gutnick model. The sun zenith angle was 30° and the reflecting surface was assumed to have a diffuse reflectivity of 0. 02. The results are obtained without considering the effect of sunlight scattered by the atmosphere; more Monte Carlo calculations are required to determine its contribution.

The results of the calculations for the SO_2 molecule in the 8. 6 μm region indicate a signal change of 10^{-6} w/cm^2 sr for a pollutant concentration of 2 ppb uniformly distributed through the troposphere, a ground emissivity of 1. 0 and a ground

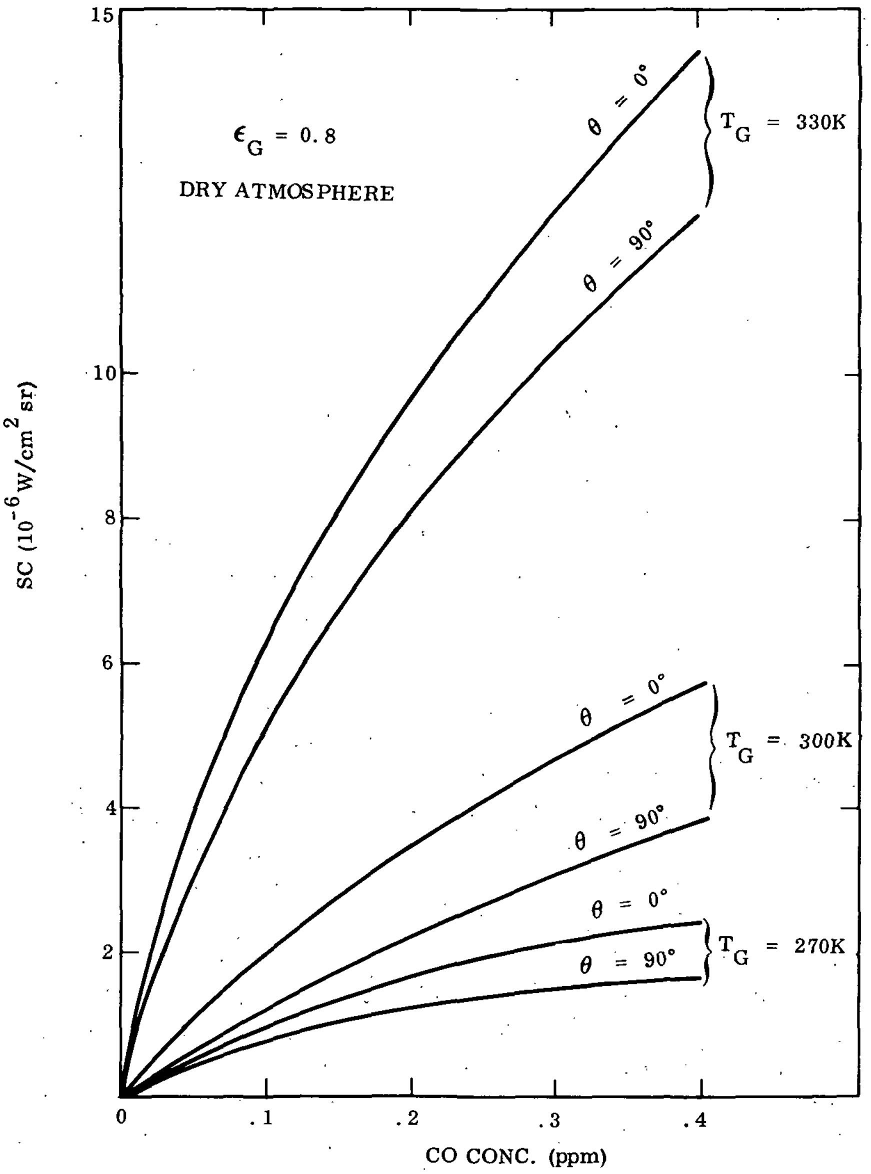

Figure 3-9. Signal Change as a Function of CO Concentration for Three Different Ground Temperatures in the Case of Overhead Sun ($\theta = 0°$) and Nighttime ($\theta = 90°$)

temperature of 300 K. The Gutnick water vapor distribution was used, but the other two interfering species O_3 and N_2O were not included in the calculations. The average absorption of the water vapor over the spectral range from 1090 to 1190 cm^{-1} is 20%. The signal change, as a percentage of the "clean" radiance is about 2% which is in qualitative agreement with our previous calculation (ref. 3), where 20 ppb of SO_2 uniformly distributed through the troposphere resulted in a 12% signal change.

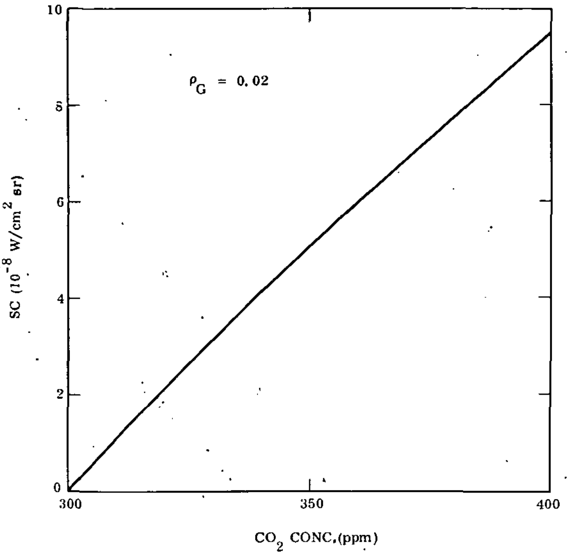

Figure 3-10. Signal Change vs. CO_2 Concentration for Sun Zenith Angle = 30°, Ground Reflectivity = 0.02, Ground Temperature = 300K

Results obtained for the NO_2 molecule at 7.6 μm show that the interference by water vapor is much more severe. The average absorption of the water vapor over the spectral range from 1300 to 1400 cm^{-1} is about 90%, which is considerably higher than that calculated for the SO_2 region. The ground was assumed to have an emissivity of 1.0 with a temperature of 300 K. Calculations for NO_2 at 3.3 μm indicate that this spectral region will be more advantageous for measuring NO_2.

The NO absorption is very heavily overlapped by H_2O absorption and previous band model calculations (ref. 3) had indicated that it will not be possible to observe NO in the troposphere. The present line-by-line calculations confirm this conclusion. Using a U.S. wet standard atmosphere, a ground emissivity of 0.8 and a ground temperature of 300 K, the signal changes range from 2×10^{-9} w/cm^2 sr at 0.2 ppb to 1.51×10^{-7} w/cm^2 sr at 20 ppb of NO uniformly distributed through the troposphere. Thus, in order to determine NO within a 20% accuracy at about 1 ppb, the sensor system must be able to record a signal change of about 3×10^{-9} w/cm^2 sr and to discriminate against the influence of water vapor and CO_2 which have an average absorptivity of about 92% in this spectral region (1800 - 1950 cm^{-1}).

The calculations for ammonia show that the measurement of less than 1 ppb at 10.5 μm appears to be feasible. Calculations were made assuming a ground temperature of 300 K and a ground emissivity of 1.0 and the standard dry atmosphere. The signal change for 20 ppb of NH_3 is greater than 2×10^{-5} w/cm^2 sr. More calculations are necessary to determine the effect of the interfering gases N_2O, CO_2, H_2O and O_3.

The calculations for formaldehyde tentatively show that the measurement of 2 ppb uniformly distributed through the troposphere at 3.5 μm appears to be feasible. The signal difference is about 10^{-7} w/cm^2 sr without the inclusion of interfering gases. More model calculations are needed to determine the influence of H_2O and HDO.

3.1.1.4 Supporting data requirements. In order to interpret the data from earth-oriented pollutant sensors it is, in general, necessary to know, or to obtain by supplementary measurements, various surface and atmospheric parameters such as surface reflectivity, emissivity and temperature, the vertical atmospheric temperature profile and the cloud cover. The accuracy with which these parameters must be known will depend on the measurement technique, the wavelength of observation and, of course, on the accuracy required for the pollutant measurement. As a particular example, we consider the analyses performed for the thermal region, where the surface radiance and the vertical atmospheric temperature profile are needed for clear skies, with the addition of an estimate of the cloud cover in cloudy conditions.

Temperature Profile

The vertical temperature profile has long been measured routinely on a global basis using radiosondes, and more recently, using radiometric techniques on satellites (e.g., SIRS). These measurements will not always be made at the same time or place as the pollutant measurement. However, it appears from an examination of methods and techniques used that the existing meteorological observation system is able to provide a satisfactory estimate of the atmospheric temperature profile.

The National Meteorological Center (NMC) routinely produces objective analyses as a best estimate of the state of the atmosphere from all available observations. Forecasts are produced from the objective analyses. The methods employed in objective analysis and forecasting can be used for the estimation of the atmospheric temperature and pressure profiles for the locations and times applicable to pollutant sensor data. The NMC verifies objective analyses and forecasts by comparing these products with observations. The resulting verification statistics give the average error between the temperature observations at different pressure levels and the smoothed best estimate of the state of the atmosphere produced from the observations. Table 3-4 gives the mean absolute temperature error at different pressure levels for four months of 1970 (J. E. McDonnel, NMC, private communication). The errors are less than 1K with essentially no difference between the statistics obtained from the 70 radiosondes in the northern hemisphere or the 19 radiosondes in the USA.

The operational analysis and forecast operation includes all available useful data from satellite temperature sounders. Reported experiments (ref. 66) have shown that SIRS data significantly improve the objective analysis in data-sparse areas (judged from forecast performance with and without inclusion of SIRS data).

TABLE 3-4. VERIFICATION OF NMC OPERATIONAL TEMPERATURE ANALYSIS

MEAN ABSOLUTE TEMPERATURE ERROR (K)

Pressure Level (mb)	1970							
	Jan		April		July		Oct	
	a	b	a	b	a	b	a	b
200	.8	.9	.7	.8	.7	.7	.7	.7
250	.7	.7	.6	.7	.6	.5	.6	.7
300	.7	.6	.7	.7	.5	.5	.6	.6
500	.6	.7	.6	.7	.5	.5	.5	.6
700	.7	.7	.6	.6	.5	.6	.6	.7
850	.8	1.0	.7	.9	.6	.7	.7	.9

a 70 radiosonde stations in Northern Hemisphere

b 19 radiosonde stations in U.S.A.

However, it appears that a SIRS sounding does not give an independent observation of temperature as a radiosonde would, but relies on the operational objective analysis and short term forecasts (up to 12 hours) to provide an initialization for SIRS analysis. The temperature profile from the objective analysis is changed if the SIRS radiances are inconsistent with it, until the computed and measured radiances agree within the expected errors of the instrument. This can be interpreted to mean that SIRS-type data can be expected to improve the analysis in data-sparse regions, but that the objective analyses will remain the best estimate of the atmospheric state.

Calculations have been made using a computer program to obtain an understanding of the Gas Filter Correlation instrument sensitivity to changes in the atmospheric temperature profile (see also Section 5.1.3.2). The atmosphere was approximated by eight layers with average temperatures and pressures in each layer. The instrument sensitivity was determined by making different calculations with the temperature in each layer changed from the standard average temperature for different CO concentrations in the 4.6-μm band, for assumed surface temperatures of 300K and 285K and a water vapor distribution according to Gutnick (ref. 63). The expected relative error in CO concentration was found to be about ±5% for temperature uncertainties of ±2K (see also fig. 5-8). Thus, it may be concluded that sufficiently accurate atmospheric temperature profiles can be obtained from operational objective analyses. An average error (from verification statistics) of ±1K would lead to an average error in estimated CO concentration of about ±2.0% at 0.1 ppm. The instrument sensitivities and expected errors would, of course, be somewhat different at other values of ground temperature, atmospheric relative humidity, other atmospheric pressure distributions, and for other species and concentrations.

Surface Temperature

For the interpretation of the data in the thermal region, a knowledge of the ground brightness temperature at the spectral location of the pollutant band is required. The brightness temperature can be obtained through a measurement of the upwelling radiance, corrected for the effect of the atmosphere. Since the atmosphere contains also the unknown pollutant, a simultaneous solution of the ground brightness temperature and pollutant concentration must be obtained. If the wavelength dependence of the ground emissivity is known, the brightness temperature measurement may be made at another spectral location, preferable in an atmospheric window, where the effect of the atmosphere is minimized.

Relative Humidity Profile

Since all infrared pollutant bands are interfered by one or more atmospheric species, the concentration profiles of these have to be known to properly interpret the pollutant data. In general these profiles are known for "normal" atmospheric species except water vapor. The water vapor profiles are highly variable both in time and space and large deviations from the so-called "standard" Gutnick model (ref. 63) may occur. It is thus important to obtain independent information about the water vapor profiles. However, these are not normally included in the "objective analyses" provided by the National Meteorology Center (NMC); instead an average relative humidity within the 1000 and 500 mb layer is included. Recently, water vapor soundings from satellites have been initiated and are found to be within 20% in the mid-troposphere (400-600 mb) and within 30% in the lower troposphere (1000 - 600 mb) of radiosonde data.

Cloud Cover

In order to correctly interpret the pollutant data from earth-oriented observations in the presence of clouds, it will be necessary to estimate the amount of cloud cover and the cloud top height. The cloud cover may be obtained from an on-board vidicon, and the cloud height may be estimated from weather reports, or from an on-board cloud-height sensor, such as a refinement of the technique reported by Saiedy et al. (ref. 67).

In the case of complete cloud cover the interpretation of the data is straightforward, if the cloud top height is constant, with the cloud replacing the earth's surface; for partial cloud cover the problem is more complex. To investigate the effect of cloud cover on the observed signals the computer program was modified so that a layer of varying amounts of cloud cover could be inserted between each atmospheric layer. The clouds were assumed to have a spatially uniform emissivity of 1.0. The radiance from the layers including the cloud cover is the average of the radiance from the cloud and from the earth and atmosphere below the cloud. Calculations were made with fractional cloud amounts of 0, 0.3, 0.6 and 1.0 at 1 km altitude. It was found that the instrument response is linear with cloud amount, as shown in fig. 3-11. The signal decreases with increasing cloud amount due to the decreasing mean surface temperature seen by the sensor, and due to the loss of signal from the CO below the clouds.

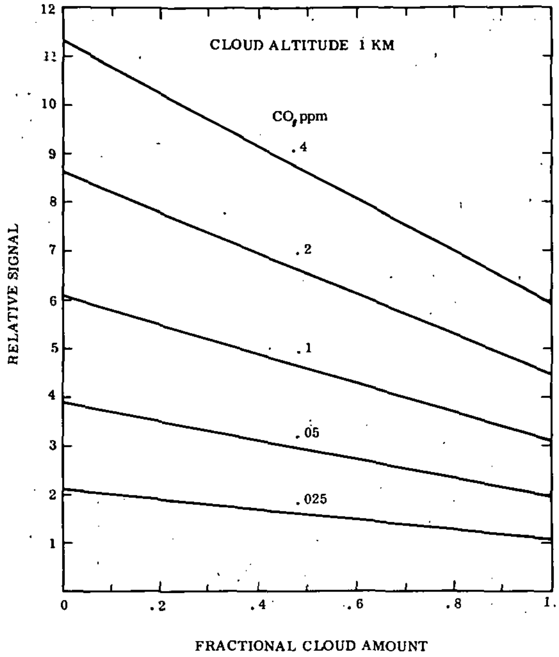

Figure 3-11. Relative Signal as a Function of Fractional Cloud Amount for Different CO Concentrations

3.1.2 Limb Experiment

3.1.2.1 General. In this experiment, the sensor is directed toward the horizon, observing the thermal emission of the atmosphere or the sun's radiation transmitted through the atmosphere. The disadvantage of the limb experiment is that the observations are restricted in general to the region of the atmosphere above the tropopause because of the extensive cloud formations in the troposphere (see Sections 4.2.2.1 and 4.2.2.2). The advantage of the limb experiment is that by scanning vertically the stratosphere distribution of the gases in question can be inferred. In addition, because of the long paths involved, very low concentrations can be detected. In the limb emission mode, signals arise only from the atmospheric gases, because the background is cold space. Also, measurements can be made from all parts of any orbit. This is not the case in the limb transmission mode (sun occultation), because the measurements have to be made during sunset or sunrise, thus restricting the observations of the stratosphere to those latitudinal regions where the instrument can be aligned for a given orbit with the sun close to the horizon.

The formation for the radiative transfer in the limb experiment has been discussed in detail by Russell (ref. 68,69). Results of calculations were presented for ozone at 9.6 μm, using band model parameters. No other calculations exist at the present time, but are scheduled to be performed in the near future (ref. 70).

In the following, we present an overview of the radiative transfer problem. The geometrical configuration is given in fig. 3-12. The line-of-sight is a tangent to any one of the atmospheric layers and may or may not have the sun as a source. In analogy to our formalism for the nadir experiment, the radiation $E(\omega)$ at the entrance pupil of the sensor can be written as the sum of four components:

$$E(\omega) = E_S(\omega) + E_\sigma(\omega) + E_{\sigma R}(\omega) + E_A(\omega) \qquad (3\text{-}10)$$

where $E_S(\omega)$ is the transmitted sun energy, $E_\sigma(\omega)$ is the forward scattered sun radiation, $E_{\sigma R}(\omega)$ is the radiation scattered from nearby clouds, and $E_A(\omega)$ is the thermal radiation from the atmosphere.

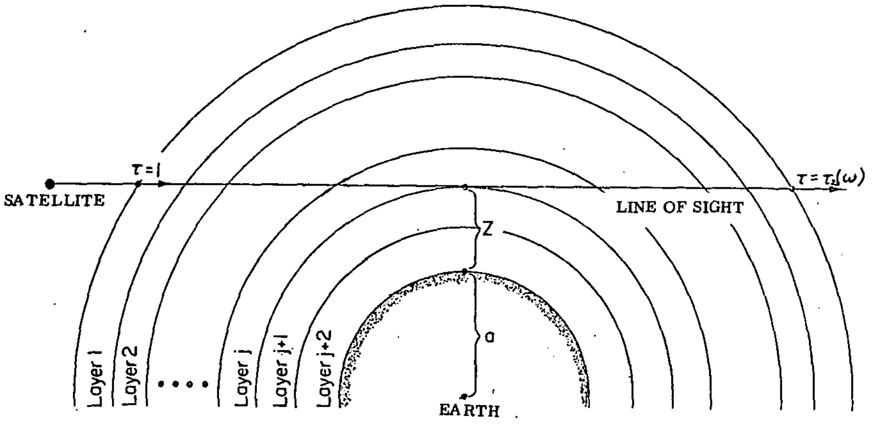

Figure 3-12. Geometry of the Limb Experiment (after ref. 68)

The functional dependence of these components of $E(\omega)$ is indicated as follows:

$$\left.\begin{aligned} E_S(\omega) &= E_S(\omega; \tau, z) \\ E_\sigma(\omega) &= E_\sigma(\omega; n\sigma, \tau, z) \\ E_{\sigma R}(\omega) &= E_{\sigma R}(\omega; \rho_c, \tau, z) \\ E_A(\omega) &= E_T(\omega; \tau, T_A, z) \end{aligned}\right\} \qquad (3\text{-}11)$$

where T_A denotes the atmospheric temperature along the line of sight, ρ_c is the effective cloud albedo, z is the minimum altitude of the line of sight, $(n\sigma)$ is the product of number of scattering centers (n) and scattering cross section (σ), τ is the transmissivity of the atmosphere, referring generically to all sources of attenuation: molecular and particulate absorption and molecular and particulate scattering.

The equation of radiative transfer for the thermal emission of a spherically symmetric atmosphere, neglecting particle scattering, and atmospheric refraction, is given by

$$E_T(\omega) = - \int_1^{\tau_z(\omega)} N^0(\omega, T)\, d\tau_z(\omega) \tag{3-12}$$

where $\tau_z(\omega)$ is the transmissivity through the line of sight having a minimum altitude of z, $N^0(\omega, T)$ is the Planck function for wavenumber ω and temperature T.

The equation of radiative transfer for the transmitted sun radiation without refraction or scattering is given by

$$E_s(\omega) = H_s(\omega)\, \tau_z(\omega) \tag{3-13}$$

where $H_s(\omega)$ is the solar irradiance and $\tau_z(\omega)$ is the previously defined transmissivity.

For the thermal emission mode on the night side of the orbit, the contributions from the sun can, of course, be neglected. On the day side, the thermal radiation can be neglected at all wavelengths in the sun occultation mode, and, in the thermal emission mode, the terms $E_s(\omega)$ and $E_\sigma(\omega)$ do not need to be considered, although the term $E_{\sigma R}(\omega)$ must be examined when there are clouds near the line of sight.

3.1.2.2 Sun-occultation. We have made band-model calculations of the transmission of various trace contaminants in the stratosphere. Water vapor will be of concern if many aircraft are flying in the stratosphere. Results of expected changes in the transmission due to changes in the water vapor mixing ratio are shown in fig. 3-13. The calculations were performed in three wavelengths: 1.869 μm, 2.581 μm and 6.557 μm.

The pairs of curves shown in fig. 3-13 were calculated for the two water vapor distributions shown in fig. 3-5, one a standard distribution having a minimum mixing ratio of 0.009g/kg at 15 km altitude, and a perturbed distribution equal to the former uniformly increased by 0.0025 g/kg.

Similar results are shown in fig. 3-14 for mean transmissivities in other spectral regions where the absorption by pollutant species would be the greatest, and the least interfered with by other species. The species and assumed concentrations are

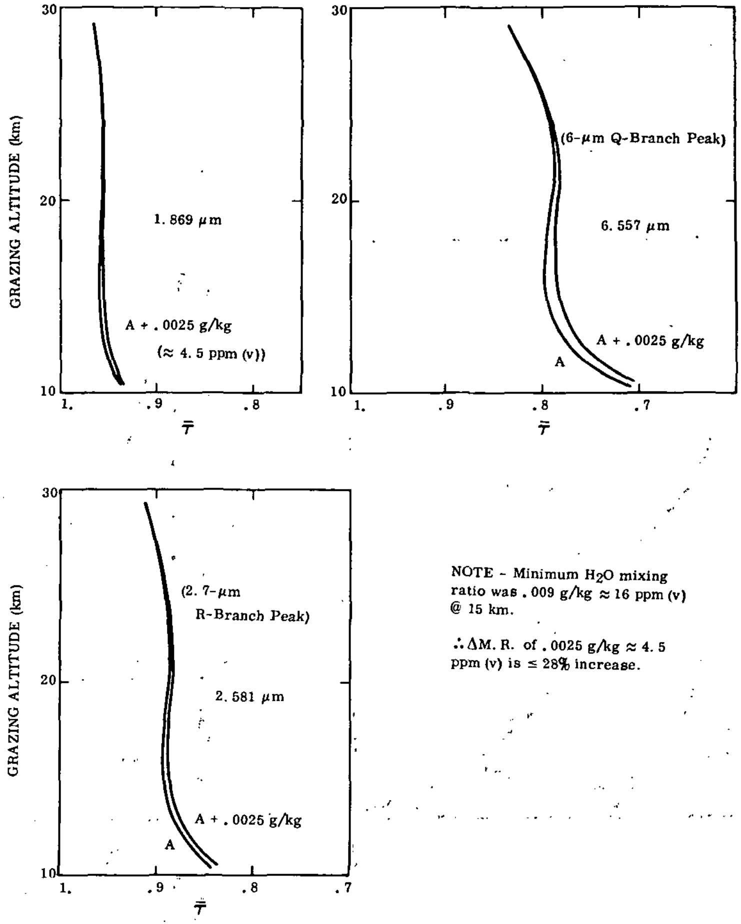

NOTE - Minimum H_2O mixing ratio was .009 g/kg ≈ 16 ppm (v) @ 15 km.

∴ ΔM. R. of .0025 g/kg ≈ 4.5 ppm (v) is ≤ 28% increase.

Figure 3-13. Band Model Calculations for Stratospheric H_2O

indicated on the graphs. The ordinates of the graphs are the grazing altitudes of the lines-of-sight.

These calculations were performed with a program which calculates transmissivities along a line-of-sight passing through a spherically symmetric atmosphere (neglecting refraction), using a generalized Curtis-Godson type approximation.

3.1.2.3 Limb emission measurements. The limb emission mode was investigated theoretically by Russell (ref. 68) for the measurement of the vertical distribution of ozone. He found that the ozone partial pressure can be determined in the altitude range from 25 or 30 km to 50 km, the lower limit being determined by the opaqueness of the atmosphere and the upper limit by the small optical thickness of ozone in

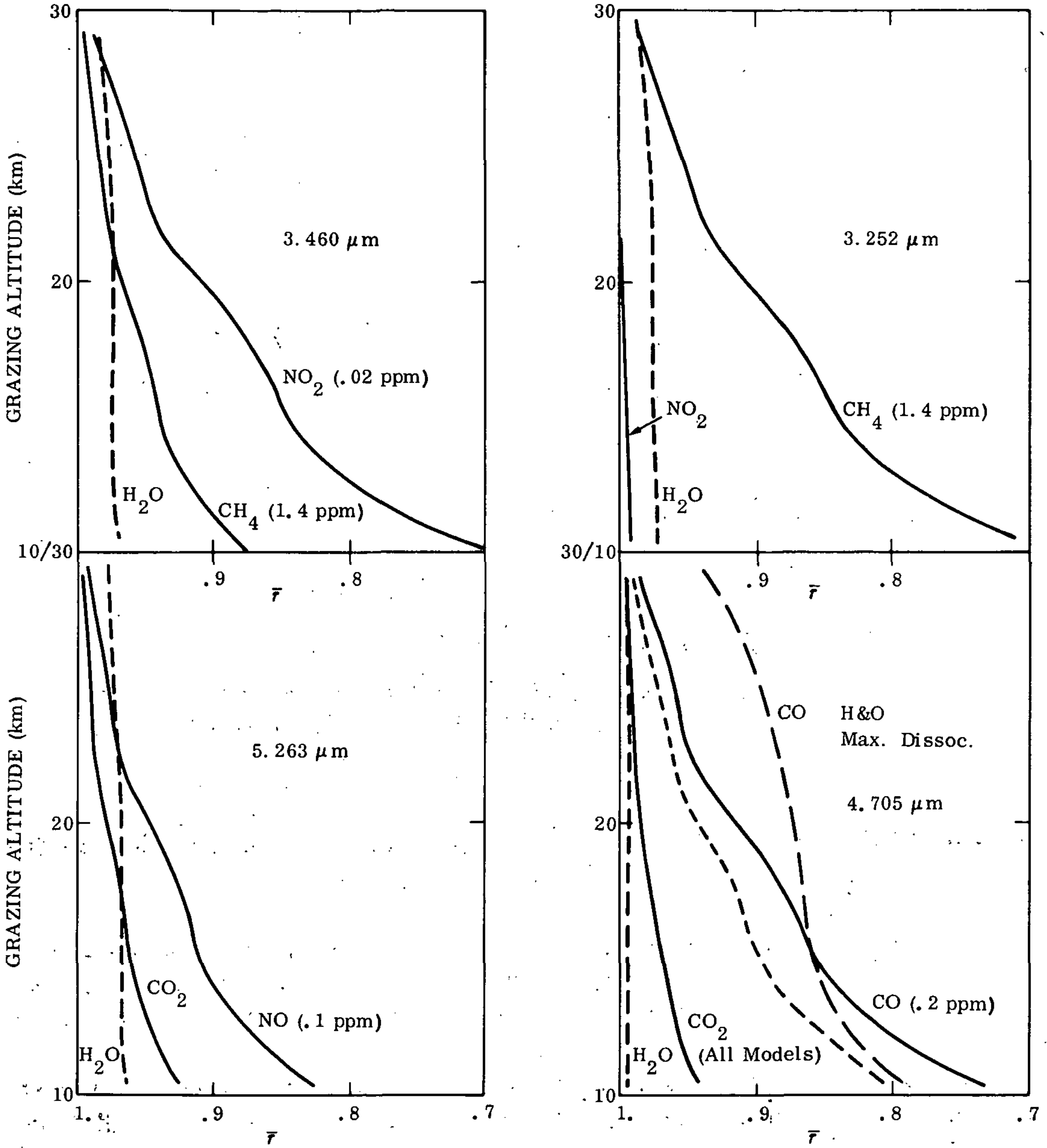

Figure 3-14. Band Model Calculations for Selected Stratospheric Constituents

that region. As in the thermal nadir experiment, the determination of the species concentration requires the knowledge of the temperature profile, which can be obtained through the inversion of radiance data taken in the 15-μm band of CO_2 (ref. 68, 71, 72). Gille and House (ref. 73) have described a method for retrieving the temperature profile from limb measurements by an iterative procedure. The problem is non-linear because the viewing geometry makes the kernel of the integral equation strongly dependent on the temperature profile. An instrument called the Limb Radiance Inversion Radiometer is being developed and is scheduled for flight on the NIMBUS F satellite, to be launched in mid-1974. Russell (ref. 68) has investigated the errors involved in the determination of the ozone partial pressure. The most significant error lies in the uncertainty of the temperature profile. An uncertainty of ±3°K causes a ±30% uncertainty in the O_3 concentration in the upper atmosphere and ±80% at 25 km. The next most significant error source is the uncertainty of the tangent height. Negligible at the upper layers, a tangent height error of ±1km at 25 km causes an ozone partial pressure error of ±20%. All other error sources were found not to exceed 7% at 25 km. Russell (ref. 68) also found, when he introduced a normally distributed random temperature error instead of the bias error, that the error in ozone concentration is reduced and that "it should ultimately be possible to determine the ozone partial pressure to within 15 or 25% for most of the range 25 to 50 km. It may be possible to reduce this error to 10% or less by smoothing the solution profile" (from Reference 68).

The application of the experiments described above are being developed under AAFE program "Lower Atmosphere Composition and Temperature Experiment (LACATE)". Besides the temperature and ozone concentration profile, the experiment is designed to measure the concentration profiles of the minor constituents N_2O, HNO_3 and H_2O. The inclusion of other species such as SO_2, NO_2, CO and CH_4 is being studied (J. Russell, NASA-LaRC, private communication, 1972).

3.2 Active Mode

3.2.1 Introduction

The continuing development of high-power and tunable lasers has made their application to remote sensing of air pollutants from satellites appear feasible. A detailed study of the feasibility of air pollution detection by active remote sensing techniques is presently being conducted by the Stanford Research Institute. In this report we will therefore limit ourselves to only a brief outline of active methods.

Several physical processes are useful for active sensing. One is the absorption method which is, of course, the same as discussed in Section 3.1.1, except an active source of radiation is used instead of "natural" sources. Other methods are fluorescence and Raman scattering. Both of these methods require an active, preferably monochromatic, source and the scattered radiation spectra are observed. The intensity of the scattered radiation provides a measure of pollutant concentration.

The normal fluorescence and Raman scattering processes are rather different in their nature. Fluorescence is a discrete two-photon, three-step process. Incident photons provided by an active source raise the system to a high energy level or band. There, non-radiative mixing may take place until the system is at a state where radiative emission preferentially takes place. On the other hand, the Raman scattering process is a two-photon single-step process. Here the emission of a Raman photon is coupled to the simultaneous absorption of an incident photon. Schematic diagrams of the processes are presented in fig. 3-15. A considerable increase in the intensity of the scattered radiation is obtained when a resonance condition is achieved. If the active source is at a resonant frequency, some fundamental conditions are changed. Resonance fluorescence deals with a two-level energy scheme where absorption and emission take place between the same two levels. The resonant Raman scattering process is one where the upper virtual level is no longer such, but is an energy level where electric dipole emission can take place strongly between it and either of the lower Raman levels.

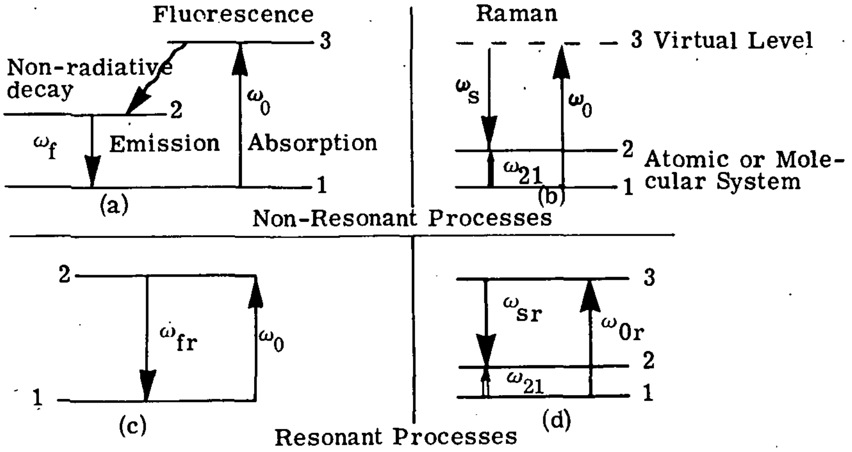

Figure 3-15. Schematic of Transitions for Fluorescence and Raman Scattering Processes

3.2.2 Resonant Raman Scattering

We now consider the case of resonant Raman scattering in some detail. The real upper state, 3, (fig. 3-15) is connected to both the ground state, 1, and the final state, 2, through the electric dipole matrix elements, μ_{32} and μ_{31}. In considering the detailed quantum mechanical problem we must include the total field of the three-level system. The interaction Hamiltonian between the molecular system and the radiation field is given by (ref. 74):

$$H'_{nK} = -\frac{\mu_{nK}}{2}\left\{\left(A_0 e^{i\omega_0 t} + A_s e^{i\omega_s t}\right) + \text{c.c.}\right\} . \tag{3-14}$$

The general solution to the transition rate problem may be obtained by solving the quantum mechanical equations of motion for the off-diagonal elements of the density matrix, viz.,

$$\left[\frac{d}{dt} + i\omega_{nK} + \frac{\gamma}{2}\right]\rho_{nK} = \frac{1}{i\hbar}\sum_m \left(H'_{nm}\rho_{mK} - \rho_{nm}H'_{nK}\right) \tag{3-15}$$

Here γ is the decay constant from random thermal motion and $\omega_{nK} = \frac{E_n - E_K}{\hbar}$. The solutions to these equations are then the time-dependent descriptions of the relevant density matrices. The amplitudes of all of these density matrices contain a resonant denominator of the form

$$R = \frac{1}{\left[\omega_{21} - \left(\omega_0 - \omega_s\right)\right] + i\frac{\gamma}{2}} . \tag{3-16}$$

Thus, the intensity distribution of the Stokes radiation exhibits resonance. Furthermore, in the case where the exciting frequency ω_0 is monochromatic, as a typical laser source may be assumed, the spectral content at the Stokes frequency will be highly dependent on rate of radiative decay to level 2 and on the collision life times. If the molecular system is of low density, the Stokes radiation is emitted with essentially the same linewidth as the incident photon. That is, if $I_0(\omega_0)$, the incident intensity of the laser light is a very narrow curve, the power output of the Stokes radiation will be

$$P_{\text{Res. Raman}}(\omega_0) \simeq \sigma_{\text{Raman}} \frac{\omega_0^2}{\left[\omega_{21} - \left(\omega_0 - \omega_s\right)\right]^2 + \frac{\gamma^2}{4}} I_0(\omega_0) \tag{3-17}$$

Thus, $P_{\text{Res. Raman}}(\omega_0)$ has the resonant denominator but retains the spectral purity of the incident beam. For resonance, $\omega_{21} = \omega_0 - \omega_s$, the enhancement in the scattering power is of the order of 10^6, determined by the ratio ω_0/γ.

If the molecular density is high, collision dephasing occurs and the spectral width of the Stokes radiation becomes comparable to the natural life time of the upper level.

Raman shifts for typical molecules are shown in fig. 3-16. The exciting frequency for resonance Raman scattering is chosen in accordance with the previous considerations. For example, for NO_2, which has absorption bands extending into the visible region, a wavelength in the 4000 Å region might be selected. In the case of CH_4, which has no significant electronic absorption bands at wavelengths greater than 1500 Å, wavelengths suitable for resonance Raman scattering will not be suitable for probing the atmosphere because of absorption by N_2 and O_2.

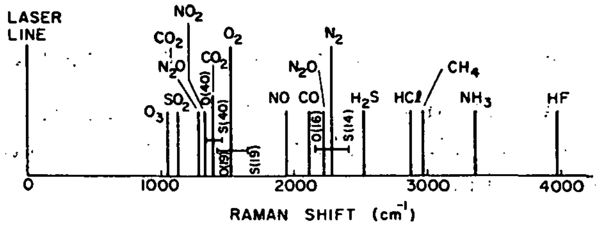

Figure 3-16. Raman Shifts of Important Pollutant Molecules in the Atmosphere Relative to the Exciting Laser Frequency (from Kildal and Byer (ref. 75)).

3.2.3 Resonant Fluorescence

When resonance fluorescence is treated in a similar fashion to Raman scattering, an analogous resonance denominator appears in the matrix elements. Consequently, for the same low density system where the radiation decay rate is fast, the fluorescence power near resonance is given by:

$$P_{\text{Res. Fluor.}}(\omega_0) \approx \sigma_{\text{Fluor.}} \frac{\omega_0^{\,2}}{\left(\omega_0 - \omega_s\right)^2 + \frac{\gamma^2}{4}} I_0(\omega_0) \tag{3-18}$$

Here, the resonance condition is obtained when $\omega_0 = \omega_s$, and the same enhancement factor as in the resonance Raman case is obtained.

Two major points become clear from the theory. First, the large enhancement of the near-resonance denominator term means that ranging may be over longer distances or the detectable level of pollutant species may be lowered significantly. Second, generation of a narrow emission spectrum by the use of laser pumping could become a significant factor in being able to use narrow-banded detection schemes to reduce system noise.

3.2.4 Sensitivity Considerations

The sensitivity of a single-ended resonant system is evaluated through the basic equation:

$$P_r = P_t \frac{A}{4\pi R^2} \left(1 - e^{-k_{p\lambda} u}\right) \zeta \tau_\lambda^2 \eta_0 \tag{3-19}$$

where P_r and P_t are the received and transmitted power, A is the receiver area, 4π results from the fact that fluorescence radiation is isotropic, R is the range, $k_{p\lambda}$ is the monochromatic absorption coefficient of the pollutant, u is the optical depth given by the pulse length ct/2 and partial pressure of the species, ζ is the quenching efficiency, η_0 is the optical efficiency and τ_λ is the transmission through the nonhomogeneous path.

The quenching efficiency is dependent on the temperature, pressure and properties of the colliding species, and can be expressed in terms of radiative life time (τ_R) and quenching life time (τ_Q): $\zeta = \tau_Q/(\tau_R + \tau_Q)$. At sea level, τ_Q is several orders smaller than τ_R while at high altitudes, (above 80 km), τ_Q is much larger than τ_R. Thus ζ is near zero at sea level and near 1 at high altitudes. The line shape (combined Lorentz and Doppler) is also a strong function of altitude and its shape must be precisely known to determine the coincidence with the laser line. The position of the laser line relative to the pollutant absorption line is influenced by the Doppler shift, which is a function of satellite speed and the angle between the zenith and line-of-sight. Changing this angle may be used to maximize the coincidence of laser line with absorption line. If a pulsed laser system is used, the S/N is calculated from Eq. (3-19) and the noise value is given by the signal and background photons and the NEP of the system. In a CW laser system, the received signal at any time is the sum of signals from all volume elements within the line-of-sight, in which the fluorescence was induced. Thus, Eq. (3-19) becomes an integral over the line-of-sight and the pollutant concentration must be obtained through a deconvolution.

If the transmitter and receiver do not have common optics and are mounted on the same platform, the distance between them is necessarily short and the useful geometrical configurations are limited to intercepted volume elements close by. This application is useful for aircraft employing gated CW lasers, especially to survey limited regions at certain altitudes of interest, such as SST corridors. Typical lengths of intercepted volumes are of the order of 10^2 meters.

The backscattered intensity is given by (ref. 75):

$$I_{sc}\left(t=\frac{2R}{c}\right) = \sigma \frac{N_0(R)T_0T_s}{R^2} \frac{c}{2} \frac{\omega_0}{\omega_s} w_0 \tag{3-20}$$

where w_0 is the energy of a single pulse of duration t_0, R is the distance from the source to the polluted area which contributes to scattered intensity at time t. $N_0(R)$ is the pollutant concentration at R. T_0 and T_s are the transmission factors at the incident and scattered frequency and σ is the resonant Raman backscattered cross section. The observed intensity comes from a region of depth $ct_0/2$.

Over long ranges the lidar equation should contain an additional term taking into consideration losses due to diffraction alone. By considering the far field radiation pattern from a collimated diffraction-limited optical system, a Gaussian Beam of source size w_0 will expand (ref. 76) to:

$$w(2R) = w_0\left[1+\left(\frac{2\lambda R}{\pi w_0{}^2}\right)^2\right]^{1/2} \tag{3-21}$$

at the point of collection where R is the range under consideration.

In addition to diffraction losses, another problem is optical beam degradation over long paths which arises from atmospheric turbulence. This degradation problem may be severe for aircraft-borne systems. For satellite probing of the stratosphere, it is not anticipated that turbulence-induced intensity fluctuation would be a major problem.

4

SATELLITE OBSERVATION OF AEROSOLS

Satellites are well suited for the monitoring of the global aerosol loading of the atmosphere, which is of great importance in determining the effect of aerosols on climate. In considering the remote detection of aerosols from a satellite, we must understand the characteristics of the aerosol in relation to its optical properties, i.e., how it scatters and absorbs radiation. Thus, it is important to know the size distribution of the particles, and their composition in order to estimate their refractive index, which is an essential input parameter to scattering calculations by the Mie theory.

4.1 Aerosol Characteristics

Aerosols exist in a wide range of sizes and shapes, from dry insoluble irregularly-shaped dust particles to liquid spherical droplets. However, in order to theoretically model the properties of aerosols, they are generally all considered to be spherical.

Junge (ref. 77) found that the natural aerosol content of the atmosphere can be represented for radii from 0.1 μm to 10 μm, by:

$$dn(r) = \gamma r^{-\nu} d(\log r) \tag{4-1}$$

where

$dn(r)$ is the number of particles with radii between r and r + dr,

γ is a constant depending on the total particle concentration,

ν characterizes the size distribution.

Junge found that on the average the natural continental aerosol distribution is best described by $\nu = 3$.

The composition of the particulates is variable (ref. 78) and will vary considerably with location. Bullrich (ref. 79), in considering natural aerosols, decided that a refractive index of m = 1.55 is most suitable for calculations of Mie scattering by the aerosols. However, it is not clear that this value is the best for all aerosol types, e.g., continental, maritime, industrial and natural vegetation hazes.

In a clean atmosphere the vertical distribution of the natural aerosol density varies with the meteorological conditions, but on the average it decreases, with a scale height of about 1.25 km (ref. 79) in the troposphere. The measurements of Chagnon and Junge (ref. 80) showed a peak in the distribution in the stratosphere at about 20 km. This peak is 10^{-3} times the surface density.

4.1.1 Optical Properties of Aerosols

The light scattering properties are always used to remotely detect aerosols. However, in addition to scattering, aerosols absorb radiation. This absorption is not useful for measuring aerosols remotely, but must be considered in calculations of atmospheric transmission. Waldram (ref. 81) and Volz (ref. 82) made estimates of aerosol absorption in the visible region, and more recently Blanco and Hoidale (ref. 83) and Volz (ref. 84) have made measurements in the infrared. The significance of aerosol absorption is generally greatest over horizontal paths at the surface. An example by Volz shows that at 9 μm, for a 10 km path and a meteorological range of 10 km, a water haze would show a 20% absorption (of the same order as the scattering loss) which is comparable to water vapor absorption at the same wavelength. For remote sensing from a satellite looking vertically down, the aerosol mass will generally be much less (by about a factor of 10 for a normal Elterman (ref. 57) atmosphere). In the visible region the absorption is much less than in the infrared, and may, in general, be neglected.

The problem of light scattering in the atmosphere due to Rayleigh and Mie scattering is discussed in a review article by Rosenberg (ref. 85) and in greater depth by Bullrich (ref. 79). Both authors emphasize that it is impossible to calculate backward from experimental measurements in the atmosphere to obtain quantitative aerosol information. This is due to the complicated scattering processes.

The scattering function and polarization function may be calculated by the Mie theory for a single spherical particle of known refractive index. However, in the real atmosphere the particles are not necessarily spherical and vary in size and composition, so that the theoretical representation of the optical properties of the real aerosol distribution can be only approximate. In addition to the approximations in the theory, the aerosol scattering is coupled with Rayleigh scattering by the molecules in the atmosphere. This coupling is very complicated due to multiple scattering.

Thus, in order to relate satellite observations of the optical properties of the atmosphere to the aerosol content of the atmosphere, it will be necessary to select from several aerosol models that one for which the calculated optical properties best match the measured properties.

4.2 Passive Observations from Satellites

Passive satellite observations may be divided into two types: earth-oriented which will determine the total loading of the atmosphere, and sun-oriented occultation which will determine the stratospheric loading, the latter being important in determining the effects of high-flying aircraft.

4.2.1 Earth-Oriented Observations

At least three techniques may be considered for determining aerosol content from earth-oriented observations: (1) Sekera (ref. 86) indicated that measurements of the polarization of backscattered radiance may be interpreted in terms of aerosol loading of the atmosphere; (2) in our previous report (ref. 3) it was suggested that measuring the contrast of known surface features would allow the aerosol thickness to be determined; (3) examination of the results of the Monte Carlo calculations for model atmospheres by Plass and Kattawar (ref. 87) shows that the backscattered radiant intensity is a sensitive indicator of aerosols. This last relationship has been examined in more detail by Plass and Kattawar who performed under subcontract some special calculations which are discussed below.

4.2.1.1 Backscattered radiant intensity. Recent work (ref. 87) by Plass and Kattawar, using Monte Carlo calculations, has coupled Rayleigh and Mie scattering effects to determine the intensity and polarization of the radiance backscattered from an atmosphere containing aerosols and ozone absorption. The calculations use a realistic model of the earth's atmosphere including (1) Rayleigh and aerosol scattering with the proportion varying with height, (2) aerosol phase function with strong forward scattering, (3) aerosol number density, varying with height, and (4) ozone absorption. Multiple scattering of all orders is included. This work assumes that the earth's surface is a perfect diffuse reflector (Lambertian) and non-polarizing. As shown by earlier work of Coulson (ref. 88) the earth's surface typically deviates from these perfect conditions with subsequent significant effects on outgoing radiation. Examination of the results of Plass and Kattawar shows that the outgoing radiance is most sensitive to aerosol amount when the surface albedo is low; hence a low albedo surface is preferred for aerosol observations. The ocean, which covers much of the earth, provides such a surface for aerosol observations; it has a low albedo (~.02) at high sun elevations and its reflectance properties are assumed to be known. (This assumption is discussed in Section 4.2.1.5.)

The calculations also indicate that observations at the longer wavelengths ($\geq 0.7 \mu m$) are more sensitive to aerosol changes. At shorter wavelengths the Rayleigh optical thickness is comparable to, or greater than, the aerosol optical thickness, so that changes in the aerosol amount have less effect. The results obtained by Plass and Kattawar for $\lambda = 0.7\ \mu m$ are plotted in fig. 4-1. It is seen that the reflected radiance for zero albedo changes significantly as a function of aerosol amount in the atmosphere. Here, they have used the 1964 Elterman distribution (ref. 53), with the following optical thicknesses: Ozone: $u = 0.008$, Rayleigh: $u = 0.037$, Aerosol: $u = 0.180$, 0.060, and 0.54.

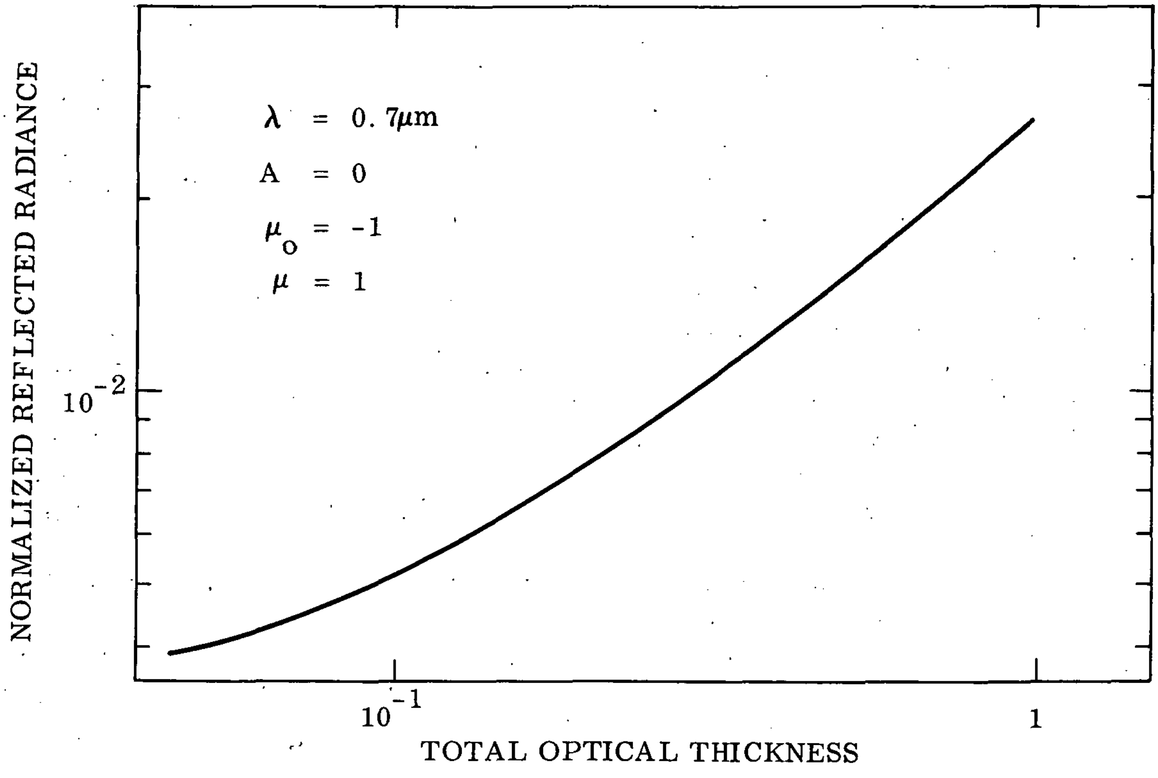

Figure 4-1. Normalized Reflected Radiance vs Total Optical Thickness (Aerosol & Rayleigh & Ozone)

In order to further investigate the effect of aerosols on the upward radiance, calculations were performed under subcontract by Plass and Kattawar for 17 specific cases of various aerosol and ozone distributions at three wavelengths ($0.7\mu m$, $0.9\mu m$, and $1.67\mu m$), all with an underlying ocean surface, assumed to be a perfectly smooth specular reflector.

With Monte Carlo techniques it is possible to calculate the complete radiation field in the atmosphere-ocean system with a realistic model for both the atmosphere and ocean. In the atmosphere, both Rayleigh and aerosol scattering (aerosol absorption is negligible) are included in the model, the latter represented by a scattering function with a strong forward peak. Absorption by atmospheric ozone is also taken into account. Both the reflected and refracted rays, as well as the rays that undergo total internal reflection, are followed from the ocean surface. The appropriate absorption and scattering by the water molecules and hydrosols of the ocean are included in the calculation. The scattering function for the hydrosols as calculated from a distribution of sizes by the Mie theory agrees well with measurements and has a strong forward maximum. The total radiation field is obtained as the three-dimensional paths of the photons are followed by the Monte Carlo method.

The realistic model used to represent the earth's atmosphere has been described by Plass and Kattawar (ref. 87). The model uses the Rayleigh attenuation coefficient, ozone absorption coefficient, and the aerosol number density as a function of height and wavelength were as tabulated by Elterman (1968) (ref. 57). (Earlier tables by Elterman (ref. 53) were originally used by Plass and Kattawar.)

The total optical thickness of the atmosphere was calculated from the Rayleigh and aerosol attenuation coefficients and the ozone absorption coefficients. The atmosphere was divided into a number of layers, and the ratios of the Rayleigh extinction to total extinction coefficient and the scattering to extinction coefficient for both the Mie and Rayleigh particles were established for each layer. The probability of ozone absorption was also calculated from the ozone absorption coefficient for each layer. All calculations were made with the optical depth as the parameter.

Five different aerosol distributions together with the normal ozone distribution are used in these calculations. Model A uses the normal aerosol distribution given by Elterman (1968) as shown by the solid line in fig. 4-2. Model B corresponds to three times the normal aerosol amount and Model C to ten times the normal amount. Model D has the normal aerosol distribution above 1 km (same as Model A), but a heavy aerosol layer between the ground and 1 km, such that the total aerosol amount is three times normal. Model E has a thick layer of aerosols between 20 and 25 km corresponding to ten times the normal amount and has the normal distribution (same as Model A) at all other altitudes.

Two other models were used to study the effect of ozone variations. Model F uses the same aerosol distribution as Model B and the ozone distribution indicated by open squares in fig. 4-2. The total ozone amount for this model is 0.23 cm, whereas it is 0.35 cm for the normal ozone distribution indicated by the solid line in fig. 4-2. Model G uses the same aerosol distribution as Model B and the ozone distribution indicated by solid squares in fig. 4-2 (total ozone amount is 0.47 cm).

The results of the calculations are shown for the three wavelengths in figs. 4-3, 4-4 and 4-5. The results for Model G are not shown since they are virtually identical to those for Model F. The upward radiance for a source of unit incident flux is shown as a function of the cosine of the nadir angle (μ) for a fixed overhead

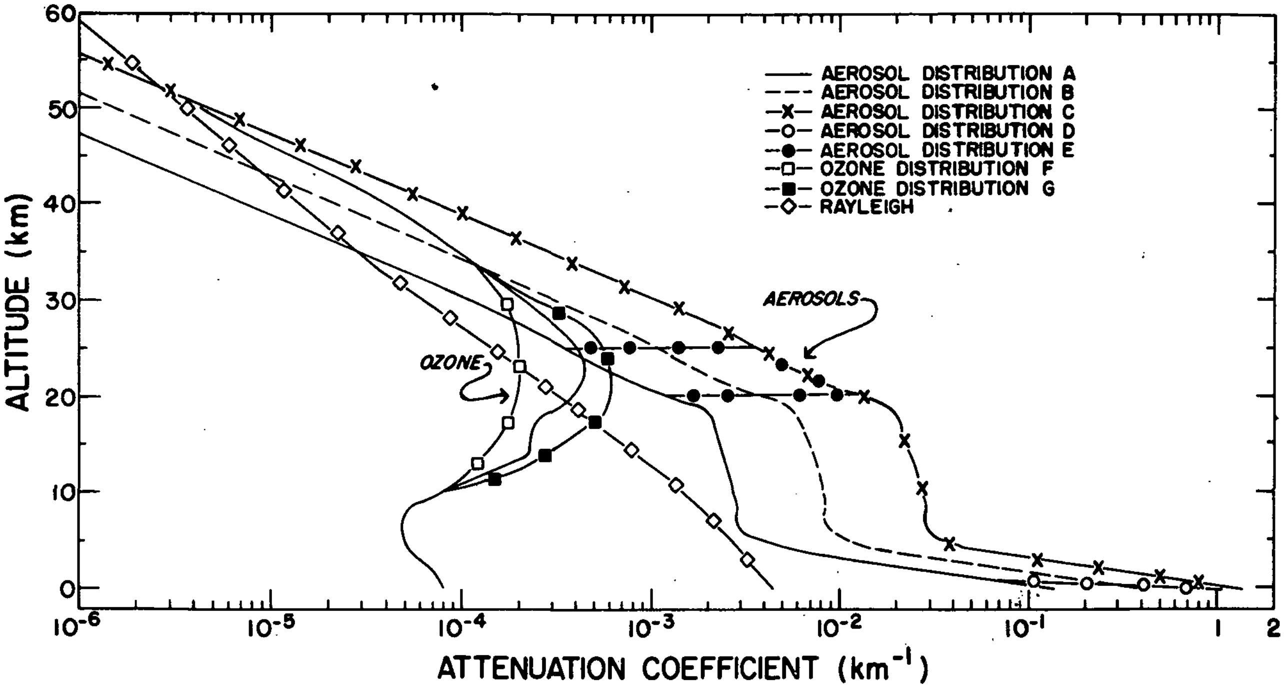

Figure 4-2. Atmospheric Models: Aerosol, Rayleigh and Ozone Attenuation Coefficients vs. Altitude

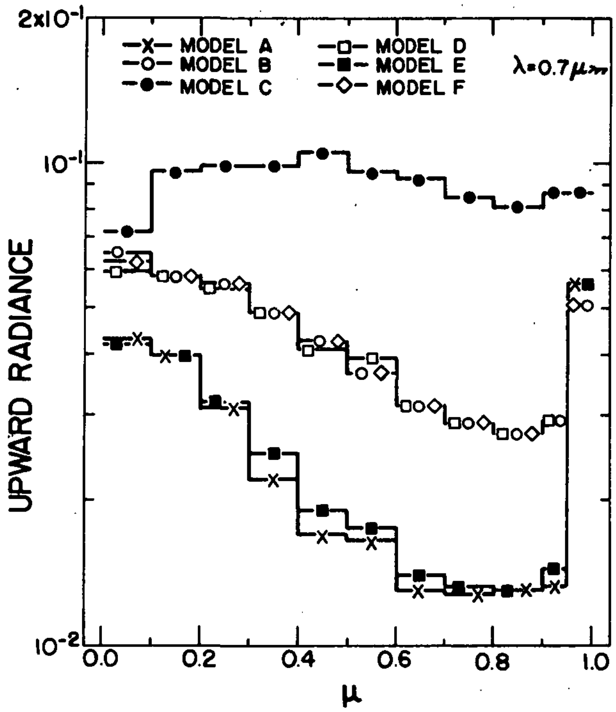

Figure 4-3. Normalized Upward Radiance vs. Nadir Angle ($\lambda = 0.7\mu m$) for Different Model Atmospheres

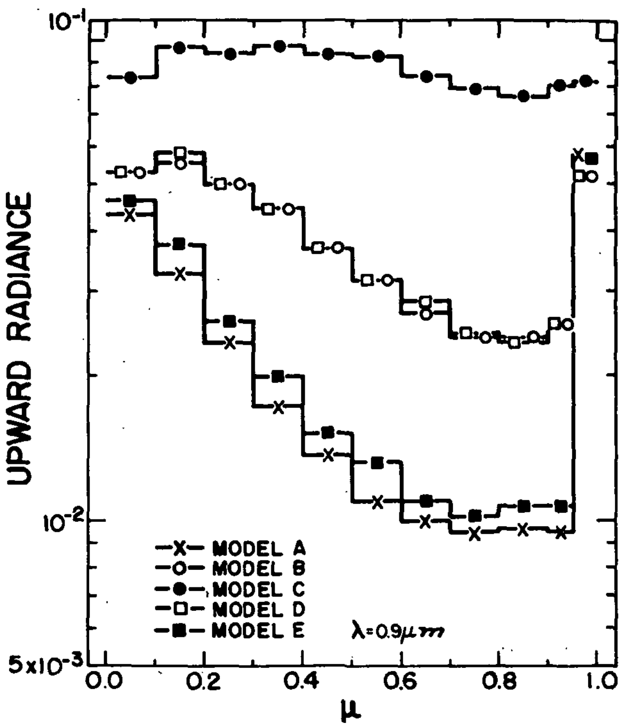

Figure 4-4. Normalized Upward Radiance vs. Nadir Angle (λ = 0.9μm) for Different Model Atmospheres

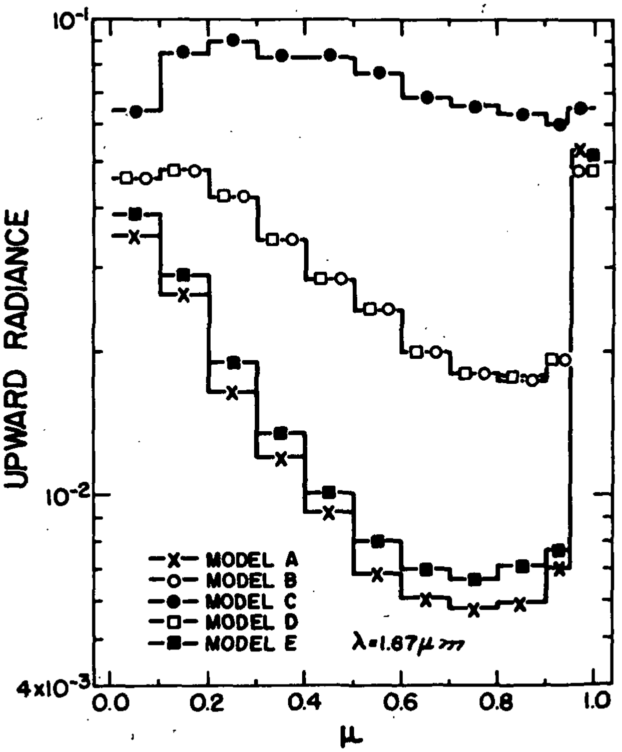

Figure 4-5. Normalized Upward Radiance vs. Nadir Angle (λ = 1.67μm) for Different Model Atmospheres

sun ($\mu_0 = -1$). These results may be converted to those of interest in this study; namely, looking vertically down ($\mu = 1$) with a variable sun zenith angle, by using the principle of reciprocity.

Symmetry relations for the reflection and transmission matrix have been rigorously studied by Hovenier (ref. 89). In this present work, polarization effects are neglected and the reciprocity principle assumes the following simple form for the reflected radiance:

$$\mu E\left(0, \mu, \phi; \mu_0, \phi_0\right) = \mu_0 E\left(0, \mu_0, \phi_0; \mu, \phi\right) \tag{4-2}$$

where $E\left(0, \mu, \phi; \mu_0, \phi_0\right)$ is the radiance at the observation angle specified by μ, ϕ due to an incoming solar beam specified by μ_0, ϕ_0. The reciprocity relation will also hold in the case of coupling the atmosphere-ocean radiation fields. This can best be imagined physically since the interface can be thought of as a degenerate reflecting volume possessing the same symmetry as a scattering function.

Examination of curves given in figs. 4-3, 4-4, and 4-5 shows a result of great importance for satellite observations of the upward radiance: the upward radiance depends strongly on the total number of aerosols, but not on their vertical distribution. Thus measurements of the upward radiance can be directly related to the total vertical aerosol content and hence the global loading.

The three wavelengths considered show comparable sensitivity to aerosol changes. However, the normalized radiance is less at the longer wavelengths, and since the incoming solar flux decreases at longer wavelengths, the absolute radiance level decreases rapidly with increasing wavelength (the absolute radiance at 1.67μm is about 6% of that at 0.7μm). Thus, 0.7μm is the preferred wavelength of observation, and although there is some ozone absorption, the calculations show a negligible effect of ozone variations (compare Model B and Model F in fig. 4-3).

The angular distribution of the backscattered radiance is not a sensitive indicator of aerosol amounts, especially in the region $\mu = 0.5$ to 1.0, where observations from a typical polar orbit of 600 nmi altitude would be constrained due to the fact that a look angle of $\mu = 0.5$ is approximately tangent to the earth's surface. Also, non-vertical look angles would have a greater probability of having clouds in the field of view.

It is concluded then, for the ideal model conditions (see discussion in Section 4.2.1.5), that the aerosol content of the atmosphere can be measured from a satellite looking vertically down at the ocean at a wavelength of 0.7μm. The calculations in fig. 4-3 show that the sensitivity is greatest in the range of solar zenith angles $\mu_0 = 0.4$ to 1.0. Figure 4-6 shows the variation of normalized radiance with μ_0 as a function of wavelength for the normal aerosol content and three times normal. The calculated points show some scatter about the smooth curves due to the statistical

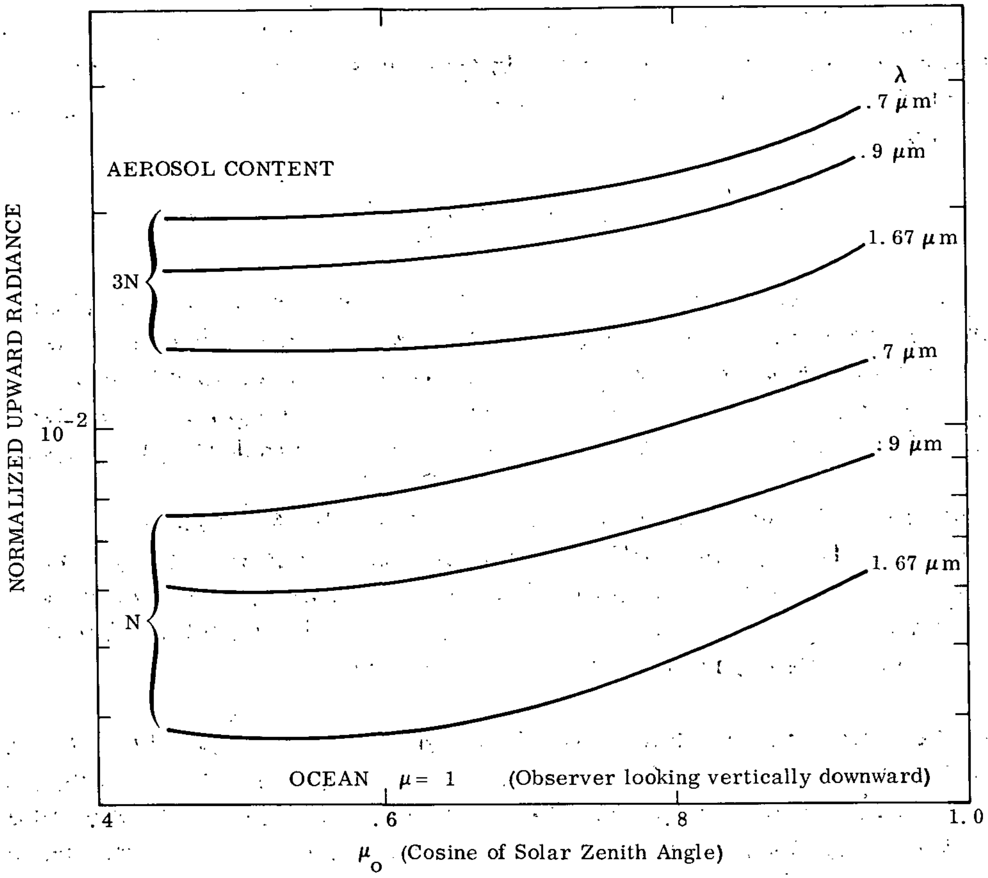

Figure 4-6. Normalized Upward Radiance vs. Sun Angle as Function of Wavelength

nature of the Monte Carlo method. The curves are not extended into the $\mu_0 = 0.95$ to 1.0 region where the specular reflection at the ocean surface would be seen by the observer, as illustrated by the sharp increases in radiance for $\mu = .95$ to 1.0 in figs. 4-3, 4-4, and 4-5. Of course, in a satellite observation such as suggested here, the detector must always avoid the sun-glitter pattern on the ocean, in order to observe a surface of low reflectivity.

The smoothed data in fig. 4-6 are replotted in fig. 4-7 to show the relationship between the upward radiance, normalized to unit incident solar flux, and the vertical mass loading of the atmosphere for various sun angles. The mass loading is determined from the aerosol optical thickness as discussed in Appendix B. A simple linear relationship is shown to exist between radiance and the mass loading. These straight lines are based on only two values of mass loading, but the linear relationship may be verified by considering the four data points for zero albedo given in fig. 4-1.

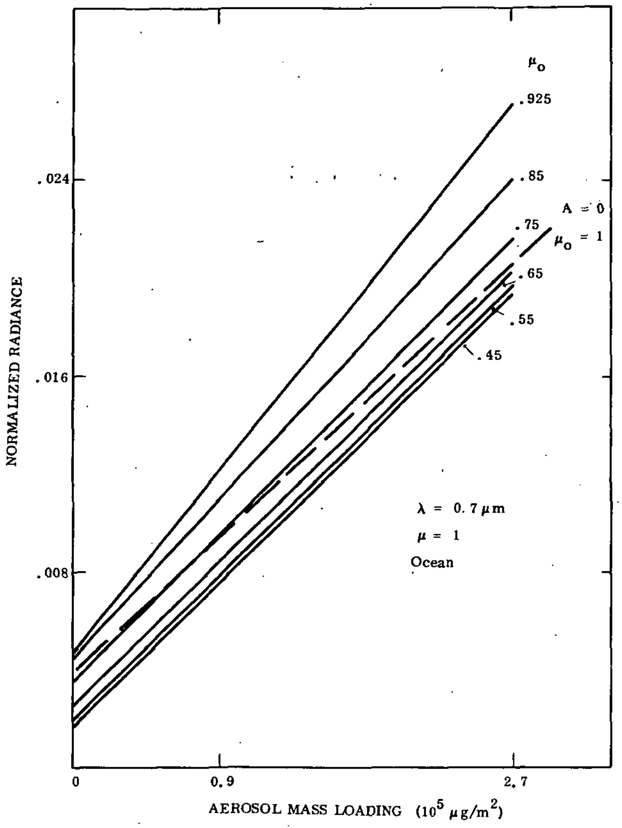

Figure 4-7. Normalized Upward Radiance vs. Aerosol Mass Loading as a Function of Look Angle

McLellan (ref. 90) recently attempted to relate reflected radiance measurements from the geosynchronous ATS-III satellite to the particle count in Los Angeles. The results, which are only qualitative, show the radiance increasing as the particulate count decreases. This is in contrast to the variation expected from theory for pure scattering aerosols, indicating that there is strong absorption by the smog, either by gases or particles, in this spectral region (0.5 μm) (suggested by G. N. Plass, private communication).

4.2.1.2 Polarization of backscattered radiation. The polarization of radiation scattered by molecules is greater than that scattered by particles. Thus the polarization of radiation scattered by the atmosphere is reduced as particles are added to the atmosphere. It is this difference in polarization from that of the theoretical Rayleigh atmosphere which must be analyzed to determine the aerosol content. The aerosol content cannot be deduced directly due to the complexities of the coupling of Rayleigh and Mie multiple scattering and the presence of non-Lambertian surfaces, and must be determined by comparing the measurements with calculations for model aerosol atmospheres.

Sekera (ref. 86) has discussed the theory of this type of observation, and Hariharan (ref. 91) has performed aircraft measurements, making some deductions about the aerosol size distribution. However, the models used did not account for multiple scattering.

Plass and Kattawar (ref. 87) have made Monte Carlo calculations, including multiple scattering of the polarization of radiation scattered by realistic model atmospheres with various aerosol contents at wavelengths from 0.27μm to 1.67μm. The wavelength most sensitive to aerosol changes is 0.7μm; at shorter wavelengths the Rayleigh optical thickness is much greater than the aerosol thickness and the molecular polarization dominates, and at longer wavelengths the polarization is small with correspondingly small effects by aerosols.

As in the case of radiant intensity observations the effect of aerosols decreases as the albedo increases, so that measurements of polarization over low-albedo surfaces are desirable. Unfortunately, as found by Coulson et al. (ref. 92), low reflectance surfaces are highly polarizing; this makes the modeling and data interpretation difficult.

For an overhead sun, the most sensitive look angle is given by $\mu = 0.35$. But, as pointed out in Section 4.2.1.1, for NIMBUS-type orbits, observations are limited to $\mu = 0.5$ to 1. The sensitivity decreases as μ increases, i.e., looking towards the horizon is preferred. However, this look angle will almost certainly include clouds in the field of view, which would greatly complicate the data interpretation.

The results for a wavelength of 0.7μm are presented in fig. 4-8. The curves illustrate the decrease of sensitivity as the look angle approaches the vertical, although there is little difference between $\mu = .55$ and $\mu = .15$. It should be noted that these curves are for zero albedo; there are currently no calculations available on the polarization of the upward radiance over an ocean surface (since polarization calculations are considerably more complex than calculations of radiance only), so the discussions here are limited to calculations for zero albedo. Thus the values of polarization and their sensitivity to aerosol content are higher than are to be expected in the real atmosphere with an underlying non-zero albedo.

The calculations of Plass and Kattawar have been made mainly for an overhead sun, whereas for satellite observations it is of more interest to consider the observer looking vertically down with a variable sun angle. Unfortunately, a simple reciprocity relationship does not exist for polarization (ref. 93). However, some inferences may be made. If a relationship for polarization similar to that for intensity in equation (4-2) existed, then the values of polarization and the sensitivity to aerosol content shown in fig. 4-8 would be reduced; if the polarization were unchanged by interchanging the observer and source then the sensitivity would be unchanged. Thus it appears that calculations for vertical observations will not indicate more sensitivity than that shown in fig. 4-8.

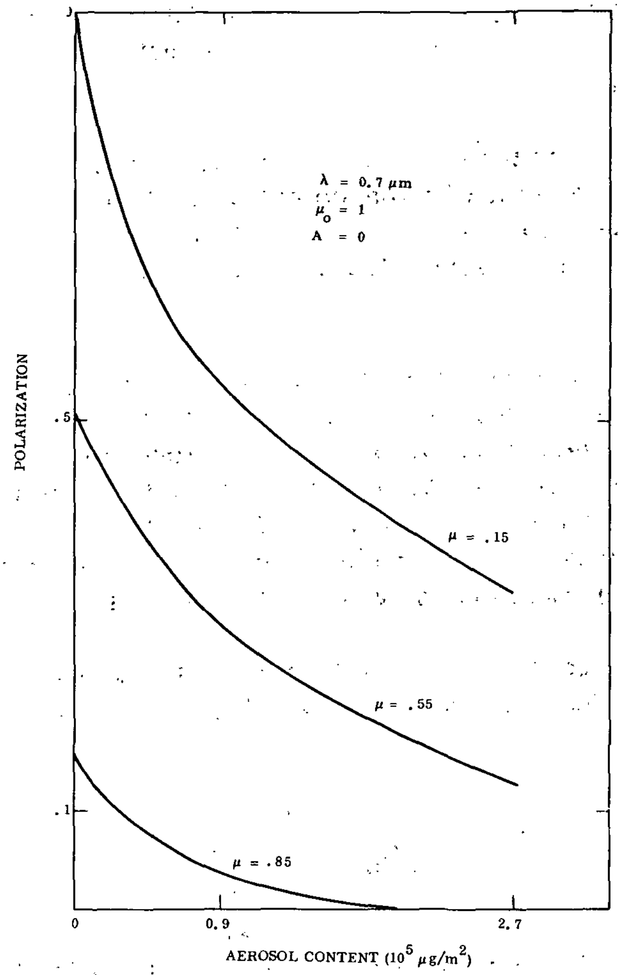

Figure 4-8. Polarization vs. Aerosol Mass Loading as a Function of Look Angle

4.2.1.3 Comparison of radiance and polarization observations. A comparison of the accuracies of the radiance and polarization observations of aerosols may be made by considering the sensitivity curves shown in fig. 4-7 and fig. 4-8. It is reasonable to assume that the radiance can be measured to ± 1%, so that from fig. 4-7 it is found that the error in aerosol content is about ± 1.3%. The polarization of back-scattered radiation can probably be measured to an accuracy of ± 1% in the range 5-75% (ref. 95), so that the error in near-normal values of aerosol content is about ± 7.5% for a look angle of $\mu \doteq .55$. It should be noted that this large error is somewhat underestimated, since it is for zero albedo; in addition, it will probably be even larger if the observer and sun are interchanged to consider more realistic conditions for satellite observations.

It should also be remembered that calculations of polarization for various vertical distributions of aerosols have not been performed, so it is not known whether polarization, like radiance, is independent of the distribution. Of course, the error estimates for both techniques assume that the theoretical relationships in figs. 4-7 and 4-8 are correct.

It is concluded from the preceding discussions, based on model calculations, that satellite measurements of radiance are preferred to measurements of polarization to determine aerosol content. This is in contrast to ground-based observations, in which the sky polarization is more sensitive to aerosol changes than is sky radiance.

4.2.1.4 Method of contrast reduction. In the previous study (ref. 3) we suggested that measurements from space of the apparent contrast of known surface features could provide a measure of the total aerosol content in the atmosphere. This section describes the theory of contrast reduction which indicates that a quantitative measure of the aerosol vertical optical thickness may be obtained from satellite photographs. The aerosol mass loading may then be determined from an empirical relationship between mass loading and optical thickness.

The theory of contrast reduction developed by Duntley (ref. 96) is briefly discussed below. The inherent contrast of an object relative to the background is defined as

$$C_0 = \frac{B_0 - B'_0}{B'_0} \qquad (4\text{-}3)$$

where B_0 and B'_0 are the luminances of the object and background, respectively. The apparent contrast, as viewed from range, R, is defined as

$$C_R = \frac{B_R - B'_R}{B'_R} \qquad (4\text{-}4)$$

where B_R and B'_R are the corresponding luminances observed at R. An object of luminance B_0 viewed through a scattering atmosphere with an optical depth, u, is assumed to have an apparent luminance, B_R, given by

$$B_R = B_0 e^{-u} + \frac{B_{a(0)}}{\kappa_0}\left[1 - e^{-u}\right] \qquad (4\text{-}5)$$

In the second term on the right, which results from scattering into the line of sight, $B_{a(0)}$ is the atmospheric luminence and κ_0 is the extinction coefficient. The contrast ratio C_R/C_0 is found to be

$$\frac{C_R}{C_0} = \frac{1}{1 + \frac{B_{a(0)}}{\kappa_0 B_0'}\left(e^u - 1\right)} \tag{4-6}$$

The coefficient $B_{a(0)}/\kappa_0 B_0'$ has been called the "sky/ground ratio."

We have fitted this equation with values of C_R/C_0 calculated for the results of Plass and Kattawar (ref. 87), and the values of $B_{a(0)}/\kappa_0 B_0'$ obtained were strongly dependent upon u. The inapplicability of Eq. (4-6) to the case of observations made through the entire atmosphere is not unexpected, since the variation of u is due to the particulate component only while the Rayleigh component remains constant.

A perfectly arbitrary generalization of Eq. (4-6) is made:

$$\frac{C_R}{C_0} = \frac{1}{1 + g(u, A)} \tag{4-7}$$

From values published by Plass and Kattawar for reflected radiance versus albedo, it is concluded that the reflected radiance is well represented by a linear function of the albedo A:

$$E(u, A) = E(u, 0) + A\left[E(u, 1) - E(u, 0)\right] \tag{4-8}$$

The apparent contrast is, consequently:

$$C_R = \frac{E(u, A) - E(u, A')}{E(u, A')}$$

$$= \frac{(A - A')\left[E(u, 1) - E(u, 0)\right]}{E(u, 0) + A'\left[E(u, 1) - E(u, 0)\right]} \tag{4-9}$$

Since

$$C_0 = \frac{A - A'}{A'} \tag{4-10}$$

we have

$$\frac{C_0}{C_R} = 1 + \frac{E(u, 0)}{A'\left[E(u, 1) - E(u, 0)\right]} \tag{4-11}$$

By identifying with Eq. (4-6) we find that the unspecified function g(u, A) may be separated into u- and A-dependent parts:

$$g(u, A) = f(u)/A \tag{4-12}$$

where

$$f(u) = \frac{E(u, 0)}{E(u, 1) - E(u, 0)} \tag{4-13}$$

Values of $E(u, A = 0, 1)$ have been calculated by Plass for five values of u (for $0.045 \leq u \leq 0.561$ at $\lambda = 0.7\ \mu m$). The derived values of f(u) are plotted in fig. 4-9 for four sun angles, for each of which f(u) is seen to be a smooth function of u. The function f(u) is related to the experimentally observable quantities C_0, C_R and A' by Eq. (4-7 and 4-12):

$$f(u) = A'(C_0/C_R - 1) \tag{4-14}$$

Thus, a measurement of the contrast ratio and knowledge of albedo and sun angle yields a value of f(u) which determines u.

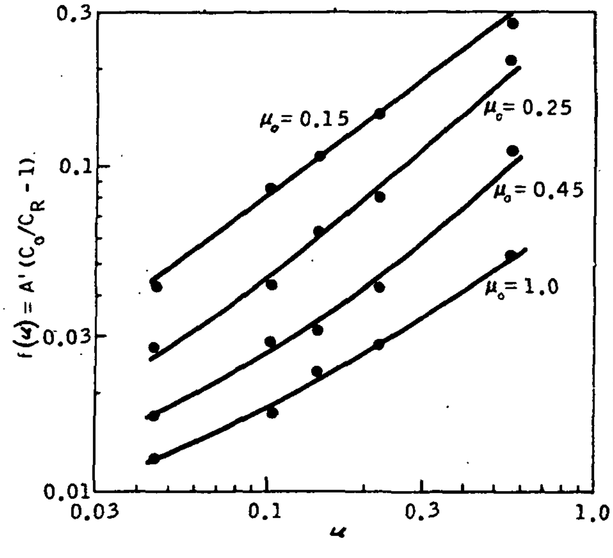

Figure 4-9. Function of $f(u) = A'(C_0/C_R - 1)$ versus u for Values of Sun Zenith Angle, θ, ($\mu_0 = \cos\theta$)

The total vertical optical thickness, u, at visible wavelengths is given by

$$u = \left(u_R + u_o + u_A\right) \tag{4-15}$$

where u_R, u_o, and u_A are the vertical optical thicknesses for Rayleigh scattering, ozone absorption, and Mie scattering, respectively. The value of u_R is known, and u_o, which is much smaller than u_R and u_A, may be determined to sufficient accuracy by assuming a mean total ozone thickness.

Experimental verification of the validity of the curves in fig. 4-9 is essential to determine not only the accuracy of the theoretical values of reflected radiance but the reasonableness of the assumption of linearity of E with A, as well as the importance of other non-ideal effects, such as the deviation of real surfaces from the assumed Lambert law of diffuse reflection.

The above theory will be tested (ref. 97) by using ERTS-1 satellite data to determine the aerosol optical thickness, which will then be compared with ground truth data obtained by measurements with a Volz photometer. One test site is the desert/Salton Sea region in Southern California. The reflectivities of the desert and the water surface are known approximately from previous work (ref. 98,99) so the inherent contrast is known approximately; however, a precise measurement of the inherent contrast will be made from a low-flying aircraft simultaneously with the satellite overflight. The apparent contrast will be determined from densitometer analysis of the satellite pictures taken in narrow spectral band-passes in the visible region.

After successfully testing the technique, the global aerosol loading may be monitored by future satellites observing widespread test-sites whose inherent contrast is known or is measured periodically with low-flying aircraft.

4.2.1.5 Problem areas. The discussions in the preceding sections on the possible methods of measuring the aerosol content are based on theoretical calculations which use a model atmosphere, a model aerosol distribution, and assume a perfect underlying surface, either specular or diffuse. In practice, of course, these model conditions are never realized, so that deviations from the theoretical relationships are to be expected. A brief outline of anticipated problems and their possible solutions is given below. Of course, even if the problems cannot be resolved theoretically, satellite and ground-truth measurements may be used to derive empirical relationships between the aerosol content and contrast transmission, radiance, and polarization, based on the theory for ideal model conditions.

Sun Glitter. If the ocean were perfectly smooth as assumed in the calculations, an image of the sun would be seen at the specular reflection angle, and the only upwelling surface radiation observable at other look angles from space would be the diffuse sky radiation reflected from the ocean surface, and the radiation scattered up from below the ocean surface. As the smooth ocean surface is increasingly disturbed, a glitter pattern becomes increasingly larger about the specular point. At sun zenith angles greater than about 30° the glitter effect has been considered negligible (except for very rough seas) at the nadir point. However, recent measurements by Hovis (private communication, R. S. Frazer, 1972) suggest that this assumption is not correct, so that the radiance and polarization of the ocean surface at the nadir are not known accurately.

This problem might be overcome by making observations at two wavelengths, assuming that the spectral variation of the surface radiance is known. However, the choice of wavelengths must be made carefully since the spectral distribution of the radiance does vary due to ocean properties such as chlorophyll content, suspended matter and depth (ref. 100).

Aerosol Properties. In order to make model calculations, assumptions must be made about the aerosol properties such as size distribution, vertical distribution, sphericity of the particles and the refractive index. All of these assumptions affect the phase function to be used in the multiple scattering calculations. The variability of each of these parameters in the real atmosphere should be investigated. Some work along these lines has been reported by Rosenberg (ref. 101) who suggests that the Junge aerosol model is not applicable to the atmosphere - in the case of humid atmospheres, because of condensation on the particles, and for dry atmospheres because the particles are non-spherical.

Non-Lambertian Surfaces. Most calculations of scattering properties of the atmosphere use an underlying Lambertian surface. However, the calculations for the ocean in Section 4.2.1.1 treat the surface correctly as a specular reflector for both the direct and sky radiation, and include the upwelling radiation scattered by the water from beneath the surface. Raschke (ref. 102) uses a two-layer model of the atmosphere-ocean system, and a rough ocean surface (equivalent to a wind speed of about 1.4 m sec^{-1}) to calculate the radiance outside the atmosphere, but does not show a quantitative comparison with calculations for a smooth surface. For the desert, which might be used in contrast measurements (Section 4.2.1.4), the surface reflectance is not perfectly diffuse, with the backscattering being greater than the forward scattering (ref. 98). However, it is close to being a diffuse reflector, and no variability of albedo with sun angle was found (ref. 103). The error resulting from assuming the desert to be a Lambertian surface should be small. Over land, whose reflectivity is generally higher than that of the ocean, the sensitivity of the radiance and the polarization measurements to aerosol content is reduced (see Sections 4.2.1.1 and 4.2.1.2). More importantly, changes in the surface reflectance properties (reflectivity and polarization), which are not readily determined from the satellite, appear to affect the observed values of radiance and polarization more than the expected changes in aerosol content. Research on these problems is continuing, and the investigations using ERTS-1 and ground-truth data will be invaluable in resolving them.

Polarization measurements will be particularly affected by the polarization of radiation by reflection at the underlying surface. Coulson et al. (ref. 92) found that the degree of polarization depends on the surface reflectivity: surfaces of low reflectance are highly polarizing, whereas high reflectance surfaces produce relatively small polarization.

Surface Reflectance Gradients. The calculations of Plass and Kattawar which are used in deriving the contrast attenuation relationship in Section 4.2.1.4 assume an underlying surface of constant reflectivity extending to infinity. However, for two adjacent surfaces of different reflectivities, the radiation reflected from one surface will be scattered into the atmosphere above the other surface, so that the apparent radiance above that surface is changed from the calculated theoretical value. This is probably a second-order effect if the radiance or polarization is measured at points well removed from the boundary of the two surfaces, and will be verified for the radiance by comparing the theoretical calculations with the aircraft measurements in the ERTS-1 program (ref. 97).

4.2.2 Sun-Oriented Observations

Satellite measurements of aerosols in the stratosphere are well suited to the occultation method (illustrated in fig. 4-10), in which observations are made of the sun's radiation as the satellite enters or leaves the earth's shadow. From the observed attenuation along successive light paths, and allowing for refraction, the vertical distribution may be determined, if the aerosols are assumed to be uniformly distributed in the horizontal. These observations are generally restricted to the stratosphere and higher due to the presence of clouds and high attenuation (scattering and absorption) in the troposphere; these problems are discussed in some detail below, and apply, of course, also to the gaseous limb experiments (Section 3.1.2).

The only satellite occultation measurements to date appear to be of ozone by Rawcliffe et al. (ref. 104), and Miller and Stewart (ref. 105). Their measurements used the full disc of the sun (0.5° angular diameter), so that the vertical resolution in the deduced ozone was only about 16 km. Improvement of this height resolution would require the use of a sun-pointing device to observe a small area of the sun. Pepin (ref. 106) has carried out many occultation measurements from balloons with a simple four-channel radiometer. The field-of-view is large (14° × 14°) so that only low vertical resolution is obtainable. In addition, Pepin (private communication) has two satellite experiments planned. The first is on Air Force satellite 72-2 in 1973, in which the full disc of the sun is used. A later experiment on OSO-J has sun-tracking capability, and Pepin hopes to achieve a vertical resolution of about 1/3 km.

4.2.2.1 Cloud interference. An obvious problem in using occultation methods to probe the lower atmosphere is the presence of clouds. Most clouds are confined to the troposphere, the height of which varies from about 17 km in the tropics to below 10 km in polar regions. If it is assumed that the clouds reach up to 10 km,

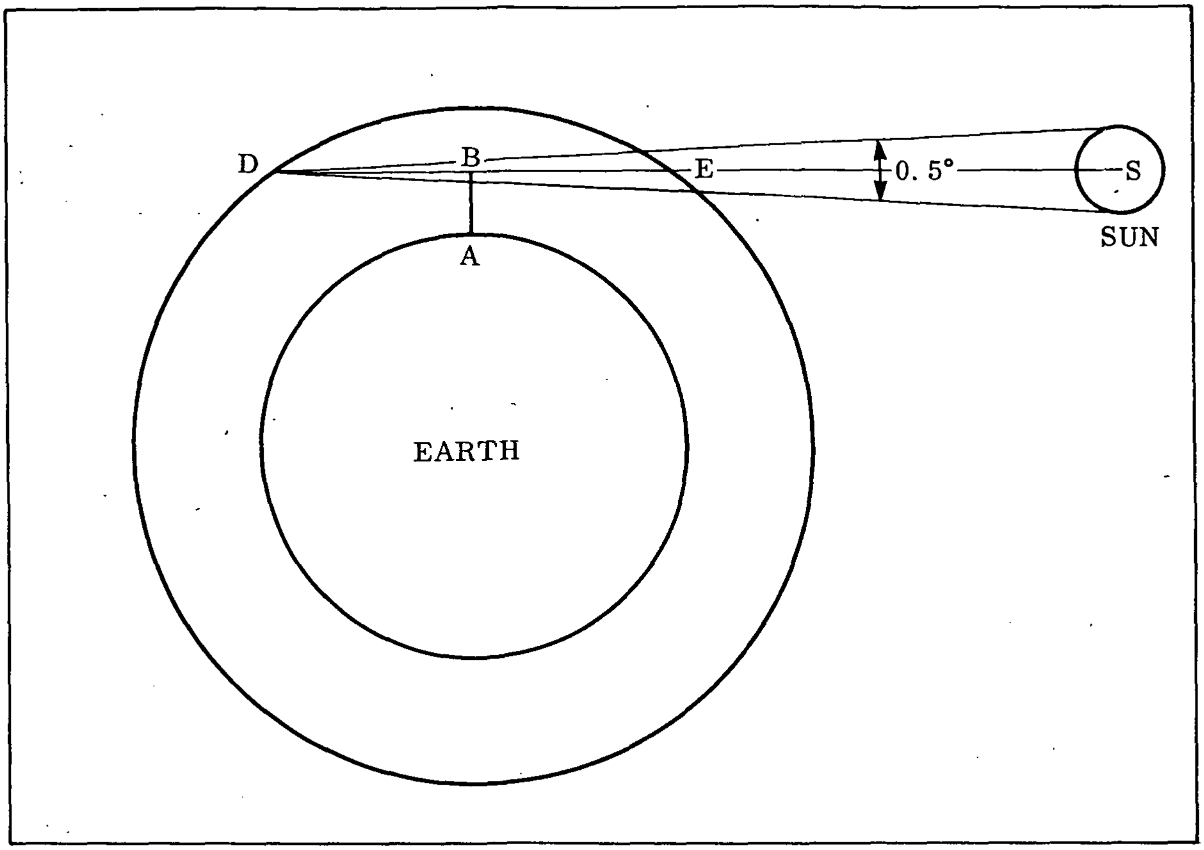

Figure 4-10. Schematic of Occultation Experiment

it may be calculated that a cloud-free region nearly 700 km wide is required for an unobstructed line-of-sight, tangent to the earth's surface, from a 300 km orbit to the sun. Such a large clear area would be very rare; even if the atmosphere were cloud-free, the strong attenuation (scattering and absorption) of the radiation through the lower atmosphere would preclude occultation probing at these low altitudes (see next section).

Even if the observations are confined to the stratosphere, the problem of clouds is not entirely eliminated; clouds do occur in the stratosphere. In addition to the occasional penetration of the tropopause by thunderheads, there are, at higher altitudes, nacreous (or mother-of-pearl) clouds and noctilucent clouds. Noctilucent clouds occur at about 80 km and are generally observed at high latitudes in the summer. The nacreous clouds are formed in the 20-30 km region and are observed in middle latitudes in the winter. This latter altitude region is where high-flying aircraft are operating; so with the addition of particles and water vapor from the exhaust products we might expect more nacreous clouds in future years. These stratospheric clouds present a problem to occultation measurements since they will attenuate the sun's radiation by an unknown amount resulting in misinterpretation of the observations. However, if the interest is in the global loading of aerosols in the stratosphere, the data may be averaged over all latitudes to minimize errors due to stratospheric clouds. It is possible that far-infrared observations (ref. 107) might be used to detect the presence of these clouds in the line-of-sight. Lidar techniques, as discussed briefly in Appendix B for cirrus clouds, might also be considered.

4.2.2.2 Atmospheric attenuation. The attenuation of the sun's radiation varies as a function of wavelength, and as a function of the grazing altitude of the radiation. Both gaseous absorption and molecular scattering must be considered. In the ultraviolet and visible region ozone absorption is important, and in the infrared beyond about 0.8μm, absorption by other atmospheric gases, particularly water vapor, is important. Rayleigh scattering is negligible in the infrared, but is a significant factor in considering shorter wavelengths for occultation. For aerosol observations an atmospheric "window" must be chosen.

Calculations of the sensitivity at various wavelengths to changes in aerosol content may be made based on the 1968 model atmosphere of Elterman (ref. 57). Figure 4-11, fig. 4-12 and fig. 4-13 show results of simplified calculations (neglecting aerosol absorption) for occultation grazing heights of 10, 15, and 20 km, respectively. The calculations are also simplified to the extent that the sun is considered as a point source, so that the variation of transmission of the light rays from different parts of the sun is neglected. In addition, refraction of the light rays in the atmosphere is ignored.

Thus the transmission τ in atmospheric windows at high altitudes where gaseous absorption is negligible, is given by

$$\tau = \exp\left(-2u(\lambda)\,\mathrm{Ch}(90^\circ)\right) \tag{4-16}$$

where u(λ) is the wavelength-dependent vertical optical thickness above the grazing altitude and is the sum of contributions from Rayleigh scattering and aerosol scattering.

Ch(90°) = 35, is the Chapman function (ref. 108) for zenith angle 90°. Ch(θ) replaces the usual secant θ when θ is large.

The factor 2 accounts for the two equal optical paths BD and BE in fig. 4-10.

The results show, as expected, that the shorter wavelengths are more sensitive to aerosol variations than the infrared region. Observation of attenuation at the shorter wavelengths would have to take into account the contribution of Rayleigh scattering, which is well known. In the infrared, the Rayleigh scattering is negligible, and, at the higher altitudes above about 12 km, the water vapor continuum

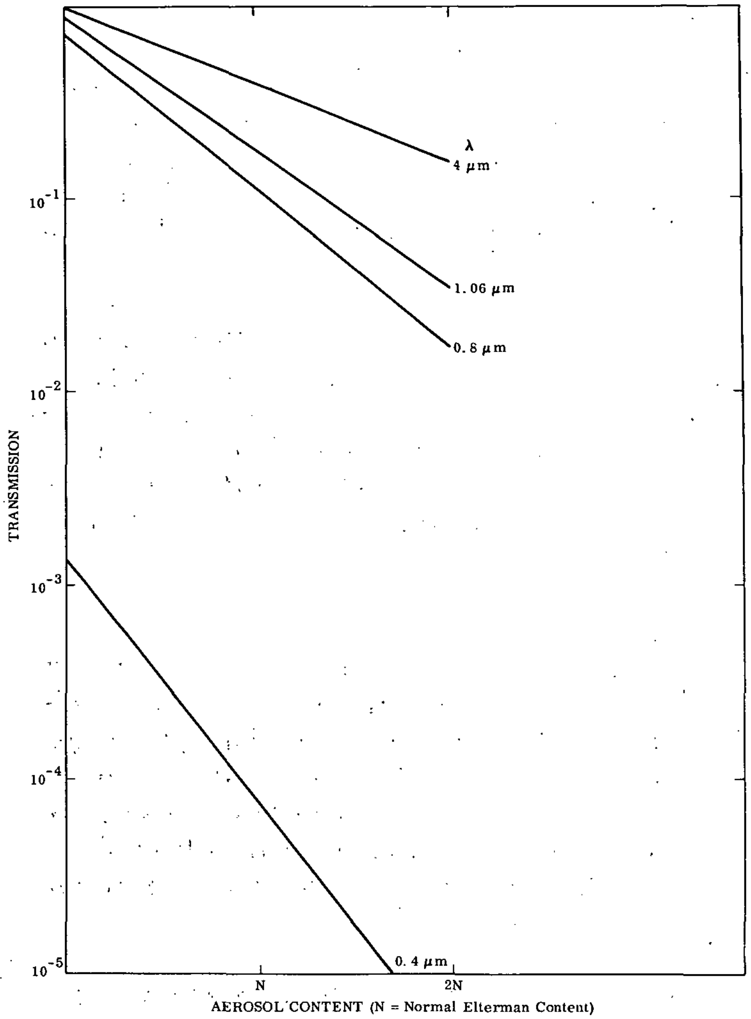

Figure 4-11.

Occultation Transmission vs. Aerosol Content as a Function of Wavelength (Grazing Altitude 10 km)

Figure 4-12. Occultation Transmission vs. Aerosol Content as a Function of Wavelength (Grazing Altitude 15 km)

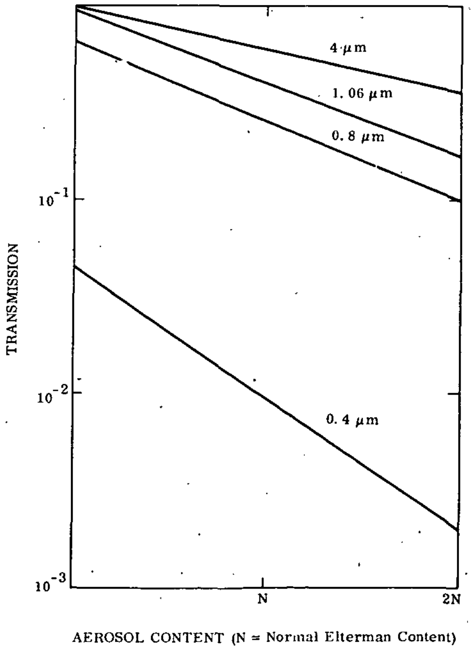

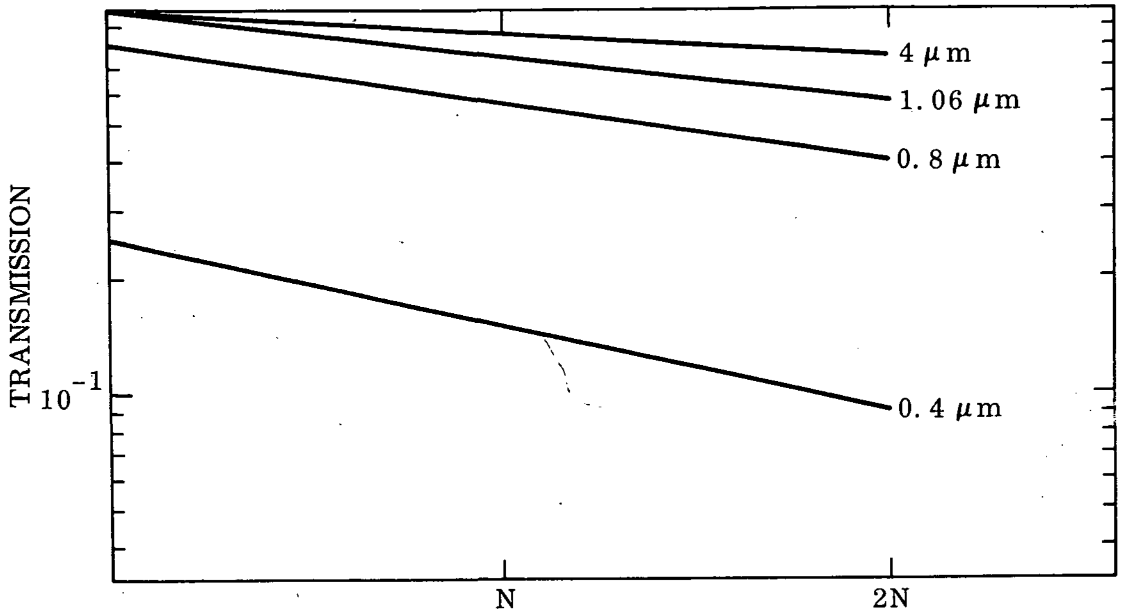

Figure 4-13. Occultation Transmission vs. Aerosol Content as a Function of Wavelength (Grazing Altitude 20 km)

absorption is negligible. Thus, no corrections to the observed data would be required at high altitudes in infrared window regions. However, the increased sensitivity, the well-established Rayleigh correction, the higher sun radiance and more sensitive detectors at shorter wavelengths would point to choosing the visible or ultraviolet region for aerosol observations by occultation.

It is seen from figs. 4-11, 4-12, and 4-13 that at shorter wavelengths the sensitivity decreases with increasing grazing altitude. At 10 km grazing altitude, a 10% change in transmission (i.e., a 10% signal change) is equivalent to a 2.5% change in aerosol optical thickness; at 15 km it is equivalent to 12%, and at 20 km it is equivalent to 25%.

An estimate (ref. 41,109) of the effect of the Supersonic Transport (SST) on the stratospheric aerosol content shows that, assuming operation of 500 SSTs in the period 1985-1990, the aerosol concentration at SST altitudes will increase by about 10% on the average, with peak increases of about 100%. These increases, which include both soot and aerosols formed photochemically from gaseous products, are strictly estimates, and may be changed considerably with different assumptions.

Assuming that these changes are distributed uniformly both horizontally and vertically through the SST altitude region (18-32 km) then it would appear from the above accuracy estimates that occultation observations could monitor changes in the stratospheric particulate content due to SST operation, within the uncertainties of the presence of stratospheric clouds. It should be noted that the SST altitude region contains only about 3% of the total aerosols in a normal atmosphere, so that the changes due to the SST do not affect the total aerosol content significantly. The total content has been predicted (ref. 47) to increase by about 10% by the year 2000 due to other activities of man, such as combustion and cultivation.

4.2.2.3 Limb observations. Work has recently been done on developing inversion techniques to determine the vertical distribution of aerosols from radiance observations of the earth's sunlit horizon. Gray et al. (ref. 110) discuss the theory of a method in which a satellite instrument measures the radiance of the horizon as a function of grazing altitude and wavelength. These measured data are inverted in a computer program using an iterative technique to obtain the aerosol profile.

The program compares the measured radiances with theoretical predictions based on a model aerosol atmosphere. The differences are used to update the theoretical predictions iteratively until the differences converge to a predetermined limit. Further work is required on this technique to determine the effects of measurement errors and the validity of various assumptions in the model atmosphere.

Similar work has been done by Marchuk et al. (ref. 111); in their method the atmospheric radiance is measured at a fixed wavelength as a function of nadir angle, so that the earth's surface is viewed as well as the horizon. The theory shows inversion of aerosol profiles down to the earth's surface, but of course, this type of observation is limited by the presence of clouds as discussed in Section 4.2.2.1.

4.3 Active Lidar Observation From Satellites

In recent years the lidar technique has rapidly developed for ground-based, and more recently for aircraft operation, and should be examined for satellite application (ref. 112).

In considering lidar systems we are concerned with the volume backscattering coefficient, β, and the volume extinction coefficient, σ, of the particles. The basic lidar equation is given by:

$$P(R) = P_t L \beta(R) A_0 R^{-2} \exp\left[-2 \int_0^R \sigma(R')dR' - 2u\right] \qquad (4-17)$$

where P is instantaneous received power, P_t is transmitted power at t_0, L is effective pulse length, ($L = c\Delta t/2$, where c is the velocity of light and Δt is pulse duration; it is the range interval from which signals are simultaneously received at time t), R is range $R = c(t-t_0)/2$, where t_0 is the time of transmission of pulse, A_0 is the effective receiver aperture, and u is the gaseous absorption and scattering optical thickness over the range R. Aerosol absorption is assumed to be negligible.

The magnitudes of β and σ depend upon the wavelength of the incident radiation and the number, size, shape, and refractive properties of the illuminated particles per unit volume.

There is considerable uncertainty (see e.g. Collis (ref. 113)) in the relationship between β and σ, due to uncertainties in the aerosol properties, and certain assumptions must be made in order to solve the lidar equation for the optical properties of the aerosols. A typical assumption is that the particles are spherical. However, Holland and Gagne (ref. 114), in scattering experiments on irregularly shaped particles, showed that while the volume scattering coefficient for a system of irregular particles is similar to that for spherical particles, serious errors arise in predicting backscattering for such particles on the basis of the spherical model. Thus the uncertainties would be less in a transmission measurement of aerosols (e.g., satellite-to-satellite) than in the conventional lidar method.

It is clear that lidar techniques at the present time can give only qualitative information on the variation of aerosol content within the atmosphere, and even this may be in error if the composition, the size distribution, or the shape of the aerosols varies through the atmosphere. It has been suggested (ref. 115) that some information on the size distribution may be derived from the lidar technique

The discussion of the aircraft lidar system by Uthe and Johnson (ref. 112) gives a detailed description of the instrumentation, and the problems involved in its use and in the data interpretation. The results demonstrate that quantitative information on aerosols is not yet available.

Lidar systems are complex with large power requirements, and as stated by Collis (ref. 113) much technological progress must be made before they can be used on satellites. It might be expected that such systems will first be developed for manned satellites.

5

INSTRUMENTATION

In this section, we examine the state-of-the-art in instrumentation for passive systems and discuss the potential of active systems.

5.1 Passive Systems

5.1.1 Introduction

The following criteria must be considered in the evaluation of spectroscopic instruments to detect air pollutants from a satellite:

a) Sensitivity of the instrument to the signal arising from changes in pollutant concentrations.

b) Specificity of the instrument, i.e., its ability to discriminate against other interfering species and backgrounds.

c) Required observation time for the instrument to sample and integrate the received signal, which must be consistent with the satellite speed and desired ground coverage.

d) Information content of the signal received by the instrument. High information content is desired in order to provide additional information such as ground reflectance, atmospheric temperature profile, atmospheric absorption and scattering, and cloud cover.

e) The complexity of the system, including weight, volume, power, and cooling requirements.

In our previous report (ref. 3), we discussed radiometers, spectrometers, interferometers and optical correlation techniques for the passive mode and an active laser system. We arrived at a qualitative evaluation of the instruments used in the passive mode; results are re-presented in Table 5-1. It was found that instruments which (1) incorporate the multiplex advantage, and have a large "throughput" (such as interferometer-spectrometers), and/or (2) use techniques

TABLE 5-1. QUALITATIVE COMPARISON AMONG SPECTROSCOPIC INSTRUMENTS FOR DETECTION OF POLLUTANTS FROM SATELLITES

Instrument	Sensitivity	Specificity	Complexity of Instrum.	Observ. Time	Info. Content	Remarks
Radiometer (filter wheel or many single filters)	Medium	Low	Low	Short	Medium	Limit $\Delta\omega \sim 3$ cm^{-1}; many channels required
Radiometer (polychromator)	Low Medium	High Low	Medium	Short Short	Medium	Assuming $\Delta\omega < 1$ cm^{-1} Assuming $\Delta\omega > 1$ cm^{-1}; multiple detectors required
Scanning spectrometer	Low Medium	High Low	Medium	Long Medium	High	Assuming $\Delta\omega <$cm^{-1} Assuming $\Delta\omega >$cm^{-1}
Optical correlation instrument	High	High	Medium	Short	Medium	Matched filter with multiple entrance slits & nondispersive
Interferometer-spectrometer	High	High	High	Medium	High	Sampling time at least 10 sec; image motion compensation required; large information content for wide spectral interval

of correlating the spectral fine-structure of pollutants with a preselected "instrument transfer function," and/or other specificity-enhancing techniques are best suited.

In this section, we re-examine our findings by using the results of the calculations of the signal change presented in the previous section. The typical signal-to-noise ratio for detector-noise-limited radiometric devices is given by

$$\mathrm{SNR} = A_o \Omega_o \eta \int_{\Delta\omega} \frac{\zeta'(\omega) E(\omega)}{\mathrm{NEP}(\omega)} d\omega \tag{5-1}$$

where A_o is the area of the entrance pupil (cm^2), Ω_o is the solid angle of the field of view at the entrance (sr), η is the overall efficiency, $\zeta'(\omega)$ is the instrument transfer function, $E(\omega)$ is the spectral radiance at the entrance pupil ($w/cm^2 cm^{-1} sr$), given by Eq. (3 - 1), and $\mathrm{NEP}(\omega)$ is the noise-equivalent power (W) given by

$$\mathrm{NEP}(\omega) = \frac{\left(A_d \Delta f\right)^{1/2}}{D^*(\omega)} \tag{5-2}$$

where Δf is the band pass (Hz), $D^*(\omega)$ is the specific detectivity ($W^{-1} cm\ Hz^{1/2}$), A_d is the area of the detector (cm^2), which is not an independent parameter but is related to the entrance optics by the throughput (étendue) of the instrument:

$$A_o \Omega_o = A_d \Omega_d \tag{5-3}$$

where Ω_d is the solid angle under which the detector is illuminated, and can be expressed approximately in terms of the f/no at the detector by $\Omega_d = \frac{\pi}{4} (f/no)^{-2}$.

By including the wavelength dependent part of the detectivity into the instrument response function $\zeta(\omega) = \zeta'(\omega)\ \delta(\omega)$, where $\delta(\omega) = D^*(\omega)/D^*_{max}$, Eq. (5-1) becomes

$$\mathrm{SNR} = \varphi \int_{\Delta\omega} E(\omega)\ \zeta(\omega)\ d\omega \tag{5-4}$$

where

$$\varphi = \frac{\pi}{4} \left(\frac{A_0 \Omega_0}{\Delta f}\right)^{1/2} \eta \frac{D^*_{max}}{f/no} \tag{5-5}$$

The noise-equivalent radiance (NER) can then be determined from Eq. (5-4) by setting SNR = 1. However, in pollutant detection we are not directly interested in NER, but in the signal change due to a pollutant concentration change. Thus, Eq. (5-4) is replaced by

$$\Delta \mathrm{SNR} = \varphi \int_{\Delta\omega} \zeta(\omega) \left[E(\omega, \tau_0) - E(\omega, \tau_p) \right] d\omega \tag{5-6}$$

where $E(\omega, \tau_0)$ and $E(\omega, \tau_p)$ are the spectral radiances due to an unpolluted and a polluted atmosphere, respectively. The minimum detectable pollutant concentration is then found by setting ΔSNR = 1 and solving for τ_p.

For the purpose of studying the relationship and influence of the different variables, one may, for the moment, replace the integrals with averaged values. However, one must keep in mind that this procedure cannot be used to obtain precise quantitative data. In the following analysis we chose an example from the thermal emission region, in which the non-homogeneous atmosphere is replaced by a one-slab uniform atmosphere according to

$$E\left(\omega, \tau_0\right) = \tau_0(\omega)\, N\left(\omega, T_G\right) + \left(1 - \tau_0(\omega)\right) N^0\left(\omega, T_A\right) \tag{5-7}$$

where $\tau_0(\omega)$ is the spectral transmissivity of the unpolluted atmosphere, $N(\omega, T_G)$ is the spectral radiance of the ground and $N_A^0(\omega, T)$ is the blackbody radiance of the atmosphere. Correspondingly, the radiance from a polluted atmosphere is expressed as

$$E\left(\omega, \tau_p\right) = \tau_0(\omega)\, \tau_p(\omega)\, N\left(\omega, T_G\right) + \left(1 - \tau_0(\omega)\, \tau_p(\omega)\right) N^0\left(\omega, T_A\right) \tag{5-8}$$

The radiance difference between the unpolluted and polluted atmosphere becomes

$$E\left(\omega, \tau_0\right) - E\left(\omega, \tau_p\right) = \tau_0(\omega) \left(1 - \tau_p(\omega)\right) \left[N\left(\omega, T_G\right) - N^0\left(\omega, T_A\right) \right] \tag{5-9}$$

Introducing Eq. (5-9) into Eq. (5-6) and using quantities averaged over the spectral band pass, we have

$$\Delta \mathrm{SNR} = \varphi\, \bar{\zeta}\, \bar{\tau}_0 \left(1 - \bar{\tau}_p\right) \overline{\Delta N} \left(T_G, T_A\right) \Delta\omega \tag{5-10}$$

Hence, the detectable threshold pollutant transmissivity becomes

$$\bar{\tau}_p = 1 - \frac{1}{\varphi\, \bar{\zeta}\, \bar{\tau}_0\, \overline{\Delta N}\left(T_G; T_A\right)\Delta\omega} \qquad (5\text{-}11)$$

It is seen that an increase in any of the parameters in the denominator increases the pollutant transmissivity and, hence, the threshold concentration value. (The relationship between transmissivity and concentration was given in Section 3.1.1.1.) However, an increase in $\Delta\omega$ results in a greater sensitivity only if more pollutant lines are encompassed in the increased spectral interval. (The product $(1 - \tau_p)\Delta\omega$ is invariant if no more lines are included in the enlarged $\Delta\omega$.) This is an important result. It involves not only the sensitivity, but also the specificity of a given instrument. Thus, while an increase may be desirable from a sensitivity standpoint, the specificity will in general be decreased.

An expression similar to Eq. (5-11) can be derived for the sun-reflected region:

$$\bar{\tau}_p^{\alpha} = 1 - \frac{\pi}{\varphi\, \bar{\zeta}\, \bar{\tau}_0^{\alpha}\, \bar{H}_s \cos(\theta)\Delta\omega} \qquad (5\text{-}12)$$

where α is a function of the sun zenith angle and H_s is the sun irradiance (see Section 3.1.1.1). The conclusions reached above for the thermal emission region also apply here.

In addition to the uncertainties introduced by the instrument accuracy and system noise, we must consider the uncertainties in the supporting data which are required in the data analysis, such as a knowledge of τ_0, $N(T_G)$, $N^0(T_A)$, α, H_s, and θ. These uncertainties will be discussed in the following sections.

5.1.2 Radiometer

Radiometers have some of the desirable instrument characteristics, such as high sensitivity, fast response and low complexity. Thus, they have been applied extensively for many remote sensing tasks from satellites. In this section, we will examine their usefulness in application to satellite observation of air pollutants.

If it were not for the requirement of high specificity, the radiometer would be in general a very useful instrument for the remote sensing of air pollutants. Instances where the high specificity is not required are the observation of reflected and/or polarized radiance in the visible spectrum to measure aerosols (see Section 5.1.5) and the observation of radiance in the stratospheric limb experiment, where the interference of other molecules, especially of water vapor, is drastically reduced. For the measurement of air pollutants in the troposphere, however, the interference of the "normal" atmospheric species makes the basic radiometer less useful. This may be demonstrated in an example by our line-by-line calculations of the upwelling thermal radiance in the 4.6μm region. The CO concentration in the troposphere was varied from 0 to 0.4 ppm, and the water vapor concentration was varied from one-half to twice the amount of the normal Gutnick concentration. The ground brightness temperature was assumed to be 300 K and the atmospheric temperature profile was that of the U.S. Standard Atmosphere (see figs. 3-4 and 3-5). The results of the calculations are shown in fig. 5-1 where we see that if the water vapor profile were known only to lie between the two limits of one-half to twice Gutnick, no meaningful interpretation of pollutant concentration data could be made. Even if the water vapor concentration were known to within ±20%, the uncertainty in CO concentration would still be nearly ±100%.

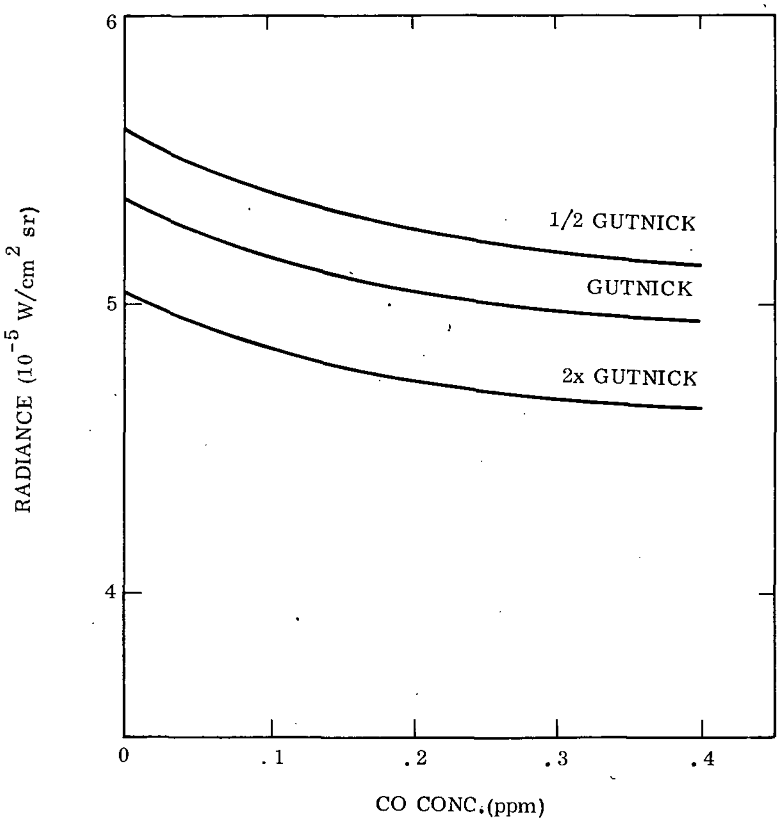

Figure 5-1. Radiance at the top of the Atmosphere as a Function of CO Concentration for Three Different Water Vapor Concentrations

In this particular spectral interval, the average transmission due to water vapor is about 80%. In spectral intervals in which the transmission due to water vapor is even less, the uncertainties in the determination of pollutant concentration would be increased. There are many spectral intervals of interest in which this would be the case. Other variable atmospheric constituents, such as ozone and perhaps methane, would add to this uncertainty.

These general results, derived here for the thermal emission, apply also to the sun-reflected region.

5.1.3 Correlation Spectroscopy

The application of dispersive correlation spectroscopy to remote sensing was first used by J. Strong in 1958, after a suggestion by Benedict (ref. 117). A number of slits are placed in the exit plane of a grating monochromator, the width and spacings of which correspond to a rotational line spectrum of a specific molecule. The energy coming through the slits is collected and focused onto a detector. In this way, the instrument has the "multiplex advantage" similar to the interferometer-spectrometer. However, it suffers from the limitation of a narrow entrance slit.

In a development by Barringer and Schock in 1965, the exit slits were replaced with a photographic plate containing the spectrum of the molecule of interest (ref. 118). However, application of this method is limited to the spectral region in which photographic emulsions exist. In later developments, Barringer et al. have replaced the photographic plate with mechanical slits (see Section 5.1.3.1).

The limitation of a single entrance slit can be minimized by using multiple entrance slits whose spacings correspond to the separation of the rotational lines at the exit plane. If the molecule has a regular line separation (as all diatomic and many simple polyatomic molecules have, especially near the band center), neighboring lines are superimposed in the exit plane and their signals enhanced (ref. 119).

In a further development of a spectrometer with multiple entrance and exit masks, the masks are inserted sequentially (ref. 120, 121). For each mask, a different combination of spectral elements falls on the detector. Intensities measured with different masks can be used to compute the intensities of m different spectral bands through the application of Hadamard matrices. However, this concept has not yet been applied to remote sensing. The complexity of the Hadamard-Transform Spectrometer appears to be high.

Another dispersive correlation method is the correlation interferometer (ref. 122), which is basically a Michelson interferometer. The correlation is carried out in Fourier space by matching the measured interferogram with a stored one, which corresponds to a given pollutant gas. Originally, this instrument was selected for the measurement of CO in the COPE experiment (ref. 123). It has been replaced by a different instrument which will be described in the section on interferometers (Section 5.1.4.2).

Another class of correlation instruments does not use dispersive elements; these instruments are appropriately named "non-dispersive infrared (NDIR)" analysers. Originally developed for in-situ measurements, their recent application to remote sensing is described in Section 5.1.3.2.

The common characteristic of the dispersive and non-dispersive optical correlation instruments is the multiplexing of the spectral intervals and the differencing of two signals, the magnitude of which is given by the incoming radiance multiplied by a correlation function $\sigma_1(\omega)$ and by a function $\sigma_2(\omega)$, used as reference. Thus, using Eq. (5-4) and (5-5), the ΔSNR becomes

$$\Delta \mathrm{SNR} = \varphi \int_{\Delta\omega} \zeta(\omega) \left[\sigma_1(\omega)\, E(\omega) - \sigma_2(\omega)\, E(\omega)\right] d\omega \qquad (5\text{-}13)$$

where $\Delta\omega$ represents the entire spectral interval, given by the instrument response function.

The spectral response of the instrument is contained in the correlation function $\sigma_1(\omega)$. The main purpose of $\sigma_1(\omega)$ is to correlate the instrument response with the spectral features of the pollutant gas of interest and not to correlate with interfering gases. The degree of correlation involves the randomness of the distribution of interfering rotational lines with respect to the pollutant rotational lines. This is shown in Appendix C.

5.1.3.1 Correlation spectrometer (COSPEC). The application of a correlation spectrometer to remote sensing of air pollutants from balloon platforms was first reported by Barringer et al. (ref. 118) in 1965. In the exit plane of the instrument a photographic plate was used to "correlate" the incoming radiation with the one recorded on the plate. The solar radiation reflected from the earth's surface and backscattered by the atmosphere at 3100Å for SO_2, and at 4400 Å for NO_2 was used in this mode of operation.

In a later development, the photographic plates were replaced by slits photo-etched in a thin foil (ref. 124,125,126). This instrument will be briefly discussed here, and is shown schematically in fig. 5-2. The incoming radiation is focused onto the entrance slit of an Ebert-Fastie spectrometer with a focal length of 25 cm. The incoming beam is collimated by the parabolic mirror, dispersed by the grating and focused onto the multi-slitted exit mask and photomultiplier tube. In the remote sensing mode the spatial modulation is achieved through two fork-driven refractor plates behind the entrance slit. Although these plates have unknown motion, there are effectively only two positions seen by the incoming light beam. A schematic of this is presented in fig. 5-3, where the two positions of the spectrum $G(\lambda)$ and $G(\lambda-\delta)$ (δ is the displacement by the refractor plates) are given in relationship to

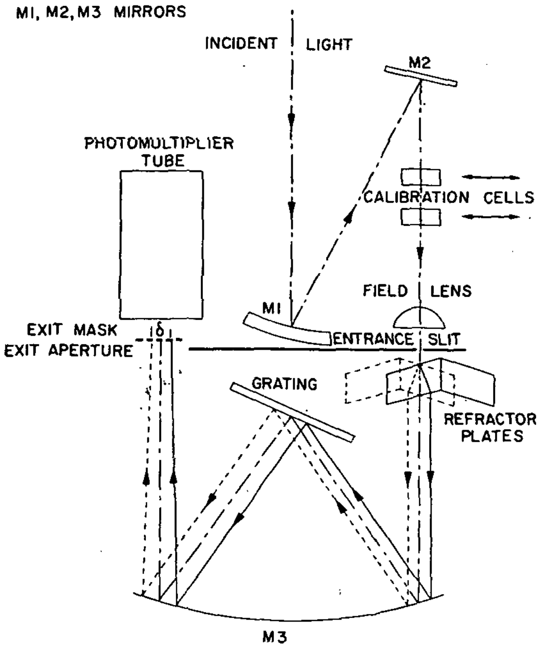

Figure 5-2. Schematic Layout of the Remote Sensor (from ref. 125)

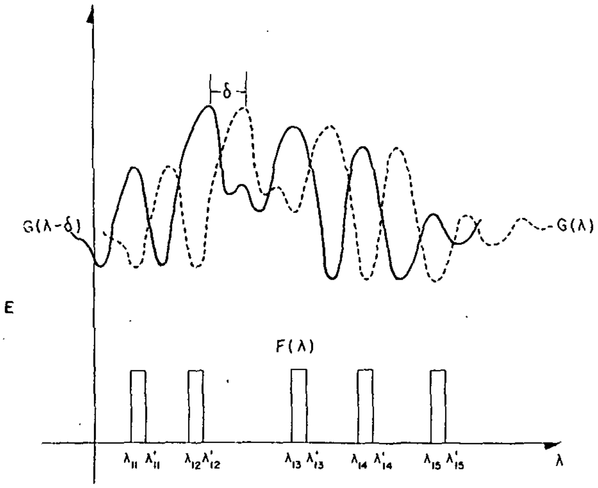

Figure 5-3. Overlap Between the Power Spectrum at Two Positions λ and λ - δ, and the Slits of the Mask (from ref. 125)

the stationary mask F(λ), which is the "correlation function" introduced in Eq. (5-13). Typical values for the slit width are 6Å and for the displacement 12Å. The energy alternately passing through the slits is recorded by the PM tube, and after synchronous rectification is recorded in analog or digital form. The relationship between the output and concentration and pathlength (ppm × m) is obtained through a calibration procedure using an absorption cell and light source. Almost linear response has been obtained for a range of 0 - 1000 ppm × m of SO_2 and NO_2.

In the balloon tests conducted over Chicago in 1969, the results were difficult to interpret (ref. 124) because of the strong unknown Rayleigh and Mie scattering components. In the meantime, it has been found that the radiation reflected from the ground has a different time variation than the radiation scattered by the atmosphere; by utilizing two different rectification frequencies, it is hoped to separate the two components.

A general treatment of problems associated with the quantitative interpretation of data from correlation - mask instruments has been given by McCreight and Tien (ref. 127).

5.1.3.2 Remote gas filter correlation instrument. "Gas Filter Correlation (GFC)" - a term introduced by us during the development of a remote sensor under NASA contract (ref. 128) - is an outgrowth of a spectroscopic method used in "Non-Dispersive Infrared (NDIR)" analysis. The first detailed description of the NDIR instrument was given by Luft (ref. 129), although elements of the techniques were already mentioned by Pfund (ref. 130) in 1939. Two different light sources, two cells and one membrane condenser as a detector were used. The detector was sensitized with the gas of interest. This method, using a sensitized detector and the gas sample in one light beam, was later classified as "positive filtering."

A different arrangement by Schmick (ref. 131) and Wright and Herscher (ref. 132) used one light source, but two cells and two detectors, which were the two opposed arms of an ac-excited bolometer. In this case, the selectivity is provided by balancing the two cells, and the detectors are non-selective. The gas sample is introduced into a cell common to both light beams. This was later classified as "negative filtering."

A further development of a negative-filter instrument was described by Fastie and Pfund, (ref. 133), using two detectors in the form of a differential thermopile.

The combination of negative and positive filtering into one instrument was described by Maley (ref. 134) in 1958. Two light sources, a chopper, a sample and comparison cell, a beam combiner and one detector, filled with the gas of interest, are the elements of this system. Results for different gas mixtures were shown and compared with the method of positive filtering. Significant improvements for discriminating CO against ethene, methane, ethane, water vapor, carbon dioxide and ethylene oxide were achieved: These results were obtained experimentally, and the author (ref. 134) warns that infrared spectrograms should only serve as a guide, but should not be used in the theoretical analysis. The reason for this cautionary remark is the fact that NDIR is based upon the fine-structure of the rotation-vibration bands and that the overlap in the band structure is no indicator whether a successful discrimination can be achieved. This was successfully demonstrated by Bartle et al. (ref. 135) who found that HCl in the ppb range can be detected in the presence of several hundred ppm of monomethyl hydrazine and unsymmetrical dimethyl hydrazine, which have intense bands at the spectral location of HCl. In addition, the development of line-by-line calculations has eliminated the need for the trial-and-error approach, and the design can be based on optimized instrument parameters, which are established by computer modeling.

A new approach to NDIR was taken by Smith et al. (ref. 136) who proposed in 1963 a "Selective Chopper Radiometer," for the atmospheric temperature sounding from satellites; this consists of a split cell, one half containing CO_2, the other half containing N_2, with the detector spectral response limited by a narrow-band interference filter. In the meantime, the SC has been built and flown on a NIMBUS satellite (ref. 137). Goody (ref. 138) developed a laboratory NDIR model, in which the one sensitizing cell was pressure modulated, thus eliminating the rotating chopper. The instrument successfully measured the N_2O amount in the atmosphere using the sun as the source. In 1968, we (ref. 3) began formulating the GFC concept for remote sensing of air pollution using aircraft and satellites. In subsequent developments, two versions of the instrument to measure CO using an aircraft were successfully flown (ref. 139, 140), and a third version for multipollutant detection from satellites is being developed (ref. 61).

The schematic of the improved aircraft version (ref. 140) of the GFC instrument is shown in fig. 5-4. The radiation enters through the front window, passes through the cell containing the pollutant of interest, is focused by the cell lens and field lens on one half of the detector. Simultaneously, radiation from the black body is reflected from the 45° chopper blade through the vacuum cell and is focused on the other half of the detector. As the chopper rotates the blades are interchanged, and the radiation from the outside passes through the vacuum cell onto the detector, while the radiation from the black body calibration source, reflected from the 45° chopper blade, passes through the gas cell onto the detector.

The correlation function $\sigma_1(\omega)$ and reference function $\sigma_2(\omega)$ in Eq. (5-13) are the transmissivities of the gas cell, $\tau_G(\omega)$, and of the vacuum cell, having a compensating aperture τ_A, which is not a function of ω. Thus, the signal difference ΔV in volts at the output of the detector for the two chopper positions can be expressed as

$$\Delta V = A_o \Omega_o \int_{\Delta\omega} E(\omega) \left[\zeta(\omega) R_o \tau_G(\omega) - \zeta'(\omega) R'_o \tau_A \right] d\omega + V_{INS} \qquad (5\text{-}14)$$

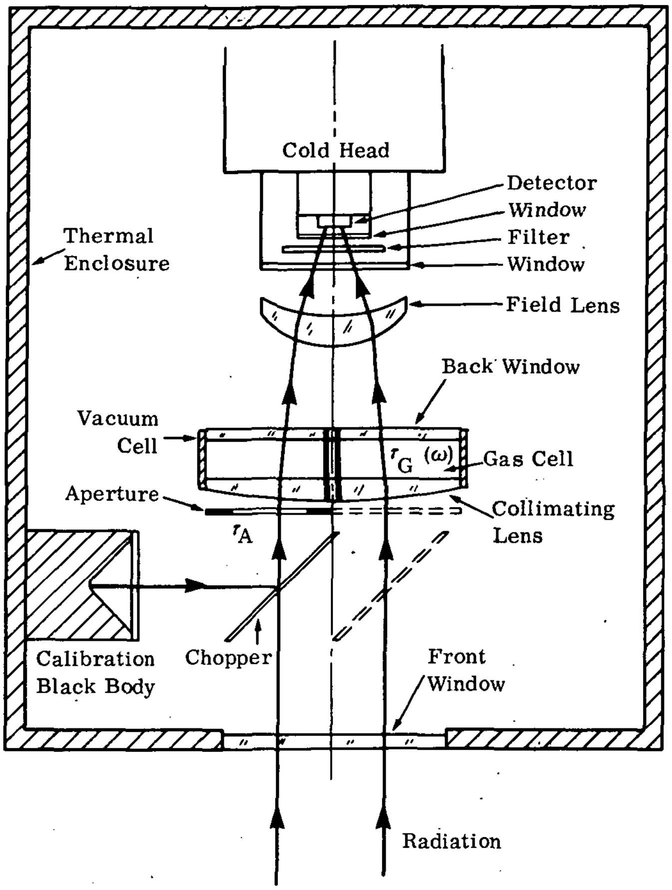

Figure 5-4. Schematic of the Gas Filter Correlation Instrument (from ref. 140)

where $A_o\Omega_o$ is the "throughput" of the instrument in cm^2 sr, $E(\omega)$ is the incident radiation in W/cm^2 sr cm^{-1}, $\zeta(\omega)$ is the response function of one half of all the optical components, R_o is the responsivity in V/Watt, τ_G is the transmission through the cell filled with the pollutant, τ_A is the transmission through a variable aperture which is in front of the vacuum cell, and $\zeta'(\omega)$ and R'_o are the corresponding response function responsivity of the other half of the instrument. The term V_{INS} is an instrument term (ref. 139) which remains constant for constant instrument temperature.

The aperture is adjusted to achieve a balanced condition, $\Delta V = V_{INS}$, with no gas in the outside beam. Experimentally, the balanced condition is established through an external calibration source at temperature T_C of radiance $N(T_C, \omega)$:

$$\tau_A = \frac{R_o \int_{\Delta\omega} N^o\left(T_C, \omega\right) \zeta(\omega)\, \tau_G(\omega)\, d\omega}{R'_o \int_{\Delta} N^o\left(T_C, \omega\right) \zeta'(\omega)\, d\omega} \qquad (5\text{-}15)$$

The radiance term $E(\omega)$ in Eq. (5-14) is given by Eq. (3-1). It contains the term for the transmission of the atmosphere, which is a product of the transmission of all contributing species at one given wavelength; when Eq. (5-14) is integrated over the wavelength interval, one finds that the pollutant in the atmosphere is strongly correlated with the transmission function of the pollutant gas in the instrument cell (i.e., $\tau_G(\omega)$) and that the other species present in the normal atmosphere are only weakly or not at all correlated. However, they do contribute to the overall transmission loss. This may be demonstrated in a calculation of ΔV for the fundamental band of CO in the 4.5 to 4.7 μm region. The earth's surface is assumed to have a brightness temperature of 300 K. The atmosphere is a U.S. Standard Atmosphere (1966) with a temperature lapse rate of -6.5° C/km. Besides CO, the atmosphere contains 0.25 ppm of N_2O and the Gutnick water distribution (CO_2 was not included in these calculations). In this small spectral interval, several hundred lines of each of the three species considered are included. The results of the line-by-line computations for ΔV versus CO concentration uniformly distributed through the troposphere are shown in fig. 5-5. The uppermost curve shows the results for a pure CO atmosphere, i.e., with no interfering species present. The other curves show the effects of adding the interfering gases H_2O, and N_2O. The influence is mostly from the transmission loss of these gases. The effect of the correlation of these interfering gases with the CO gas in the instrument cell is observable at zero CO concentration. The signal difference becomes slightly negative, which means that the lines of the interfering gases correlate weakly with the CO spectrum.

The results in fig. 5-5 also indicate that ΔV^* is a stronger function of the CO concentration in the atmosphere, than of the other species$^+$. Of these, only H_2O is variable and somewhat unpredictable. The influence of a variable H_2O concentration is shown in fig. 5-6 where three different H_2O distributions were used with 1/2, 1 and 2 times the standard Gutnick concentration. (See Footnote on p. 36.) Thus, with no knowledge of the H_2O concentration, but assuming that it is within this range, the CO concentration can be determined within ±21 percent. In practice, it is probable that the water distribution will be known to within ±20%, which reduces the uncertainty in CO concentration to less than ±10%.

The effect of a variation in the temperature profile is shown in fig. 5-7, where 2° C has been added and subtracted uniformly from the standard atmospheric temperature profile. The results indicate that the uncertainty limits in CO concentration become larger for a lower ground temperature because the temperature difference between the ground and the effective mean air temperature is smaller.

$^+$ ΔV^* is the signal difference per $A_o \Omega_o \bar{R}_o$.

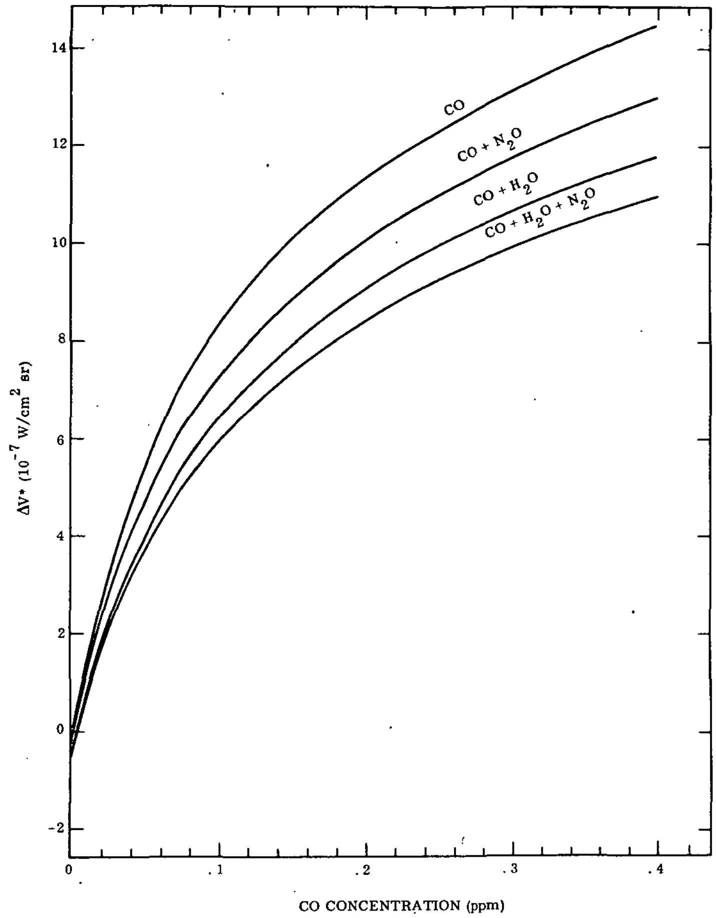

Figure 5-5. Signal Difference Measured by GFC as a Function of CO Concentration in the Presence of Different Interfering Gases

The test flight conducted on September 9, 1971 over Southern California is discussed in ref. 139. The results in terms of ground temperature and mean CO concentration (ppm in air volume below aircraft at 3000m) are shown in fig. 5-8.

5.1.4 Interferometer-spectrometer

In our previous report, we presented a general discussion of interferometer-spectrometers and listed several special and advanced developments. In the meantime, progress has been made and interferometers are employed on the ground in an increasing number. Since we are mainly interested in satellite application, we will restrict the following discussion to three instruments, one of which is flying on NIMBUS Satellites (IRIS), used for making temperature inversion, ozone and water vapor measurements, and the other two are being developed for the remote measurement of pollutants.

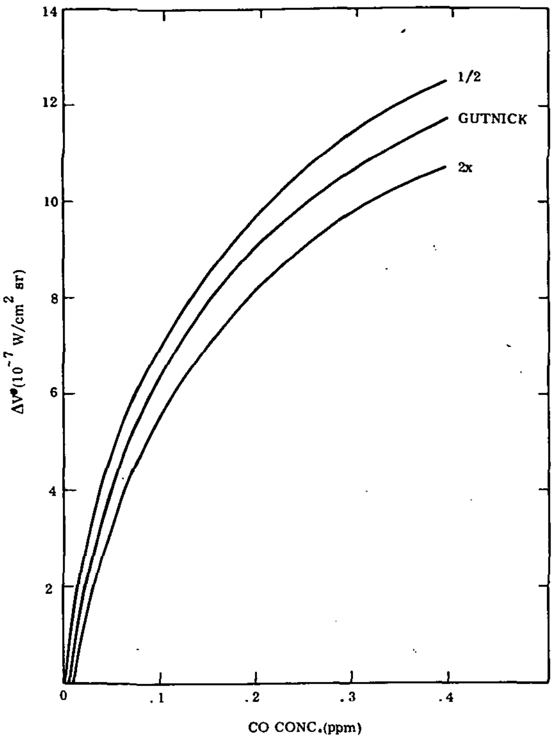

Figure 5-6. Signal Difference Measured by GFC as a Function of CO Concentration for Three Water Vapor Distributions

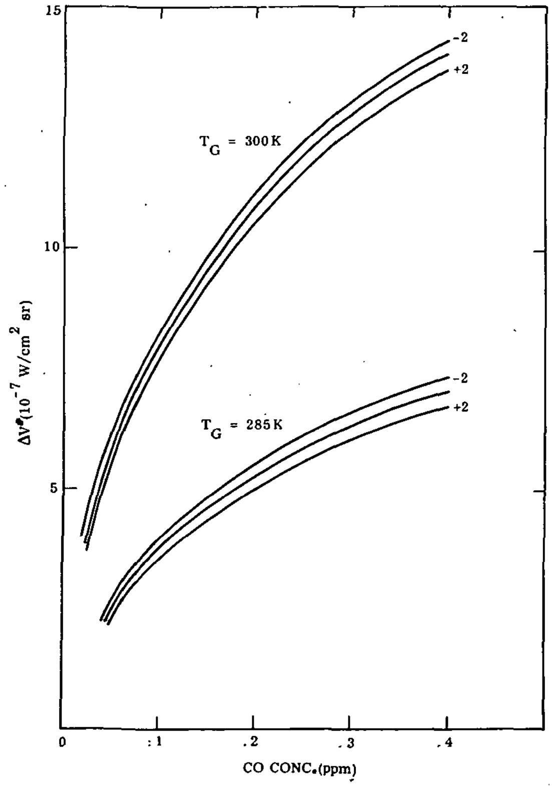

Figure 5-7. Signal Difference Measured by GFC as a Function of CO Concentration for Two Different Ground Temperatures and ± 2K Variations in the Atmospheric Temperature Profile

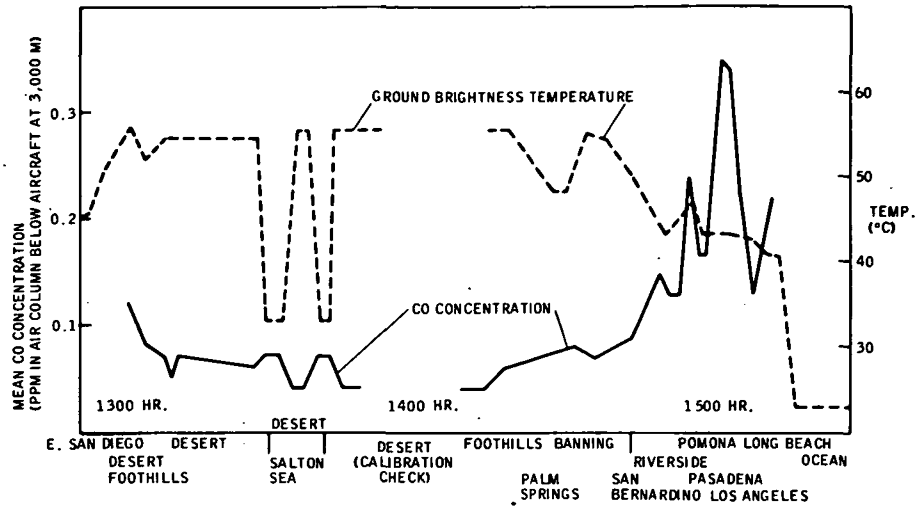

Figure 5-8. Schematic of Flight Test Result (9 September 1971) (from ref. 139)

Interferometer-spectrometers have all the potential advantages one wishes a remote sensor for air pollution detection to possess: high sensitivity, the potential for high specificity, and large information content. The latter is useful for obtaining auxiliary information about ground and atmospheric parameters, such as temperature and humidity profiles, ground temperature, surface emissivity, reflectivity, etc.

In general, specificity and observation time are directly related. High specificity demands high spectral resolution, which can be achieved only with a large mirror displacement and a resulting long scan time. This long scan time (e.g., 77 sec for the JPL instrument (ref. 153)) requirement is one of the most severe limitations in the application of interferometer-spectrometers to satellite measurements of air pollution.

5.1.4.1 Infrared-Interferometer-Spectrometer (IRIS). In our previous report, we gave a brief description of the IRIS instrument, which was later designated as IRIS A. This instrument was developed by U. of Michigan and NASA-GSFC for balloon application (ref. 141, 142). Since then, new versions have been developed for space application. The IRIS B and D flown on NIMBUS 3 and 4, respectively, have been described by Hanel et al. in refs. 143 and 144 respectively. A schematic of the instrument is shown in fig. 5-9. The radiation enters the instrument from top left through reflection by the image motion compensation and calibration mirror, which can be oriented to accept radiation from the earth, deep space, or from an on-board blackbody. The radiation is then split into two approximately equal components by the KBr beam splitter and then reflected from the stationary and moving mirrors. The beams are recombined at the beam splitter and one-half of the total energy is

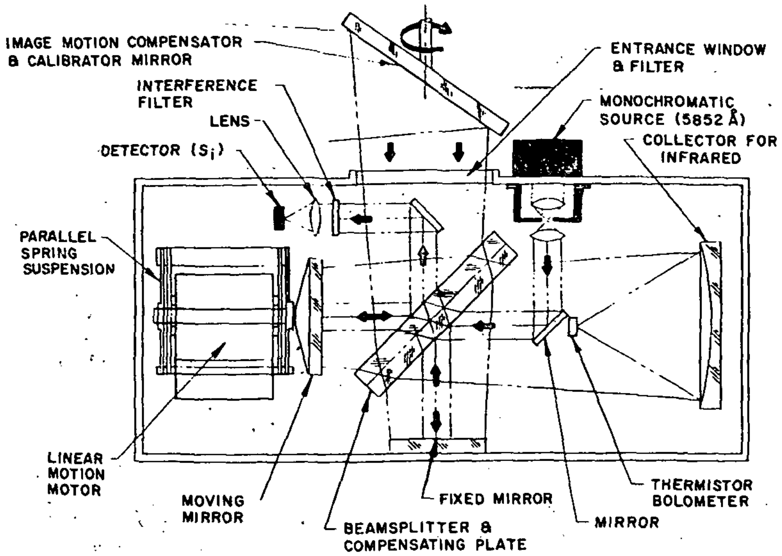

Figure 5-9. Simplified Diagram of IRIS. The image motion compensation and calibration mirror can be oriented so that IRIS sees earth, deep space, or an on-board blackbody. (From ref. 143.)

focused onto the detector, where the intensity is recorded as a function of path difference; the other half is reflected back to the source. The monochromatic light source (5852 Å) and a detector, together with the fixed and moving mirror and the beam splitter make up the reference interferometer, which provides velocity control for the moving mirror and pulses for sampling the interferograms. To conserve dynamic range, the operating temperature of the cube was held close to the midrange point of expected brightness temperatures (about 250K). The desired accuracy of 1% of the measured radiance (SNR = 100) was achieved by the on-board calibration procedure. To quote Hanel et al. (ref. 143): "A 1% accuracy in the measurement of radiances is difficult to achieve in the laboratory. To approach this accuracy in a remotely operated instrument in space was probably the most ambitious part of this program."

One of the main developments in the IRIS was the mirror drive. The problems of linearity in the mirror drive and the oscillatory motion due to vibration were of prime concern. Linearity was achieved by a feedback control, using a velocity transducer and the fringe-control interferometer. The oscillation of the mirror around its desired position was overcome through a phase-lock operation of the motor drive and low pass filtering. A block diagram of the single side band-phase locked loop that "slaves" the mirror motion to the highly stable NIMBUS clock frequency is shown in fig. 5-10. An overall block diagram linking the main and fringe-control interferometer, the image motion compensator, the programmer, IR data channel, and auxiliary controls is shown in fig. 5-11.

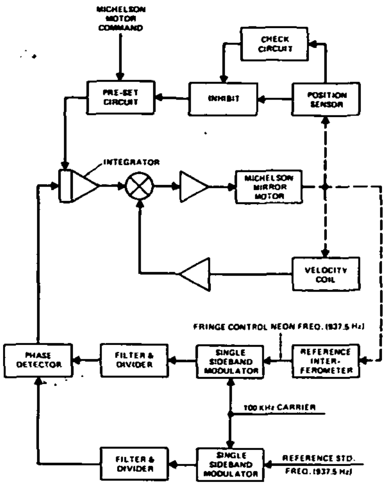

Figure 5-10. Block Diagram of the Single Side-Band Phase Locked Loop that Slaves the Michelson Mirror Motion to the Spacecraft Clock Frequency. Negative feedback using a velocity coil suppresses motor resonances and provides a suitable and stable transfer function of the motor. (From ref. 144.)

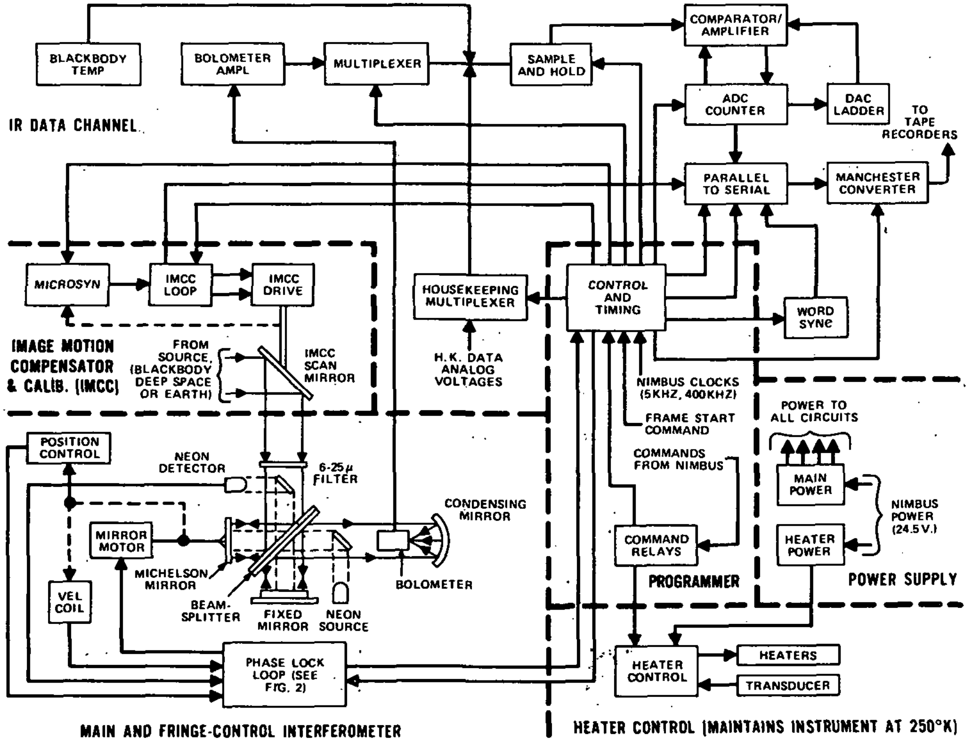

Figure 5-11. Block Diagram of the IRIS-D System. Circuitry to the spacecraft telemetry subsystem to record housekeeping data is omitted. (From ref. 144.)

The spectral responsivity of the IRIS as measured on the ground two months before launch and during orbits 33 and 2167 (separated by 5-1/2 months) is shown in fig. 5-12, indicating a high degree of optical and mechanical stability. The low wave number cut-off at 25 μm is given by the KBr beam splitter material. The shape of the response curves is given by the beam splitter coatings, entrance window transmission and thermistor spectral response.

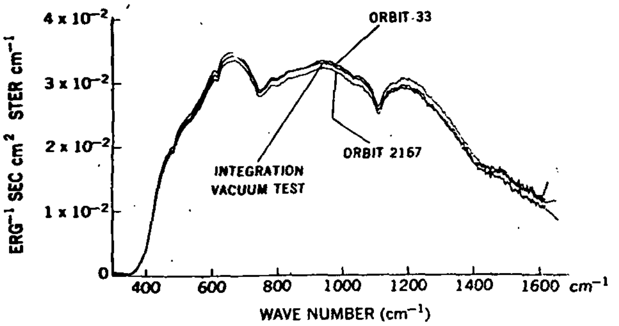

Figure 5-12. Spectral Responsivity of IRIS-D During the Thermal Vacuum Test of the Spacecraft about 2 Months Before Launch, Shortly after the Instrument was Turned On (Orbit 33), and After Approximately 5-1/2 Months (Orbit 2167) of Continuous Operation in Earth's Orbit. (From ref. 144.)

The spectral resolution is stated by Hanel et al. to be a nominal 1.4 cm^{-1} because $\Delta\omega = 1/2\delta$ where δ is the mirror displacement (0.36 cm for IRIS D). This resolution corresponds to the unapodized mode of data reduction and is not expected to be fully realized due to the natural apodizing effect of the off-axis rays. Estimates from atmospheric spectra indicate an unapodized resolution close to 2 cm^{-1} at 1000 cm^{-1} and 2.5 cm^{-1} at the higher wave number end of the spectrum. "In the apodized mode of data reduction the nominal spectral resolution of IRIS D is 2.8 cm^{-1} and in reality probably closer to 3 cm^{-1}" (ref. 143). The effect of the apodization function used is discussed by Blackman and Tukey (ref. 145).

The instrument performance has been expressed by Hanel et al. in terms of the noise-equivalent-radiance (NER), i.e., the radiance at which SNR = 1:

$$\text{NER} = \left[\eta_1 \eta_2 D^* \Delta\omega\right]^{-1} \left[A_o \Omega_o \Omega_d t\right]^{-1/2}$$

where η_1 and η_2 are the systems and optical efficiencies, respectively, and t is the observation time. Using the numerical values given in Table 5-2, the calculated NER for IRIS B is 1.6×10^{-8} W/cm^2 sr cm^{-1}. Quoting from Hanel et al.: "The

TABLE 5-2. INSTRUMENT PARAMETERS OF THE IRIS B AND IRIS D

	IRIS B	IRIS D
Systems Efficiency, η_1	0.35	0.35
Optical Efficiency, η_2	0.25	0.25
Spectral Resolution, $\Delta\omega(cm^{-1})$	5	2.8
Thermistor Bolometer, $D^*\left(cm(Hz)^{1/2}W^{-1}\right)$	10^8	1.02×10^8
Area of Non-Moving Mirror, $A(cm^2)$	13	15
Solid Angle of Instrument, Ω (sr)	0.016	.01
Solid Angle of Detector, Ω_d (sr)	1	1
Observation Time per Interferogram, (sec)	10.9	13.1
Spectral Range, cm^{-1}	400-2000	400-1600
f.o.v. (Half cone angle, degrees)	4	2.5
No. of 12-Bit Words per Interferogram	3408	4096

observed NER is about three to five times higher. Most of the difference is accounted for by the noise introduced by the bolometer power supply and by imperfect alignment. The preamplifier and the quantization process also contribute small amounts of noise. The performance of the instrument [IRIS B] came fairly close to the theoretically possible limit; however, there is still room for improvement."

The equivalent NER for IRIS D is calculated to be 3.2×10^{-8} W/cm^2 sr cm^{-1}. The actual NER was measured during the ground tests and was a factor 1.8 higher than the calculated value (see fig. 5-13). This nearly detector-noise-limited operation became possible through improvements in the detector bias regulator and preamplifier circuit design. Thus, the effective NER of IRIS D is about the same as that of IRIS B, while the spectral resolution was improved by a factor of 2.

Typical spectra taken at three different locations are shown in fig. 5-14. The apodized spectra have a spectral resolution between 2.8 and 3 cm^{-1}. In the upper two spectra, the ground temperature is warmer than the mean temperature of the atmosphere, while in the lowest spectrum, the atmosphere is warmer, showing the H_2O, CO_2 and O_3 bands in emission. The structure between 1000 and 1200 cm^{-1} for the spectrum over the Sahara is attributed to SiO_2 reststrahlen effects (ref. 146).

While the achievements in the development and fabrication of the IRIS instrument are outstanding, and the scientific objectives of deriving profiles of atmospheric

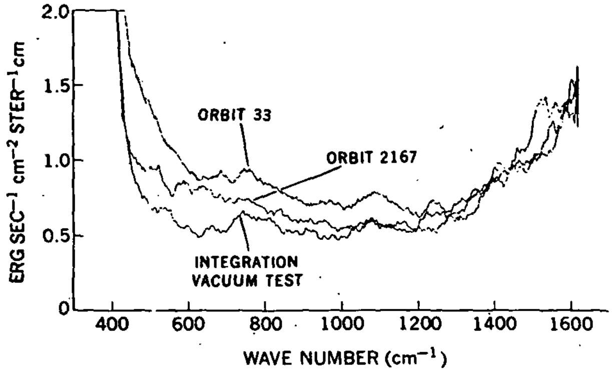

Figure 5-13. Noise Equivalent Radiance (NER) of IRIS-D Calculated from the Standard Deviation of Individual Responsivity Measurements. The NER curves have been smoothed for display purposes by averaging over 25 cm^{-1}. The NER values obtained while in orbit contain also systematic variations due to orbital temperature changes that will be removed in the final data reduction process. (From ref. 144.)

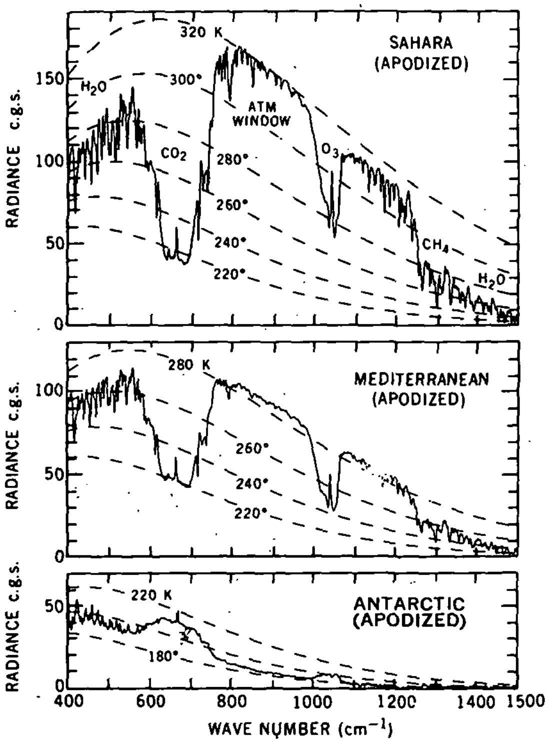

Figure 5-14. Thermal Emission Spectra Recorded by IRIS-D on NIMBUS 4. The apodized spectra have a spectral resolution between 2.8 cm^{-1} and 3 cm^{-1}. A hot desert case, an intermediate case over water, and an extremely cold spectrum recorded over the Antarctic are shown. Radiances of blackbodies at several temperatures are superimposed. (From ref. 144.)

temperatures, humidity and ozone concentrations, and other meteorological studies have been met, the overall performance of this instrument is not sufficient to measure air pollutants. To meet the requirements for gaseous air pollutant measurements, the spectral region would have to be shifted to 800-8000 cm^{-1} and the spectral resolution improved more than tenfold, while maintaining the same observation time.

5.1.4.2 Interferometer used in COPE. COPE is the acronym for "Carbon Monoxide Pollution Experiment," conducted by General Electric under NASA-LRC sponsorship. This program "involves the development of both the experiment concept and the remote sensor required to measure atmospheric carbon monoxide with sufficient accuracy to locate the CO sink, whether it be at the earth's surface or in the upper atmosphere." The program calls for the development of a remote sensor to "look for surface sinks by mapping the vertical CO burden in the atmosphere on a global basis, and which can look for an upper atmosphere sink by means of measurements of total CO in a horizontal path through the limb of the earth's atmosphere using the sun as a source." [Excerpts from ref. 147.] The remote sensor being developed by Barringer Research Laboratory for this task is a modification of the Michelson interferometer.

A schematic of the instrument, taken from ref. 147, is shown in fig. 5-15. The incoming energy (from left) passes through a spectral filter and is split into two equal amounts by the beam splitter. The two beams are reflected by the plane mirrors and are recombined after passing through the beam splitter. One half of the energy passes through the collecting lens on to the detector; the other half is reflected back to the entrance aperture and is lost for detection purposes. The refractor plate is introduced into that arm in which the beam is merely reflected from the beam splitter after returning from the plane mirror to compensate for the loss of the other beam passing through the beam splitter. In the usual Michelson interferometer, one of the mirrors is moved linearly to cause a phase difference which gives rise to the interferograms. In this instrument, the mirrors are kept stationary at an initial path difference while the refractor plate is oscillated to cause the change in path difference in the two beams. The advantage is a reduction in complexity for the movement of the mirrors. However, the path difference scanned is limited to a distance of 1 or 2 mm (ref. 146) which is equivalent to a spectral resolution of 5 or 2.5 cm^{-1}. The systems parameters of the breadboard instrument are shown in Table 5-3 (from ref. 147).

To analyze the output of the COPE instrument certain linear approximations are made to the spectrum and the resulting interferogram, so that a set of linear equations is obtained, relating the interferogram amplitudes measured at various path differences to the absorber optical depth (assuming a known surface reflectivity and no scattering effects in the reflected sunlight measurement).

From the available publications (ref. 122-124, 147), it is not easy to follow the mathematical development for the data interpretation. Apparently, since the

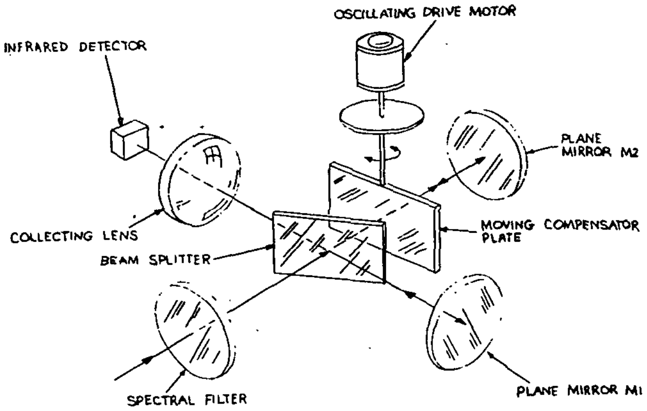

Figure 5-15. Interferometer Used in COPE (from ref. 147)

TABLE 5-3. COPE BREADBOARD - SYSTEM PARAMETERS

APERTURE	
INTERFEROMETER	6.6 CM DIA.
TELESCOPE	22.0 CM DIA.
FIELD-OF-VIEW	
INTERFEROMETER	0.12 RADIAN DIA.
TELESCOPE	0.34 RADIAN DIA.
SPECTRAL BAND	4240 - 4360 CM^{-1}
DELAY SCAN RANGE	2.5 - 4.0 MM
NO. OF SAMPLE POINTS	0 - 64
SAMPLE LENGTH	1 - 63 FRINGES
SCAN RATE	1 HZ
NO. OF SCANS ACCUMULATED	0 - 100^{+} SCANS
NOISE EQUIVALENT POWER	1.6 E^{-11} $WATT/HZ^{1/2}$
NOISE EQUIVALENT CO AMOUNT (2% ALBEDO, τ = 1 SEC)	.004 ATM-CM
DETECTOR	LN_2 COOLED PbS IMMERSED ON Sr Ti O_3
WEIGHT	
INTERFEROMETER	10 LB.
TELESCOPE	20 LB.
ELECTRONICS	50 LB.
POWER	100 WATT

interferograms are sensitive to variations of many parameters, weighting functions are introduced to enhance the sensitivity to the variation of CO and to minimize the sensitivity to other parameters. It is necessary to determine the weighting functions over the entire range of interfering effects (ref. 147). These determinations have to be done under controlled laboratory conditions, which are difficult to make since they involve the simulation of the highly variable and non-homogeneous water vapor distribution, together with a great number of atmospheric and ground parameters.

5.1.4.3 High speed Fourier Interferometer (HSI). A small high-speed Fourier interferometer-spectrometer (HSI) for sensing environmental pollutants from spacecraft in the spectral range from 1.2 to 5.5 μm has been developed at the Jet Propulsion Laboratory under NASA sponsorship (ref. 148-154). The basic optics are shown in fig. 5-16. The source radiation enters from the left and is focused by an off-axis paraboloid onto a tuning-fork chopper. The chopper blade is made of calcium fluoride. Half of its area is reflective so that radiation is alternately chopped between source and reference radiation. A second off-axis paraboloid collimates the beam, which enters the beam splitter cube. The cube is composed of two calcium fluoride prisms which are cemented together with a non-absorbing grease. The two beams are reflected back not by the usual plane mirrors, but by cat's eye retro-reflectors. These act similar to cube corner reflectors; the light ray returns parallel to the incident ray, but is displaced. The beams in both arms are reflected from the mirrored surfaces of the beam splitter cube back into the cat's eye retro-reflectors, from which they are reflected again. Since they are now farther displaced, they miss the mirrored surfaces of the beam splitter cube. In the cube the two beams are recombined and are focused onto the detector. The use of the cat's eye retro-reflector make this instrument insensitive to angular displacement and the double passing make it insensitive to lateral displacements of the retro-reflectors. The path difference between the two beams is effected by moving one of the retro-reflectors. The movement is in steps under servo control using an He-Ne laser. Each step is equal in length and is an integral multiple of the reference wavelength. The tuning fork chops at 830 Hz and is synchronized with the stepping of the retro-reflector. To compensate for source intensity fluctuations, which is essential for a successful data reduction, the total power is measured with a second detector. It was recently found (ref. 154) that this task can be accomplished by low-pass filtering of the IR data during the data-reduction process, thus replacing the need for the second total power detector. In addition, the scan time may be reduced by changing the step length multiple with which the retro-reflector is moved. It was found that the original scan time of 165 seconds can be reduced to 77 seconds using a step-size larger by a factor of 6, while maintaining the chopping frequency and optimum spectral resolution, which is quoted to be 0.2 cm^{-1}.

Two typical atmospheric spectra taken with the instrument from the ground (ref. 160), presumably pointed at the sun, are shown in figs. 5-17 and 5-18. The spectrum between 4840 and 4860 cm^{-1} contains lines of the 20^01 band of CO_2. The

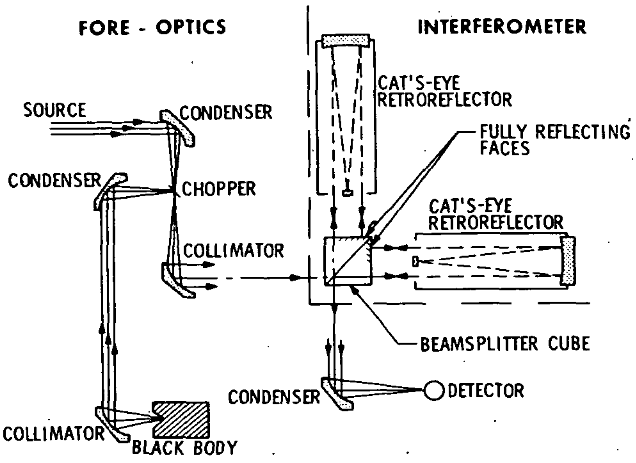

Figure 5-16. Optics Diagram (From ref. 154)

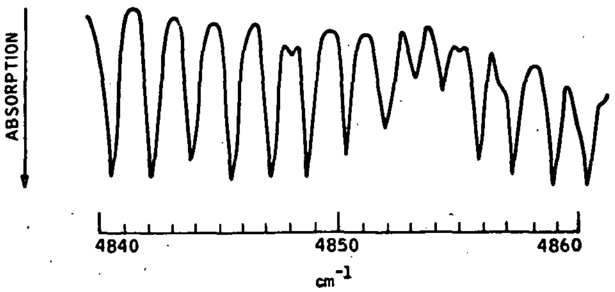

Figure 5-17. Portion of HSI Spectrum Showing the $(20^01)_{III}$ Band of CO_2 (From ref. 60)

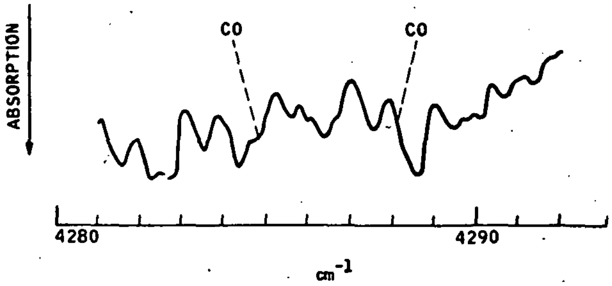

Figure 5-18. Portion of HSI Spectrum (From ref. 60)

authors determined the equivalent width of lines with J > 30, by estimating I_0. The resulting concentration of 330 ±20 ppm for CO_2 averaged over a path of 8 km is uncertain within the uncertainty limits of I_0. This procedure was also applied to the determination of CO from its overtone band at 2.3 μm (see fig. 5-18, which is reproduced from ref. 60 together with the identification of lines R6 and R7). The authors obtained a value of 8 ± 1 ppm of CO averaged over a path of 1 km, presumably the height of the inversion layer. The authors did not reveal how they obtained the level of I_0 nor do they mention making the correction necessary for the contribution from solar CO lines.

Toth and Farmer (ref. 60) have also made preliminary calculations of the minimum detectable concentrations of 10 major pollutants. They define "the minimum detectable feature as one which produces a change in the continuum level equal to the RMS noise magnitude. At a resolution of 0.5 cm^{-1} and a SNR = 100, the minimum detectable equivalent width is 0.005 cm^{-1}." The authors then proceed to apply this definition to the band strength of pollutant molecules and derive the minimum concentrations, contained either in the first km, or the entire troposphere (8.4 km). The values obtained this way range from less than 10 ppb for CO, HCℓ, C_2H_2 and HCHO to less than 500 ppb for O_3, NO_2 and SO_2.

The major difficulty in the preceeding analysis is the requirement of SNR = 100. At 3.5 μm, for example, the upwelling radiance (sun reflected and thermal) is about 6×10^{-8} W/cm^2 sr cm^{-1}, so that NER = 6×10^{-10} W/cm^2 sr cm^{-1}, which is roughly two orders of magnitude lower than the IRIS D performance (see Section 5.1.4.1), while demanding an improvement in spectral resolution by a factor of 10.

5.1.5 Polarimeter

Sekera (ref. 86) originally suggested that information about the aerosol characteristics might be obtained by satellite observations of the Stokes polarization parameters of the radiation backscattered from the earth and atmosphere. A polarimeter was designed and built for aircraft use to test the feasibility of the technique (ref. 95), and is now being further developed for satellite application under NASA sponsorship in the AAFE program.

A schematic of the polarimeter is shown in fig. 5-19. The instrument consists basically of three channels, one (a) having no polarizing device but with a 50% transmission neutral density filter, and the other two channels (b and d) having polarizing prisms which transmit light polarized at 90° and 135° to the vertical, respectively. The intensities I(A), I(B) and I(D) of the light transmitted by the three channels are directly related to the Stokes parameters, as outlined below.

When polarized light is passed through an analyzer with its transmission plane at angle ϕ to the vertical, and then through a retardation plate which introduces a

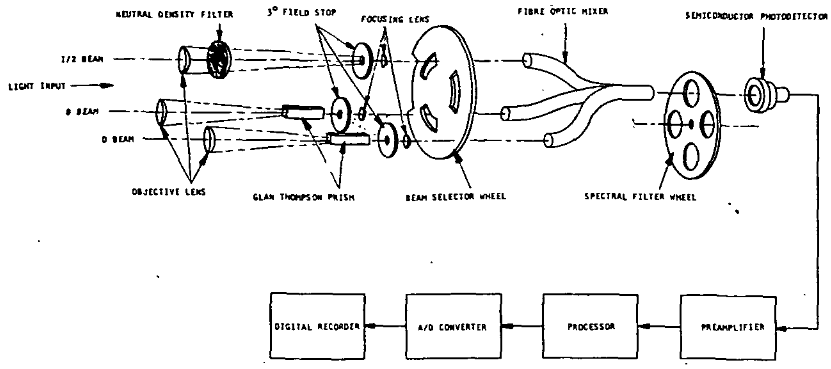

Figure 5-19. Schematic of Polarimeter
(After ref. 95)

phase difference θ between the vertical and horizontal oscillations of the electric vector, the intensity of the emerging light is given by:

$$I(\phi) = 1/2 \left[I + Q \cos 2\phi + (U \cos\theta - V \sin\theta) \sin 2\phi \right] \tag{5-16}$$

where I, Q, U, and V are the Stokes parameters.

The degree of polarization is

$$P = \frac{\left(Q^2 + U^2\right)^{1/2}}{I} \tag{5-17}$$

and the inclination (γ) of the plane of polarization to the vertical is given by

$$\tan 2\gamma = \frac{U}{Q} \tag{5-18}$$

The ellipticity (defined by $V/I = \sin 2\beta$, where β is the ratio of the minor and major axes of the ellipse described by the electric vector) is small in the case of atmospheric scattering so that the retardation plate is omitted and $\theta = 0$. Hence

$$I(\phi) = \frac{1}{2} \left[I + Q \cos 2\phi + U \sin 2\phi \right] \tag{5-19}$$

From this equation it follows that the outputs of the instrument channels are differenced to obtain the Stokes parameters Q and U:

$$\begin{aligned} Q &= 2\,[I(A) - I(B)] \\ U &= 2\,[I(A) - I(D)] \\ I &= 2I(A) \end{aligned}$$

These differences are small and are performed electronically in the instrument. The channel selection is made by a rotating beam selector wheel, which sequentially passes the light from the different channels A, B, A, D, A, as illustrated in fig. 5-20.

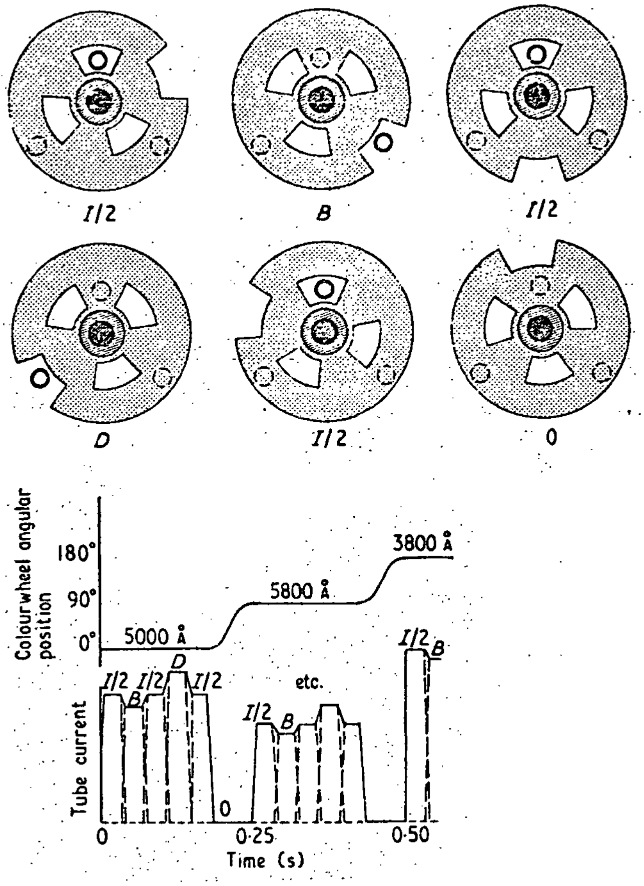

Figure 5-20. Polarimeter Detector Output Representation (After ref. 95)

After one complete rotation of the beam selector, the spectral filter wheel behind the fiber optics light guides is rotated by a Geneva mechanism to perform another sequence of measurements in another narrow spectral bandpass. A complete set of measurements with four filters is made in one second. Preliminary tests by Hariharan (ref. 95) indicate that an accuracy of 1% may be achievable in measuring the degree of polarization in the range 5-75%, and the dynamic range of the measurements of Q and U may be as high as 10^4.

A test program using the NASA CV990 aircraft has been conducted at altitudes up to 40, 000 ft over the desert and the Salton Sea. These surfaces approximate diffuse and specular reflectors, respectively, so that the difficulties in the data interpretation are somewhat reduced. However, for more general satellite use, as discussed in Section 4.2.1.5, the uncertainties in the reflectance and polarizing properties of the earth's surface may greatly hamper the data interpretation. Sekera suggests that these problems can be overcome by making ground-truth measurements, or by using days of "low turbidity" to obtain information on the underlying surface.

5.2 Active Systems

In our previous analysis (ref. 3) we considered a single-ended laser system, which, by observing radiation back scattered from the ground, may give an indication of the presence of a pollutant. We concluded that a quantitative measurement of a pollutant was not possible because of the high-power and stability requirements for the laser. Because of the development of high-powered and stable lasers and tunable lasers, the application of these systems to measure pollutants from satellites is re-examined, especially for resonant Raman and fluorescence techniques.

5.2.1 Systems Considerations

5.2.1.1 General. We define single-ended active systems as illustrated in fig. 5-21 where the transmitter (laser) and receiver are combined in a single instrument. (Other workers may consider the system double-ended if the transmitter and receivers are adjacent, but do not have common optics.) For the absorption method (a), the radiation back-scattered from the earth's surface is monitored. For the lidar, resonant Raman and resonant fluorescent methods (b), the radiation back-scattered from the atmosphere is monitored. In all methods, the effects due to absorption and Rayleigh and Mie scattering must be accounted for.

An illustration of double-ended system applications is presented in fig. 5-22. For the satellite-to-ground (a) and ground-to-satellite (b) systems, which would be used in local pollution monitoring, the absorption is measured directly, and resonant Raman and fluorescence methods may be used as illustrated to map out pollution profiles at a particular location. The satellite-to-satellite systems (c) may be used to monitor gaseous and particulate pollutants on a global basis.

A detailed study of satellite-to-satellite observations should include consideration of refractive effects which cause the grazing altitude to be greater than that for an unrefracted ray, and result in an elongation of the path length. These effects are illustrated in fig. 5-22 (c). In addition, the Doppler shift of the radiation must be taken into account if the line of sight is not normal to the direction of motion of

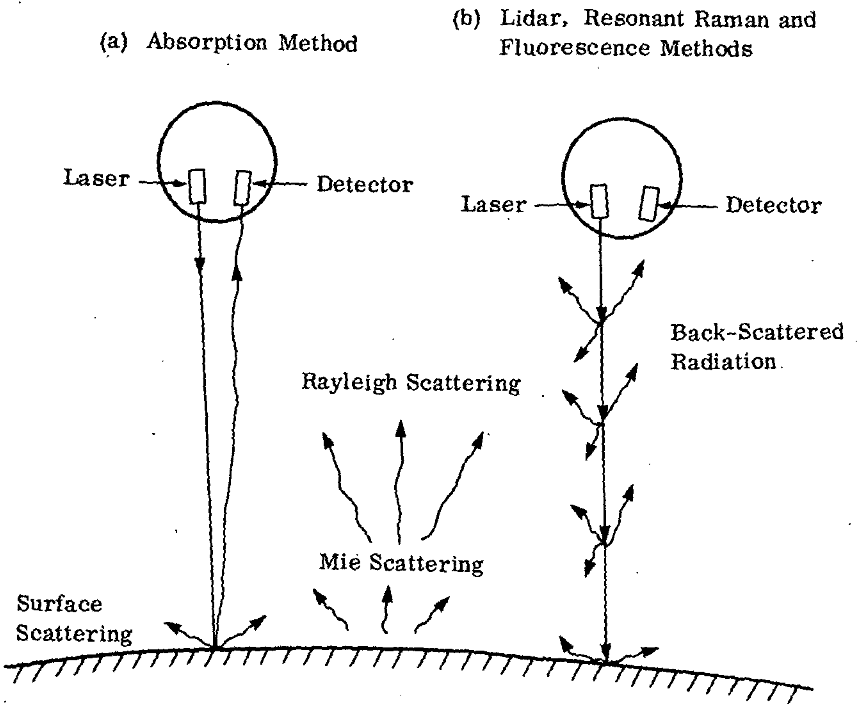

Figure 5-21. Schematics of Single-Ended Systems

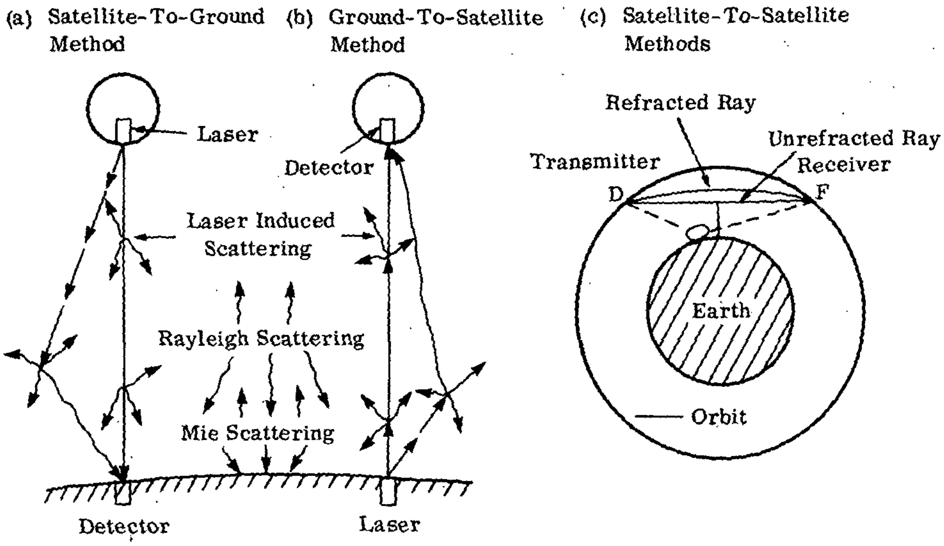

Figure 5-22. Schematics of Double-Ended Systems

the satellite. Another effect is the multiple scattering of the laser radiation contributing to the signal, although this is probably negligible, particularly in comparison to other uncertainties. One of the problems to be solved is that of the receiver satellite successfully tracking the laser beam from the transmitting satellite. The relative positions of the satellites will vary due to eccentricity of the orbits, differences in the orbit period and oblateness of the earth. These should be minimized by correct choice of orbit, so that the desired altitude regime may be continuously monitored and so that the tracking system does not have to cover a wide range of look angles. The tracking requirements for the receiver satellite might be reduced in the absorption technique by having a corner reflector on it, with the receiver on the transmitter satellite. This would double the pathlength through the atmosphere, but would result in a weaker signal due to beam divergence and increase the uncertainties due to the radiance of the laser being non-uniform over its cross-section. A detailed study of the satellite-to-satellite method should include the following considerations in addition to other systems characteristics: (1) number of satellites required to provide satisfactory vertical and global coverage; (2) relative motion of satellites; (3) capability of tracking systems; (4) laser beam divergence and size of collecting optics and (5) non-uniform radiance over laser beam cross-section.

In order to measure atmospheric pollutants using the absorption method, the laser frequency must coincide with a portion of the absorption line of the pollutant, and preferably not be absorbed by other pollutants or species in the clean atmosphere. As previously discussed, measurements in the infrared spectral region are the most practical, since all pollutants have absorption lines in this region, and interference due to Rayleigh scattering will be negligible. However, the importance of selecting the proper frequencies should be noted. For example, consider monitoring CO in the 4.6 μm region. If the laser frequency is monochromatic and coincides with any of the frequencies of the P1 to 15 or R0 to 15 CO line centers, for 0.1 ppm of CO uniformly distributed through the troposphere no sensitivity to CO concentration will be observed. This is due to the fact that in this case the line centers are effectively black, i.e., all radiation emitted by a satellite-borne laser would be absorbed before it reached the earth's surface. This means frequencies away from the line centers, on the wings of the lines, must be used in order to obtain sensitivity to varying amounts of CO in the atmosphere. For the resonant Raman and resonant fluorescence techniques, many of the electronic transition frequencies are in the ultraviolet. Thus, high-power tunable lasers operating in the UV are required. Contrary to the absorption mode, sensitivity saturation is not a problem, the main requirement being a monochromatic laser frequency to obtain the resonance condition.

5.2.1.2 Absorption mode. System signal-to-noise calculations for the absorption mode may be made in a fashion similar to that shown for passive sensing systems (Section 5.1).

Assuming an air-borne laser, reflecting from a diffuse surface, and neglecting atmospheric attenuation, the return signal is given by:

$$S = \frac{P \rho A}{\pi H^2}$$

where P is the laser output power, ρ is the reflectivity of the earth's surface, A is the area of the collecting optics and H is the altitude. The change in signal due to the presence of a pollutant is given by:

$$\Delta S = S \left(\tau_o - \tau_p \right)$$

where τ_o is the transmission through the clean atmosphere and τ_p is the transmission resulting from the presence of a pollutant; both transmissions are for the double optical path.

Detector-noise-limited systems are evaluated by considering the change-in-signal-to-noise ratio.

$$\frac{\Delta S}{N} = \frac{\Delta S}{NEP}$$

NEP, the noise equivalent power for IR detection is usually expressed by:

$$NEP = \frac{1}{D^*} \sqrt{\frac{A_d}{t_{obs}}}$$

where D* is the detectivity, A_d is the area of the detector and t_{obs} is the observation time. Recently developed (ref. 155) heterodyne detection systems significantly decrease the NEP. In this case:

$$NEP = \frac{2h\nu}{\eta} \sqrt{\frac{B_{IF}}{t}}$$

where $h\nu$ is the energy of each quantum of the laser radiation, η is the quantum efficiency of the mixer and B_{IF} is the intermediate frequency bandwidth of the detection system, and t is the post-detection integration time. NEP's of the order of 10^{-16} watts are possible.

Menzies and Shumate (ref. 156) have considered an airborne system operating at 10 μm with a heterodyne receiver and 2-watt laser at an altitude of 10 km detecting the radiation from a diffusely reflecting surface ($\rho = 0.01$); assuming the NEP = 2.5×10^{-16} watts, they calculate S/N = 300 for a 5 cm diameter receiver aperture. Since $\Delta S/S \sim 0.01$ is typical for most pollutants, a ±30% measurement would be possible, i.e., $\Delta S/N = 3$. For even low satellite orbits ($H \sim 330$ km), either a substantially more powerful laser (>2 kw) or collecting optics (>165 cm diameter) are required to achieve the same S/N. Of course, the return signals must also be considered in relation to the statistical noise of the earth-atmosphere background signal in order to determine the feasibility of the technique. The interpretation of the backscattered signal is further complicated since (1) the reflectivity of the earth's surface varies spectrally, spatially, and in its directional properties; (2) Rayleigh and Mie scattering have to be considered; (3) the laser beam may be degraded due to atmospheric turbulence effects; and (4) the radiance of the laser beam is inherently non-uniform over its cross-section.

In our initial study (ref. 3) we indicated that quantitative measurement of pollutants by the laser absorption technique from satellites would not be feasible. The S/N calculations presented above and the difficulties of interpreting the data suggest that the state-of-the-art has not yet advanced sufficiently to permit the use of this technique in the near future.

5.2.1.3 Resonance Methods. Both resonant Raman and resonant fluorescence scattering methods give increased sensitivity over their non-resonance counterparts. However, the full capabilities of these methods can be determined only after detailed study. Contradictory assessments of their utility have been reported (ref. 75,157,158) as will be described. Presumably, the NASA-sponsored study by the Stanford Research Institute now underway will provide definitive answers.

The basic equations describing the signal strengths of the two methods were presented in Section 3.2. As stated previously, these systems may operate in the UV, where photomultiplier tubes will be used as detectors. A brief discussion of the noise in these systems is presented here.

The noise is given by the photomultiplier current, which is due to the signal photons, the background photons and the dark current. Thus,

$$N = \left(\eta N_r + \eta N_B + N_D\right)^{1/2}$$

where η is the quantum efficiency, N_r is the signal photons/second, N_B is the background photons/sec, and N_D is the dark current equivalent noise input. The background radiance collected by the receiver is given by

$$W_B = BA\Omega\Delta\lambda \text{ (watt)}$$

$$= \frac{BA\Omega\Delta\lambda}{hc/\lambda} \text{ (photons/sec)}$$

where B is the radiance in W cm^{-2} $\mathring{A}^{-1}$ sr^{-1}, h is the Planck constant, and $A\Omega$ is the throughput of the receiver in cm^2 sr.

Thus, at the cathode, for a pulse width of t sec and n pulses/sec, the number of background photons in a gated system is given by

$$N_B = W_B\,nt = \frac{BA\Omega\Delta\lambda\lambda}{hc}\,nt$$

The dark current noise may be neglected in comparison with background noise, particularly when the photomultiplier is cooled. Thus, the signal-to-noise ratio becomes

$$SNR = \frac{\eta N_r}{\left(\eta N_r + \eta N_B\right)^{1/2}}$$

Kildal and Byer (ref. 75) present an excellent overview of active sensing techniques for remote detection of pollutants. Although their analyses, using realistic systems parameters are directed towards ground-based application, the results are relevant for earth-oriented satellite systems. Some of their conclusions are paraphrased below:

1. Resonance backscattering observations require sophisticated optical systems.
2. Very high power lasers, large optics, and expensive signal-processing equipment are required.
3. Tunable lasers with linewidths narrower than the width of the resonance transitions are needed.
4. While potential sensitivity is high for the electronic fluorescence scheme, interferences are a severe problem due to the very wide fluorescence bands.
5. Atmospheric transmittance limits the range of resonance backscattering techniques to hundreds of meters at sea level.
6. Depth resolution depends on gatewidth and laser pulse length; this creates a trade-off between sensitivity and depth resolution.
7. The straightforward absorption scheme is the only one sensitive enough to detect dispersed pollutants using state-of-the-art laser systems.

In contrast, Pikus (ref. 158) et al. have considered a satellite-borne system for detecting NO based on resonant fluorescence at 1927 cm^{-1} and optimistic theoretical results were obtained for the system parameters employed. The calculations assume a CO laser and compute the signal (resonant energy backscattered) to noise (thermal background of the earth). A threshold NO concentration sensitivity (S/N = 1) of 2×10^{11} cm^{-3} (7.4 ppb) at sea level results if a 5-joule laser is used. This would require a 5-Mw laser if one-μsec pulse duration is assumed. Calculations were also made for detecting NO at an altitude of 20 km; a threshold NO concentration sensitivity of 10^{10} cm^{-3} (5.4 ppb) results using a 0.5-joule laser.

Even assuming that a 5-joule laser were available for satellite use, these results may be over-optimistic since the calculations neglect detector and system noise sources, 80 cm diameter collecting optics are required, a 50% efficiency is assumed, and interferences due to other species are neglected. (At 1927 cm^{-1}, H_2O is a strong absorber over the 0.1 micron band pass assumed.)

5.2.2 Space-Qualified Lasers

The development of lasers for use in space appears to be directed presently only to communications systems rather than to atmospheric probing applications. The main advances have been made by Sylvania (ref. 159) for a 1-watt CW CO_2 laser, and by Hughes (ref. 160) for a 5-milliwatt CW He-Ne laser. The Nd:YAG laser is discussed by Forster et al. (ref. 161) in comparison with the CO_2 laser for satellite laser communications systems. It is apparent that the space-qualification of lasers is very time-consuming and very expensive, and that the high power lasers required for single-ended atmospheric probing will not be readily developed for unmanned satellites. Presumably, the qualification requirements for manned satellites are reduced (e.g., more electrical power should be available), so that high-power lasers may eventually be used for atmospheric probing from these platforms.

6

CONCLUDING REMARKS

This work is the continuation of a study on remote sensing of air pollutants from satellites and the present report is an update of our previous NASA report "Study of Air Pollutant Detection by Remote Sensors" (CR 1380, July 1969), in which the feasibility of detecting certain gaseous pollutants from earth-oriented sensors was tentatively established. The present report is written in cognizance of the "Study of Critical Environmental Problems (SCEP)" (MIT Press 1970), the "Study of Man's Impact on Climate (SMIC)" (MIT Press 1971), and finally, the study of "Remote Measurement of Pollution" (NASA SP-285, 1971). In the latter one the reasons and requirements for measuring pollution from satellites were established by a working group of 50 leading authorities in the field of remote sensing of pollution.

While these previous studies were concerned with the need for global monitoring of pollution and with various aspects of the potential and established feasibility of remote sensing, the present work is concerned with the detailed analysis of the actual task.

The first section of this report contains an introduction and a recapitulation of the NASA report CR 1380. In the second section, trace contaminants, (man-made and natural) which are of concern in either the troposphere or stratosphere are briefly discussed. In the third and fourth section, the principles of observation for gaseous and particulate pollutants are investigated and the results of detailed calculations are presented. In the last section, the various instruments which are candidates for the remote measurement of air pollutants are discussed. In the Appendix, selected details on pollutant spectra in the infrared, on scattering theory, on optical correlation, and on band models, are given.

Global Distribution of Pollutants

The relevancy of the various pollutants treated in this section has evolved over the past few years and has been summarized recently in the 1971 study of "Remote Measurement of Pollution" (NASA SP-285, 1971) in terms of requirements for measuring pollutants on a global and regional scale. In that study, the pollutants were categorized as (a) pollutants with a recognized near-term environmental impact and (b) pollutants for which concern is speculative or long-term.

This distinction is not made here, but we do classify them according to the regions of the atmosphere in which the pollutants are of concern, since the techniques for measuring trace gases in the troposphere and in the stratosphere are distinctly different. Thus, the pollutants are grouped according to Table 6-1; of course, some pollutants are of concern in both the troposphere and stratosphere.

TABLE 6-1. POLLUTANTS WHICH ARE OF CONCERN IN THE TROPOSPHERE AND STRATOSPHERE

	Troposphere	Stratosphere
C-compounds (Inorganic)	CO_2, CO	CO_2, CO
S-compounds	SO_2, H_2S	SO_2
N-compounds	NO, NO_2, NH_3	NO, NO_2, N_2O, NHO_3, NH_3
HC-compounds	HCHO, PAN, CH_4	CH_4, <HC>
Oxidants	O_3	O_3
Halogens	I_2, HF, Br_2	
Water Vapor		H_2O
Particles	Total Aerosol Content	Layered Aerosol Content

In the following, the reasons for concern about the different pollutants are summarized:

CO_2	The global mean concentration of CO_2 is increasing and it has an effect on the global climate;
CO	Although its fate is less mysterious than it appeared a few years ago, the possible implication in the formation of photochemical smog makes CO an important pollutant to be monitored;
SO_2	Accumulation has toxic effects; in addition it contributes to particle formation, thus influencing the global heat balance;
H_2S	Contributes to the formation of SO_2 through oxidation;

N_yO_x	Accumulation has toxic effects and the oxides of nitrogen are a vital ingredient in the formation of photochemical smog; they also contribute to the formation of particles; nitrous oxide may be important in the chemistry of the stratosphere;
NH_3	Contributes to the formation of particles;
<HC>	Are ingredients of photochemical smog and contribute to particle formation; formaldehyde, a product of photochemical smog, has a concentration greater than that of other HC's except CH_4;
HNO_3	Probably influences the chemistry and particle formation in the stratosphere;
O_3	Changes in the stratospheric ozone layer have great effects in the amount of UV radiation reaching the earth's surface; ozone is an ingredient of photochemical smog;
H_2O	Is important in the chemistry of the stratosphere and particle size distribution;
Others	Fluorocarbons and halogens are toxic and are probably accumulating in the troposphere.

Satellite Observation of Gaseous Pollutants

In this study, three different modes of observation are distinguished, namely passive earth-oriented, passive horizon-oriented and active single or double-ended modes.

In the passive earth-oriented mode, also called the nadir experiment, the signal observed on a satellite arises mainly from pollutants in the troposphere. The radiance sources are provided mainly by the reflected sunlight for wavelengths shorter than about 3 μm and by the thermal emission of the ground and the atmosphere for wavelengths longer than about 5 μm. An overview of the different contributions to the radiance emerging at the top of the atmosphere in the spectral interval from 3000 Å to 10 μm is given in fig. 6-1. Although pollutants can have spectral signatures in regions extending from the ultraviolet to the microwaves, it is found that only the infrared region from 2 to 13 μm is useful for the measurement of pollutants in the nadir experiment.

The absorption bands of the pollutants and interfering molecules in the infrared are summarized in Table 6-2. From this table it is evident that all pollutant infrared bands are overlapped by bands of one or more normal atmospheric molecules.

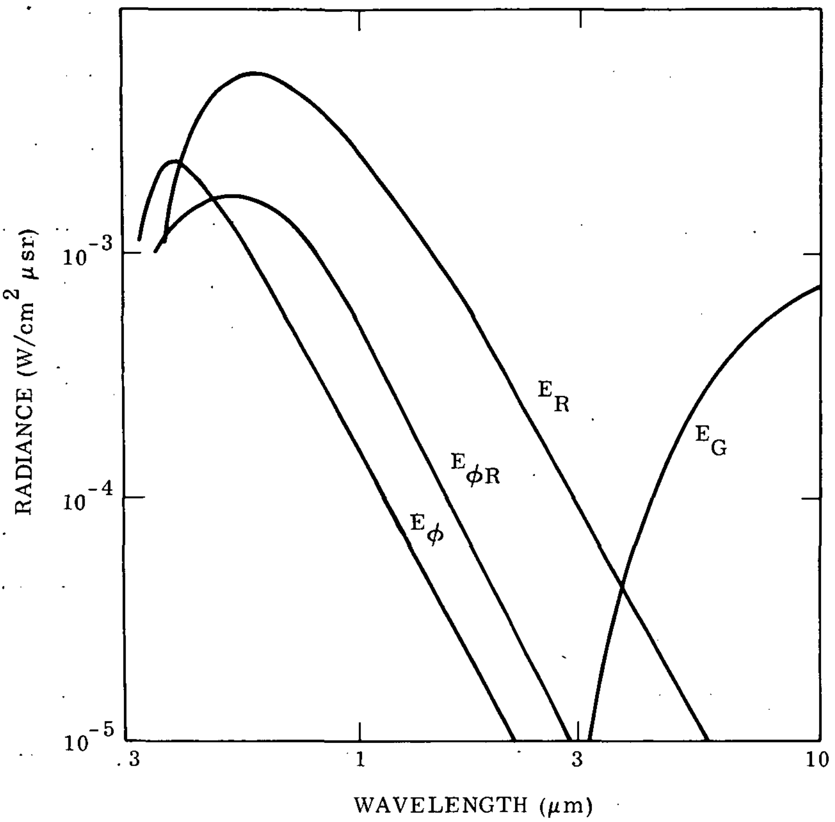

Figure 6-1. Contributions to the upwelling radiation at the top of the atmosphere for a ground reflectance of 0.2 and ground emissivity of 0.8 and a sun zenith angle of 45°. E_G is the thermal radiation emitted by the underlying surface and the atmosphere, E_R is the incident solar radiation reflected by the surface, E_ϕ is the radiation scattered by the atmosphere without having been reflected from the ground, and $E_{\phi R}$ is the radiation scattered by the atmosphere which has undergone a reflection from the surface.

Therefore, the simplified approach of employing band models in the radiative transfer calculations is restricted in value because these models do not indicate the severity of the interference problem. At the present time the line parameters for most of the pollutant molecules are not well established. Work in this area is being carried out under separate programs and a selected number of line parameters of pollutant and interfering species were available to this study. Model calculations were performed to evaluate the signal change, i.e., the radiance difference between "clean" and "polluted" atmospheres, choosing the postulated background levels of pollutants as the concentrations of interest, i.e., 0.1 ppm for CO, 320 ppm for CO_2 and 2 ppb for the other molecules. The signal changes were

TABLE 6-2. POLLUTANTS AND INTERFERING SPECIES

	Interfering Species							
Pollutant λ (μm)	CO_2	CO	H_2O	N_2O	CH_4	O_3	HDO	Solar Lines
CO_2 2.1			X					X
CO 4.6	X		X	X		X		X
CO 2.3			X		X		X	X
SO_2 8.6			X	X	X	X	X	
SO_2 4.0				X				X
NO_2 7.6			X	X	X		X	
NO_2 3.4			X		X			X
NH_3 10.5	X		X	X		X		
NH_3 3.3	X		X	X	X			X
NO 5.3	X	X	X					
HCHO 3.5			X	X	X			X
HCl 3.3	X		X	X	X			X
HF 2.7	X		X					X
H_2S 3.9				X				X
HNO_3 11.0	X		X	X				
CH_4 8.0			X	X	X			

computed on the basis of single lines, integrated over the rotation-vibration bands. Water vapor interferences - because of the variability of the humidity - have been treated in depth and were found to be the limiting factor in the measurements of some pollutants (NO and partly NO_2). Although more model calculations have to be performed to assess the influence of ground and atmospheric parameters over a wider range than has been considered here, the following tentative conclusions about the detectability of pollutants are drawn: A number of tropospheric pollutants listed in Table 6-1 are measurable within their background levels from satellites: CO_2, CO, SO_2, NO_2, CH_4, NH_3 and HCHO. However, the signal changes are small, even when the total band is observed simultaneously. Hence, highly sensitive and specific sensors must be used. Measurements leading to the determination of the vertical distribution of pollutants in the troposphere will be very difficult to make; however, indications are that some measurement methods together with the appropriate atmospheric modeling will give information about the gross structure of the vertical distribution of a number of pollutants.

In the passive horizon-oriented mode, also called the limb experiment, information is obtained about the vertical distribution of trace gases in the stratosphere by means of spatial scanning. Because the water vapor interferences are reduced, the requirements for high-resolution instruments are relaxed. In the thermal region, the emission originates from the atmospheric gases only, because the background is cold space, in contrast to the nadir experiment, where the warm earth contributes a large background level. In the occultation mode, the sun provides a powerful radiation source, which makes the observation of very low concentrations of trace gases in absorption possible. However, the signal changes due to small variations in pollutant concentrations are small and instruments with high sensitivity and satellites with high pointing accuracy are required. It appears that all of the pollutants listed in Table 6-1 to be of concern in the stratosphere can be measured through a limb experiment.

In the discussion of the active mode, a brief theoretical overview of the two most promising methods, resonance Raman and resonance fluorescence, is given. The requirements for the power and tuning of lasers are discussed in the section on instruments.

Satellite Observation of Aerosols

The measurement of aerosols on a global scale is important in monitoring their effect on climate. Satellite passive observations are well suited, and may be divided into two types: earth-oriented which determine the total loading of the atmosphere, and limb observation to determine the stratospheric loading.

Three techniques for the earth-oriented observation are considered, namely contrast measurements, polarization measurements and radiance measurements, using theoretical calculations for ideal model atmospheres. On the basis of these calculations, the radiance observation in the visible region appears most promising for general global applications. It is more sensitive than a polarization measurement, while the contrast measurement is best made over pre-selected targets, reducing its suitability for global coverage.

It is recognized that the discussions are based on ideal model calculations, and that these model conditions will never be realized in the real atmosphere, so that deviations from the theoretical relationships are expected. The problem areas are difficult to analyze theoretically, and will probably be best resolved by using satellite data, such as those from ERTS-1 to derive empirical relationships based on the ideal model atmosphere theory.

The problem areas include aerosol properties, non-Lambertian surfaces, ocean sun glitter, and surface reflectance gradients. The aerosol properties such as size distribution, vertical distribution, sphericity of the particles and the refractive index, are quite variable within the real atmosphere. In most calculations an underlying Lambertian surface is generally assumed, whereas in practice this is not true. This is mainly a problem over land surfaces which fluctuate in reflectance and polarizing properties. The ocean surface reflectance properties are relatively well known for a calm sea, but care has to be taken to avoid the sun glitter pattern which is most apparent on rough seas. The problem of surface reflectance gradients applies mainly to the contrast measurements since the theoretical data used in the analysis were based on underlying surfaces with constant reflectivity extending to infinity.

An analysis of the sun occultation measurement indicates that the stratospheric aerosol content may be readily measured from a satellite, with an accuracy sufficient to monitor the anticipated effects of high-flying aircrafts. The discussion points out the possible interference by stratospheric clouds.

Instrumentation

Both passive and active sensor systems were considered. Instruments to be used in the passive earth-oriented mode (where the interference problem by the "normal" atmosphere is severe) must be sensitive, specific and fast in time response. Theoretically, instruments with a large throughput and the multiplex advantage fulfill these requirements. Examples are optical correlation instruments and interferometer-spectrometers. These two types are discussed and those sensor systems which are currently under development are treated in greater detail.

Instruments used in the horizon-oriented mode do not require the high specificity for many trace gases because the interference from water vapor is very much reduced. Thus, low resolution, sensitive radiometers, whose complexity is less than that for other instruments, can be used. Their high sensitivities make measurements with high spatial resolution possible.

The present status of the instruments used in the passive nadir and limb experiments, which are in various stages of laboratory development and field testing, is summarized in Table 6-3.

As far as active sensor systems are concerned we have considered the application of lasers for the absorption scheme and the resonant Raman and resonant fluorescence backscattering schemes. Our conclusions are that the absorption scheme for earth-oriented satellite-borne lasers does not appear feasible unless very high-power lasers are used, creating a possible safety hazard. In addition, a number of difficulties arise in interpreting the data. Thus, quantitative measurements of air pollutants using this scheme do not appear possible at this time. The satellite-to-

TABLE 6-3. SURVEY OF SATELLITE INSTRUMENTATION FOR POLLUTION MEASUREMENTS

Instrument	Program	Type	Pollutants	Status	Remarks
Matched Filter Spectrometer	Barringer Research Laboratory	Photographic and/or slit mask in uv; Resolution: 6Å	SO_2 NO_2	Balloon and A/C flights	Problems in data interpretation because of atmospheric scattering.
Gas Filter Correlation Instrument	AAFE/MAPS	Gas filter correlation in the infrared. Resolution: spectral line width, spectral range 2-12 μm	CO, SO_2, NO_2 NH_3, HCHO, CO_2, CH_4	Under development	Prototype for CO has been flown on A/C.
Interferometer-Spectrometer	NASA-GSFC IRIS D	Interferometer-spectrometers. Resolution: 2.8 cm^{-1}, spectral range 7-18 μm	Not specified	Flown on NIMBUS 4	Used for temperature inversion and water vapor and ozone measurements; additional species identified in spectra includes CH_4.
Correlation Interferometer-Spectrometer	AAFE/COPE	Interferometer-spectrometer with rotating compensating plate. Resolution: ~5 cm^{-1}, spectral range 1-5 μm	CO	Under development	Uses reflected sunlight.
High-speed Interferometer	AAFE/JPL	Interferometer-spectrometer; Resolution: 0.15 cm^{-1}, spectral range from 1-5 μm	Not specified	Ready to be A/C flight tested	Scan time long compared with look-time available.
Radiometer	AAFE/LACATE	Infrared Region Filter-wheel	O_3, N_2O, HNO_3, H_2O	Under development; four-channel version to be flown on NIMBUS F	Limb experiment: vertical distribution of pollutants in stratosphere.
Polarimeter	AAFE/UCLA	Visible Region Filter-wheel	Total Particles	Under development	Prototype has been flown on A/C.
Radiometer	U. of Wyoming	Visible Region Filter-wheel	Stratospheric Particles	To fly on OSO-J, AF 72-2	Sun occultation. Flown on balloons.
Radiometer	AAFE/MIT	Visible Region Filter-wheel	Stratospheric Particles	Under development	Limb scattering.

satellite absorption scheme is hampered by the requirement of high pointing and tracking accuracies. It would of course be restricted to the stratosphere due to clouds in the troposphere.

The resonant Raman and resonant fluorescence backscattering schemes may be useful for probing the stratosphere with the potential of providing some depth resolution. However, these schemes do not appear promising for determining pollutant concentrations near the earth's surface because of severe atmospheric attenuation.

All laser applications to remote sensing require high power, which may make the use of unmanned satellites impractical. However, manned satellites (Skylab, shuttle, etc.) could provide the necessary power more easily.

APPENDIX A

POLLUTANT SPECTRA IN THE INFRARED

A-1. Carbon Monoxide

The fundamental bands of $C^{12}O^{16}$ and $C^{13}O^{16}$ have been studied extensively in the laboratory and the line locations, strengths and half-widths are tabulated (ref. 162). We have used these line parameters together with the tabulated values for water vapor (ref. 163, 164) to calculate the solar spectrum between 2135 and 2165 cm^{-1} and to compare the results with an experimental spectrum (ref. 165), taken at an altitude of 12, 000 ft. The comparison is shown in fig. A-1. For this calculation, a triangular slit function with a half width of 0. 2 cm^{-1} was introduced. The sun zenith angle was about 25°. A CO concentration of 0. 1 ppm in the troposphere was assumed. For the water distribution, we initially used the Gutnick (ref. 63) model, but had to reduce its average amount by a factor of 5 in order to match the observed transmission of the H_2O lines with the calculated one.

A more extended solar spectrum (ref. 166) between 2080 and 2180, recorded from the ground, is shown in fig. A-2, in which the CO lines are indicated by a dot. It is seen that the CO lines are separated from neighboring lines in most cases. Similar spectra were used in 1949 by Migeotte to deduce the average amount of CO concentration in the atmosphere by determining the equivalent widths of single lines and compare them with laboratory data. We have used the tabulated data of Benedict et al. (ref. 162) to generate band model parameters which are listed in Appendix D.

The first overtone band of the carbon monoxide molecule has not been studied as extensively and no listing similar to that for the fundamental band is available. Thus, we have generated the line strength and locations for 160 lines of the $C^{12}O^{16}$ and $C^{13}O^{16}$ molecules (ref. 61), from which the band model parameters listed in Appendix D have been derived.

The appearance of lines of the CO first overtone in the solar spectrum is shown in the measurements by Mohler (ref. 167), who also estimated the equivalent widths of some of the lines. Portions of the solar spectrum are reproduced in fig. A-3, in which the most prominent CO lines are indicated. The CO lines are very weak and are heavily overlapped by strong telluric CH_4 and H_2O lines and CO Fraunhofer lines. In reducing these data to obtain the equivalent widths of lines, Mohler finds great variation in the telluric lines and a significant increase for transitions involving the larger rotational quantum numbers, due to the stronger influence of the solar lines.

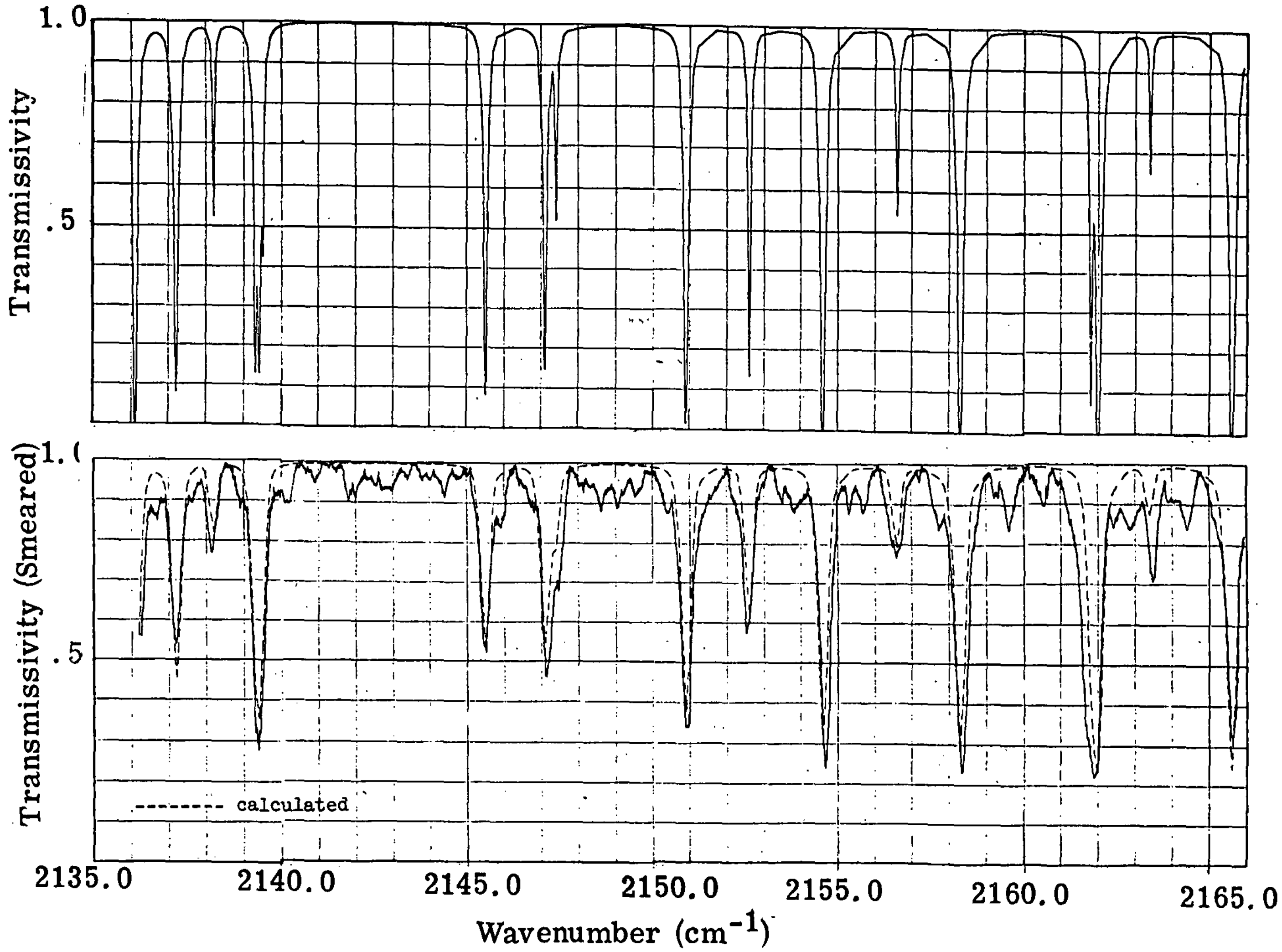

Figure A-1. Transmissivity of atmosphere between 2135 and 2165 cm^{-1}. Upper trace calculated monochromatically; lower trace calculated with slit function (dashed), experimental curve solid line.

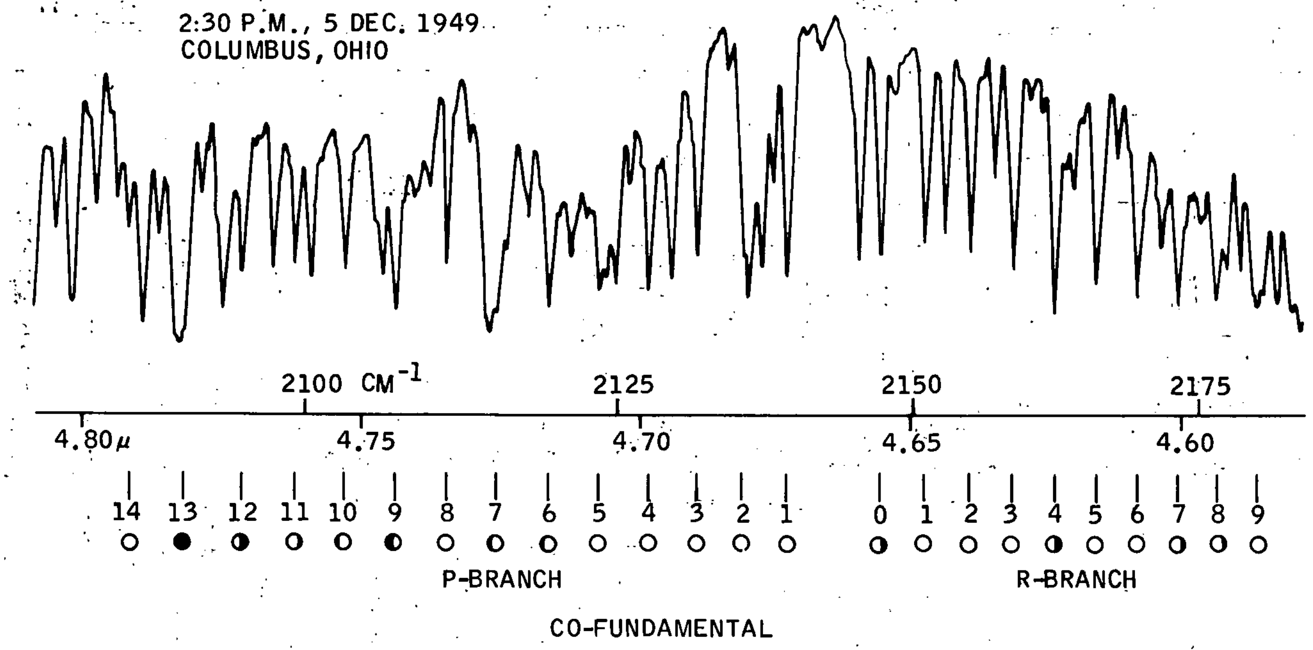

Figure A-2. Solar CO Spectrum at 4.6 μm (from ref. 166). The CO lines are indicated by dots.

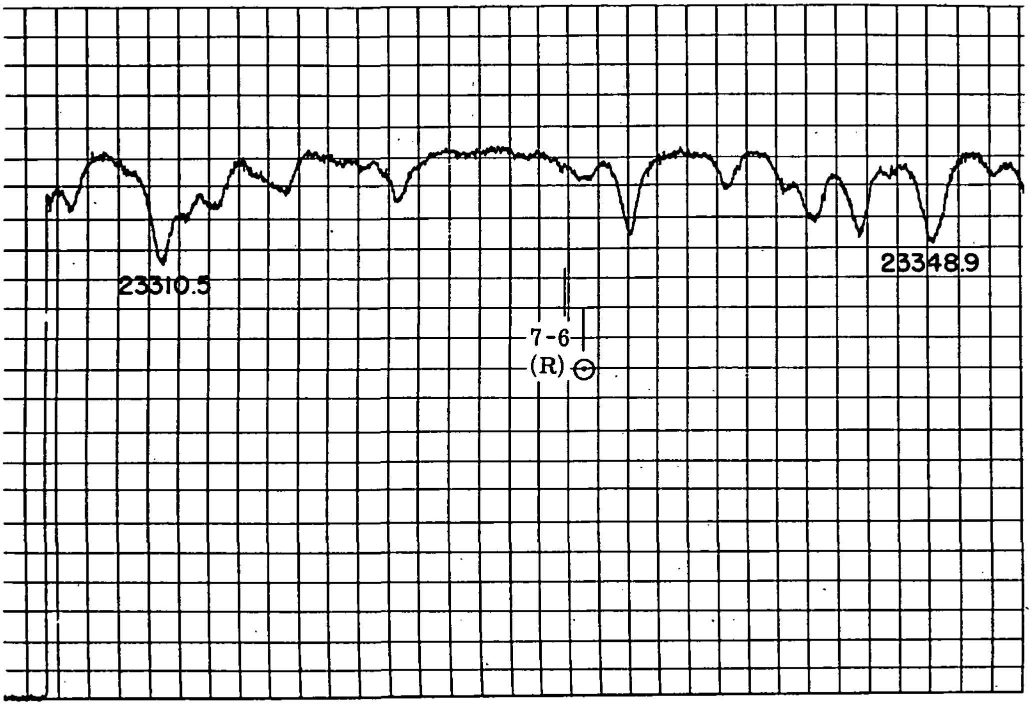

Figure A-3. Solar Spectrum at 2.33 μm (from ref. 167). The R(7) line of CO is indicated. Numbers refer to Angstroms, i.e., 23348.9Å = 2.3349 μm.

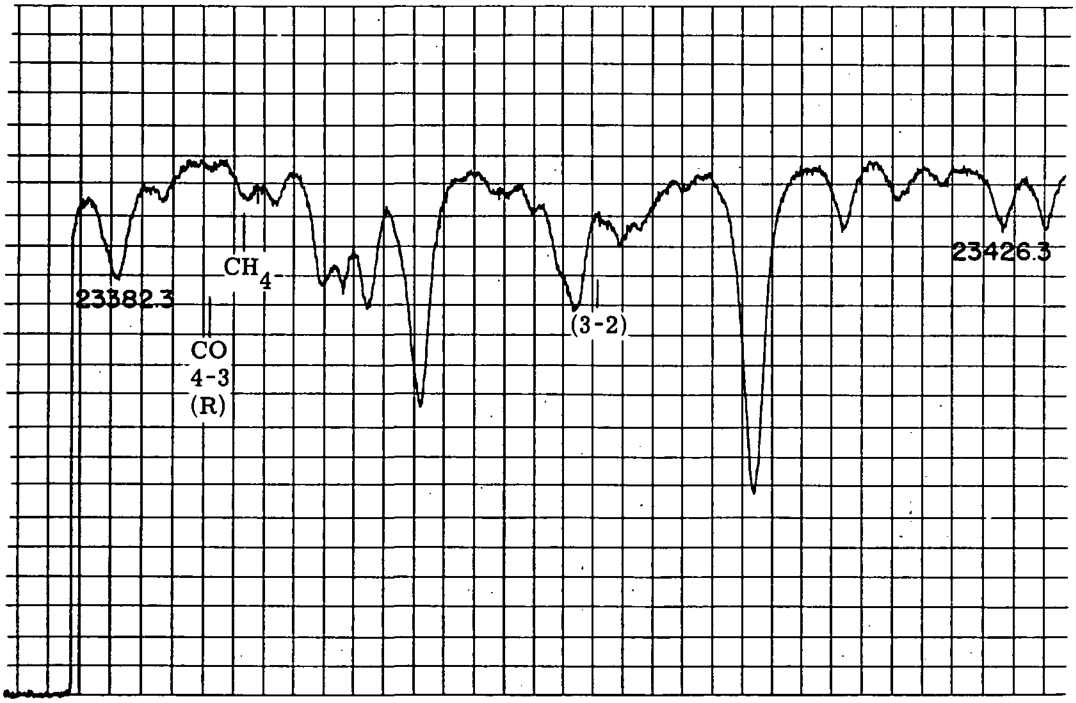

Figure A-3 (Continued). R(3) Line of CO Indicated

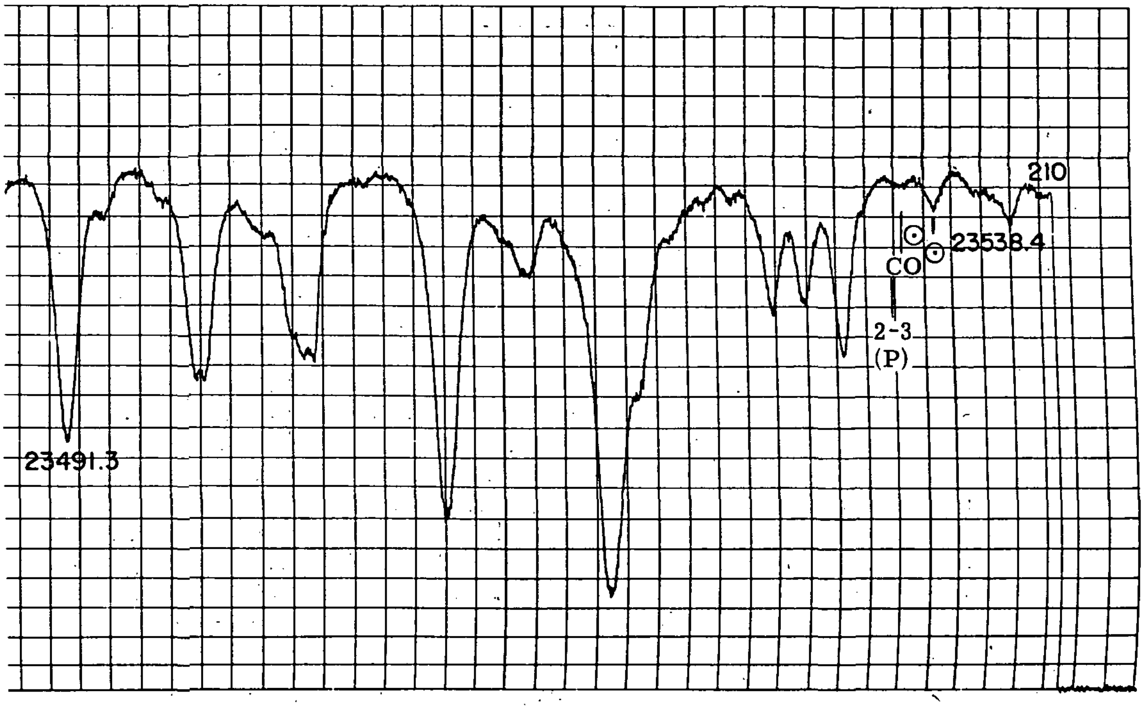

Figure A-3 (Continued). P(2) Line of CO Indicated

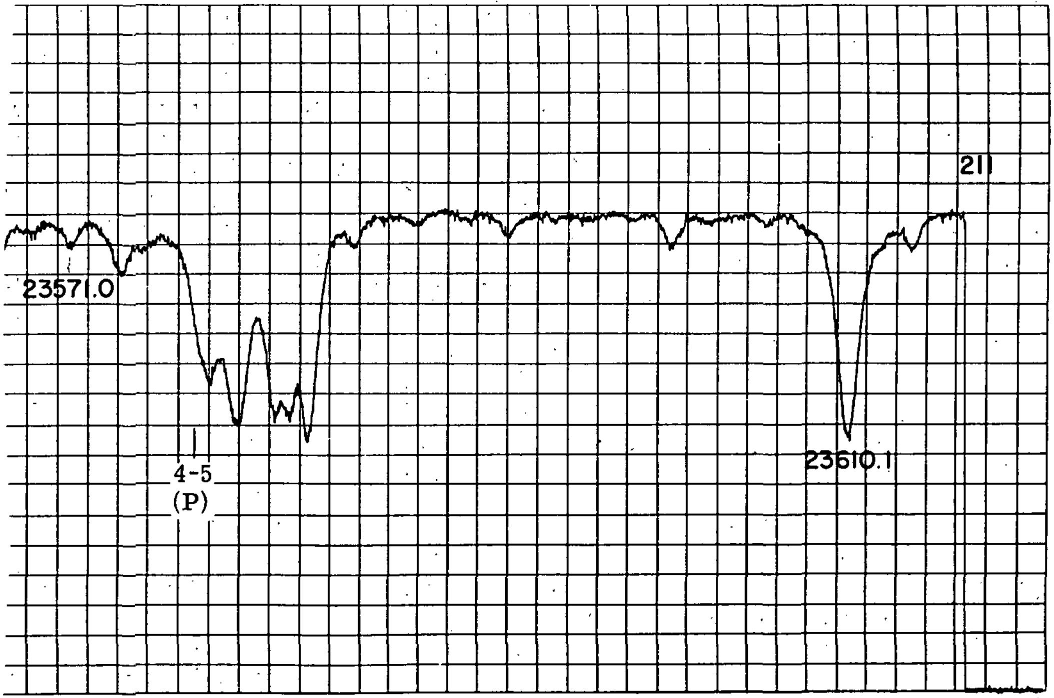

Figure A-3 (Continued). Line P(4) of CO Indicated

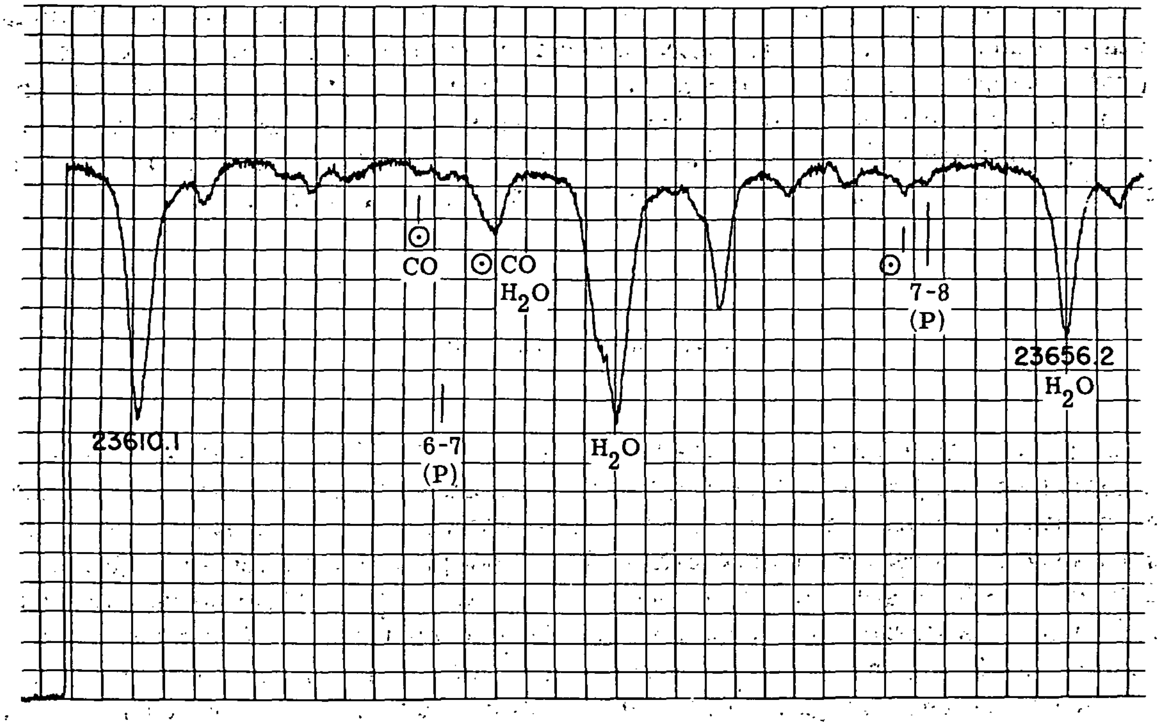

Figure A-3 (Continued). Lines P(6) and P(7) of CO Indicated

The influence of solar CO on the P(6) line is also discussed by Howard and Shaw (ref. 168). Results for some telluric lines showing least interference, which Mohler analyzed, are given in Table A-1. Two lines (R(12) and R(15)) greatly influenced by solar CO are included as examples.

TABLE A-1. ANALYSIS OF SELECTED LINES OF THE 2.3 μm - CO BAND

	Equivalent Width W		Line Strength	Path Length	Concentration
	mÅ	cm^{-1}	cm^{-2} atm^{-1}	cm-atm	ppm
R(3)	12	2.2×10^{-3}	0.46	4.8×10^{-2}	.06
R(6)	8	1.45	0.57	2.6	.03
R(12) ⊙	30	5.5	.033	16.6	.20
R(15) ⊙	35	6.5	.017	38.	.47
P(2)	6	1.1	.040	2.76	.035
P(4)	4	0.735	.058	1.26	.015
P(6)	9	1.65	.067	2.46	.03
P(7)	19	3.5	.067	5.2	.06
P(9)	10	1.84	.061	3.	.034

In the conversion of the path length from cm-atm to the concentration in ppm, it was assumed that CO is distributed uniformly through the atmosphere with an equivalent height of 8 km at 1 atm pressure. The wide fluctuations in the results demonstrate how difficult it is to deduce the concentration of a pollutant, when the lines are very weak, such as in the 2.3 μm first overtone of CO. In addition, in this particular case, the solar Fraunhofer CO lines must be accounted for.

A-2. Carbon Dioxide

There are many infrared active bands of CO_2. The 15-μm band is routinely being used for temperature sounding from satellites, assuming a known, constant concentration. In order to measure the global and seasonal fluctuation in the CO_2 concentration accurately, it is desirable to use the pure sun-reflected region in order not to rely on atmospheric temperature satellite data, which were obtained based on the assumption of known, constant CO_2 concentration. For satellite measurements to determine the CO_2 concentration, the rotation-vibration band to be used must be strong enough to absorb sufficient amounts of reflected sun radiation, yet it must not become black except for the line centers and it should not be significantly interfered by other species. One such band system is the $2\nu_1 + \nu_3$ transition at 2.1 μm. We have generated the line parameters of over 1000 lines, based on the molecular constants given by Courtoy (ref. 170). A comparison of the spectrum between 6330 and 6336 cm^{-1} with the experimental results of Boese et al. (ref. 171) is shown in fig. A-4. The appearance of this band system in the solar spectrum together with interfering lines is shown in fig. A-5.

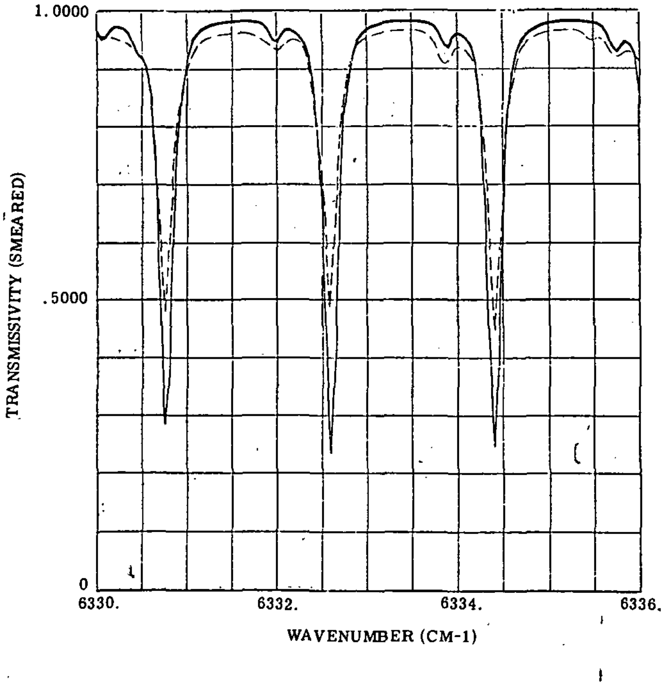

Figure A-4. Degraded Transmissivity (slit width of 0.08 cm^{-1}) of CO_2 between 6330 and 6336 with u = 800 cm-atm, p = 0.5 atm and T = 296° K. (Calculated spectrum solid. Laboratory spectrum (ref. 171) dashed.)

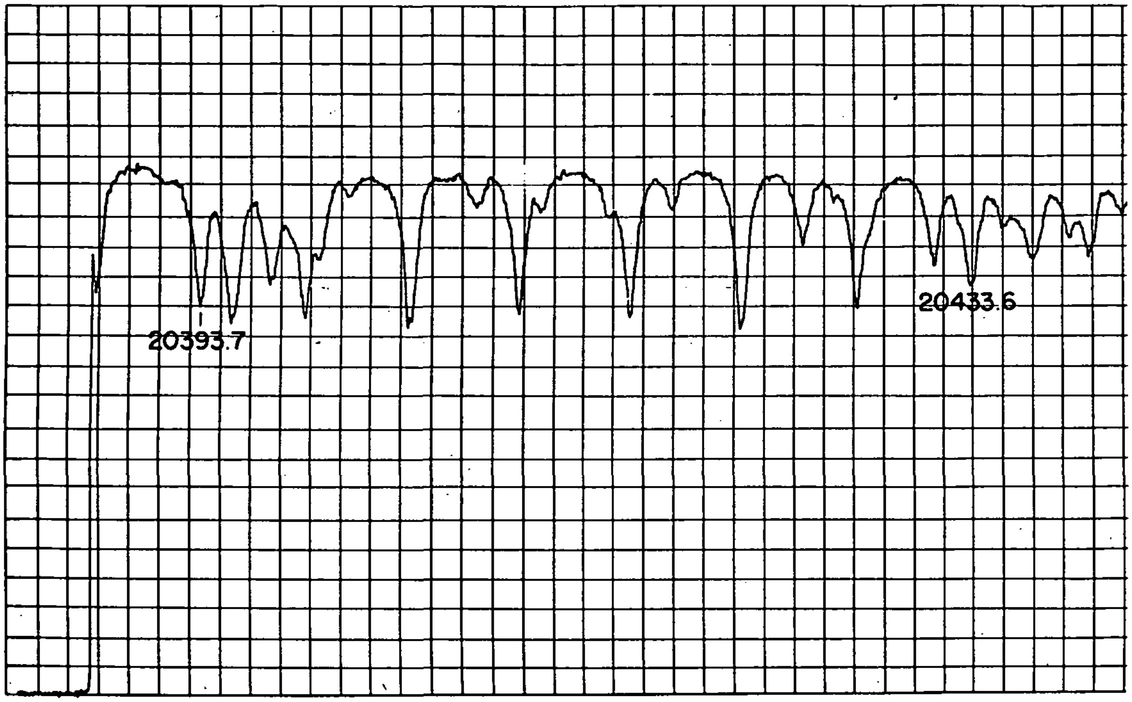

Figure A-5. Solar Spectrum of CO_2 Spectrum at 2.04 μm (from ref. 167)

A-3. Sulfur Dioxide

Information about the spectral bands of SO_2 is scarce. We have attempted to generate the line parameters of the fundamental band ν_1 at 8.6 μm, and of the combination band $\nu_1 + \nu_3$ at 4 μm based on the theory of a slightly asymmetric top molecule (ref. 61), including the perturbations of the energy levels for the lowest values of K.

A portion of the 8.6-μm band including the band center and the R-branch maximum is shown in fig. A-6, and the same spectrum viewed with a triangular slit of width 1 cm^{-1} is compared with the results of Burch et al. (ref. 172) in fig. A-7.

Tables of SO_2 energy levels have been obtained from G. Steenbeckeliers (private communication, 1971). Comparison of these tables shows that some of the perturbed energy levels are very accurately calculated by our program, while certain others are not. This discrepancy should be investigated, and should lead to a further improvement in the calculated spectrum.

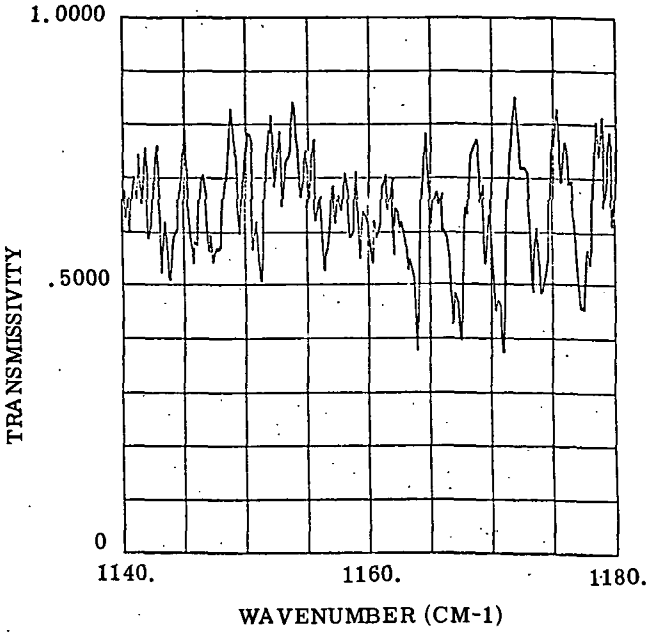

Figure A-6. Monochromatic transmissivity of the $SO_2 - \nu_1$ band between 1140 and 1180 cm^{-1} (showing band center and R-branch maximum)

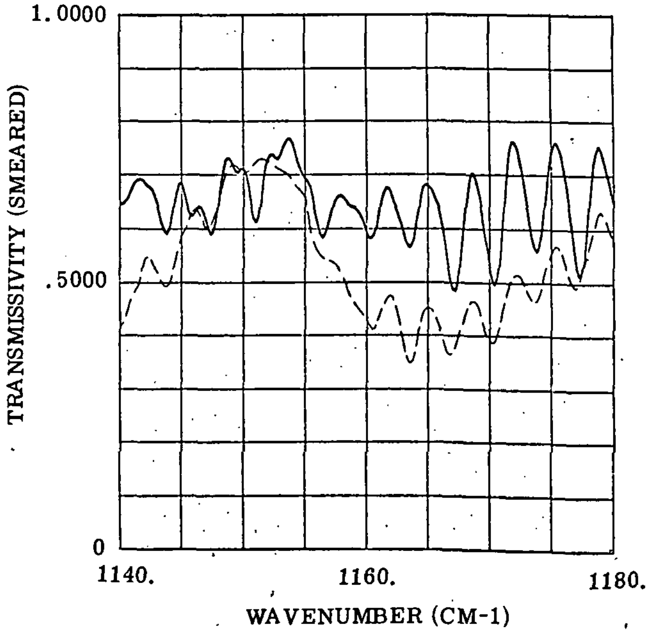

Figure A-7. Degraded transmissivity (slit width is 1 cm^{-1}) from fig. A-6, for $u = .577$ cm atm_{STP}, $P_e = 1.59$ atm and T = 298°K (calculated spectrum solid, laboratory spectrum dashed)

The entire spectrum as measured by Burch et al. (ref. 171) is shown in fig. A-8 for the conditions of 0.5×10^{19} and 1.55×10^{19} molecules/cm^2 at 298K and a cell length of 2 cm.

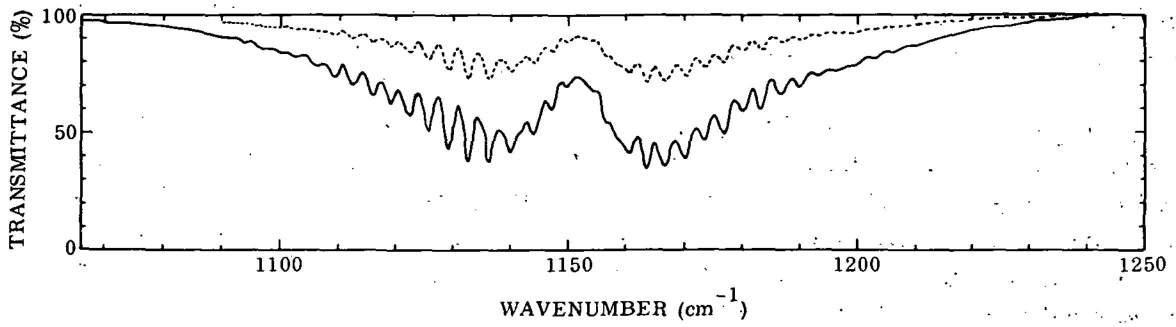

Figure A-8. Spectral Curves of Transmittance Between 1060 and 1250 cm^{-1} for Two Samples of SO_2 having Different Absorber Thicknesses. Spectral slitwidth ≅ 1 cm^{-1}. $\theta = 298$ K. (From ref. 171.)

Curve	P_e (atm)	L (cm)	u (cm-atm) 298K
Broken	1.40	1.99	.199
Solid	1.59	1.99	.630

A set of line parameters based on the theory of an asymmetric rotor has recently been generated by Calfee (private communication, 1972). They indicate excellent agreement with the experimental data obtained by Burch (ref. 172). In order to show how the SO_2 spectrum at 8.6 μm relates to the solar spectrum, we have indicated in fig. A-9 the positions of the Q-branches in the spectrum taken by Shaw (ref. 173).

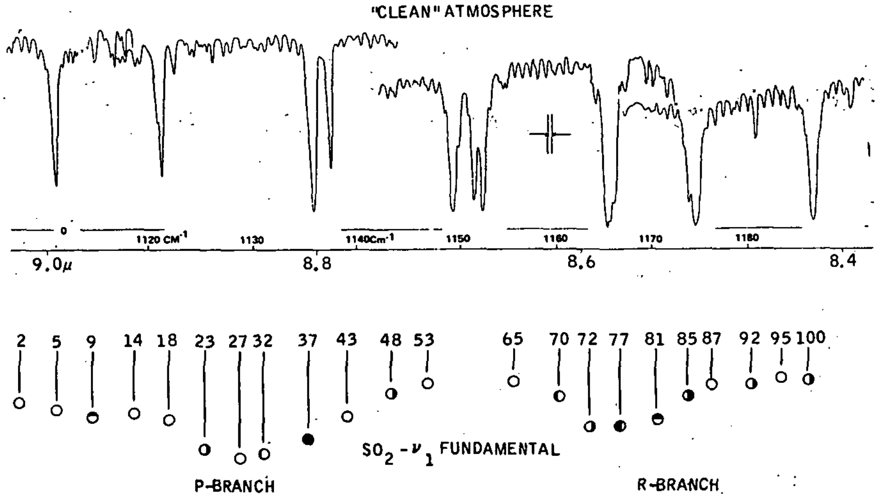

Figure A-9. Solar Spectrum Between 1110 and 1190 cm^{-1} and $SO_2 - \nu_1$ Fundamental Band at 8.6μm (from ref. 173)

A-4. Nitrogen Dioxide

Information about the spectrum of NO_2 is even scarcer than for SO_2. A literature search indicated that insufficient data for NO_2 are available for our needs.

The SO_2 version of our computer program has been used to generate a set of parameters for 2583 lines of the ν_1 band of NO_2. The molecular constants were taken from Abe et al. (ref. 174). Because of the large numbers of lines (and consequent heavy overlapping) we have neglected the level-splitting effects of the unpaired electron, which were considered in the case of NO (see below). We have found no good spectra for comparison.

A laboratory spectrum of the combination band $\nu_1 + \nu_3$ at 3.44μm taken by Hanst (ref. 175) is shown in fig. A-10. The optical depth is 0.13 cm-atm, which is about two orders of magnitude larger than the amount expected in the troposphere. The interference of the band by atmospheric lines is shown in fig. A-11. The fundamental band at 7.6μm is also heavily overlapped by the 6.3μm band of water vapor as is seen in fig. A-12.

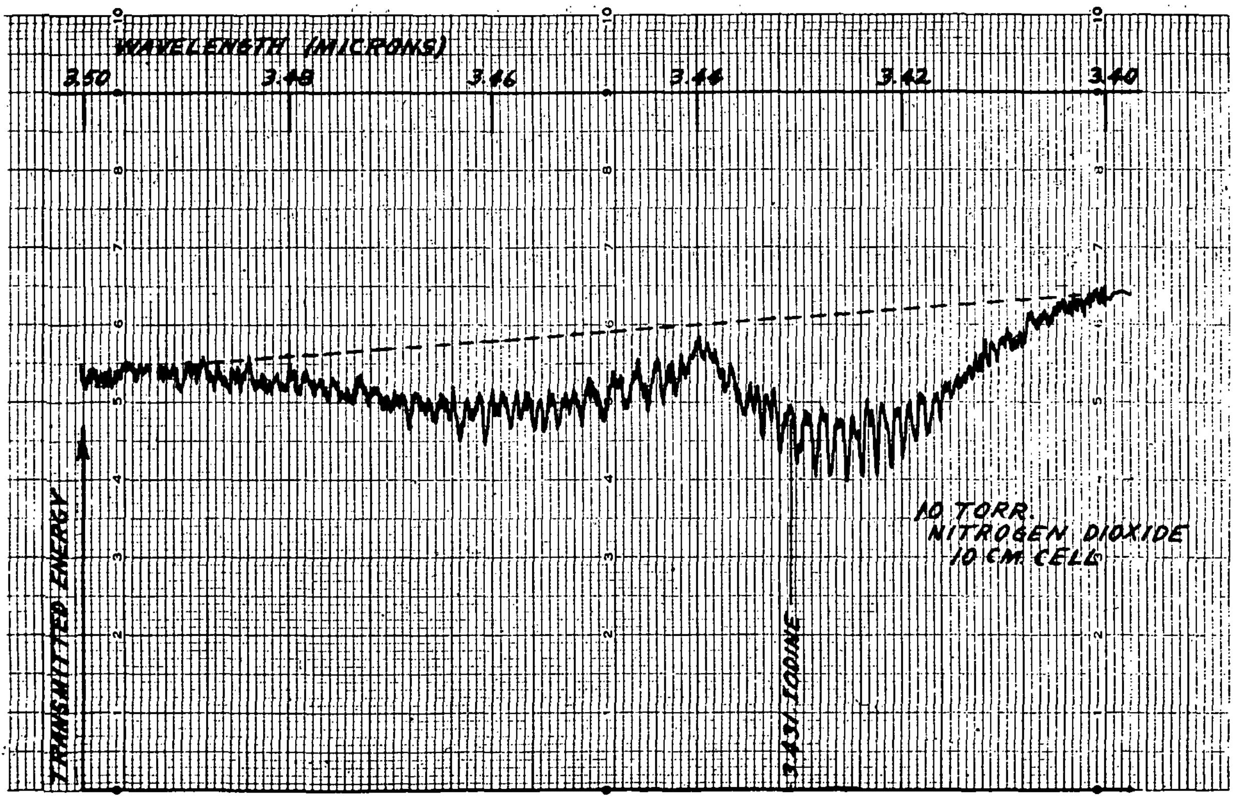

Figure A-10. Laboratory Spectrum of NO_2 (from ref. 175)

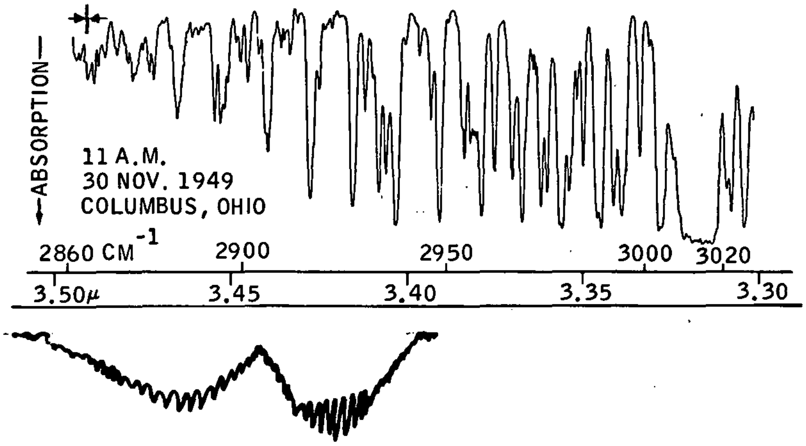

Figure A-11. Solar Spectrum Between 2860 and 3020 cm^{-1} (ref. 166) and NO_2 $\nu_1 + \nu_3$ Band Contour

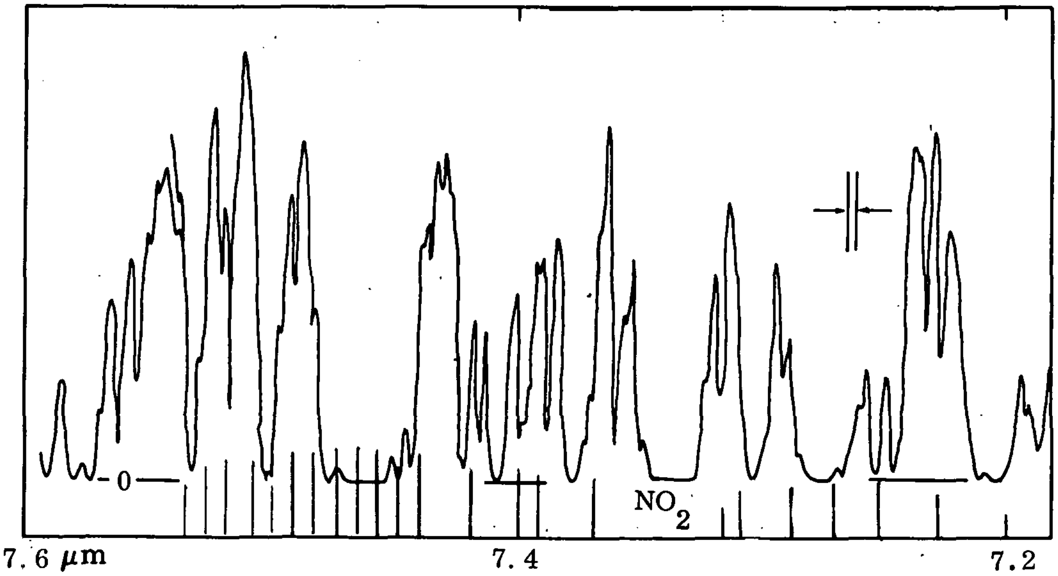

Figure A-12. Solar Spectrum Between 7.2 and 7.6μm (from ref. 173)

A-5. Nitric Oxide

Because of the unpaired electron, the ground electronic state of NO is a $^2\Pi$ state. The two levels $^2\Pi_{1/2}$ and $^2\Pi_{3/2}$ describe the state of the molecule, and divide the band into two sub-bands. Each line of the band is further split in two by Λ-doubling.

In fig. A-13 we compare our calculated and the measured spectrum (ref. 176) of the $R(5\text{-}1/2)_{1/2}$ and $R(5\text{-}1/2)_{3/2}$ lines. Unfortunately, this band is heavily overlapped by water vapor, as demonstrated in a measured spectrum (ref. 175) shown in fig. A-14. The H_2O lines apparent in the trace labeled "Empty Cell" are presumably from the unflushed optical path, from the light source to the detector. Assuming a geometrical length of about 3m and a relative humidity of about 60% at room temperature, the optical thickness of the water vapor becomes about 4×10^{-3} pr cm or 5 atm-cm, which is 16 times the optical thickness of NO in the 10 cm cell. In the troposphere, the ratio of H_2O to NO is more like 10^6, which provides a severe limitation on the measurement of NO. The conditions for observing the first overtone of NO are even worse, because the weak 0-2 band is located in the strong 2.7-μm bands of water vapor and carbon dioxide.

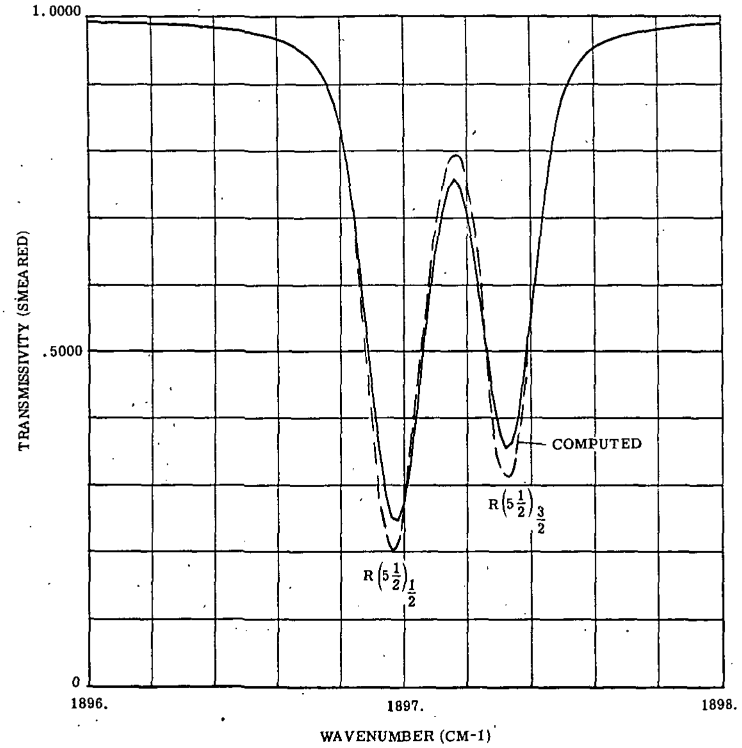

Figure A-13. Degraded NO transmissivity (slit width is 0.13 cm^{-1} for u = 0.263 cm-atm, p = 200 torr and T = 300 K) (calculated spectrum solid, laboratory spectrum (ref. 176) dashed)

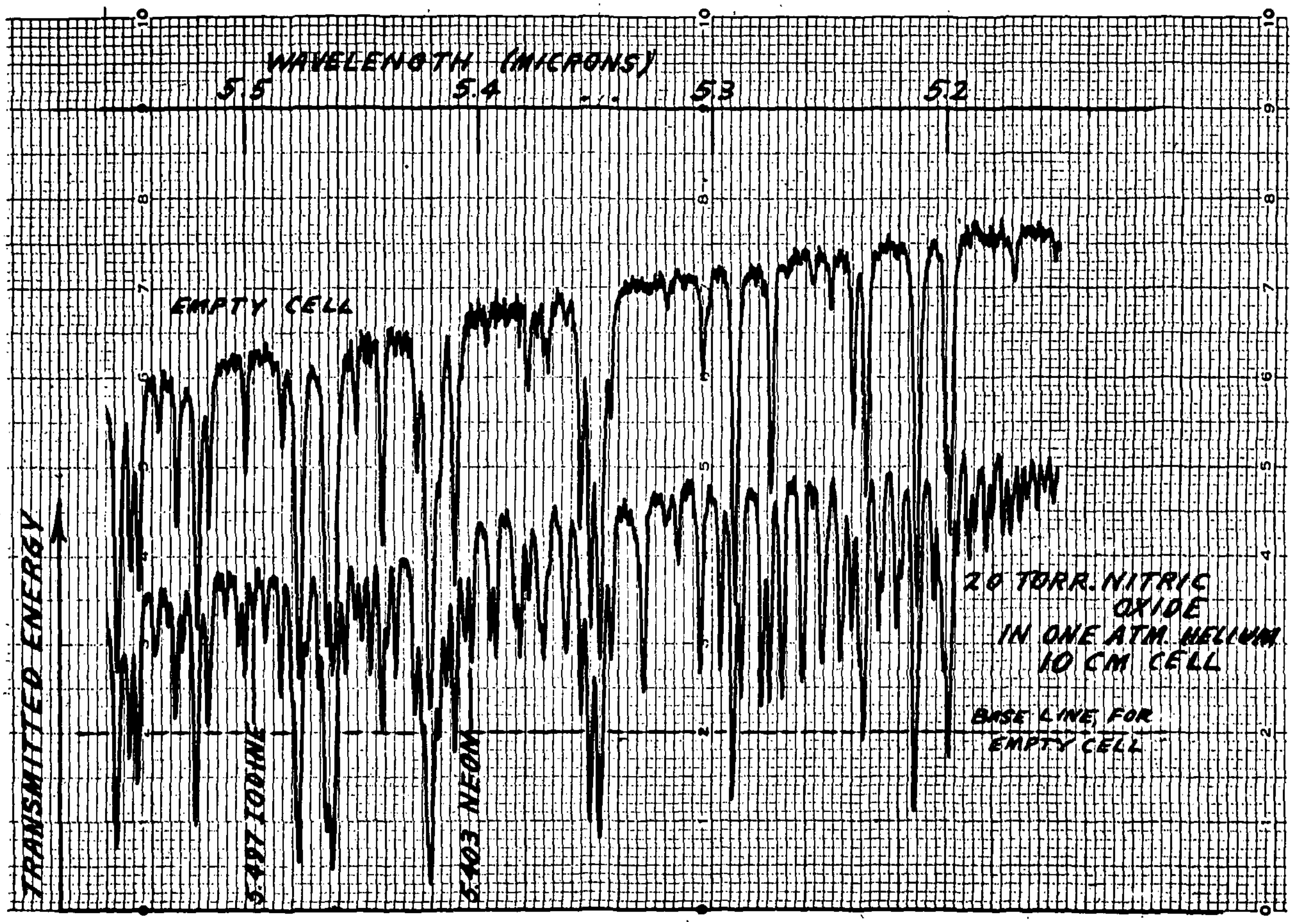

Figure A-14. Laboratory Spectrum of the Fundamental Band of NO (ref. 175) and Water Lines

A-6. Nitrous Oxide

Because this molecule exists in the "clean" atmosphere and its many rotation-vibration bands interfere with the measurement of many pollutant bands, the line parameters have to be known.

The parameters for 976 lines were generated (ref. 61) for the ν_3 band, the wing of which overlaps the CO fundamental band. The computed wavenumbers were compared with the solar spectrum of Migeotte et al. (ref. 165); of 201 measured lines being compared, 179 lines are found to be within 0.05 cm^{-1}, 199 within 0.1 cm^{-1}, and the worst discrepancy is 0.18 cm^{-1}.

A spectrum generated by computer is compared in fig. A-15 with a laboratory spectrum measured by Plyler et al. (ref. 177). The band strength of 1920 (cm^{-2} atm^{-1} STP) was adopted from Yale et al (ref. 178). The apparent inconsistencies at 2204.2 cm^{-1} and 2205.8 cm^{-1} are believed to be due to measurement noise.

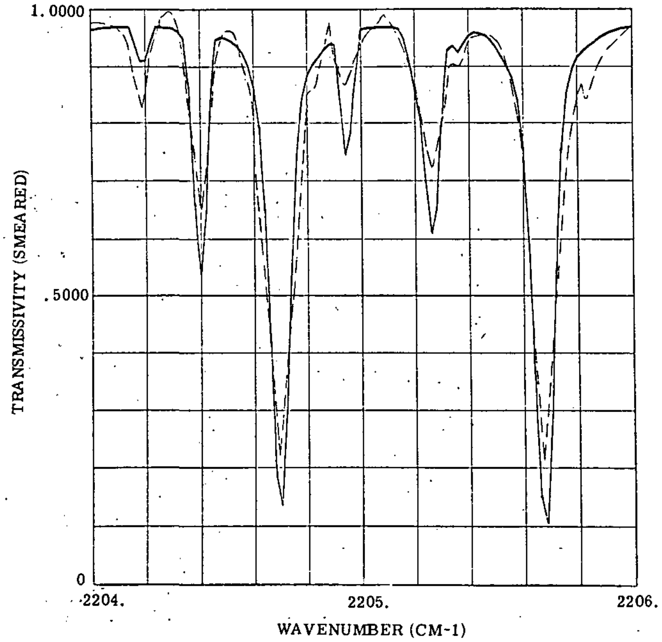

Figure A-15. Degraded N_2O transmissivity (slit width of 0.05 cm^{-1}) between 2204 and 2206 cm^{-1} for u = 0.31 cm atm, p = 2 torr and T = 220 K (calculated spectrum solid, laboratory spectrum (ref. 177) dashed)

The nitrous oxide vibration-rotation bands which overlap bands of other species SO_2 (4.0μm, 8.6μm), NO_2 (7.6μm), NH_3 (3.0μm, 10.5μm) include the following transitions: $\nu_1 + 2\nu_2$, $2\nu_1$, $2\nu_2 + \nu_3$, $\nu_1 + \nu_3$, and $2\nu_2$. All of the bands mentioned above are parallel bands. The program used to generate the line parameters of the 4.5μm band was applied directly to generate the same line parameters of these bands. Of the ν_1 and $2\nu_2$ transitions, molecular constants are available from the solar spectrum of Migeotte et al. (ref. 165). For the ν_1 transition, the line parameters were accurately reproduced. However, for the $2\nu_2$ transition, there were apparently misprints in the molecular constants, and a curve-fitting technique was applied to improve the computed values.

The molecular constants for the rest of the transitions mentioned above are available from the data of Tidwell et al. (ref. 179). They also computed the line positions and compared them with their observations. We are able to reproduce their computed values with a typical accuracy of about 0.01 cm^{-1}.

A total of 1308 lines were computed for all transitions. The band strengths were taken from Goody (ref. 180) except for one transition $(2\nu_2 + \nu_3)$ whose value was not available and was estimated.

A-7. Ammonia

An effective representation of the NH_3 10.5-μm band system has been produced. We have compared the calculated locations of some of the 1050 lines generated with the locations measured by Garing et al. (ref. 181). Of 463 measured lines, 188 are found to be within 0.1 cm^{-1}, 351 within 0.5 cm^{-1}, and 415 within 1.0 cm^{-1}. The smallest discrepancies are quite strongly correlated with the most intense (the most important) lines.

Further verification of the generated data is provided by comparison with a laboratory spectrum taken by France and Williams (ref. 182). The authors did not state the slit width that they used; we assumed 8 cm^{-1}.

The comparison is quite good as seen in fig. A-16. The presentation of the spectrum in France and Williams' paper is extremely small and their wavenumber scale cannot be read to an accuracy of better than 2 or 3 cm^{-1}. The comparison might be improved by assuming a slightly narrower slit width or a more realistic slit function than the assumed triangular shape.

This band is located in the least-interfered region of the atmospheric spectrum as is seen in fig. A-17.

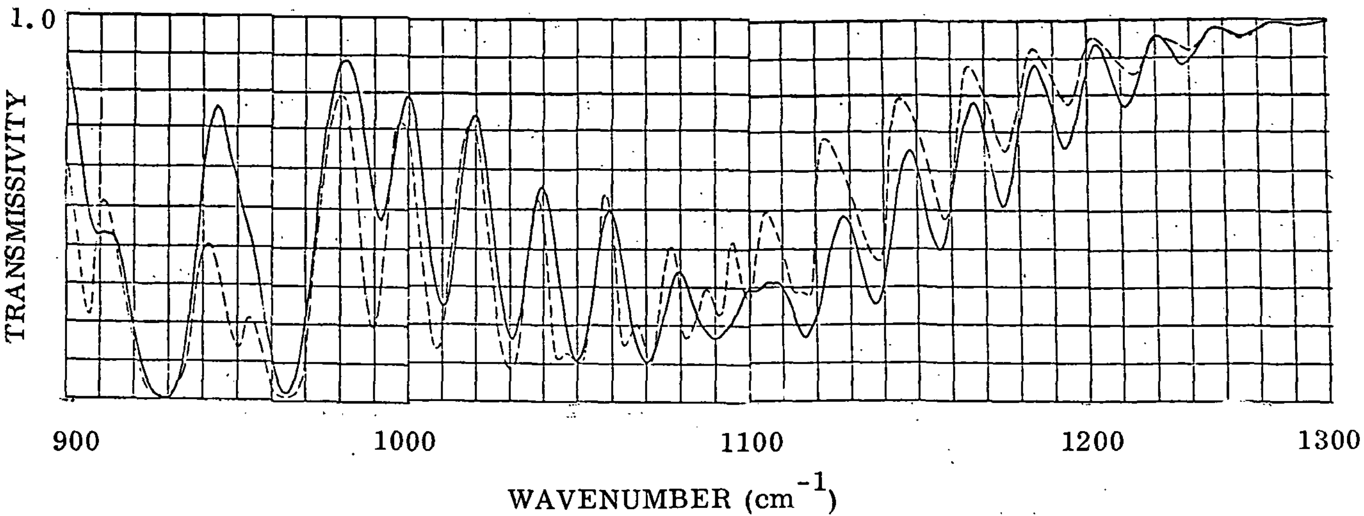

Figure A-16. Degraded transmissivity (slit width of 8 cm^{-1}) of a portion of the 10.5-μm band system of NH_3 between 900 and 1300 cm^{-1} for u = 1.617 cm atm_{STP}, p_e = 4185 torr and T = 299°K (calculated spectrum solid, laboratory spectrum (ref. 182) dashed)

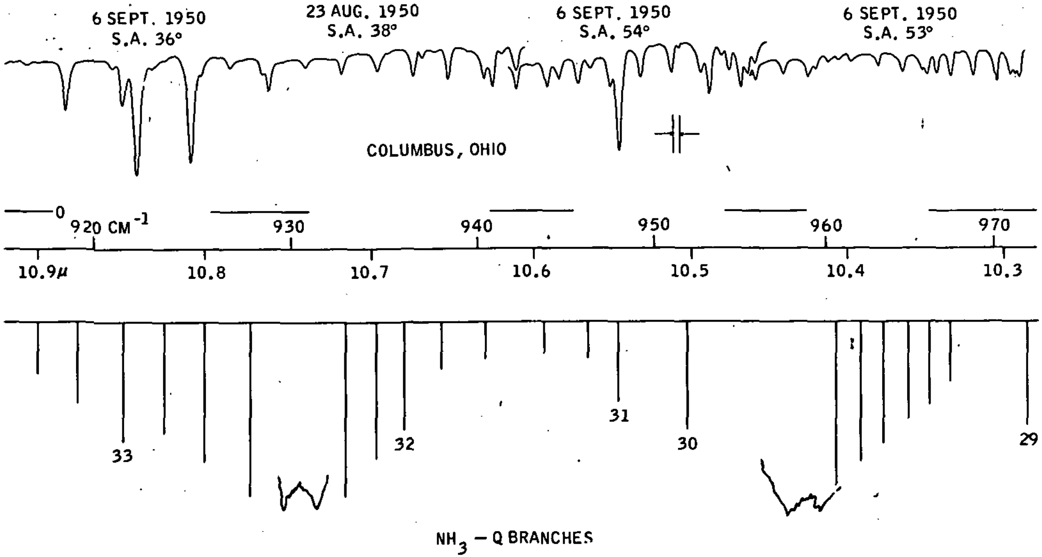

Figure A-17. Solar Spectrum Between 920 cm^{-1} and 970 cm^{-1} (ref. 173) and the Location of the Q-branches of NH_3

The same version of the computer program used to generate the spectral data for the 10-μm(ν_2) ammonia band has been applied to generate data for the 3-μm (ν_1) region (ref. 61). The molecular constants were taken from the experimental data of Benedict et al. (ref. 183), and the generated line positions were compared with their observations. 1015 lines were recorded on the magnetic tape. Of 257 observed lines compared, 195 were found to be within 0.5 cm^{-1}, 225 with 1 cm^{-1}. The comparison shows the agreement being as good as that in the 10-μm band.

The ammonia 2.3-μm region consists of a parallel band $\nu_1 + \nu_2$ ($\nu_0 = 4293.716$ and 4320.06 cm^{-1}) and a perpendicular band $\nu_2 + \nu_3$ ($\nu_0 = 4416.908$ and 4434.610 cm^{-1}). The band strengths of the parallel and perpendicular bands which are 2.9 and 19.7 (cm^{-2} atm^{-1} STP), respectively, were taken from a detailed study of these bands performed by Benedict et al. (ref. 184). The set of molecular constants presented by them has been used to reproduce the parameters of 3007 lines. Unfortunately, the generated data do not reproduce their computed values to the same degree of accuracy achieved in the other NH_3 bands. The reason for these discrepancies is not presently apparent.

A-8. Formaldehyde

The formaldehyde molecule HCHO, which is an asymmetric top, has been modeled (ref. 61). The asymmetry parameter κ is nearly -1 (-.9623), so that HCHO does not deviate greatly from being a symmetric top.

There is a great lack of quantitative spectra for making comparisons. Herzberg (ref. 185) shows a spectrum taken by Nielsen (ref. 186), but the experimental conditions specified are clearly incorrect. A recent spectrum taken by Hanst (ref. 175) with a resolution of apparently better than 1 cm^{-1} is shown in fig. A-18. The Nielsen and Hanst spectra do not seem to be completely consistent, even allowing for the difference in resolution.

A sample portion of the calculated high-resolution HCHO spectrum is shown in fig. A-19. The large absorption peaks are Q-branches, which are well reproduced in wavenumber location. The finer R-branch structure in between the Q-branch peaks is also approximately reproduced. No attempt was made to match the resolution of the Hanst spectrum, which is also shown in fig. A-19 for comparison.

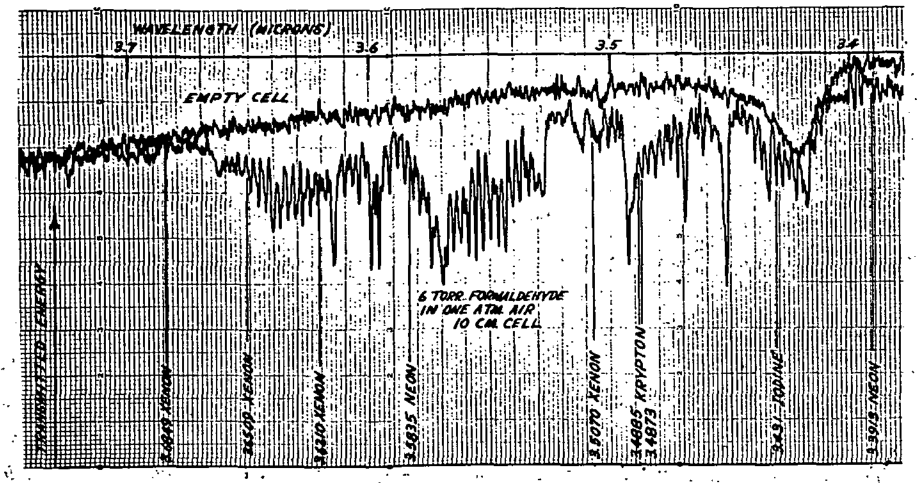

Figure A-18. Laboratory Spectrum of HCHO at 3.5μm (from ref. 175)

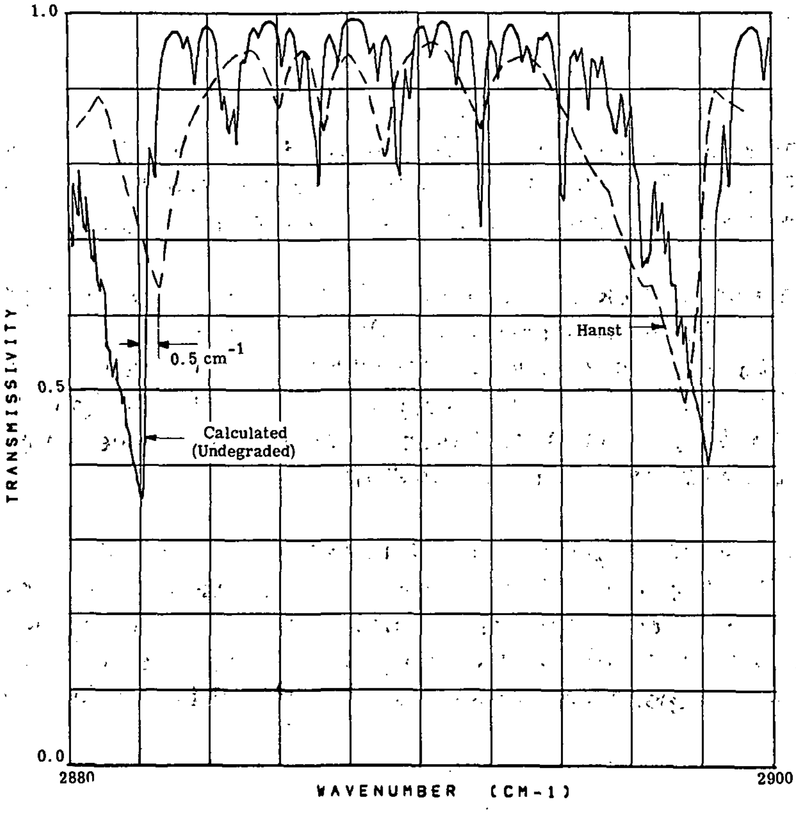

Figure A-19. Monochromatic transmissivity (calculated) of HCHO between 2880 and 2900 cm^{-1} (solid curve). Degraded transmissivity (measured by Hanst (ref. 175)) for u = 0.08 cm atm, p = 6 torr and T = 300K (dashed curve)

A-9. Methane

Methane is a spherical top molecule, and it is this fact which results in considerable complication in calculating its spectrum. The symmetric top approximation predicts that all rotational levels of the same J value will have the same energy level. This increased degeneracy results in the appearance of higher-order perturbations which separate the energy levels in a manner difficult to treat analytically. First-order corrections were incorporated into the program and used to generate the correct total strength and spectral location of the unsplit P- and R-branch lines from 2870 to 3170 cm^{-1}. The problem remaining is that of representing the fine structure of these "lines" which are split into several components because of the molecular symmetry; approximate expressions for this splitting will be developed in future work. The appearance of methane in the solar spectrum is shown in fig. A-20.

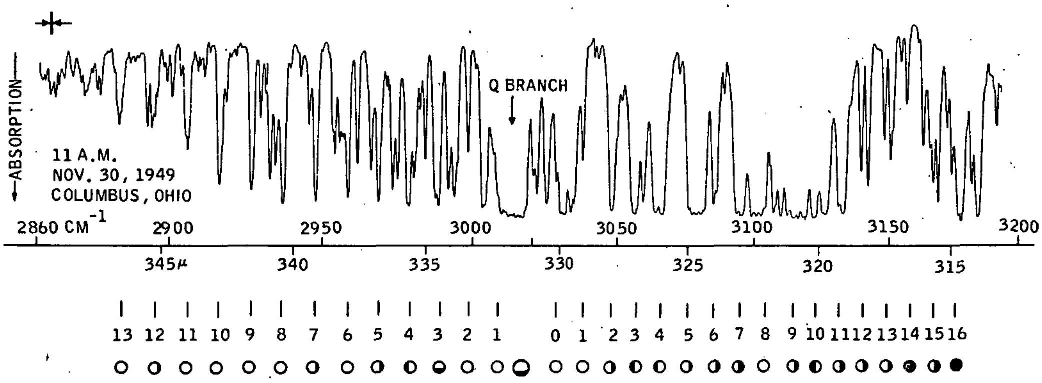

Figure A-20. Solar Spectrum Between 2860 and 3200 cm^{-1} (ref. 166).

APPENDIX B

SCATTERING THEORY

B-1. Scattering Terminology and Notation

Notation and terminology used in Rayleigh and Mie scattering theory are not standardized and different authors may use conflicting notation. The notation used here has been selected for compatibility with other systems, as well as for internal logic and consistency.

The following notation for several commonly used parameters will be followed throughout:

$m = n_1 - in_2$ = complex index of refraction

R = distance of observer from scattering particle

r = radius of particle

λ = wavelength of radiation

$k = 2\pi/\lambda$

$a = 2\pi r/\lambda$ ($=kr$) = size parameter

The three points representing the source, the scattering center, and the observer define a plane (in general) called the "plane of scattering." The intensity of radiation scattered depends on the polarization of the incident radiation (whether polarized (1) perpendicular to the plane or (2) parallel to the plane of scattering). Even if the incident radiation is unpolarized, the scattered radiation is, in general, partly polarized.

The <u>scattering cross section</u> σ_s of a particle is defined as follows: If I_0 is the intensity of incident radiation (units of power/area) and P_s is the total power scattered by the particle (units of power), the scattering cross section σ_s (units of area) is defined by

$$P_s = \sigma_s I_0 \tag{B-1}$$

If the volume density of scattering centers is N, an "attenuation coefficient for scattering" γ_s may be defined:

$$\gamma_s = N\sigma_s \tag{B-2}$$

If only single scattering is important, the attenuation of a beam of light passing through a scattering (but non-absorbing) medium a distance ℓ is described by

$$I = I_0 \exp\left(-\gamma_s \ell\right) \tag{B-3}$$

When multiple scattering becomes important, some radiation which has been scattered out of the incident light beam will be scattered back into it; thus the observed intensity will be greater than that indicated by the preceding equation.

If the intensity at distance R of radiation scattered at an angle θ is given by $I_s(\theta, R)$, the <u>angular scattering cross section</u> $\sigma_s(\theta)$ (sometimes called the differential scattering cross section) is defined by

$$I_s(\theta, R)\, R^2 d\Omega = \sigma_s(\theta)\, I_0\, d\Omega \tag{B-4}$$

The differential and total scattering cross sections are related by

$$\sigma_s = \int \sigma_s(\theta)\, d\Omega = 2\pi \int_0^{\pi} \sigma_s(\theta) \sin\theta\, d\theta \tag{B-5}$$

If the particle is spherical with radius r, a convenient dimensionless quantity, the "efficiency factor for scattering," may be defined as the ratio of the scattering cross section to the geometrical cross section πr^2:

$$Q_s = \sigma_s / \pi r^2 \tag{B-6}$$

Similar definitions are made for the cross sections and efficiency factors for absorption (referring to radiation actually absorbed by the particle) and extinction (referring to radiation removed from the path of a light ray) by both absorption and scattering. These quantities are related by

$$\sigma_e = \sigma_a + \sigma_s$$

and

$$Q_e = Q_a + Q_s \tag{B-7}$$

I_0 is polarized with components I_{01} and I_{02}, perpendicular and parallel to the plane of scattering, respectively; thus

$$I_0 = I_{01} + I_{02}$$

and for unpolarized radiation:

$$I_{01} = I_{02} = \frac{1}{2} I_0 \tag{B-8}$$

A similar convention is applied to the components of the scattered radiation:

$$I_s(\theta) = I_{s1}(\theta) + I_{s2}(\theta) \tag{B-9}$$

The "intensity functions" i_1 and i_2 comprise a set of functions which are very commonly used, and are defined as follows:

$$\left.\begin{aligned} I_{s1}(\theta) &= \left(k^2R^2\right)^{-1} I_{01}\, i_1(a, m, \theta) \\ &\text{and} \\ I_{s2}(\theta) &= \left(k^2R^2\right)^{-1} I_{02}\, i_2(a, m, \theta) \end{aligned}\right\} \tag{B-10}$$

Since i_1 and i_2 are, in general, different, the scattered radiation is polarized to some extent, even if the source is unpolarized. If the source is assumed unpolarized, and the total scattered radiation (independent of its state of polarization) is measured, the two previous equations may be combined:

$$I_s(\theta, R) = \left(k^2R^2\right)^{-1} \frac{1}{2} I_0 \left[i_1(a, m, \theta) + i_2(a, m, \theta)\right]$$

or

$$I_s(\theta, R) = \left(k^2R^2\right)^{-1} I_0\, i(a, m, \theta) \tag{B-11}$$

where

$$i(a, m, \theta) = \frac{1}{2}\left[i_1(a, m, \theta) + i_2(a, m, \theta)\right]$$

The angular scattering cross section and the intensity functions are thus related by

$$\sigma_s(k, a, m, \theta) = k^{-2} \frac{1}{2}\left[i_1(a, m, \theta) + i_2(a, m, \theta)\right] \tag{B-12}$$

The intensity functions i_1 and i_2 are generally used, rather than σ_s, because they are functions of $a = 2\pi r/\lambda$, in the Mie theory, and not of r and λ separately (or, equivalently, k and a), as is σ_s.

B-2. Rayleigh Scattering

Rayleigh scattering is a special case of Mie scattering (the limiting case for sufficiently small particle size/wavelength ratio). Since Rayleigh scattering by atmospheric molecules always occurs, and since the equations for Rayleigh scattering are much simpler in form than for Mie scattering, a separate section is devoted to Rayleigh scattering.

According to Penndorf (ref. 187), Rayleigh scattering may be used for particles of radius less than 0.03 μm for radiation of $\lambda = 1 \mu$m (for $r \leq 0.03\lambda$, in general), with an error of $\leq 1\%$.

In the Rayleigh limit of small $a = 2\pi r/\lambda$ and small $|m|\,a$, the intensity functions are found to be

$$i_1 = \left|\frac{m^2 - 1}{m^2 + 2}\right|^2 a^6$$

and

$$i_2 = \left|\frac{m^2 - 1}{m^2 + 2}\right|^2 a^6 \cos^2\theta \qquad \text{(B-13)}$$

Thus, the radiation polarized perpendicular to the plane of scattering is scattered isotropically, whereas the radiation polarized parallel to the plane of scattering is scattered preferentially toward the forward and backward directions.

The angular scattering cross section is therefore given by

$$\sigma_s(\theta) = \left|\frac{m^2 - 1}{m^2 + 2}\right|^2 \frac{(2\pi)^4 r^6}{\lambda^4} \frac{1}{2} \left(1 + \cos^2\theta\right) \qquad \text{(B-14)}$$

in which form the familiar λ^{-4} law of scattering is evident.

For scattering by molecules, it is convenient to express the scattering in terms of either the mean molecular polarizability or the index of refraction of air. Since the scattering centers (primarily N_2 and O_2 molecules) are not spherically symmetric, their polarizability is not isotropic. As a result, initially polarized light is no longer completely polarized after scattering, and the relationships previously given for small spheres do not apply precisely (see ref. 58).

The scattering cross section for a single molecule is given by

$$\sigma_s = \frac{8\pi}{3} k^4 \alpha^2 f \tag{B-15}$$

where α is the mean polarizability, and the factor f differs slightly from unity because of the nonisotropic polarizability.

By use of the relationship between the index of refraction of the air and the molecular polarizability, the attenuation coefficient for scattering by air can be written

$$\gamma_s = \frac{2k^4}{3\pi} \frac{\left(m_a - 1\right)^2}{N_s} f \tag{B-16}$$

where, for air, $f = 1.054$. The apparent inverse dependence of γ_s on the air molecule number density N_s is deceptive; since $m_a - 1$ is proportional to N_s, γ_s is directly proportional to N_s, consistent with Eq. (B-2).

B-3. Mie Scattering

The Mie theory assumes that the scattering particle is a homogeneous sphere of radius r with a complex index of refraction $m = n_1 - in_2$. Equations for a spherical wavefront emanating from the particle are found by matching boundary conditions inside and outside the surface of the spherical particle. The equations presented here are formal; actual calculations would utilize other forms more convenient for computation, involving recursion relations between the coefficients of the infinite series.

The intensity functions i_1 and i_2 are given by the following:

$$i_1 = \left| \sum_{n=1}^{\infty} \frac{2n+1}{n(n+1)} \left(a_n \pi_n + b_n \tau_n\right) \right|^2$$

and

$$i_2 = \left| \sum_{n=1}^{\infty} \frac{2n+1}{n(n+1)} \left(a_n \tau_n + b_n \pi_n\right) \right|^2 \tag{B-17}$$

The functions π_n and τ_n depend on the scattering angle θ as follows:

$$\pi_n = \frac{d}{dz} P_n(z)$$

$$\tau_n = z\,\pi_n - \left(1-z^2\right) \frac{d}{dz}\,\pi_n \qquad \text{(B-18)}$$

where $z = \cos\theta$, and $P_n(z)$ is the Legendre polynomial

$$P_n(z) = \left(2^n n!\right)^{-1} \frac{d^n}{dz^n} \left(z^2-1\right)^n$$

The Mie coefficients a_n and b_n are functions of a and m, as follows:

$$a_n = \frac{\psi_n(a)\,\psi_n'(ma) - m\psi_n'(a)\,\psi_n(ma)}{\zeta_n(a)\,\psi_n'(ma) - m\zeta_n'(a)\,\psi_n(ma)}$$

and

$$b_n = \frac{m\,\psi_n(a)\,\psi_n'(ma) - \psi_n'(a)\,\psi_n(ma)}{m\zeta_n(a)\,\psi_n'(ma) - \zeta_n'(a)\,\psi_n(ma)} \qquad \text{(B-19)}$$

where ψ_n and ζ_n are Ricatti-Bessel functions:

$$\psi_n(z) = \left(\frac{\pi z}{2}\right)^{1/2} J_{n+\frac{1}{2}}(z) = z^{n+1} \left(-\frac{1}{z}\frac{d}{dz}\right)^n \frac{\sin z}{z}$$

and

$$\zeta_n(z) = \left(\frac{\pi z}{2}\right)^{1/2} H^{(2)}_{n+\frac{1}{2}}(z) = iz^{n+1} \left(-\frac{1}{z}\frac{d}{dz}\right)^n \frac{\exp(-iz)}{z}$$

and primes indicate derivatives. Highly efficient methods have been developed for calculating the Mie coefficients.

In the Rayleigh limit (small a and $|m|a$), the coefficient a_1 becomes dominant, producing the results previously presented. However, for general calculations in the Mie region, very large numbers of coefficients may have to be computed to achieve acceptable accuracy.

The scattering cross section, in terms of the Mie coefficients, is given by

$$\sigma_s = \frac{\lambda^2}{2\pi} \sum_{n=1}^{\infty} (2n+1)\left(\left|a_n\right|^2 + \left|b_n\right|^2\right) \tag{B-20}$$

The cross section for extinction is given by

$$\sigma_e = \frac{\lambda^2}{2\pi} \sum_{n=1}^{\infty} (2n+1)\, \mathrm{Re}\left(a_n + b_n\right) \tag{B-21}$$

When the index of refraction is real, $\sigma_s = \sigma_e$; in fact, $\mathrm{Re}(a_n) = \left|a_n\right|^2$ and $\mathrm{Re}(b_n) = \left|b_n\right|^2$, so that the series are equal, term by term.

B-4. Representation of the Radiation Field

When radiation is scattered it generally becomes polarized to some extent. In order to describe a general radiation field, four parameters should be specified to give the intensity, the degree of polarization, the plane of polarization, and the ellipticity of the radiation at each point and in any given direction. An elegant method of completely characterizing polarized light by a set of four parameters was developed by Stokes in 1852.

A brief discussion of the Stokes parameters is given below. For a complete discussion the reader is referred to Chandrasekhar (ref. 93) and van de Hulst (ref. 58).

The most general polarization of a simple wave is elliptical. The polarization is defined in terms of the intensities of the two components along the major and minor axis of the ellipse. Let $\vec{\ell}$ and $\vec{r}$ be two unit vectors forming an orthogonal set with $\vec{s}$, the direction of propagation.

A simple electromagnetic wave representing a single coherent wave train is characterized by electric and magnetic vectors $\vec{E}$ and $\vec{H}$. These are uniquely related, so that the wave may be represented without loss of generality by the electric vector only:

$$E = \mathrm{Re}\left[E_\ell \vec{\ell} + E_r \vec{r}\right] \tag{B-22}$$

where E_ℓ and E_r are complex, oscillating functions. The Stokes parameters I, Q, U, and V are real quantities defined by

$$I = E_\ell E_\ell^* + E_r E_r^* \tag{B-23a}$$

$$Q = E_\ell E_\ell^* - E_r E_r^* \tag{B-23b}$$

$$U = E_\ell E_r^* + E_r E_\ell^* \tag{B-23c}$$

$$V = i\left(E_\ell E_r^* - E_r E_\ell^*\right) \tag{B-23d}$$

These four parameters are not independent, being related by;

$$I^2 = Q^2 + U^2 + V^2 \tag{B-24}$$

Normal light consists of a large number of such simple waves with independent phases. The Stokes parameters for a beam of light are defined by

$$I = \Sigma I_i, \text{ etc.}$$

where i denotes the individual simple wave. For such a beam of light the following relationship holds

$$I^2 \geq Q^2 + U^2 + V^2 \tag{B-25}$$

The equality is true only for fully polarized light. For partially polarized light the inequality holds; in the case of natural (unpolarized) light $Q = U = V = 0$.

B-5. Scattering Functions

Following the notation of van de Hulst (ref. 58), the amplitude and phase of a spherical light wave scattered by a single particle may be represented by

$$u = S(\theta, \varphi) \frac{e^{-ikR + ikz}}{ikR} u_0 \tag{B-26}$$

where $S(\theta, \varphi)$ is the complex amplitude function of the scattering particle.

A more general formulation must include polarization effects. Let the components of the electric vector be $E_{\ell 0}$ and E_{r0} for the incident wave, and E_ℓ and E_r

for the scattered spherical wave, and since a linear relationship exists between incident and scattered amplitudes according to Maxwell's equations, Eq. (B-26) may be replaced by

$$\begin{pmatrix} E_\ell \\ E_r \end{pmatrix} = \frac{e^{-ikR+ikz}}{ikR} \begin{pmatrix} S_2 & S_3 \\ S_4 & S_1 \end{pmatrix} \begin{pmatrix} E_{\ell 0} \\ E_r \end{pmatrix} \tag{B-27}$$

The matrix $\begin{pmatrix} S_2 & S_3 \\ S_4 & S_1 \end{pmatrix}$ is the amplitude scattering matrix; the numbering of the elements follows established usage.

For spherical homogeneous particles an important simplification is that $S_3 = S_4 = 0$, so that

$$E_\ell = S_2(\theta) \frac{e^{-ikR + ikz}}{ikR} E_{\ell 0} \tag{B-28a}$$

$$E_r = S_1(\theta) \frac{e^{-ikR+ikz}}{ikR} E_{r0} \tag{B-28b}$$

By taking the squares of the moduli we obtain for perpendicular polarization:

$$I = \frac{i_1 I_0}{k^2 R^2} \tag{B-29a}$$

and, for parallel polarization:

$$I = \frac{i_2 I_0}{k^2 R^2} \tag{B-29b}$$

where $i_1 = |S_1(\theta)|^2$ and $i_2 = |S_2(\theta)|^2$ are the intensity functions discussed in Section 4.1.4.

In the case of a beam of light passing through an optical system, such as an atmosphere, a cloud of particles or simply an optical instrument, the Stokes parameters of the emerging beam (I, Q, U, V) are related to the Stokes parameters of the incident beam (I_0, Q_0, U_0, V_0) by a linear transformation:

$$\begin{pmatrix} I \\ Q \\ U \\ V \end{pmatrix} = F \cdot \begin{pmatrix} I_0 \\ Q_0 \\ U_0 \\ V_0 \end{pmatrix} \tag{B-30}$$

where F is a matrix of 16 coefficients, each of which is a real number. For an arbitrary cloud of particles, the matrix contains 16 independent constants. For special cases, the number of independent constants is reduced; for example, for a single particle the number is 7, and for a spherical homogeneous particle there are only 3 independent constants.

B-6. Relationship of Aerosol Optical Thickness and Aerosol Mass Loading

The aerosol mass loading of the atmosphere is used by the Air Pollution Control Office as one of the parameters to characterize local air quality. Thus, it is desirable to determine a relationship between the optical thickness and the mass loading of the aerosol content.

The mass loading M ($\mu g/m^3$) has been found by Charlson et al. (ref. 188) to be related empirically to the total scattering coefficient γ (m^{-1}) for air at 0.5 μm by

$$M = 3.8 \times 10^5 \gamma \tag{B-31}$$

The total scattering coefficient, γ, is the sum of the aerosol and molecule scattering coefficients, γ_A and γ_R, respectively; i.e.,

$$\gamma = \gamma_A + \gamma_R \tag{B-32}$$

As a result of Eq. (B-32), care must be taken in using Eq. (B-31) since it does not yield a zero value of M when there are no particles, i.e., when $\gamma_A = 0$. This does not cause a problem at the surface where $\gamma_R < \gamma_A$, but at higher altitudes, where $\gamma_R > \gamma_A$, large errors occur in using Eq. (B-31). This problem is overcome by replotting M, given by Eq. (B-31), against γ_A to obtain, for a wavelength of 0.5 μm,

$$M = 4.2 \times 10^5 \gamma_A \ \mu g/m^3 \tag{B-33}$$

This equation gives the same value of M for a clear atmosphere with 25-km visibility, defined by Elterman (ref. 57) where

$$\gamma_A = 1.67 \times 10^{-4} \mathrm{m}^{-1} \quad \text{and} \quad \gamma = 1.84 \times 10^{-4} \mathrm{m}^{-1}$$

at the surface; for more turbid atmospheres, it gives M about 10% larger than Eq. (B-31).

The independence of M with respect to σ_R allows the vertical mass loading (M_v) to be obtained by integrating Eq. (4-35) over altitude:

$$M_v = \int_0^\infty M\,dh = 4.2 \times 10^5 \int_0^\infty \gamma_A\,dh$$

$$M_v = 4.2 \times 10^5 u_A \ \mu g/m^2 \tag{B-34}$$

where u_A is the aerosol optical thickness of the atmosphere for unit air mass. A detailed discussion of this relationship is given by Griggs (ref. 190).

Eq. (B-34) allows the optical thickness determined by the satellite observations (and by the Volz sun photometer) to be translated into a vertical mass loading and used on a global basis to estimate the total mass of aerosols suspended in the earth's atmosphere.

Eq. (B-34) gives a value of M greater than that given by a theoretical relationship derived earlier by McCormick and Baulch (ref. 189), but the present relationship is preferred since it is based upon direct nephelometer observations that agree with other independent observations.

B-7. The Detection of Cirrus Clouds by Lidar

Cirrus clouds are of concern for satellite optical probing of the atmosphere, particularly in earth-oriented tropospheric observations, since existing techniques do not always detect the presence of these clouds, which may well influence measurements in the infrared region. Recent work (ref. 116) suggests that lidar observations from satellites might detect most cirrus clouds of importance. Another study (ref. 107) demonstrates that far-infrared wavelengths near 50 μm and 120 μm may be used to measure the cirrus cloud emission and to deduce the cloud thickness.

The available information on cirrus clouds suggests that the ice crystals are mostly hexagonal prisms or plates up to several hundred μm in length and about fifty μm wide. The axes of these prisms or plates are generally oriented randomly, although evidence exists that they sometimes have a preferred vertical orientation (ref. 191). The scattering properties of the cirrus cloud particles appear to be equivalent to spheres having radii in the range of 10 to 100 μm with a mean radius of about 40 μm (ref. 107, 116). Particle concentrations range from about 10^5 m^{-3} for clouds which are just visible up to about $10^7 m^{-3}$ for dense cirrocumulus (ref. 192).

Cirrus clouds are confined to the troposphere and most of the time are below 30, 000 ft, with thicknesses up to 20, 000 ft on occasions (ref. 193). It has been estimated (ref. 192) that between latitudes 50° and 70° N cirrus clouds occur 35% of the time.

The optical thickness of cirrus clouds depends on the wavelength of observation, and varies with the particle concentration in the cloud. Hansen and Pollack (ref. 194) used measured values of cloud reflectance in the 1. 2- to 2. 5-μm region to deduce that dense cirrus clouds have an optical depth $\tau \geq 10$ which is equivalent to being essentially opaque. In the 8-to 13-μm region Valovcen (ref. 192) found that cirrus transmission varied widely over the range 0. 05 to 1. 0.

Analysis of the lidar return signal enables the height of the cloud and optical thickness to be determined if the ratio of backscattering to extinction coefficients is assumed constant (ref. 116). A useful concept in considering cirrus cloud effects on lidar systems is the "backscattering optical thickness" (u_β) introduced by Evans (ref. 116), viz.,

$$u_\beta = \int_0^L \beta \, d\ell \qquad \text{(B-35)}$$

where β is the average volume backscattering coefficient and L is the thickness of the cloud.

In a lidar measurement program Evans found typical medium visibility cirrus to be about 1 km thick, with a transmission of about 80% and $u_\beta = 0.1$ for 0. 7-μm radiation. For a 3 km cloud, the transmission was 8% with $u_\beta = 1.0$. It was found that for detection in satellite photographs, cirrus clouds must have $u_\beta \geq 0.2$, whereas visual detection from the ground requires only $u_\beta \geq 0.01$ under good daylight conditions, and $u_\beta \geq 0.1$ at night with a full moon.

APPENDIX C

OPTICAL CORRELATION THEORY

If the spectral transmissivity $\tau_i(\omega)$ is written as a product of two components, $\tau_j(\omega)$ and $\tau_k(\omega)$, due to species j and k, the mean transmissivity is given by

$$\overline{\tau}_i = \overline{\tau_j \tau_k} \tag{C-1}$$

in which the latter term is specifically the mean of the product. Under many conditions, it is found that the mean of the product equals the product of the means:

$$\overline{\tau_j \tau_k} = \overline{\tau}_j \overline{\tau}_k \tag{C-2}$$

This result is valid, for example, if one of the τ's is constant over the interval, or if the τ's result from line spectra in which the lines in one spectrum are randomly located with respect to the lines in the other spectrum. This result has been obtained theoretically and has been verified experimentally for a number of different spectra (ref. 195).

Equation (C - 2) notably is <u>not</u> valid when τ_j and τ_k result from the line spectra of two samples of the same gas and it is this fact on which the GFC principle is based. In this case there is a complete coincidence between line locations in the two spectra, under which conditions it is usually found that

$$\overline{\tau_j \tau_k} > \overline{\tau}_j \overline{\tau}_k \tag{C-3}$$

When the two gases are different, the equality will generally be valid to a very close approximation, although experimental or theoretical verification is desirable for particular gases and spectral regions. For example, for two gases with overlapping absorption bands, it may be possible to find an accidental near-coincidence of spectral lines in some small region.

If two spectra have the property that $\overline{\tau_i \tau_j} = \overline{\tau}_i \overline{\tau}_j$, these spectra will be referred to as "uncorrelated." (This is the case, as previously mentioned, if the lines of one spectrum are randomly located with respect to the lines in the second spectrum.)

If $\overline{r_i r_j} > \bar{r}_i \, \bar{r}_j$, the spectra will be called "correlated." (This is interpreted to mean a greater-than-random overlapping of the lines of i and j on one another.) In general, for the spectra of different gases, this inequality is expected to be quite weak. If the spectra result from the same gas, the coincidence of lines is complete, and the inequality is quite significant. In the event that $\overline{r_i r_j} < \bar{r}_i \, \bar{r}_j$, the spectra will be said to be "negatively correlated." (This is interpreted to mean a less-than-random overlapping of the lines of the two spectra.) In general, such an inequality will be expected to be quite weak.

APPENDIX D

BAND MODELING

In this Appendix we present a set of band model parameters for pollutant and interfering molecules, which were derived (a) from calculated line parameters, (b) from laboratory data, and (c) from band modeling procedures. The band model parameters under (a) were generated under contract NAS1-11111 for molecules CO_2, CO, NO_2, NO, N_2O, SO_2, NH_3, and HCHO and are averaged here for wavenumber intervals of 5 and 20 cm^{-1}. The band model parameters under (b) were taken from our previous study, reported in ref. 3; they were derived from low resolution data with assumed values of (γ/d). The theoretical background underlying this procedure is included in this Appendix. The band model parameters under (c) were taken from the theoretical calculations by Malkmus and Thomson (ref. 196).

D-1. The Use of Band Models

The molecular spectrum in the infrared consists of the superposition of a large number of individual spectral lines. This complex fine structure is normally not apparent in most measured spectra because of the finite spectral resolution of the spectrometers used. However, its importance is indicated if the measured transmission, τ, of a uniform volume of gas is found not to obey Beer's law. Beer's law may be written in the form

$$-\frac{d}{d\ell} \ln(\bar{\tau}) = \text{constant} \tag{D-1}$$

This relationship is satisfied for the monochromatic function, τ; however, it may or may not be satisfied for the mean transmissivity, $\bar{\tau}$. If $k_\lambda \ell$ is small ($<<1$) or does not vary greatly over the interval $\Delta\lambda$, corresponding to the spectrometer resolution, then $\overline{\exp(-k_\lambda \ell)}^{\Delta\lambda}$ can be closely approximated by $\exp(-\overline{k_\lambda}^{\Delta\lambda} \ell)$. If $k_\lambda \ell$ does vary greatly and is large somewhere in the interval, this approximation cannot be made, and Beer's law (Equation D-1) is not satisfied. Thus Equation D-1 may be used to extrapolate thin-gas emissivity measurements to any thickness if k_λ is a slowly varying function of wavelength (such as for solid carbon particles). However, a different approach is normally required for molecular emission.

Approximate theoretical techniques for treating molecular emission have been developed for isothermal gas volumes. These techniques directly evaluate the average or "smeared" emissivity which the spectrometer measures. These are the so-called band model procedures (statistical model, regular model, etc.). They treat large groups of spectral lines as regular or random arrays and carry out the wavelength averages of the transmission or emissivity analytically.

A very good representation of the curve of growth for a homogeneous gas is given by the Goody model, which predicts an emissivity of the form

$$\bar{\epsilon} = 1 - \exp\left[- ku\,(1+ku/4a)^{-1/2}\right] \tag{D-2}$$

where k is the mean absorption coefficient, and the fine-structure parameter "a" represents the effective ratio of line half-width γ to line spacing d.

This equation is exact for a random band model composed of Lorentz-shaped lines with an exponential line strength distribution function and provides a very close approximation for other models with quite different line intensity distribution functions.

In an inhomogeneous gas (pressure and/or temperature not constant along the line of sight), the Curtis-Godson approximation is used to replace a multi-layered medium (in each layer of which a given spectral line may have a different intensity and half-width) by a homogeneous medium with an equivalent line intensity and an equivalent half-width. These two equivalent values are determined by the condition that the approximation be exact in the linear and square-root regions.

This approximation has been extended to the use of band models by similar defining relations between the mean absorption coefficient, k, and the fine-structure parameter, a, which expresses this ratio of mean line half-width to mean line spacing.

The error introduced by the use of the Curtis-Godson approximation has been investigated by Thomson (ref. 197) and is found to be large only when great differences of temperature or line widths occur.

The effective absorption coefficient in the Curtis-Godson approximation is defined by the condition

$$k = \sum_i k_i u_i / u , \tag{D-3}$$

and the parameter a by the condition

$$a = \sum_i k_i u_i a_i / ku , \tag{D-4}$$

where the quantities k_i, u_i, and a_i are the values for layer number i.

D-2. Derivation of Band Model Parameters From Line Parameters

The molecules of interest to the present program are either symmetric top or nearly symmetric top molecules (with the exception of H_2O). A symmetric top molecule (i.e., a molecule for which at least two of the principal moments of inertia are equal) may be treated analytically much more readily than an asymmetric top molecule. An asymmetry parameter κ may be defined:

$$\kappa = \frac{2B - (A+C)}{A-C} \tag{D-5}$$

where the rotational constants A, B, and C are inversely proportional to the principal moments of inertia. The parameter κ equals -1 for a prolate symmetric top, 0 for a most asymmetric top, and +1 for an oblate symmetric top. A list of the types of molecules considered is given in Table D-1.

TABLE D-1. TYPES OF MOLECULES CONSIDERED IN ATMOSPHERE

Linear Molecules	
CO	
NO	
CO_2	
N_2O	
Spherical Top Molecules	
CH_4	
Other Symmetric Top Molecules	
NH_3	
Nearly Symmetric Top Molecules	
NO_2	$\kappa = -.9939$
SO_2	$\kappa = -.9416$
HCHO	$\kappa = -.9623$
Asymmetric Top Molecules	
H_2O	$\kappa = -.4377$

The energy levels for a rigid symmetric top molecule are given by

$$F_v(J, K) = \omega_v + BJ(J+1) + (A-B)K^2 \qquad \text{(D-6)}$$

where J and K are the rotational quantum numbers and v represents the set of vibrational quantum numbers. For a non-rigid top, Eq. (D-6) can be written more precisely as a multiple power series in J(J+1) and K^2, with coefficients different for each vibrational state. For a transition between any two states, the wavenumber of the transition can be expressed simply as the difference between the energy levels:

$$\omega(v', J', K' - v, J, K) = F_{v'}(J', K') - F_v(J, K) \qquad \text{(D-7)}$$

Selection rules for J and K are obeyed: for a perpendicular band (change of electric dipole moment perpendicular to the top axis, e.g., ν_4 band of NH_3 at 6.1 μm),

$$\Delta J = -1, 0, +1 \; ; \; \Delta K = -1, +1 . \qquad \text{(D-8)}$$

For a parallel band (change of electric dipole moment parallel to the top axis, e.g., ν_2 band of NH_3 at 10.5 μm),

$$\Delta J = -1, 0, +1 \; ; \Delta K = 0 . \qquad \text{(D-9)}$$

By starting with J = 0, K = 0, the wavenumbers of all rotational transitions may be calculated. Relative strengths of the lines are known from quantum mechanics: e.g., in a perpendicular band, when $\Delta J = +1$ and $\Delta K = +1$, the line strength is proportional to

$$A_{KJ} = \frac{(J+2+K)\,(J+1+K)}{(J+1)\,(2J+1)} \qquad \text{(D-10)}$$

and the Boltzmann factor and statistical weight of the lower state.

Similar expressions exist for all combinations of $\Delta J = -1, 0, +1$ and $\Delta K = -1, +1$. For a parallel band, when $\Delta J = +1$ (and $\Delta K = 0$), the analogous expression is

$$A_{KJ} = \frac{(J+1)^2 - K^2}{(J+1)\,(2J+1)} \qquad \text{(D-11)}$$

Similar expressions exist for $\Delta J = -1, 0$ and $\Delta K = 0$.

Thus it is possible to generate a systematic list of transitions and relative line strengths for a symmetric top molecule. The absorption coefficient for a spectral line with Lorentz shape centered at ω_0 is then given by

$$k(\omega) = \frac{S\,\gamma/\pi}{\left(\omega-\omega_0\right)^2 + \gamma^2} \tag{D-12}$$

where S is the line strength and γ is the line half-width. The line half-width γ is related to pressure, temperature and foreign gas- and self-broadening through

$$\gamma = \gamma_0\, p_e \sqrt{\frac{T_0}{T}}$$

where γ_0 is the line half width at 1 atm for nitrogen broadening at the standard temperature T_0. The equivalent pressure p_e is given by

$$p_e = p_G B + p_N = p_T \left[c_G (B-1) + 1\right] \tag{D-13}$$

where p_G and p_N are the partial pressures of the pollutant and nitrogen, respectively, and B is the ratio of self-broadening to nitrogen-broadening efficiency. A partial list of B for several species is given in Table D-2.

TABLE D-2. BROADENING EFFICIENCY RATIO B
FOR VARIOUS MOLECULES

Species	B	Ref.
CO	1.02	Burch et al. (ref. 198)
CO_2	1.3	Burch et al. (ref. 198)
SO_2	5.	Burch et al. (ref. 172)
NO_2	5.	Estimate
NO	1.1	Estimate
HCHO	5.	Estimate
NH_3	6.	France and Williams (ref. 182)
CH_4	1.3	Burch et al. (ref. 198)

Since many of the species of interest are symmetric top molecules or slightly asymmetric tops, we have developed a program which calculates the energy level structure of a symmetric top molecule, and from the selection rules and matrix elements for transitions between these energy levels, calculates the wavenumbers and (relative) strengths of the allowed vibration-rotation transitions. A value of the total band strength is required to produce dimensionalized line strengths. As the transitions are calculated, the spectral data are written on magnetic tape.

The general form of the computer program which was developed required modifications for almost every different molecule to which it was applied. In general, intensity alternation results from statistical weight factors which depend on the symmetry of the molecule and the spins of identical nuclei. CO_2^{16}, for example, has missing alternate levels (i.e., the statistical weight factor = 0) for both the C^{12} and C^{13} species. However, $CO^{16}O^{18}$ lacks this symmetry, and does not have such intensity alteration. In the case of NH_3, levels with $K=3N+1$ and $3N+2$ have statistical weight of 1, while it is 2 for $K=3N$. Certain molecules such as NH_3 and CH_4, having particular symmetry properties, require special modifications to calculate the statistical weights.

Certain molecules (e.g., SO_2 and NO_2) are not symmetric tops, but are very nearly so. The first-order effect of asymmetry on the spectrum is to change the wavenumbers of the transitions slightly. In such a case, we have calculated the line parameters for the equivalent symmetric top, and made first-order corrections for asymmetry to the wavenumbers of the transitions.

In several instances, existing tabulations of line parameters were available from the literature. This was the case for three H_2O band systems, as well as for the CO fundamental band.

The tabulated values of k and a_0 were calculated by a program which scanned tapes containing lines of several species sorted by wavenumber, selected those of the species of interest and calculated, for a given $\Delta\omega$, the quantities

$$k = \sum_i S_i/\Delta\omega$$

and

$$a_0 \equiv \left[\sum_i S_i^{1/2}\, \gamma_i^{1/2}\right]^2 \Big/ \sum_i S_i\, \Delta\omega$$

These averages were calculated over intervals of 5 and 20 cm^{-1}.

D-3. Derivation of Band Model Parameters From Laboratory Data

The parameter "a" in the equation for the curve of growth of a random exponential Lorentz band model is defined as the ratio of the half-width to the effective mean line spacing. In applying this model to a particular molecule, sufficiently extensive observations should be made to evaluate the parameters $\bar{k}$ and a separately, while verifying the applicability of the model to the molecule.

In the absence of observations extensive enough to evaluate $\bar{k}$ and a uniquely, it may be necessary to estimate a in advance, and determine $\bar{k}$ based on this assumed value. The exponential intensity distribution is not derived from any physical properties of the molecule, hence any theoretical relationship between a and the molecular parameters is necessarily tenuous. However, in the region where the strongest lines dominate the properties of the spectrum, some approximate relationship can be obtained. In the spectrum of a diatomic molecule, the separation of the lines in the fundamental band is given by 2B, where B is the rotational constant of the molecule. For a rigid symmetric-top molecule, a similar expression is valid, at least for the parallel bands. For perpendicular bands, and bands of asymmetric-top molecules, appropriate effective rotation constants can be chosen to give reasonable estimates of the mean line spacing. Additionally, where sufficiently high resolution spectra are available, the number density of intense lines can be determined by counting. Reasonably consistent results have been obtained from these two procedures.

The line width can also be estimated with reasonable accuracy. For a nonpolar molecule, the air-broadened half-width can be taken to be about 0.05 cm^{-1}. For highly polar molecules higher values are appropriate. Sophisticated methods of calculating line widths exist, but are probably not justified for this purpose.

We note that in no case does the parameter a enter into the expression for absorptivity with more than a square-root dependence; generally it is less. The results of the procedure described may be quite insensitive to the particular value of a which was chosen.

In general, the procedure is to select a quantitative spectral measurement, assume an "a", and determine an effective $\bar{k}$ based on this value of a. This set of values is used to extrapolate to other values of path length. If the measurements are in the linear region, $\bar{k}$ (as well as absorptivity) is completely insensitive to the value of a. On the other hand, in the square-root region the absorptivity is dependent only on the product $\bar{k}$ a, so that while the individual values of $\bar{k}$ and a may be in considerable error, the product is unaffected. In the intermediate region, an error in "a" will have some effect on the predicted absorptivities. The largest inaccuracies will result from extrapolations to largely different conditions, using parameters determined from restricted and insufficient measurements.

Values of $\bar{k}$ and a_0 (=a/p) have been extracted for the molecules HCl, HF, O_3, CH_4, C_2H_4, C_6H_6, and PAN. The data for the diatomic molecules were taken from the theoretical calculations of Malkmus and Thomson (ref. 196). The data for most of the other molecules were based on Pierson, Fletcher, and Gantze (ref. 199). Walshaw (ref. 200) was used for O_3, and Leighton (ref. 201) for PAN.

Spectral absorption measurements are generally available over a more restricted range of parameters (path length, pressure) than one might hope for. In fact, such data may be available for only one pressure and path length. If such a spectrum is known to be in the linear region of the curve of growth (e.g., if it is fully pressure-broadened), the spectral absorption coefficient, $\bar{k}$, can be derived from it. If it is known to be in the square-root region, the product $a\bar{k}$ of the fine-structure parameter and the spectral absorption coefficient can be determined (but not the two separately). If, as is quite likely, the measurement is in some intermediate region (or is not known to be in the linear or square-root region), some assumption regarding the value of the fine-structure parameter may be made to determine an absorption coefficient.

If, for example, the measurement happens to be in the square-root region, any assumed value of "a" will yield a corresponding value of $\bar{k}$. If these values are used to extrapolate to other points in the square-root region, since only the product $a\bar{k}$ is involved, no error results even if $\bar{k}$ and a are separately in considerable error. If an extrapolation is made to other regions of the curve of growth, some degree of error is introduced. A similar argument holds for measurements and extrapolations within the linear region of the curve of growth.

D-4. Tables

The band model parameters of 16 pollutant and atmospheric species are listed. In Tables D-3 and D-4, an overview of the species is given. For the species CO, CO_2, SO_2, NO_2, NO, N_2O, NH_3, HCHO and H_2O, the band model parameters are derived from line parameters; for the species HCl and HF, the band model parameters are taken from the Malkmus-Thomson theory (ref. 196), for the remaining species the band model parameters are derived from laboratory data (ref. 199, 200, 201).

The absorption coefficients, except for H_2O, are given in units of cm^{-1} atm^{-1} at 300 K. They may be converted into other commonly used units by

$$k\left(\mathrm{cm}^{-1}\ \mathrm{atm}^{-1}\right)_{\mathrm{STP}} = k\left(\mathrm{cm}^{-1}\ \mathrm{atm}^{-1}\ \text{at } 300\ \mathrm{K}\right)\ \left(\frac{300}{273}\right)$$

$$k\left(\mathrm{cm}^{2}/\mathrm{molecule}\right) = \frac{1}{2.69 \times 10^{19}}\ k\left(\mathrm{cm}^{-1}\ \mathrm{atm}^{-1}\right)_{\mathrm{STP}}$$

$$k\left(\mathrm{cm}^{2}/\mathrm{g}\right) = \frac{2.24 \times 10^{4}}{(\text{Molec. Weight})}\ k\left(\mathrm{cm}^{-1}\ \mathrm{atm}^{-1}\right)_{\mathrm{STP}}.$$

The absorption coefficients for H_2O are given in units of cm^2/g, which is numerically equivalent to (precipitable cm$)^{-1}$. Thus,

$$k_{H_2O}(\mathrm{pr\ cm})^{-1} = k_{H_2O}\left(\mathrm{cm}^{2}/\mathrm{g}\right) = 1.245 \times 10^{+3}\ k_{H_2O}\left(\mathrm{cm}^{-1}\ \mathrm{atm}^{-1}\right)_{\mathrm{STP}}$$

TABLE D-3. BAND STRENGTHS AND BAND-AVERAGED ABSORPTION COEFFICIENTS AND FINE STRUCTURE PARAMETERS OF POLLUTANTS

Species	λ (μm)	Transition	$\omega_1 - \omega_2$ cm^{-1}	$\Delta\omega$ cm^{-1}	No. Lines	α cm^{-2} atm^{-1}	$\bar{k}$ cm^{-1} atm^{-1}	$\bar{a}_0$ atm^{-1}
CO	4.6	0 - 1	1960 - 2240	280	142	217.9	0.7263	0.0093
	2.3	0 - 2	4180 - 4320	140	40	1.99	0.0142	0.0125
CO_2	10.0	$\begin{cases}\nu_3 - \nu_1 \\ \nu_3 - 2\nu_2\end{cases}$	880 - 1100	220	419	0.0673	0.000306	0.0507
	4.9	$\begin{cases}2\nu_1 - \gamma_2 \\ \nu_1 + \nu_2\end{cases}$	1880 - 2180	300	448	0.9096	0.00303	0.0544
	2.9	$\begin{cases}3\nu'_2 - \nu'_2 + \nu_3 \\ 2\nu_2 + \nu_3\end{cases}$	3460 - 3560	100	112	0.8286	0.00829	0.0546
	2.0	$2\nu_1 + \nu_3$	4700 - 5160	460	596	1.597	0.00347	0.0388
SO_2	8.7	ν_1	1040 - 1260	220	6311	99.801	0.4536	1.3534
	4.0	$\nu_1 + \nu_3$	2340 - 2640	300	3073	22.530	0.07510	0.5032
NO_2	7.6	ν_1	1200 - 1440	240	2583	105.1 *	0.438	0.566
	3.4	$\nu_1 + \nu_3$	2800 - 2980	180	1410	62.64	0.3480	0.3833
NO	5.3	0 - 1	1760 - 1980	220	305	110.9	0.504	0.0442
N_2O	8.1	ν_1 $2\nu_2$	1120 - 1340	220	235	249.1	1.132	0.0408
	4.5	ν_3	2140 - 2260	120	942	1746.7	14.556	0.1472
	3.9	$\begin{cases}2\nu_1 \\ \nu_1 + 2\nu_2\end{cases}$	2460 - 2640	180	210	40.33	0.2240	0.0444
	2.9	$\begin{cases}\nu_1 + \nu_3 \\ 2\nu_2 + \nu_3\end{cases}$	3300 - 3500	200	242	29.13	0.1456	0.0374
NH_3	10.4	ν_2	680 - 1240	560	477	1576.9 **	2.816	0.0402
	3.0	ν_3	3100 - 3660	560	473	85.53	0.1527	0.0399
HCHO	3.5	ν_4	2620 - 3140	520	1861	299.9	0.577	1.0598
H_2O	9.0		960 - 1260	300	129			0.0119
	5.3		1760 - 1980	220	370			0.0099
	4.7		1980 - 2240	260	186			0.0096
	3.3		2900 - 3140	240	203			0.0323
	3.0		3140 - 3460	320	490			0.0456
	2.4		3980 - 4360	380	321			0.0198
	2.0		4700 - 5160	460	349			0.0199

Note added in proof

* Value too high by a factor of about 50

** Value too high by a factor of about 2

TABLE D-4. BAND STRENGTHS AND FINE STRUCTURE PARAMETERS OF POLLUTANTS NOT INCLUDED IN TABLE D-3

Species		$\omega_1 - \omega_2$ cm^{-1}	α $\text{cm}^{-2}\ \text{atm}^{-1}$	$\overline{a_0}$ atm^{-1}
HCl	3.5 μm	2200-3200	143	.003
HF	2.5	3000-4400	450	.0015
CH_4	7.8	1195-1667	418	.01
	3.3	2700-3200	270	.01
	2.3	4082-4552	(80)	.01
C_2H_4	10.5	813-1149	365	.03
	3.2	2939-3187	(4500)	.03
PAN	12.3	757- 847	(1600)	.5
	8.3	1111-1333	(4200)	.5
C_6H_6	9.6	1007-1064	(950)	.08
	3.2	3011-3150	(9600)	.08
O_3	9.6	1006-1063	400	.05

NOTE: Values of α in parenthesis are integrals of absorption coefficients derived from limited laboratory data and may be of low accuracy.

Band Model Parameters for CO in 5 and 20 cm^{-1} intervals.

Δω (1/cm)		k(300K) (1/cm-atm)	a_o(300K) (1/atm)
1960	1965	1.160000E-05	7.000000E-03
1965	1970	2.820000E-05	1.344549E-02
1970	1975	4.960000E-05	1.364476E-02
1975	1980	8.720000E-05	1.382088E-02
1960	1980	4.415000E-05	1.126716E-02
1980	1985	1.510000E-04	1.414421E-02
1985	1990	2.560000E-04	1.419167E-02
1990	1995	7.560000E-04	2.204864E-02
1995	2000	8.840000E-04	1.479875E-02
1980	2000	5.117500E-04	1.495869E-02
2000	2005	1.422000E-03	1.477750E-02
2005	2010	2.264000E-03	1.486904E-02
2010	2015	3.572000E-03	1.487009E-02
2015	2020	5.576000E-03	1.478510E-02
2000	2020	3.208500E-03	1.394287E-02
2020	2025	8.628000E-03	1.486012E-02
2025	2030	1.761200E-02	2.320637E-02
2030	2035	2.102200E-02	1.522507E-02
2035	2040	3.086000E-02	1.512884E-02
2020	2040	1.953050E-02	1.614877E-02
2040	2045	4.484000E-02	1.497952E-02
2045	2050	8.034000E-02	2.226788E-02
2050	2055	9.240000E-02	1.472463E-02
2055	2060	2.866400E-01	2.201983E-02
2040	2060	1.260550E-01	1.688605E-02
2060	2065	3.788000E-01	1.888469E-02
2065	2070	3.311000E-01	1.858739E-02
2070	2075	4.033400E-01	1.315909E-02
2075	2080	5.141400E-01	1.282293E-02
2060	2080	4.068450E-01	1.544472E-02
2080	2085	6.533000E-01	1.573729E-02
2085	2090	7.828400E-01	1.184840E-02
2090	2095	2.032954E+00	2.124131E-02
2095	2100	1.259640E+00	1.157379E-02
2080	2100	1.182183E+00	1.464140E-02
2100	2105	1.408360E+00	1.224353E-02
2105	2110	1.529820E+00	1.267373E-02
2110	2115	1.627780E+00	1.559609E-02
2115	2120	3.223820E+00	2.522987E-02
2100	2120	1.947445E+00	1.641082E-02
2120	2125	1.517040E+00	1.733434E-02
2125	2130	1.317840E+00	1.496077E-02
2130	2135	1.086120E+00	1.869466E-02
2135	2140	1.142320E+00	3.011861E-02
2120	2140	1.265830E+00	1.963149E-02
2140	2145	2.538000E-02	1.977818E-02
2145	2150	4.038400E-01	1.768828E-02
2150	2155	1.918710E+00	3.087914E-02
2155	2160	1.429034E+00	1.485678E-02
2140	2160	9.442410E-01	1.628659E-02
2160	2165	1.655178E+00	1.306170E-02
2165	2170	3.712002E+00	2.470612E-02
2170	2175	1.910730E+00	1.204678E-02
2175	2180	3.610112E+00	2.197084E-02
2160	2180	2.722005E+00	1.791142E-02
2180	2185	1.606644E+00	1.061575E-02
2185	2190	1.434266E+00	1.052852E-02
2190	2195	2.308301E+00	1.999320E-02
2195	2200	1.593636E+00	1.913159E-02
2180	2200	1.735712E+00	1.488384E-02
2200	2205	5.660080E-01	9.260309E-03
2205	2210	7.728000E-01	1.877483E-02
2210	2215	2.482000E-01	8.600000E-03
2215	2220	3.098000E-01	1.649928E-02
2200	2220	4.742020E-01	1.271076E-02
2220	2225	1.520000E-01	1.567894E-02
2225	2230	4.160000E-02	7.800000E-03
2230	2235	4.508000E-02	1.484450E-02
2235	2240	1.876000E-02	1.416033E-02
2220	2240	6.436000E-02	1.153738E-02
2240	2245	6.780000E-03	1.377639E-02
2245	2250	2.340000E-03	1.373985E-02
2250	2255	7.500000E-04	1.370900E-02
2255	2260	2.200000E-04	1.369725E-02
2240	2260	2.522500E-03	1.018744E-02

Band Model Parameters for CO in 5 and 20 cm^{-1} intervals.

$\Delta\omega$		k(300K)	a_o(300K)
(1/cm)		(1/cm-atm)	(1/atm)
4180	4185	2.863846E-03	1.000000E-02
4185	4190	3.771603E-03	1.000000E-02
4190	4195	4.859892E-03	1.000000E-02
4195	4200	1.366755E-02	1.994595E-02
4180	4200	6.290724E-03	1.215339E-02
4200	4205	9.075409E-03	1.000000E-02
4205	4210	1.065622E-02	1.000000E-02
4210	4215	1.219889E-02	1.000000E-02
4215	4220	1.359679E-02	1.000000E-02
4200	4220	1.138183E-02	9.944081E-03
4220	4225	1.472946E-02	1.000000E-02
4225	4230	1.547173E-02	1.000000E-02
4230	4235	1.570526E-02	1.000000E-02
4235	4240	1.533161E-02	1.000000E-02
4220	4240	1.530952E-02	9.998602E-03
4240	4245	2.682928E-02	1.997892E-02
4245	4250	1.013602E-02	1.000000E-02
4250	4255	7.149860E-03	1.000000E-02
4255	4260	3.712673E-03	1.000000E-02
4240	4260	1.195746E-02	1.192743E-02
4260	4265	3.788554E-03	1.000000E-02
4265	4270	7.445104E-03	1.000000E-02
4270	4275	2.437383E-02	1.993241E-02
4275	4280	1.580567E-02	1.000000E-02
4260	4280	1.285329E-02	1.186508E-02
4280	4285	1.731003E-02	1.000000E-02
4285	4290	3.628301E-02	1.999997E-02
4290	4295	3.431369E-02	1.999553E-02
4295	4300	1.523733E-02	1.000000E-02
4280	4300	2.578602E-02	1.498656E-02
4300	4305	2.538465E-02	1.997541E-02
4305	4310	1.830267E-02	1.995587E-02
4310	4315	1.203134E-02	1.993230E-02
4315	4320	7.243012E-03	1.990509E-02
4300	4320	1.574042E-02	1.897163E-02

Band Model Parameters for CO_2 in 5 and 20 cm^{-1} intervals.

Δω (1/cm)		k(300K) (1/cm-atm)	a_0(300K) (1/atm)
880	885	4.816954E-07	2.795528E-02
885	890	2.086870E-06	6.927074E-02
890	895	4.070696E-06	6.947013E-02
895	900	7.114161E-06	6.964470E-02
880	900	3.438356E-06	5.452399E-02
900	905	1.215480E-05	9.103929E-02
905	910	2.117769E-05	1.082344E-01
910	915	3.204195E-05	1.250205E-01
915	920	3.514707E-05	1.092283E-01
900	920	2.513038E-05	1.056519E-01
920	925	5.788376E-05	1.046989E-01
925	930	6.144504E-05	8.961229E-02
930	935	1.606785E-04	8.733744E-02
935	940	1.690879E-04	7.822484E-02
920	940	1.122738E-04	8.273724E-02
940	945	3.063910E-04	8.977904E-02
945	950	3.319027E-04	7.871395E-02
950	955	2.751116E-04	7.232278E-02
955	960	1.285266E-04	5.981962E-02
940	960	2.604830E-04	7.423433E-02
960	965	9.771268E-05	3.852677E-02
965	970	2.600596E-04	4.181423E-02
970	975	4.491714E-04	5.599443E-02
975	980	3.811069E-04	5.585439E-02
960	980	2.970126E-04	4.650849E-02

Δω (1/cm)		k(300K) (1/cm-atm)	a_0(300K) (1/atm)
980	985	2.270013E-04	5.548925E-02
985	990	1.126177E-04	6.786514E-02
990	995	2.681795E-05	6.631503E-02
995	1000	3.955754E-06	5.324597E-02
980	1000	9.259816E-05	4.435178E-02
1000	1005	2.238974E-06	2.765829E-02
1005	1010	1.001117E-05	4.089040E-02
1010	1015	1.693375E-05	2.776913E-02
1015	1020	3.395262E-05	2.780849E-02
1000	1020	1.578413E-05	2.566877E-02
1020	1025	6.485138E-05	3.520349E-02
1025	1030	1.978487E-04	5.944969E-02
1030	1035	2.356395E-04	4.320074E-02
1035	1040	5.639100E-04	6.167159E-02
1020	1040	2.655624E-04	4.631549E-02
1040	1045	5.444639E-04	5.074378E-02
1045	1050	9.945830E-04	6.623037E-02
1050	1055	1.062078E-03	7.578136E-02
1055	1060	8.046885E-04	7.553358E-02
1040	1060	8.514533E-04	6.668147E-02
1060	1065	3.233264E-04	1.008995E-01
1065	1070	5.555637E-04	8.384374E-02
1070	1075	1.337755E-03	8.824586E-02
1075	1080	1.470025E-03	9.096856E-02
1060	1080	9.216673E-04	8.290743E-02
1080	1085	1.089871E-03	1.045956E-01
1085	1090	6.139384E-04	1.270518E-01
1090	1095	3.068994E-04	1.773993E-01
1095	1100	6.504955E-05	2.082419E-01
1080	1100	5.189395E-04	1.125364E-01

Band Model Parameters for CO_2 in 5 and 20 cm^{-1} intervals.

Δω (1/cm)		k(300K) (1/cm-atm)	a_0(300K) (1/atm)
1880	1885	0.	1.000000E+00
1885	1890	0.	1.000000E+00
1890	1895	1.994017E-05	5.384093E-02
1895	1900	4.589103E-05	4.136924E-02
1880	1900	1.645790E-05	2.213003E-02
1900	1905	1.047561E-04	4.156243E-02
1905	1910	3.012379E-04	5.539111E-02
1910	1915	3.833997E-04	4.190158E-02
1915	1920	4.923317E-04	4.198320E-02
1900	1920	3.204314E-04	4.229724E-02
1920	1925	6.385579E-04	5.591446E-02
1925	1930	2.618098E-04	4.107388E-02
1930	1935	5.260943E-03	3.555155E-01
1935	1940	4.233003E-04	4.170360E-02
1920	1940	1.646153E-03	1.220765E-01
1940	1945	6.006603E-04	4.198117E-02
1945	1950	6.092269E-04	4.198995E-02
1950	1955	4.921961E-04	4.192251E-02
1955	1960	3.295213E-04	4.181175E-02
1940	1960	5.079012E-04	4.136211E-02
1960	1965	1.863184E-04	4.166766E-02
1965	1970	8.992188E-05	4.149460E-02
1970	1975	3.728782E-05	4.129512E-02
1975	1980	1.334332E-05	4.107116E-02
1960	1980	8.171786E-05	3.432409E-02
1980	1985	0.	1.000000E+00
1985	1990	0.	1.000000E+00
1990	1995	0.	1.000000E+00
1995	2000	0.	1.000000E+00
1980	2000	0.	1.000000E+00
2000	2005	0.	1.000000E+00
2005	2010	0.	1.000000E+00
2010	2015	0.	1.000000E+00
2015	2020	0.	1.000000E+00
2000	2020	0.	1.000000E+00
2020	2025	2.609992E-06	1.400000E-02
2025	2030	2.115278E-05	4.064729E-02
2030	2035	7.507122E-05	4.091006E-02
2035	2040	3.764636E-04	5.402410E-02
2020	2040	1.188244E-04	2.865268E-02

Δω (1/cm)		k(300K) (1/cm-atm)	a_0(300K) (1/atm)
2040	2045	8.202241E-04	4.143661E-02
2045	2050	1.778158E-03	4.162105E-02
2050	2055	3.314957E-03	5.307460E-02
2055	2060	7.321276E-03	7.740739E-02
2040	2060	3.308654E-03	5.010615E-02
2060	2065	7.052240E-03	6.567171E-02
2065	2070	6.836904E-03	8.363799E-02
2070	2075	4.566186E-03	1.081142E-01
2075	2080	7.140384E-02	4.039341E-01
2060	2080	2.246479E-02	1.569067E-01
2080	2085	7.010080E-03	1.032869E-01
2085	2090	8.670567E-03	7.734583E-02
2090	2095	2.465065E-02	5.874627E-01
2095	2100	7.422165E-03	1.378407E-01
2080	2100	1.193837E-02	2.202866E-01
2100	2105	5.664181E-03	1.291474E-01
2105	2110	4.376787E-03	1.614844E-01
2110	2115	2.789915E-03	1.726478E-01
2115	2120	1.688631E-03	1.651683E-01
2100	2120	3.629878E-03	1.466217E-01
2120	2125	9.600525E-04	1.621330E-01
2125	2130	3.281512E-03	4.577591E-01
2130	2135	2.156575E-04	1.368414E-01
2135	2140	2.825482E-04	8.928045E-02
2120	2140	1.184942E-03	2.007212E-01
2140	2145	3.108708E-04	5.128582E-02
2145	2150	2.832316E-04	4.197045E-02
2150	2155	2.637703E-04	5.565720E-02
2155	2160	1.080617E-04	4.170155E-02
2140	2160	2.414836E-04	4.643890E-02
2160	2165	5.388447E-05	4.153185E-02
2165	2170	2.301533E-05	4.133536E-02
2170	2175	6.588061E-06	2.778405E-02
2175	2180	0.	1.000000E+00
2160	2180	2.087197E-05	2.516896E-02

Band Model Parameters for CO_2 in 5 and 20 cm^{-1} intervals.

Δω (1/cm)		k(300K) (1/cm-atm)	a_o(300K) (1/atm)
3460	3465	0.	1.000000E+00
3465	3470	0.	1.000000E+00
3470	3475	5.613639E-05	4.082230E-02
3475	3480	9.786486E-05	2.775244E-02
3460	3480	3.850031E-05	1.622906E-02
3480	3485	2.015276E-04	2.779274E-02
3485	3490	6.906153E-04	4.136595E-02
3490	3495	1.580994E-03	4.155864E-02
3495	3500	1.856743E-03	2.792392E-02
3480	3500	1.082470E-03	3.059104E-02
3500	3505	4.427554E-03	4.181805E-02
3505	3510	6.537214E-03	4.192975E-02
3510	3515	7.927370E-03	4.354303E-02
3515	3520	7.585487E-03	5.737431E-02
3500	3520	6.619406E-03	4.574340E-02
3520	3525	4.852249E-03	6.280731E-02
3525	3530	1.378733E-03	7.611276E-02
3530	3535	7.844144E-03	1.127590E-01
3535	3540	1.183303E-02	1.086995E-01
3520	3540	6.477039E-03	8.400842E-02
3540	3545	1.865778E-02	1.348682E-01
3545	3550	2.221128E-02	1.416281E-01
3550	3555	2.858052E-02	1.328889E-01
3555	3560	3.939894E-02	1.183776E-01
3540	3560	2.721213E-02	1.281068E-01

Band Model Parameters for CO_2 in 5 and 20 cm^{-1} intervals.

Δω (1/cm)		k(300K) (1/cm-atm)	a_o(300K) (1/atm)
4740	4745	4.215487E-05	5.498383E-02
4745	4750	0.	1.000000E+00
4750	4755	3.299388E-05	4.158821E-02
4755	4760	4.963611E-05	4.197265E-02
4740	4760	3.119621E-05	3.429219E-02
4760	4765	5.143885E-05	4.199225E-02
4765	4770	6.760458E-05	8.228514E-02
4770	4775	6.152353E-05	8.338291E-02
4775	4780	1.199330E-04	8.330800E-02
4760	4780	7.512500E-05	7.124722E-02
4780	4785	2.078185E-04	8.362373E-02
4785	4790	2.460264E-04	6.991204E-02
4790	4795	3.541352E-04	8.398161E-02
4795	4800	3.506101E-04	9.331729E-02
4780	4800	2.896476E-04	8.196226E-02
4800	4805	2.542661E-04	1.085886E-01
4805	4810	2.067664E-04	9.806101E-02
4810	4815	4.400534E-04	1.036588E-01
4815	4820	1.103698E-03	1.251322E-01
4800	4820	5.011961E-04	9.961333E-02
4820	4825	1.890871E-03	1.194971E-01
4825	4830	1.811132E-03	7.830026E-02
4830	4835	3.448546E-03	7.631305E-02
4835	4840	4.297422E-03	5.670240E-02
4820	4840	2.861993E-03	7.543347E-02
4840	4845	4.378088E-03	4.199079E-02
4845	4850	3.252606E-03	4.694369E-02
4850	4855	1.125293E-03	5.684686E-02
4855	4860	2.296902E-03	5.171770E-02
4840	4860	2.763222E-03	4.542198E-02
4860	4865	5.893080E-03	7.045053E-02
4865	4870	4.807793E-03	5.265265E-02
4870	4875	5.039944E-03	7.499589E-02
4875	4880	2.859686E-03	7.944571E-02
4860	4880	4.650126E-03	6.737352E-02
4880	4885	1.218336E-03	8.270743E-02
4885	4890	4.215904E-04	9.582105E-02
4890	4895	2.061508E-04	8.647457E-02
4895	4900	3.071357E-04	5.596220E-02
4880	4900	5.383033E-04	7.119148E-02
4900	4905	2.888299E-04	5.591552E-02
4905	4910	1.938167E-04	6.473066E-02
4910	4915	1.380799E-04	1.074626E-01
4915	4920	1.289306E-04	8.837469E-02
4900	4920	1.874143E-04	7.293158E-02
4920	4925	2.563509E-04	7.428924E-02
4925	4930	9.304358E-04	1.061919E-01
4930	4935	1.315668E-03	6.877421E-02
4935	4940	2.590189E-03	8.983231E-02
4920	4940	1.273161E-03	7.493581E-02
4940	4945	4.013484E-03	7.670157E-02
4945	4950	9.146948E-03	8.302789E-02
4950	4955	9.746588E-03	7.371415E-02
4955	4960	1.795418E-02	7.744098E-02
4940	4960	1.021530E-02	7.295232E-02
4960	4965	2.065594E-02	6.305100E-02
4965	4970	1.961628E-02	7.495088E-02
4970	4975	1.343813E-02	9.861278E-02
4975	4980	4.245385E-03	1.300022E-01
4960	4980	1.448893E-02	7.783870E-02
4980	4965	1.781074E-02	1.165578E-01
4985	4990	2.925170E-02	9.848767E-02
4990	4995	2.670216E-02	7.991863E-02
4995	5000	1.709341E-02	7.203288E-02
4980	5000	2.271450E-02	8.966811E-02
5000	5005	9.186600E-03	8.076848E-02
5005	5010	2.697037E-03	1.118718E-01
5010	5015	2.380049E-04	1.222938E-01
5015	5020	7.583970E-06	1.400000E-02
5000	5020	3.032357E-03	5.221165E-02
5040	5045	2.352361E-05	2.768692E-02
5045	5050	5.333970E-05	2.773144E-02
5050	5055	2.079513E-04	4.114917E-02
5055	5060	3.111711E-04	2.783035E-02
5040	5060	1.489964E-04	2.612152E-02
5060	5065	9.763470E-04	4.149806E-02
5065	5070	1.195317E-03	2.791046E-02
5070	5075	2.987875E-03	4.177342E-02
5075	5080	4.681232E-03	4.189716E-02
5060	5080	2.460193E-03	3.537896E-02
5080	5085	6.113701E-03	4.952395E-02
5085	5090	6.367227E-03	5.473697E-02
5090	5095	4.789566E-03	6.144148E-02
5095	5100	1.607208E-03	7.482264E-02
5080	5100	4.719426E-03	5.456615E-02
5100	5105	3.782132E-03	8.760565E-02
5105	5110	6.389617E-03	7.063932E-02
5110	5115	9.495893E-03	8.817157E-02
5115	5120	7.265206E-03	8.635910E-02
5100	5120	6.733212E-03	8.103259E-02
5120	5125	3.909078E-03	7.750350E-02
5125	5130	1.907729E-03	1.177488E-01
5130	5135	1.145349E-03	1.635005E-01
5135	5140	7.000944E-04	1.387208E-01
5120	5140	1.915563E-03	1.020752E-01
5140	5145	5.584206E-04	1.250768E-01
5145	5150	2.403349E-04	1.103607E-01
5150	5155	8.405146E-05	9.614020E-02
5155	5160	0.	1.000000E+00
5140	5160	2.207017E-04	7.570354E-02

Band Model Parameters for SO_2 in 5 and 20 cm^{-1} intervals.

Δω (1/cm)		k(300K) (1/cm-atm)	a_0(300K) (1/atm)
1040	1045	2.151834E-02	9.119830E-02
1045	1050	1.310995E-02	3.458881E-02
1050	1055	7.465834E-03	5.244718E-02
1055	1060	2.410903E-02	1.125416E-01
1040	1060	1.655079E-02	7.136461E-02
1060	1065	3.806459E-02	2.439590E-01
1065	1070	3.363220E-02	6.994772E-01
1070	1075	3.902193E-02	1.126357E+00
1075	1080	7.905252E-02	1.479112E+00
1060	1080	4.744281E-02	8.459449E-01
1080	1085	1.397075E-01	1.705297E+00
1085	1090	1.648241E-01	1.434754E+00
1090	1095	2.355684E-01	1.282353E+00
1095	1100	3.356223E-01	2.458339E+00
1080	1100	2.189306E-01	1.688986E+00
1100	1105	4.099271E-01	2.127417E+00
1105	1110	5.361855E-01	1.968320E+00
1110	1115	6.420741E-01	1.935790E+00
1115	1120	7.026137E-01	1.877171E+00
1100	1120	5.727001E-01	1.947601E+00
1120	1125	7.426081E-01	2.042507E+00
1125	1130	9.183290E-01	2.239452E+00
1130	1135	9.397568E-01	2.317352E+00
1135	1140	9.934214E-01	2.160237E+00
1120	1140	8.985288E-01	2.186252E+00
1140	1145	8.978266E-01	2.220101E+00
1145	1150	8.170546E-01	2.331354E+00
1150	1155	6.969964E-01	2.179098E+00
1155	1160	1.084347E+00	2.445188E+00
1140	1160	8.740562E-01	2.284838E+00
1160	1165	1.076796E+00	2.364475E+00
1165	1170	1.086842E+00	2.222371E+00
1170	1175	1.074942E+00	2.070205E+00
1175	1180	8.264351E-01	1.749699E+00
1160	1180	1.016254E+00	2.100414E+00
1180	1185	9.776472E-01	1.890513E+00
1185	1190	8.177241E-01	1.798747E+00
1190	1195	6.950119E-01	1.712538E+00
1195	1200	6.276525E-01	1.789129E+00
1180	1200	7.795089E-01	1.788506E+00
1200	1205	5.206751E-01	1.769688E+00
1205	1210	3.735280E-01	1.487231E+00
1210	1215	3.370692E-01	1.405702E+00
1215	1220	2.239230E-01	1.168621E+00
1200	1220	3.637988E-01	1.449949E+00
1220	1225	1.982987E-01	1.156111E+00
1225	1230	1.541947E-01	9.993011E-01
1230	1235	1.097415E-01	9.241392E-01
1235	1240	1.203697E-01	6.145769E-01
1220	1240	1.456512E-01	9.169307E-01
1240	1245	6.178575E-02	7.193671E-01
1245	1250	5.605424E-02	6.139658E-01
1250	1255	5.657581E-02	4.643494E-01
1255	1260	5.202813E-02	3.233667E-01
1240	1260	5.661098E-02	5.227796E-01

Band Model Parameters for SO_2 in 5 and 20 cm^{-1} intervals.

Δω (1/cm)		k(300K) (1/cm-atm)	a_o(300K) (1/atm)
2340	2345	0.	1.000000E+00
2345	2350	0.	1.000000E+00
2350	2355	3.098098E-04	3.052613E-02
2355	2360	7.292820E-05	1.600000E-02
2340	2360	9.568451E-05	1.127927E-02
2360	2365	1.291668E-04	1.600000E-02
2365	2370	1.495693E-03	4.219651E-02
2370	2375	1.798394E-03	1.600000E-02
2375	2380	3.642958E-04	3.065158E-02
2360	2380	9.468873E-04	2.159481E-02
2380	2385	7.325996E-04	3.191703E-02
2385	2390	0.	1.000000E+00
2390	2395	3.416238E-03	4.189161E-02
2395	2400	2.193621E-03	4.131378E-02
2380	2400	1.598115E-03	2.742373E-02
2400	2405	0.	1.000000E+00
2405	2410	1.628601E-03	3.199090E-02
2410	2415	4.338897E-03	4.325148E-02
2415	2420	4.362732E-03	5.248128E-02
2400	2420	2.582558E-03	3.144897E-02
2420	2425	1.832884E-03	2.191223E-02
2425	2430	7.639905E-03	6.168569E-02
2430	2435	0.	1.000000E+00
2435	2440	1.141301E-02	6.839772E-02
2420	2440	5.221451E-03	3.756566E-02
2440	2445	6.407334E-03	1.099587E-01
2445	2450	1.433933E-02	3.184393E-01
2450	2455	1.530784E-02	6.632604E-01
2455	2460	3.154879E-02	8.391264E-01
2440	2460	1.690082E-02	4.728606E-01
2460	2465	5.270432E-02	1.088783E+00
2465	2470	9.827346E-02	1.222093E+00
2470	2475	1.479137E-01	1.344552E+00
2475	2480	2.452213E-01	1.505669E+00
2460	2480	1.360282E-01	1.235315E+00
2480	2485	3.003053E-01	1.530417E+00
2485	2490	3.802703E-01	1.656309E+00
2490	2495	3.295310E-01	1.699432E+00
2495	2500	7.558317E-01	6.289136E+00
2480	2500	4.414846E-01	2.740953E+00

Δω (1/cm)		k(300K) (1/cm-atm)	a_o(300K) (1/atm)
2500	2505	2.457484E-01	1.393854E+00
2505	2510	5.027689E-01	1.905605E+00
2510	2515	4.938582E-01	2.127517E+00
2515	2520	3.843430E-01	2.486867E+00
2500	2520	4.066796E-01	1.955140E+00
2520	2525	1.775262E-01	2.783078E+00
2525	2530	6.152538E-02	2.294704E+00
2530	2535	3.064289E-02	2.142747E-01
2535	2540	3.050013E-02	9.539228E-02
2520	2540	7.504865E-02	1.226586E+00
2540	2545	2.265153E-02	7.763293E-02
2545	2550	1.572009E-02	5.092004E-02
2550	2555	1.076335E-02	6.233046E-02
2555	2560	2.264143E-02	6.645336E-02
2540	2560	1.794910E-02	6.340592E-02
2560	2565	5.173353E-03	3.557397E-02
2565	2570	1.518827E-02	5.645436E-02
2570	2575	1.175601E-02	6.096945E-02
2575	2580	3.016740E-03	3.181590E-02
2560	2580	8.783592E-03	4.487863E-02
2580	2585	1.269780E-02	5.138001E-02
2585	2590	1.084802E-03	1.600000E-02
2590	2595	9.041922E-03	5.680339E-02
2595	2600	5.056240E-03	3.454066E-02
2580	2600	6.970191E-03	3.857177E-02
2600	2605	6.558353E-03	2.649384E-02
2605	2610	4.849186E-04	1.600000E-02
2610	2615	3.612322E-04	1.600000E-02
2615	2620	1.110743E-02	7.308795E-02
2600	2620	4.627962E-03	2.965926E-02
2620	2625	5.530238E-03	2.187031E-02
2625	2630	0.	1.000000E+00
2630	2635	6.234706E-04	2.929382E-02
2635	2640	2.102527E-04	3.196180E-02
2620	2640	1.590990E-03	1.253591E-02

Band Model Parameters for NO_2 in 5 and 20 cm^{-1} intervals.

Δω (1/cm)		k(300K)* (1/cm-atm)	a_o(300K) (1/atm)
1200	1205	8.620960E-02	8.238305E-01
1205	1210	7.390421E-02	3.564795E-01
1210	1215	7.768848E-02	5.869614E-01
1215	1220	1.468360E-01	6.437247E-01
1200	1220	9.615958E-02	5.863410E-01
1220	1225	1.094817E-01	4.274616E-01
1225	1230	2.425989E-01	8.556629E-01
1230	1235	1.404589E-01	3.405396E-01
1235	1240	1.602911E-01	5.551997E-01
1220	1240	1.632077E-01	5.413509E-01
1240	1245	3.377547E-01	6.795134E-01
1245	1250	2.339236E-01	5.433319E-01
1250	1255	3.240567E-01	7.355857E-01
1255	1260	4.442392E-01	6.362344E-01
1240	1260	3.349935E-01	6.423071E-01
1260	1265	2.819585E-01	4.873144E-01
1265	1270	4.325047E-01	6.104842E-01
1270	1275	6.110820E-01	7.596672E-01
1275	1280	3.422564E-01	6.032684E-01
1260	1280	4.169504E-01	6.117964E-01
1280	1285	8.934598E-01	8.255373E-01
1285	1290	5.022126E-01	7.548224E-01
1290	1295	4.295554E-01	5.543352E-01
1295	1300	7.534405E-01	6.786733E-01
1280	1300	6.446671E-01	6.950697E-01
1300	1305	8.220042E-01	7.012991E-01
1305	1310	3.990966E-01	4.193054E-01
1310	1315	7.408249E-01	5.643225E-01
1315	1320	7.711361E-01	5.509277E-01
1300	1320	6.832655E-01	5.565787E-01
1320	1325	3.397734E-01	5.511240E-01
1325	1330	3.591304E-01	4.012202E-01
1330	1335	8.474156E-01	5.699518E-01
1335	1340	5.375714E-01	6.037167E-01
1320	1340	5.209727E-01	5.621117E-01
1340	1345	7.280038E-01	5.348202E-01
1345	1350	9.653043E-01	7.629634E-01
1350	1355	3.853070E-01	6.793213E-01
1355	1360	5.831324E-01	5.038748E-01
1340	1360	6.654369E-01	6.039723E-01
1360	1365	1.042469E+00	7.937797E-01
1365	1370	4.043430E-01	5.226476E-01
1370	1375	4.652566E-01	4.350593E-01
1375	1380	9.188962E-01	7.206220E-01
1360	1380	7.077412E-01	6.122278E-01
1380	1385	3.098967E-01	4.260096E-01
1385	1390	4.996256E-01	6.771143E-01
1390	1395	6.890895E-01	6.540480E-01
1395	1400	2.807089E-01	3.883510E-01
1380	1400	4.448302E-01	5.323440E-01
1400	1405	3.539553E-01	5.926529E-01
1405	1410	4.973029E-01	5.799233E-01
1410	1415	2.200354E-01	3.656770E-01
1415	1420	3.034190E-01	6.320079E-01
1400	1420	3.436761E-01	5.358796E-01
1420	1425	3.517448E-01	6.287858E-01
1425	1430	1.453927E-01	3.600546E-01
1430	1435	2.269250E-01	6.325053E-01
1435	1440	2.127018E-01	5.563814E-01
1420	1440	2.341911E-01	5.396117E-01

Note added in proof

* Values too high by a factor of about 50

Band Model Parameters for NO_2 in 5 and 20 cm^{-1} intervals.

Δω (1/cm)		k(300K) (1/cm-atm)	a_o(300K) (1/atm)
2800	2805	2.726722E-04	1.600000E-02
2805	2810	2.439914E-03	2.810323E-02
2810	2815	1.054555E-03	4.417539E-02
2815	2820	1.336027E-03	3.040040E-02
2800	2820	1.275792E-03	2.721058E-02
2820	2825	4.256886E-03	3.105556E-02
2825	2830	6.820719E-03	5.167140E-02
2830	2835	3.742421E-03	2.950333E-02
2835	2840	1.120163E-02	6.549564E-02
2820	2840	6.505415E-03	4.424836E-02
2840	2845	2.004062E-02	2.201452E-01
2845	2850	3.340169E-02	2.821185E-01
2850	2855	5.005520E-02	3.833862E-01
2855	2860	7.751526E-02	4.390413E-01
2840	2860	4.525319E-02	3.268908E-01
2860	2865	1.374496E-01	5.918720E-01
2865	2870	2.484359E-01	6.765592E-01
2870	2875	3.721437E-01	6.231591E-01
2875	2880	5.671812E-01	6.143329E-01
2860	2880	3.313026E-01	5.890527E-01
2880	2685	8.432834E-01	7.920779E-01
2885	2890	1.164414E+00	8.130177E-01
2890	2895	1.080168E+00	8.576145E-01
2895	2900	9.429581E-01	1.090652E+00
2880	2900	1.007706E+00	8.800453E-01
2900	2905	7.906476E-01	1.646614E+00
2905	2910	4.554846E-01	1.128263E+00
2910	2915	1.532684E+00	1.164514E+00
2915	2920	1.907525E+00	1.158148E+00
2900	2920	1.171585E+00	1.168511E+00
2920	2925	1.201004E+00	9.311807E-01
2925	2930	5.709842E-01	6.808681E-01
2930	2935	2.161665E-01	3.347887E-01
2935	2940	1.122853E-01	1.239224E-01
2920	2940	5.251100E-01	5.090197E-01
2940	2945	7.873895E-02	1.152501E-01
2945	2950	4.067645E-02	1.030101E-01
2950	2955	1.623097E-02	6.627097E-02
2955	2960	1.342846E-02	6.102130E-02
2940	2960	3.726871E-02	8.221437E-02
2960	2965	1.169718E-02	7.224181E-02
2965	2970	7.222416E-03	6.118790E-02
2970	2975	6.672055E-04	1.600000E-02
2975	2980	4.106459E-03	4.523010E-02
2960	2980	5.923315E-03	4.734757E-02

Band Model Parameters for NO in 5 and 20 cm^{-1} intervals.

Δω (1/cm)		k(300K) (1/cm-atm)	a_o(300K) (1/atm)
1760	1765	4.598413E-03	4.905174E-02
1765	1770	6.285940E-03	3.970133E-02
1770	1775	9.566322E-03	3.968669E-02
1775	1780	1.430782E-02	3.967091E-02
1760	1780	8.689623E-03	3.951958E-02
1780	1785	3.909623E-02	5.865177E-02
1785	1790	3.803694E-02	3.870926E-02
1790	1795	7.735046E-02	5.867116E-02
1795	1800	8.211852E-02	3.957017E-02
1780	1800	5.915054E-02	4.687629E-02
1800	1805	1.989554E-01	5.879227E-02
1805	1810	1.721714E-01	3.880976E-02
1810	1815	3.118416E-01	5.867981E-02
1815	1820	2.974341E-01	3.941231E-02
1800	1820	2.451006E-01	4.790636E-02
1820	1825	6.357906E-01	5.883366E-02
1825	1830	4.827254E-01	3.885468E-02
1830	1835	7.665886E-01	5.854457E-02
1835	1840	1.112655E+00	5.874814E-02
1820	1840	7.494400E-01	5.309011E-02
1840	1845	7.443375E-01	3.881786E-02
1845	1850	1.034112E+00	5.818655E-02
1850	1855	1.301225E+00	5.839557E-02
1855	1860	7.215630E-01	3.857706E-02
1840	1860	9.503094E-01	4.839074E-02
1860	1865	1.163906E+00	7.628900E-02
1865	1870	3.721359E-01	3.932427E-02
1870	1875	2.840768E-01	2.502282E-01
1875	1880	4.046734E-01	1.874279E-01
1860	1880	5.561981E-01	1.037701E-01
1880	1885	5.608018E-01	5.695423E-02
1885	1890	5.615086E-01	3.806664E-02
1890	1895	1.503917E+00	7.691200E-02
1895	1900	8.757434E-01	3.869164E-02
1880	1900	8.754928E-01	5.146852E-02
1900	1905	1.833549E+00	7.756226E-02
1905	1910	1.751168E+00	7.767579E-02
1910	1915	1.264344E+00	5.878563E-02
1915	1920	8.692237E-01	5.858478E-02
1900	1920	1.429571E+00	6.768073E-02
1920	1925	1.006325E+00	7.761140E-02
1925	1930	6.938262E-01	7.750816E-02
1930	1935	3.780433E-01	5.883830E-02
1935	1940	2.888681E-01	7.870018E-02
1920	1940	5.917657E-01	6.951515E-02
1940	1945	1.609339E-01	7.869529E-02
1945	1950	8.343249E-02	7.866499E-02
1950	1955	4.030341E-02	7.861267E-02
1955	1960	1.816083E-02	7.854091E-02
1940	1960	7.570767E-02	6.828710E-02
1960	1965	8.420676E-03	9.600770E-02
1965	1970	1.740661E-03	3.941752E-02
1970	1975	0.	1.000000E+00
1975	1980	0.	1.000000E+00
1960	1980	2.540334E-03	3.316746E-02

Band Model Parameters for N_2O in 5 and 20 cm^{-1} intervals.

Δω (1/cm)		k(300K) (1/cm-atm)	a_o(300K) (1/atm)
1120	1125	0.	1.000000E+00
1125	1130	5.185552E-03	5.543656E-02
1130	1135	1.839898E-02	8.250378E-02
1135	1140	5.431202E-02	9.642334E-02
1120	1140	1.947414E-02	5.281533E-02
1140	1145	9.554180E-02	8.342920E-02
1145	1150	1.548308E-01	8.373789E-02
1150	1155	2.055062E-01	8.394600E-02
1155	1160	2.459817E-01	9.794139E-02
1140	1160	1.754651E-01	8.541980E-02
1160	1165	1.385662E-01	8.297485E-02
1165	1170	3.560182E-02	6.706687E-02
1170	1175	1.243493E-01	8.225949E-02
1175	1180	1.763583E-01	6.991068E-02
1160	1180	1.187189E-01	7.139762E-02
1180	1185	2.375555E-01	8.399767E-02
1185	1190	2.069651E-01	8.388702E-02
1190	1195	1.452267E-01	8.364597E-02
1195	1200	7.392597E-02	6.962416E-02
1180	1200	1.659183E-01	7.797832E-02
1200	1205	4.706623E-02	8.298235E-02
1205	1210	1.789772E-02	6.917082E-02
1210	1215	7.839586E-03	6.892190E-02
1215	1220	0.	1.000000E+00
1200	1220	1.820088E-02	5.021368E-02
1220	1225	2.479049E-03	2.789506E-02
1225	1230	1.486963E-02	6.820324E-02
1230	1235	4.429427E-02	6.851240E-02
1235	1240	1.185583E-01	6.879855E-02
1220	1240	4.505031E-02	4.777157E-02
1240	1245	2.846274E-01	6.906054E-02
1245	1250	6.114521E-01	6.929710E-02
1250	1255	1.171644E+00	6.950676E-02
1255	1260	1.993344E+00	6.968750E-02
1240	1260	1.015267E+00	6.206919E-02
1260	1265	3.707354E+00	8.373667E-02
1265	1270	4.051840E+00	6.996177E-02
1270	1275	5.200834E+00	8.399303E-02
1275	1280	4.073151E+00	8.357540E-02
1260	1280	4.258297E+00	7.995374E-02
1280	1285	1.384579E+00	6.587179E-02
1285	1290	1.956350E+00	7.855794E-02
1290	1295	4.613252E+00	8.368612E-02
1295	1300	5.673478E+00	8.399609E-02
1280	1300	3.406915E+00	7.379887E-02
1300	1305	5.872387E+00	9.784191E-02
1305	1310	3.890340E+00	9.739298E-02
1310	1315	1.999931E+00	9.675432E-02
1315	1320	8.152551E-01	9.596264E-02
1300	1320	3.144479E+00	8.708149E-02
1320	1325	2.837841E-01	1.075160E-01
1325	1330	6.044176E-02	1.057540E-01
1330	1335	8.106079E-03	6.802398E-02
1335	1340	0.	1.000000E+00
1320	1340	8.808299E-02	5.487961E-02

Band Model Parameters for N_2O in 5 and 20 cm^{-1} intervals.

$\Delta\omega$ (1/cm)		k(300K) (1/cm-atm)	a_0(300K) (1/atm)
2140	2145	1.370115E-02	3.903639E-01
2145	2150	3.147045E-02	3.855501E-01
2150	2155	7.582610E-02	4.062745E-01
2155	2160	1.678102E-01	3.982772E-01
2140	2160	7.220197E-02	3.298836E-01
2160	2165	3.434221E-01	3.820376E-01
2165	2170	8.307887E-01	4.172246E-01
2170	2175	1.466835E+00	3.498711E-01
2175	2180	2.829857E+00	3.468126E-01
2160	2180	1.382726E+00	3.243840E-01
2180	2185	5.693340E+00	3.260305E-01
2185	2190	8.001471E+00	2.688256E-01
2190	2195	1.401624E+01	2.347549E-01
2195	2200	2.092456E+01	2.335691E-01
2180	2200	1.215890E+01	2.414566E-01
2200	2205	2.610236E+01	1.961026E-01
2205	2210	2.353002E+01	2.392485E-01
2210	2215	2.941918E+01	1.802952E-01
2215	2220	2.861617E+01	2.629501E-01
2200	2220	2.841693E+01	2.184747E-01
2220	2225	1.182871E+01	3.210736E-01
2225	2230	2.013990E+01	2.444309E-01
2230	2235	4.046403E+01	1.901201E-01
2235	2240	4.319052E+01	1.577362E-01
2220	2240	2.890579E+01	1.972516E-01
2240	2245	3.299479E+01	1.349937E-01
2245	2250	2.275338E+01	1.471367E-01
2250	2255	7.874572E+00	1.273190E-01
2255	2260	1.971160E+00	1.348192E-01
2240	2260	1.639848E+01	1.134965E-01

Band Model Parameters for N_2O in 5 and 20 cm^{-1} intervals.

Δω (1/cm)		k(300K) (1/cm-atm)	a_0(300K) (1/atm)
2460	2465	0.	1.000000E+00
2465	2470	0.	1.000000E+00
2470	2475	0.	1.000000E+00
2475	2480	1.859253E-05	5.444794E-02
2460	2480	4.648133E-06	1.361199E-02
2480	2485	6.024518E-05	5.460703E-02
2485	2490	1.173570E-04	4.148910E-02
2490	2495	4.020932E-04	5.486877E-02
2495	2500	1.085382E-03	5.500841E-02
2480	2500	4.162694E-04	4.060117E-02
2500	2505	3.888941E-03	6.833425E-02
2505	2510	7.916225E-03	5.529491E-02
2510	2515	1.712409E-02	5.540940E-02
2515	2520	3.454070E-02	5.551567E-02
2500	2520	1.586749E-02	4.924762E-02
2520	2525	8.787144E-02	6.925521E-02
2525	2530	1.288273E-01	5.572329E-02
2530	2535	2.705949E-01	6.962124E-02
2535	2540	4.266215E-01	6.978263E-02
2520	2540	2.284788E-01	6.108042E-02
2540	2545	5.894511E-01	6.990841E-02
2545	2550	7.023498E-01	6.998688E-02
2550	2555	8.245995E-01	8.394628E-02
2555	2560	5.450515E-01	8.296987E-02
2540	2560	6.653630E-01	7.616528E-02
2560	2565	1.084118E-01	5.308573E-02
2565	2570	5.180476E-01	9.431683E-02
2570	2575	8.419712E-01	8.387843E-02
2575	2580	1.065844E+00	1.039497E-01
2560	2580	6.335687E-01	7.911048E-02
2580	2585	9.487031E-01	1.454343E-01
2585	2590	5.449148E-01	1.745694E-01
2590	2595	2.594071E-01	2.087307E-01
2595	2600	9.904586E-02	2.528762E-01
2580	2600	4.630177E-01	1.547872E-01
2600	2605	2.889199E-02	2.171643E-01
2605	2610	9.141276E-03	1.662176E-01
2610	2615	7.553947E-04	2.794583E-02
2615	2620	0.	1.000000E+00
2600	2620	9.697166E-03	9.716877E-02

Band Model Parameters for NH_3 in 5 and 20 cm^{-1} intervals (Cont'd)

Δω (1/cm)		k(300K)* (1/cm-atm)	a_0(300K) (1/atm)
1040	1045	0.	1.000000E+00
1045	1050	1.159219E+01	7.717927E-02
1050	1055	8.332595E+00	6.225673E-02
1055	1060	0.	1.000000E+00
1040	1060	4.981197E+00	3.483057E-02
1060	1065	0.	1.000000E+00
1065	1070	1.072821E+01	7.643756E-02
1070	1075	4.490932E+00	4.591053E-02
1075	1080	3.784427E+00	4.799933E-02
1060	1080	4.750892E+00	4.195538E-02
1080	1085	1.103748E+01	9.241917E-02
1085	1090	1.642963E+00	2.987264E-02
1090	1095	1.460453E+00	3.199404E-02
1095	1100	3.056401E+00	4.663413E-02
1080	1100	4.299325E+00	4.842969E-02
1100	1105	8.449294E+00	1.045546E-01
1105	1110	3.725461E-01	1.600000E-02
1110	1115	1.703984E+00	4.674591E-02
1115	1120	2.092406E+00	6.221935E-02
1100	1120	3.154558E+00	5.460568E-02
1120	1125	7.157838E+00	1.371139E-01
1125	1130	4.436812E-01	3.198310E-02
1130	1135	6.943463E-01	3.101595E-02
1135	1140	4.472815E+00	1.615352E-01
1120	1140	3.192170E+00	8.688437E-02
1140	1145	8.519628E-01	4.744971E-02
1145	1150	1.203818E-01	1.600000E-02
1150	1155	4.465445E-01	4.659230E-02
1155	1160	3.244951E+00	2.367136E-01
1140	1160	1.165960E+00	8.586188E-02
1160	1165	5.670513E-02	1.600000E-02
1165	1170	1.731642E-01	3.095731E-02
1170	1175	1.873205E-01	4.649670E-02
1175	1180	1.578805E+00	2.328574E-01
1160	1180	4.989987E-01	8.076173E-02
1180	1185	2.687803E-02	1.600000E-02
1185	1190	7.195338E-02	3.079398E-02
1190	1195	6.946081E-01	2.075737E-01
1195	1200	1.625716E-01	1.216977E-01
1180	1200	2.390028E-01	9.046866E-02
1200	1205	2.197763E-02	3.197622E-02
1205	1210	1.809512E-02	1.600000E-02
1210	1215	3.135406E-01	1.973848E-01
1215	1220	1.843696E-02	3.199662E-02
1200	1220	9.301257E-02	6.734778E-02

Note added in proof

---

* Values too high by a factor of about 2

Band Model Parameters for NH_3 in 5 and 20 cm^{-1} intervals.

Δω (1/cm)		k(300K)* (1/cm-atm)	a_o(300K) (1/atm)
3100	3105	2.761012E-03	6.361065E-02
3105	3110	5.479422E-04	1.600000E-02
3110	3115	0.	1.000000E+00
3115	3120	1.540336E-02	2.009238E-01
3100	3120	4.678078E-03	6.896190E-02
3120	3125	8.246944E-03	1.232945E-01
3125	3130	0.	1.000000E+00
3130	3135	7.486038E-03	4.773241E-02
3135	3140	4.459650E-02	2.486694E-01
3120	3140	1.508237E-02	1.009736E-01
3140	3145	0.	1.000000E+00
3145	3150	0.	1.000000E+00
3150	3155	3.781295E-02	9.165641E-02
3155	3160	6.256061E-02	1.707464E-01
3140	3160	2.509339E-02	6.554734E-02
3160	3165	0.	1.000000E+00
3165	3170	0.	1.000000E+00
3170	3175	9.701949E-02	1.237947E-01
3175	3180	8.656547E-02	1.079017E-01
3160	3180	4.589624E-02	5.792213E-02
3180	3185	0.	1.000000E+00
3185	3190	0.	1.000000E+00
3190	3195	1.364484E-01	9.362774E-02
3195	3200	1.578601E-01	1.095913E-01
3180	3200	7.357712E-02	5.080434E-02
3200	3205	0.	1.000000E+00
3205	3210	0.	1.000000E+00
3210	3215	2.165015E-01	9.241241E-02
3215	3220	1.802793E-01	7.641474E-02
3200	3220	9.919518E-02	4.220666E-02
3220	3225	0.	1.000000E+00
3225	3230	0.	1.000000E+00
3230	3235	2.189104E-01	6.161398E-02
3235	3240	2.766800E-01	7.761410E-02
3220	3240	1.238976E-01	3.480700E-02
3240	3245	0.	1.000000E+00
3245	3250	0.	1.000000E+00
3250	3255	2.140209E-01	4.788044E-02
3255	3260	2.917096E-01	6.386531E-02
3240	3260	1.264326E-01	2.793564E-02
3260	3265	0.	1.000000E+00
3265	3270	0.	1.000000E+00
3270	3275	0.	1.000000E+00
3275	3280	3.556730E-01	7.904559E-02
3260	3280	8.891825E-02	1.976140E-02

Δω (1/cm)		k(300K) (1/cm-atm)	a_o(300K) (1/atm)
3280	3285	0.	1.000000E+00
3285	3290	0.	1.000000E+00
3290	3295	0.	1.000000E+00
3295	3300	2.089084E-01	4.780029E-02
3280	3300	5.222710E-02	1.195007E-02
3300	3305	0.	1.000000E+00
3305	3310	0.	1.000000E+00
3310	3315	0.	1.000000E+00
3315	3320	5.258979E-02	1.600000E-02
3300	3320	1.314745E-02	4.000000E-03
3320	3325	0.	1.000000E+00
3325	3330	0.	1.000000E+00
3330	3335	4.920651E+00	8.784077E-01
3335	3340	1.718920E+00	3.220163E-01
3320	3340	1.659893E+00	3.000721E-01
3340	3345	6.532596E-02	1.367724E-01
3345	3350	2.939566E-02	5.504914E-02
3350	3355	1.568870E-02	7.287550E-02
3355	3360	6.583729E-02	2.554927E-02
3340	3360	4.406190E-02	6.230249E-02
3360	3365	4.905719E-03	4.425852E-02
3365	3370	5.332754E-04	1.600000E-02
3370	3375	9.370504E-02	2.067110E-02
3375	3380	2.125635E-01	3.185501E-02
3360	3380	7.792689E-02	1.662049E-02
3380	3385	0.	1.000000E+00
3385	3390	0.	1.000000E+00
3390	3395	3.889220E-01	4.744548E-02
3395	3400	2.342023E-01	3.165714E-02
3380	3400	1.557811E-01	1.976331E-02
3400	3405	0.	1.000000E+00
3405	3410	0.	1.000000E+00
3410	3415	1.069935E+00	1.117405E-01
3415	3420	0.	1.000000E+00
3400	3420	2.674837E-01	2.793513E-02
3420	3425	0.	1.000000E+00
3425	3430	0.	1.000000E+00
3430	3435	1.263141E+00	1.392310E-01
3435	3440	0.	1.000000E+00
3420	3440	3.157851E-01	3.480775E-02
3440	3445	0.	1.000000E+00
3445	3450	0.	1.000000E+00
3450	3455	1.220123E+00	1.688397E-01
3455	3460	0.	1.000000E+00
3440	3460	3.050307E-01	4.220992E-02

Note added in proof

* Values too high by a factor of about 2

Band Model Parameters for NH_3 in 5 and 20 cm^{-1} intervals (Cont'd).

Δω (1/cm)		k(300K) * (1/cm-atm)	a_0(300K) (1/atm)
3460	3465	0.	1.000000E+00
3465	3470	4.482409E-01	7.821677E-02
3470	3475	6.426288E-01	1.251581E-01
3475	3480	0.	1.000000E+00
3460	3480	2.727174E-01	5.080698E-02
3480	3485	0.	1.000000E+00
3485	3490	3.859599E-01	1.079114E-01
3490	3495	4.348191E-01	1.238028E-01
3495	3500	0.	1.000000E+00
3480	3500	2.051948E-01	5.792735E-02
3500	3505	0.	1.000000E+00
3505	3510	2.666837E-01	1.244268E-01
3510	3515	2.742418E-01	1.378822E-01
3515	3520	0.	1.000000E+00
3500	3520	1.352314E-01	6.555438E-02
3520	3525	0.	1.000000E+00
3525	3530	1.288850E-01	1.036264E-01
3530	3535	2.098146E-01	1.876500E-01
3535	3540	0.	1.000000E+00
3520	3540	8.467490E-02	7.405383E-02
3540	3545	0.	1.000000E+00
3545	3550	0.	1.000000E+00
3550	3555	1.646220E-01	2.939366E-01
3555	3560	2.086082E-02	3.017044E-02
3540	3560	4.637070E-02	8.094412E-02
3560	3565	0.	1.000000E+00
3565	3570	0.	1.000000E+00
3570	3575	3.747430E-02	1.375454E-01
3575	3580	5.075459E-02	2.000942E-01
3560	3580	2.205722E-02	8.438369E-02
3580	3585	2.962445E-03	1.600000E-02
3585	3590	0.	1.000000E+00
3590	3595	0.	1.000000E+00
3595	3600	1.935961E-02	1.828724E-01
3580	3600	5.580513E-03	4.935732E-02
3600	3605	2.151438E-02	1.830537E-01
3605	3610	2.960283E-03	1.600000E-02
3610	3615	0.	1.000000E+00
3615	3620	0.	1.000000E+00
3600	3620	6.118666E-03	4.953537E-02
3620	3625	5.411217E-03	1.093831E-01
3625	3630	7.854382E-03	1.384004E-01
3630	3635	1.731822E-03	1.600000E-02
3635	3640	6.972575E-04	1.600000E-02
3620	3640	3.923670E-03	6.918354E-02
3640	3645	0.	1.000000E+00
3645	3650	4.243089E-04	1.600000E-02
3650	3655	1.120403E-03	3.154029E-02
3655	3660	6.978049E-04	1.600000E-02
3640	3660	5.606291E-04	1.576444E-02

– Note added in proof

* Values too high by a factor of about 2

Band Model Parameters for HCHO in 5 and 20 cm^{-1} intervals

$\Delta\omega$ (1/cm)		k(300K) (1/cm-atm)	a_o(300K) (1/atm)
2620	2625	4.733933E-04	3.192748E-02
2625	2630	1.191962E-03	6.352845E-02
2630	2635	7.897370E-04	3.192610E-02
2635	2640	1.548539E-03	6.267147E-02
2620	2640	1.000908E-03	4.709324E-02
2640	2645	2.369013E-03	6.317061E-02
2645	2650	4.020224E-03	8.984690E-02
2650	2655	4.454658E-03	7.643067E-02
2655	2660	3.671176E-03	7.252039E-02
2640	2660	3.628768E-03	7.504206E-02
2660	2665	6.912860E-03	7.586226E-02
2665	2670	1.091447E-02	9.929802E-02
2670	2675	1.232839E-02	9.766043E-02
2675	2680	1.486134E-02	1.295906E-01
2660	2680	1.125427E-02	1.003212E-01
2680	2685	1.444031E-02	8.299157E-02
2685	2690	2.518741E-02	9.434348E-02
2690	2695	2.976605E-02	1.183053E-01
2695	2700	3.815227E-02	2.089082E-01
2680	2700	2.688651E-02	1.251012E-01
2700	2705	4.619817E-02	1.060695E-01
2705	2710	6.315084E-02	1.046507E-01
2710	2715	6.062716E-02	2.800110E-01
2715	2720	6.639573E-02	1.013014E-01
2700	2720	5.909298E-02	1.398281E-01
2720	2725	9.312703E-02	1.107336E-01
2725	2730	1.413749E-01	2.072084E-01
2730	2735	1.285228E-01	2.059826E-01
2735	2740	1.317761E-01	1.050588E-01
2720	2740	1.237002E-01	1.545518E-01
2740	2745	1.495605E-01	1.337134E-01
2745	2750	3.425065E-01	3.460118E-01
2750	2755	1.693321E-01	1.137329E-01
2755	2760	2.097456E-01	9.976391E-02
2740	2760	2.177862E-01	1.697523E-01
2760	2765	4.504073E-01	3.418800E-01
2765	2770	4.729124E-01	2.121920E-01
2770	2775	2.792447E-01	1.202614E-01
2775	2780	4.104112E-01	2.358239E-01
2760	2780	4.032439E-01	2.245106E-01

$\Delta\omega$ (1/cm)		k(300K) (1/cm-atm)	a_o(300K) (1/atm)
2780	2785	9.058029E-01	3.676909E-01
2785	2790	4.322599E-01	1.371073E-01
2790	2795	3.495528E-01	1.592586E-01
2795	2800	1.376869E+00	4.755664E-01
2780	2800	7.661212E-01	2.839634E-01
2800	2805	5.906059E-01	1.574766E-01
2805	2810	5.709654E-01	1.826280E-01
2810	2815	1.000704E+00	3.594161E-01
2815	2820	1.544515E+00	3.147942E-01
2800	2820	9.266975E-01	2.498936E-01
2820	2825	7.072629E-01	1.865213E-01
2825	2830	7.944371E-01	3.112085E-01
2830	2835	2.618108E+00	4.730949E-01
2835	2840	7.024129E-01	2.101617E-01
2820	2840	1.205555E+00	2.881546E-01
2840	2845	7.854110E-01	2.940587E-01
2845	2850	3.382788E+00	5.212820E-01
2850	2855	6.518175E-01	2.092614E-01
2855	2860	6.947937E-01	2.716180E-01
2840	2860	1.378702E+00	3.093413E-01
2860	2865	2.174626E+00	4.888299E-01
2865	2870	2.547816E+00	3.439945E-01
2870	2875	6.857068E-01	2.753219E-01
2875	2880	1.149864E+00	4.446651E-01
2860	2880	1.639503E+00	3.703191E-01
2920	2925	9.309696E-01	2.102982E-01
2925	2930	1.990880E+00	4.053384E-01
2930	2935	1.538502E+00	2.599133E-01
2935	2940	6.052163E-01	1.494217E-01
2920	2940	1.266392E+00	2.551781E-01
2880	2885	3.880696E+00	4.644716E-01
2885	2890	7.417107E-01	2.540570E-01
2890	2895	8.254837E-01	3.364658E-01
2895	2900	3.846110E+00	5.152331E-01
2880	2900	2.323500E+00	3.705203E-01
2900	2905	7.314618E-01	2.049205E-01
2905	2910	8.861813E-01	2.630051E-01
2910	2915	3.518207E+00	5.516501E-01
2915	2920	8.216312E-01	1.807872E-01
2900	2920	1.489370E+00	2.943532E-01

Band Model Parameters for HCHO in 5 and 20 cm^{-1} intervals (Cont'd).

$\Delta\omega$ (1/cm)		k(300K) (1/cm-atm)	a_o(300K) (1/atm)
2940	2945	1.464374E+00	3.452007E-01
2945	2950	1.855120E+00	3.487781E-01
2950	2955	5.848839E-01	1.246670E-01
2955	2960	7.622234E-01	2.510735E-01
2940	2960	1.166650E+00	2.647055E-01
2960	2965	1.436713E+00	3.521564E-01
2965	2970	6.027342E-01	1.363439E-01
2970	2975	6.583588E-01	1.946095E-01
2975	2980	1.048935E+00	3.698945E-01
2960	2980	9.366852E-01	2.612715E-01
2980	2985	4.813007E-01	1.067291E-01
2985	2990	3.996844E-01	1.453372E-01
2990	2995	5.474445E-01	3.506742E-01
2995	3000	5.564699E-01	1.377455E-01
2980	3000	4.962249E-01	1.761693E-01
3000	3005	2.302254E-01	1.149513E-01
3005	3010	3.318188E-01	3.262460E-01
3010	3015	2.227730E-01	9.728490E-02
3015	3020	2.384782E-01	1.155825E-01
3000	3020	2.708238E-01	1.570393E-01
3020	3025	2.790461E-01	3.001996E-01
3025	3030	1.081934E-01	9.768035E-02
3030	3035	1.480653E-01	1.026042E-01
3035	3040	1.299722E-01	2.268622E-01
3020	3040	1.663193E-01	1.774628E-01
3040	3045	1.075428E-01	1.365010E-01
3045	3050	6.681135E-02	9.997208E-02
3050	3055	6.871896E-02	1.580768E-01
3055	3060	4.920239E-02	1.310099E-01
3040	3060	7.306887E-02	1.283701E-01
3060	3065	4.195006E-02	1.102839E-01
3065	3070	3.599604E-02	1.218331E-01
3070	3075	2.485553E-02	9.919845E-02
3075	3080	1.716114E-02	9.299775E-02
3060	3080	2.999069E-02	1.044214E-01
3080	3085	1.860007E-02	1.145134E-01
3085	3090	1.208333E-02	8.751000E-02
3090	3095	8.431222E-03	9.466814E-02
3095	3100	5.541345E-03	7.536370E-02
3080	3100	1.116399E-02	9.080406E-02
3100	3105	6.817508E-03	1.043484E-01
3105	3110	3.566443E-03	7.466702E-02
3110	3115	2.238173E-03	6.175460E-02
3115	3120	1.811493E-03	6.241978E-02
3100	3120	3.608404E-03	7.403968E-02
3120	3125	1.754351E-03	7.877905E-02
3125	3130	6.084417E-04	3.192802E-02
3130	3135	2.253297E-04	1.600000E-02
3135	3140	0.	1.000000E+00
3120	3140	6.470306E-04	3.151418E-02

Band Model Parameters for H_2O in 5 and 20 cm^{-1} intervals.

Δω (1/cm)		k(300K, (cm^2/gm)	a_o(300K) (1/atm)
960	965	0.	1.000000E+00
965	970	0.	1.000000E+00
970	975	0.	1.000000E+00
975	980	2.170000E-02	1.306000E-02
960	980	5.425000E-03	3.265000E-03
980	985	0.	1.000000E+00
985	990	0.	1.000000E+00
990	995	0.	1.000000E+00
995	1000	1.270000E-02	1.226000E-02
980	1000	3.175000E-03	3.065000E-03
1000	1005	2.538000E-02	2.160924E-02
1005	1010	0.	1.000000E+00
1010	1015	9.898000E-02	2.413211E-02
1015	1020	4.848000E-02	1.952380E-02
1000	1020	4.321000E-02	1.536228E-02
1020	1025	0.	1.000000E+00
1025	1030	9.148000E-02	4.403440E-02
1030	1035	1.332000E-02	2.299563E-02
1035	1040	1.178000E-02	1.064000E-02
1020	1040	2.914500E-02	1.821603E-02
1040	1045	0.	1.000000E+00
1045	1050	2.796000E-02	1.389000E-02
1050	1055	2.130000E-02	1.382000E-02
1055	1060	2.888000E-02	2.166923E-02
1040	1060	1.953500E-02	1.224815E-02
1060	1065	5.316000E-02	2.316476E-02
1065	1070	2.210600E-01	1.388999E-02
1070	1075	8.964000E-02	1.807273E-02
1075	1080	1.000000E-02	9.600000E-03
1060	1080	9.346500E-02	1.321003E-02
1080	1085	0.	1.000000E+00
1085	1090	1.468000E-02	1.254000E-02
1090	1095	1.106600E-01	1.134000E-02
1095	1100	8.862000E-02	1.318000E-02
1080	1100	5.349000E-02	8.082099E-03
1100	1105	1.305000E-01	1.374000E-02
1105	1110	2.616800E-01	1.134000E-02
1110	1115	2.320800E-01	1.810318E-02
1115	1120	1.270000E-02	1.226000E-02
1100	1120	1.592400E-01	1.189874E-02

Δω (1/cm)		k(300K) (cm^2/gm)	a_o(300K) (1/atm)
1120	1125	2.939600E-01	2.597169E-02
1125	1130	0.	1.000000E+00
1130	1135	0.	1.000000E+00
1135	1140	1.084000E+00	3.023772E-02
1120	1140	3.444900E-01	1.307198E-02
1140	1145	1.398000E-02	1.238000E-02
1145	1150	2.468400E-01	1.280000E-02
1150	1155	2.456800E-01	2.622524E-02
1155	1160	0.	1.000000E+00
1140	1160	1.266250E-01	1.105150E-02
1160	1165	0.	1.000000E+00
1165	1170	4.008200E-01	4.772146E-02
1170	1175	2.330880E+00	2.392463E-02
1175	1180	0.	1.000000E+00
1160	1180	6.829250E-01	1.283201E-02
1180	1185	4.248000E-02	2.493297E-02
1185	1190	1.658680E+00	2.007523E-02
1190	1195	2.152000E-02	4.360561E-02
1195	1200	9.489400E-01	1.786948E-02
1180	1200	6.679050E-01	1.322067E-02
1200	1205	0.	1.000000E+00
1205	1210	4.712000E-02	8.498496E-02
1210	1215	2.832360E+00	3.153891E-02
1215	1220	8.670400E-01	3.000248E-02
1200	1220	9.366300E-01	1.828349E-02
1220	1225	6.307400E-01	5.684659E-02
1225	1230	2.229960E+00	4.337197E-02
1230	1235	7.940000E-03	7.680000E-03
1235	1240	3.857600E-01	4.244758E-02
1220	1240	8.136000E-01	3.109495E-02
1240	1245	2.938580E+00	4.007291E-02
1245	1250	1.481600E-01	3.818537E-02
1250	1255	3.021600E-01	1.036377E-01
1255	1260	6.795600E-01	4.546467E-02
1240	1260	1.017115E+00	3.653765E-02

Band Model Parameters for H_2O in 5 and 20 cm^{-1} intervals.

Δω (1/cm)		k(300K) (cm^2/gm)	a_o(300K) (1/atm)
1760	1765	0.	1.000000E+00
1765	1770	0.	1.000000E+00
1770	1775	0.	1.000000E+00
1775	1780	1.941988E+01	2.274773E-02
1760	1780	4.854970E+00	5.686932E-03
1780	1785	4.182225E+02	7.325240E-02
1785	1790	6.051980E+00	6.157870E-02
1790	1795	9.472365E+02	3.679286E-02
1795	1800	3.053691E+02	7.388713E-02
1780	1800	4.192200E+02	4.207307E-02
1800	1805	2.011017E+02	2.983736E-02
1805	1810	4.750410E+01	3.730237E-02
1810	1815	1.799125E+02	3.243615E-02
1815	1820	3.726922E+01	2.502440E-02
1800	1820	1.164469E+02	2.753228E-02
1820	1825	1.870604E+01	3.353651E-02
1825	1830	4.467748E+02	4.598317E-02
1830	1835	3.448316E+02	2.703129E-02
1835	1840	5.350678E+01	4.684149E-02
1820	1840	2.159548E+02	2.871490E-02
1840	1845	7.617215E+02	3.779761E-02
1845	1850	9.643022E+01	6.418238E-02
1850	1855	2.630440E+00	2.975850E-02
1855	1860	1.557868E+01	5.603416E-02
1840	1860	2.190902E+02	2.345553E-02
1860	1865	1.155430E+01	4.517320E-02
1865	1870	4.943634E+02	5.659126E-02
1870	1875	1.589272E+01	1.274000E-02
1875	1880	4.992000E+00	4.774316E-02
1860	1880	1.317006E+02	2.292195E-02
1880	1885	1.461742E+01	2.334611E-02
1885	1890	1.746575E+02	2.091129E-02
1890	1895	2.499060E+00	6.190777E-02
1895	1900	5.494126E+01	2.949685E-02
1880	1900	6.167880E+01	1.754980E-02
1900	1905	9.408720E+00	4.073146E-02
1905	1910	6.318754E+01	3.809347E-02
1910	1915	9.590200E-01	3.999346E-02
1915	1920	2.558071E+02	2.470789E-02
1900	1920	8.234059E+01	1.807919E-02
1920	1925	1.014053E+02	3.337627E-02
1925	1930	3.379800E-01	3.640187E-02
1930	1935	5.301680E+00	2.941043E-02
1935	1940	6.781800E-01	8.703336E-02
1920	1940	2.693077E+01	1.554930E-02
1940	1945	1.384659E+02	3.538673E-02
1945	1950	2.881154E+01	4.326048E-02
1950	1955	7.323520E+00	2.682454E-02
1955	1960	1.726600E+00	7.254761E-02
1940	1960	4.408188E+01	2.414999E-02
1960	1965	5.167680E+00	1.975295E-02
1965	1970	6.070570E+01	2.684596E-02
1970	1975	2.464000E-02	1.256000E-02
1975	1980	9.354800E-01	3.188833E-02
1960	1980	1.670837E+01	1.193724E-02

Band Model Parameters for H_2O in 5 and 20 cm^{-1} intervals.

Δω (1/cm)		k(300K) (cm^2/gm)	a_o(300K) (1/atm)
1960	1985	2.879200E-01	7.820005E-02
1965	1990	1.934264E+01	1.628879E-02
1990	1995	7.416360E+01	3.022176E-02
1995	2000	4.304860E+00	1.999866E-02
1960	2000	2.452475E+01	1.638143E-02
2000	2005	5.366000E-02	6.447633E-02
2005	2010	3.724120E+00	3.708239E-02
2010	2015	6.006000E-02	6.376716E-02
2015	2020	3.733958E+01	4.179331E-02
2000	2020	1.029435E+01	1.841400E-02
2020	2025	2.560100E+00	1.730125E-02
2025	2030	2.004680E+00	3.890753E-02
2030	2035	3.315400E-01	3.397646E-02
2035	2040	2.838000E-01	3.611100E-02
2020	2040	1.295030E+00	2.345304E-02
2040	2045	1.443184E+01	3.662225E-02
2045	2050	6.188600E-01	2.767480E-02
2050	2055	7.776000E-02	8.881421E-02
2055	2060	5.720000E-03	1.102000E-02
2040	2060	3.783545E+00	1.487414E-02
2060	2065	1.361988E+01	2.602473E-02
2065	2070	3.011420E+00	1.295135E-02
2070	2075	1.163040E+00	3.141895E-02
2075	2080	3.231200E-01	2.586659E-02
2060	2080	4.529365E+00	1.595904E-02
2080	2085	2.118000E-01	1.282000E-02
2085	2090	1.408400E+00	3.101801E-02
2090	2095	4.036300E+00	1.765944E-02
2095	2100	3.403400E-01	2.727027E-02
2080	2100	1.499210E+00	1.625542E-02
2100	2105	4.103000E-01	1.280000E-02
2105	2110	3.992400E-01	3.807656E-02
2110	2115	6.439000E-01	4.493301E-02
2115	2120	1.075100E+00	1.491402E-02
2100	2120	6.321350E-01	2.398076E-02

Δω (1/cm)		k(300K) (cm^2/gm)	a_o(300K) (1/atm)
2120	2125	4.389800E-01	7.458217E-02
2125	2130	0.	1.000000E+00
2130	2135	0.	1.000000E+00
2135	2140	2.060020E+00	6.111795E-02
2120	2140	6.247500E-01	2.871665E-02
2140	2145	4.738000E-02	3.400730E-02
2145	2150	5.432200E-01	4.576554E-02
2150	2155	2.805000E-01	2.678050E-02
2155	2160	1.143600E-01	2.222714E-02
2140	2160	2.463650E-01	2.845357E-02
2160	2165	4.880800E-01	2.586469E-02
2165	2170	7.820000E-03	1.136000E-02
2170	2175	1.330600E-01	2.406459E-02
2175	2180	1.828000E-02	3.437020E-02
2160	2180	1.618100E-01	1.598536E-02
2180	2185	1.974200E-01	2.383690E-02
2185	2190	1.615600E-01	3.859526E-02
2190	2195	4.256000E-02	2.363975E-02
2195	2200	9.500000E-03	1.978000E-02
2180	2200	1.027600E-01	2.265335E-02
2200	2205	5.010000E-02	8.800000E-03
2205	2210	2.262800E-01	4.100347E-02
2210	2215	1.082600E-01	7.024402E-02
2215	2220	5.608000E-02	4.590258E-02
2200	2220	1.101800E-01	3.696153E-02
2220	2225	0.	1.000000E+00
2225	2230	3.168000E-02	4.597181E-02
2230	2235	5.924000E-02	1.948819E-02
2235	2240	3.812000E-02	6.091813E-02
2220	2240	3.226000E-02	2.805174E-02

Band Model Parameters for H_2O in 5 and 20 cm^{-1} intervals.

$\Delta\omega$ (1/cm)		k(300K) (cm^2/gm)	a_0(300K) (1/atm)
2900	2905	1.710000E-02	1.564000E-02
2905	2910	4.778000E-02	1.780000E-02
2910	2915	4.638000E-02	2.315529E-02
2915	2920	8.200000E-03	1.550000E-02
2900	2920	2.986500E-02	1.678658E-02
2920	2925	8.000000E-03	6.760000E-03
2925	2930	0.	1.000000E+00
2930	2935	4.236600E-01	7.076811E-02
2935	2940	3.904400E-01	4.479433E-02
2920	2940	2.055250E-01	2.974545E-02
2940	2945	5.820000E-03	7.180000E-03
2945	2950	7.146000E-02	2.555437E-02
2950	2955	3.169800E-01	2.128604E-02
2955	2960	2.789000E-01	7.595845E-02
2940	2960	1.682900E-01	2.847301E-02
2960	2965	2.870400E-01	3.125480E-02
2965	2970	6.591400E-01	4.389671E-02
2970	2975	1.143080E+00	3.170089E-02
2975	2980	1.173740E+00	3.304648E-02
2960	2980	8.157500E-01	3.258237E-02
2980	2985	8.877000E-01	8.308683E-02
2985	2990	1.423580E+00	3.961383E-02
2990	2995	2.094880E+00	5.136008E-02
2995	3000	3.766200E-01	1.452569E-02
2980	3000	1.195695E+00	4.338372E-02
3000	3005	1.910620E+00	5.727028E-02
3005	3010	3.973800E-01	2.726058E-02
3010	3015	7.070140E+00	9.283212E-02
3015	3020	2.112380E+00	1.698901E-02
3000	3020	2.872630E+00	4.476869E-02

$\Delta\omega$ (1/cm)		k(300K) (cm^2/gm)	a_0(300K) (1/atm)
3020	3025	7.330200E-01	3.117127E-02
3025	3030	2.233960E+00	2.785103E-02
3030	3035	1.254778E+01	8.844314E-02
3035	3040	1.195140E+00	2.167732E-02
3020	3040	4.177475E+00	3.902247E-02
3040	3045	1.628000E-02	2.867783E-02
3045	3050	3.781880E+00	5.076429E-02
3050	3055	7.870000E-02	6.211927E-02
3055	3060	7.199900E+00	5.570041E-02
3040	3060	2.769190E+00	3.052522E-02
3060	3065	6.582840E+00	2.188949E-02
3065	3070	5.735560E+00	3.563131E-02
3070	3075	6.440000E-03	7.120000E-03
3075	3080	6.384340E+00	6.947279E-02
3060	3080	4.677295E+00	3.024308E-02
3080	3085	4.056500E+00	5.051840E-02
3085	3090	8.019200E-01	2.371092E-02
3090	3095	1.496580E+00	3.761542E-02
3095	3100	1.037412E+01	6.475515E-02
3080	3100	4.182280E+00	4.056022E-02
3100	3105	9.413160E+00	5.604365E-02
3105	3110	3.161200E+00	6.374782E-02
3110	3115	4.828080E+00	1.009323E-01
3115	3120	1.291956E+01	8.656706E-02
3100	3120	7.580500E+00	7.082258E-02
3120	3125	8.470000E+00	6.497553E-02
3125	3130	5.630340E+00	1.126016E-01
3130	3135	8.380140E+00	3.050693E-02
3135	3140	1.074000E-02	1.788000E-02
3120	3140	5.622805E+00	4.705790E-02

Band Model Parameters for H_2O in 5 and 20 cm^{-1} intervals.

$\Delta\omega$ (1/cm)		k(300K) (cm^2/gm)	a_o(300K) (1/atm)
3140	3145	0.	1.000000E+00
3145	3150	0.	1.000000E+00
3150	3155	4.448400E-01	5.707469E-02
3155	3160	5.764000E-02	4.192277E-02
3140	3160	1.256200E-01	2.162818E-02
3160	3165	1.421400E-01	3.818435E-02
3165	3170	8.328200E-01	1.017799E-01
3170	3175	2.151800E-01	8.870563E-02
3175	3180	9.280040E+00	2.633084E-02
3160	3180	2.617545E+00	2.374819E-02
3180	3185	1.649720E+00	5.050077E-02
3185	3190	3.922840E+00	2.589892E-02
3190	3195	1.634000E-02	2.131325E-02
3195	3200	1.133434E+01	6.265894E-02
3180	3200	4.230810E+00	3.186893E-02
3200	3205	2.778600E-01	6.006676E-02
3205	3210	8.248440E+00	2.607892E-02
3210	3215	9.528220E+00	3.142576E-02
3215	3220	9.177380E+00	4.210724E-02
3200	3220	6.807975E+00	2.849647E-02
3220	3225	4.010300E+00	4.678618E-02
3225	3230	8.515340E+00	6.449138E-02
3230	3235	4.315680E+00	7.846444E-02
3235	3240	4.044160E+00	2.590940E-02
3220	3240	5.221370E+00	5.177888E-02
3240	3245	1.458964E+01	6.012836E-02
3245	3250	1.607280E+00	4.088451E-02
3250	3255	9.128220E+00	2.293237E-02
3255	3260	3.974600E+00	3.392579E-02
3240	3260	7.324935E+00	3.473668E-02
3260	3265	4.063460E+00	5.255033E-02
3265	3270	3.128140E+00	4.185840E-02
3270	3275	1.327948E+01	8.306299E-02
3275	3280	1.014236E+01	5.995489E-02
3260	3280	7.653360E+00	5.752169E-02
3280	3285	4.928780E+00	8.749814E-02
3285	3290	4.177440E+00	3.884275E-02
3290	3295	1.065558E+01	1.007616E-01
3295	3300	4.045600E+00	5.966249E-02
3280	3300	5.951850E+00	7.027819E-02

$\Delta\omega$ (1/cm)		k(300K) (cm^2/gm)	a_o(300K) (1/atm)
3300	3305	9.396800E-01	4.282782E-02
3305	3310	9.988160E+00	4.983652E-02
3310	3315	7.391400E+00	6.215151E-02
3315	3320	1.236220E+00	5.791961E-02
3300	3320	4.888865E+00	4.382508E-02
3320	3325	3.776480E+00	6.762981E-02
3325	3330	3.280340E+00	9.400055E-02
3330	3335	1.712460E+00	2.522301E-02
3335	3340	6.647600E+00	6.249317E-02
3320	3340	3.854220E+00	5.934592E-02
3340	3345	1.761800E+00	5.256264E-02
3345	3350	9.728200E-01	6.844199E-02
3350	3355	2.047280E+00	7.647100E-02
3355	3360	3.520600E+00	8.320767E-02
3340	3360	2.075625E+00	6.768372E-02
3360	3365	9.480220E+00	1.263572E-01
3365	3370	1.587156E+01	8.339692E-02
3370	3375	6.570400E-01	6.901627E-02
3375	3380	1.242960E+00	6.726448E-02
3360	3380	6.812945E+00	6.922867E-02
3380	3385	3.636000E+00	4.685170E-02
3385	3390	6.283440E+00	3.366906E-02
3390	3395	1.347260E+01	6.623492E-02
3395	3400	1.018380E+00	6.498648E-02
3380	3400	6.102605E+00	4.407896E-02
3400	3405	4.723920E+00	9.937204E-02
3405	3410	1.173480E+00	6.467432E-02
3410	3415	1.133160E+00	5.074792E-02
3415	3420	5.225160E+00	7.358328E-02
3400	3420	3.063930E+00	6.760604E-02
3420	3425	2.235618E+01	7.410374E-02
3425	3430	1.523220E+00	4.781374E-02
3430	3435	5.221740E+00	8.043255E-02
3435	3440	2.773140E+00	2.171435E-01
3420	3440	7.968570E+00	6.970130E-02
3440	3445	1.530296E+01	9.431856E-02
3445	3450	2.862378E+01	1.063442E-01
3450	3455	2.754000E-02	1.292000E-02
3455	3460	0.	1.000000E+00
3440	3460	1.098857E+01	5.000069E-02

Band Model Parameters for H_2O in 5 and 20 cm^{-1} intervals.

$\Delta\omega$ (1/cm)		k(300K) (cm^2/gm)	a_o(300K) (1/atm)
3980	3985	1.398596E+01	6.773658E-02
3985	3990	1.049524E+01	5.041934E-02
3990	3995	2.184140E+01	6.683676E-02
3995	4000	1.429798E+01	7.460738E-02
3980	4000	1.515514E+01	6.407850E-02
4000	4005	3.800740E+00	1.236323E-01
4005	4010	3.179608E+01	3.815846E-02
4010	4015	8.048140E+00	6.265781E-02
4015	4020	1.406664E+01	9.839532E-02
4000	4020	1.442790E+01	5.845969E-02
4020	4025	5.852800E-01	4.055709E-02
4025	4030	1.702744E+01	3.989627E-02
4030	4035	4.785400E+00	6.388479E-02
4035	4040	6.017400E-01	5.935423E-02
4020	4040	5.749965E+00	3.216364E-02
4040	4045	1.443256E+01	4.273756E-02
4045	4050	8.152240E+00	2.313270E-02
4050	4055	1.530220E+00	3.321405E-02
4055	4060	6.826600E-01	1.739902E-02
4040	4060	6.199420E+00	2.434819E-02
4060	4065	4.665940E+00	3.831239E-02
4065	4070	1.477200E-01	2.112989E-02
4070	4075	2.582320E+00	3.777456E-02
4075	4080	5.702920E+00	3.869164E-02
4060	4080	3.274725E+00	3.033566E-02
4080	4085	2.790240E+00	4.234074E-02
4085	4090	7.320600E+00	4.716274E-02
4090	4095	3.459000E-01	3.027278E-02
4095	4100	0.	1.000000E+00
4080	4100	2.614185E+00	2.554330E-02
4100	4105	3.537560E+00	2.774423E-02
4105	4110	9.787140E+00	5.151048E-02
4110	4115	4.736000E-02	2.516774E-02
4115	4120	0.	1.000000E+00
4100	4120	3.343015E+00	2.092084E-02
4120	4125	9.234200E-01	2.516386E-02
4125	4130	7.449800E-01	3.856715E-02
4130	4135	4.309080E+00	3.769435E-02
4135	4140	2.848080E+00	2.727268E-02
4120	4140	2.206390E+00	2.853490E-02
4140	4145	9.116000E-01	2.111480E-02
4145	4150	1.410160E+00	5.436328E-02
4150	4155	1.142460E+00	2.792154E-02
4155	4160	1.053320E+00	3.998775E-02
4140	4160	1.129385E+00	3.536883E-02

$\Delta\omega$ (1/cm)		k(300K) (cm^2/gm)	a_o(300K) (1/atm)
4160	4165	2.356000E-02	1.146000E-02
4165	4170	4.109800E-01	2.378882E-02
4170	4175	1.085620E+00	2.464935E-02
4175	4180	7.480000E-02	2.595780E-02
4160	4180	3.987400E-01	1.634860E-02
4180	4185	1.118360E+00	1.532037E-02
4185	4190	7.540200E-01	1.578784E-02
4190	4195	1.343180E+00	4.738973E-02
4195	4200	3.397600E-01	3.038429E-02
4180	4200	8.888300E-01	2.480224E-02
4200	4205	9.340400E-01	2.173745E-02
4205	4210	3.649400E-01	3.443246E-02
4210	4215	9.932000E-02	2.428103E-02
4215	4220	5.198400E-01	3.950425E-02
4200	4220	4.795350E-01	2.604197E-02
4220	4225	3.170200E-01	3.840487E-02
4225	4230	0.	1.000000E+00
4230	4235	2.513600E-01	2.651494E-02
4235	4240	7.134000E-02	2.408377E-02
4220	4240	1.599300E-01	2.129421E-02
4240	4245	1.003800E-01	3.555871E-02
4245	4250	0.	1.000000E+00
4250	4255	6.524400E-01	5.798780E-02
4255	4260	1.675400E-01	2.780157E-02
4240	4260	2.300900E-01	2.825177E-02
4260	4265	5.618000E-02	1.148000E-02
4265	4270	1.372000E-01	9.980000E-03
4270	4275	2.081800E-01	3.887755E-02
4275	4280	1.072600E-01	1.392000E-02
4260	4280	1.272050E-01	1.792496E-02
4280	4285	3.936000E-02	1.583755E-02
4285	4290	1.778000E-02	2.125943E-02
4290	4295	2.794000E-02	1.890998E-02
4295	4300	0.	1.000000E+00
4280	4300	2.127000E-02	1.334655E-02
4300	4305	6.178000E-02	2.570590E-02
4305	4310	1.550000E-01	1.688390E-02
4310	4315	2.452000E-02	1.268000E-02
4315	4320	1.364000E-02	8.920000E-03
4300	4320	6.373500E-02	1.404361E-02
4320	4325	0.	1.000000E+00
4325	4330	1.374000E-02	1.835152E-02
4330	4335	0.	1.000000E+00
4335	4340	1.510000E-02	1.288000E-02
4320	4340	7.210000E-03	7.710974E-03

Band Model Parameters for H_2O in 5 and 20 cm^{-1} intervals.

Δω (1/cm)		k(300K) (cm^2/gm)	a_o(300K) (1/atm)
4700	4705	0.	1.000000E+00
4705	4710	1.514000E-02	2.088000E-02
4710	4715	0.	1.000000E+00
4715	4720	1.338000E-02	3.807495E-02
4700	4720	7.130000E-03	1.427225E-02
4720	4725	3.664000E-02	1.988000E-02
4725	4730	0.	1.000000E+00
4730	4735	0.	1.000000E+00
4735	4740	2.118000E-02	4.023075E-02
4720	4740	1.445500E-02	1.364638E-02
4740	4745	0.	1.000000E+00
4745	4750	0.	1.000000E+00
4750	4755	0.	1.000000E+00
4755	4760	5.252000E-02	3.471327E-02
4740	4760	1.313000E-02	8.678318E-03
4760	4765	4.776000E-02	5.546265E-02
4765	4770	0.	1.000000E+00
4770	4775	0.	1.000000E+00
4775	4780	2.438000E-02	1.922000E-02
4760	4780	1.803500E-02	1.852540E-02
4780	4785	9.700000E-03	1.940000E-02
4785	4790	0.	1.000000E+00
4790	4795	0.	1.000000E+00
4795	4800	2.480000E-02	1.924000E-02
4780	4800	8.625000E-03	9.164008E-03
4800	4805	0.	1.000000E+00
4805	4810	6.420000E-03	1.262000E-02
4810	4815	2.762000E-02	3.597515E-02
4815	4820	6.500000E-03	1.898000E-02
4800	4820	1.013500E-02	1.643862E-02
4820	4825	5.760000E-03	1.342000E-02
4825	4830	1.804000E-02	2.761683E-02
4830	4835	0.	1.000000E+00
4835	4840	0.	1.000000E+00
4820	4840	5.950000E-03	1.016798E-02
4840	4845	2.498000E-02	2.666541E-02
4845	4850	8.040000E-03	1.768000E-02
4850	4855	2.818000E-02	3.341523E-02
4855	4860	1.522000E-02	2.874497E-02
4840	4860	1.910500E-02	2.610766E-02
4860	4865	2.340000E-02	1.768000E-02
4865	4870	6.000000E-03	1.776000E-02
4870	4875	0.	1.000000E+00
4875	4880	2.034000E-02	3.354385E-02
4860	4880	1.243500E-02	1.620595E-02

Δω (1/cm)		k(300K) (cm^2/gm)	a_o(300K) (1/atm)
4880	4885	0.	1.000000E+00
4885	4890	0.	1.000000E+00
4890	4895	1.528000E-02	2.746261E-02
4895	4900	0.	1.000000E+00
4880	4900	3.820000E-03	6.665654E-03
4900	4905	5.160000E-02	4.776003E-02
4905	4910	1.792000E-02	1.622000E-02
4910	4915	0.	1.000000E+00
4915	4920	4.852000E-02	3.669602E-02
4900	4920	2.951000E-02	2.511121E-02
4920	4925	1.614000E-02	2.853148E-02
4925	4930	5.280000E-02	5.397257E-02
4930	4935	3.770000E-02	4.366997E-02
4935	4940	3.542000E-02	2.510242E-02
4920	4940	3.551500E-02	3.712068E-02
4940	4945	3.106000E-02	1.466000E-02
4945	4950	3.930000E-02	3.196763E-02
4950	4955	5.872000E-02	4.022184E-02
4955	4960	2.156600E-01	1.000397E-01
4940	4960	8.618500E-02	4.614895E-02
4960	4965	1.233200E-01	4.524400E-02
4965	4970	1.075000E-01	3.026804E-02
4970	4975	0.	1.000000E+00
4975	4980	0.	1.000000E+00
4960	4980	5.770500E-02	1.879706E-02
4980	4985	2.577200E-01	4.921116E-02
4985	4990	4.624400E-01	7.411647E-02
4990	4995	1.650400E-01	2.981456E-02
4995	5000	8.098000E-02	2.094794E-02
4980	5000	2.415450E-01	4.330209E-02
5000	5005	4.052000E-01	3.998905E-02
5005	5010	1.564400E-01	2.391030E-02
5010	5015	7.382000E-01	4.743236E-02
5015	5020	0.	1.000000E+00
5000	5020	3.249600E-01	2.712958E-02
5020	5025	7.791600E-01	5.098769E-02
5025	5030	1.408600E-01	4.150631E-02
5030	5035	7.217200E-01	4.236620E-02
5035	5040	2.766600E-01	2.527967E-02
5020	5040	4.796000E-01	3.731458E-02
5040	5045	3.166400E-01	4.110362E-02
5045	5050	5.117800E-01	7.422455E-02
5050	5055	1.793520E+00	4.776309E-02
5055	5060	6.716000E-02	4.915356E-02
5040	5060	6.722750E-01	4.038952E-02

Band Model Parameters for H_2O in 5 and 20 cm^{-1} intervals (Cont'd).

Δω (1/cm)		k(300K) (cm^2/gm)	a_o(300K) (1/atm)
5060	5065	2.950800E-01	9.075015E-02
5065	5070	7.833200E-01	7.947063E-02
5070	5075	2.150200E+00	5.786203E-02
5075	5080	8.354000E-02	1.582761E-02
5060	5080	8.280350E-01	4.857689E-02
5080	5065	7.048200E-01	6.973457E-02
5085	5090	9.139800E-01	8.997215E-02
5090	5095	3.656020E+00	7.637437E-02
5095	5100	3.668120E+00	6.142457E-02
5080	5100	2.235735E+00	6.387123E-02
5100	5105	1.965260E+00	6.382954E-02
5105	5110	3.152340E+00	1.034877E-01
5110	5115	3.754440E+00	8.608766E-02
5115	5120	7.978900E+00	4.610853E-02
5100	5120	4.212735E+00	6.545165E-02
5120	5125	8.451200E-01	8.819241E-02
5125	5130	2.823600E+00	1.306756E-01
5130	5135	7.088680E+00	9.514976E-02
5135	5140	3.271040E+00	1.080296E-01
5120	5140	3.507160E+00	9.395874E-02
5140	5145	1.816410E+01	1.148952E-01
5145	5150	1.323260E+00	5.231989E-02
5150	5155	1.065332E+01	1.473064E-01
5155	5160	3.630418E+01	9.774202E-02
5140	5160	1.661121E+01	8.829245E-02

Absorption Coefficients for HCl

1/CM	MICRON	K(300°K) (atm^{-1} cm^{-1})	K(600°K) (atm^{-1} cm^{-1})
2200.	4.545	.000E-32	.562E-06
2225.	4.494	.000E-32	.431E-05
2250.	4.444	.000E-32	.806E-05
2275.	4.395	.000E-32	.118E-04
2300.	4.347	.000E-32	.155E-04
2325.	4.301	.000E-32	.918E-04
2350.	4.255	.000E-32	.168E-03
2375.	4.210	.000E-32	.244E-03
2400.	4.166	.722E-07	.320E-03
2425.	4.123	.451E-05	.139E-02
2450.	4.081	.896E-05	.247E-02
2475.	4.040	.134E-04	.354E-02
2500.	4.000	.178E-04	.462E-02
2525.	3.960	.112E-03	.140E-01
2550.	3.921	.207E-03	.235E-01
2575.	3.883	.105E-02	.330E-01
2600.	3.846	.191E-02	.424E-01
2625.	3.809	.767E-02	.852E-01
2650.	3.773	.134E-01	.127E 00
2675.	3.738	.411E-01	.170E 00
2700.	3.703	.688E-01	.213E 00
2725.	3.669	.154E 00	.280E 00
2750.	3.636	.240E 00	.348E 00
2775.	3.603	.375E 00	.380E 00
2800.	3.571	.509E 00	.412E 00
2825.	3.539	.566E 00	.370E 00
2850.	3.508	.465E 00	.260E 00
2875.	3.478	.168E 00	.867E-01
2900.	3.448	.258E 00	.129E 00
2925.	3.418	.644E 00	.339E 00
2950.	3.389	.815E 00	.493E 00
2975.	3.361	.720E 00	.555E 00
3000.	3.333	.469E 00	.515E 00
3025.	3.305	.272E 00	.386E 00
3050.	3.278	.756E-01	.257E 00
3075.	3.252	.390E-01	.156E 00
3100.	3.225	.240E-02	.547E-01
3125.	3.200	.120E-02	.289E-01
3150.	3.174	.596E-05	.320E-02
3175.	3.149	.298E-05	.160E-02
3200.	3.125	.693E-10	.129E-04

Absorption Coefficients for HF

1/CM	MICRON	K(300°K) (atm^{-1} cm^{-1})	K(600°K) (atm^{-1} cm^{-1})
3000.	3.333	.112E-12	.684E-06
3025.	3.305	.266E-09	.115E-04
3050.	3.278	.532E-09	.224E-04
3075.	3.252	.799E-09	.333E-04
3100.	3.225	.106E-08	.441E-04
3125.	3.200	.133E-08	.550E-04
3150.	3.174	.159E-08	.659E-04
3175.	3.149	.186E-08	.768E-04
3200.	3.125	.213E-08	.877E-04
3225.	3.100	.137E-05	.785E-03
3250.	3.076	.274E-05	.148E-02
3275.	3.053	.411E-05	.218E-02
3300.	3.030	.549E-05	.287E-02
3325.	3.007	.686E-05	.357E-02
3350.	2.985	.823E-05	.427E-02
3375.	2.962	.961E-05	.497E-02
3400.	2.941	.109E-04	.566E-02
3425.	2.919	.126E-02	.496E-02
3450.	2.898	.252E-02	.425E-02
3475.	2.877	.378E-02	.354E-02
3500.	2.857	.504E-02	.284E-02
3525.	2.836	.629E-02	.213E-02
3550.	2.816	.755E-02	.142E-02
3575.	2.797	.881E-02	.721E-03
3600.	2.777	.100E-01	.144E-04
3625.	2.758	.996E-01	.108E 00
3650.	2.739	.189E 00	.215E 00
3675.	2.721	.278E 00	.323E 00
3700.	2.702	.368E 00	.431E 00
3725.	2.684	.458E 00	.539E 00
3750.	2.666	.547E 00	.647E 00
3775.	2.649	.637E 00	.755E 00
3800.	2.631	.726E 00	.863E 00
3825.	2.614	.772E 00	.824E 00
3850.	2.597	.817E 00	.784E 00
3875.	2.580	.863E 00	.744E 00
3900.	2.564	.909E 00	.704E 00
3925.	2.547	.954E 00	.664E 00
3950.	2.531	.100E 01	.625E 00
3975.	2.515	.104E 01	.585E 00
4000.	2.500	.109E 01	.545E 00
4025.	2.484	.119E 01	.722E 00
4050.	2.469	.130E 01	.899E 00
4075.	2.453	.141E 01	.107E 01
4100.	2.439	.152E 01	.125E 01
4125.	2.424	.117E 01	.107E 01
4150.	2.409	.835E 00	.886E 00
4175.	2.395	.490E 00	.703E 00
4200.	2.380	.145E 00	.519E 00
4225.	2.366	.109E 00	.398E 00
4250.	2.352	.728E-01	.277E 00
4275.	2.339	.366E-01	.156E 00
4300.	2.325	.477E-03	.359E-01
4325.	2.312	.357E-03	.269E-01
4350.	2.298	.238E-03	.180E-01
4375.	2.285	.119E-03	.904E-02
4400.	2.272	.163E-08	.719E-04

Absorption Coefficients for CH_4

1/CM	MICRON	K (300°K) (atm^{-1} cm^{-1})
1195.	8.368	.857E-01
1216.	8.223	.420E 00
1234.	8.105	.133E 01
1246.	8.026	.322E 01
1250.	8.000	.101E 01
1256.	7.960	.201E 01
1263.	7.915	.485E 01
1266.	7.900	.322E 01
1277.	7.828	.121E 01
1288.	7.762	.209E 01
1293.	7.736	.734E 01
1299.	7.697	.946E 01
1305.	7.664	.689E 00
1314.	7.610	.246E 00
1325.	7.550	.195E 01
1333.	7.500	.366E 01
1341.	7.455	.443E 01
1351.	7.400	.379E 01
1352.	7.395	.555E 01
1370.	7.300	.205E 01
1389.	7.200	.143E 00
1404.	7.125	.264E-01
1429.	7.000	.323E-01
1449.	6.900	.353E-01
1471.	6.800	.304E-01
1493.	6.700	.157E-01
1504.	6.650	.122E-01
1515.	6.600	.989E-02
1527.	6.550	.762E-02
1541.	6.489	.412E-01
1563.	6.400	.804E-02
1575.	6.350	.573E-02
1587.	6.300	.673E-02
1613.	6.200	.940E-02
1639.	6.100	.103E-01
1667.	6.000	.757E-02
2700.	3.704	.150E-01
2800.	3.571	.400E-01
2850.	3.509	.720E-01
2885.	3.466	.152E 00
2900.	3.448	.253E 00
2915.	3.431	.400E 00
2925.	3.419	.570E 00
2940.	3.401	.900E 00
2957.	3.382	.100E 01
2975.	3.361	.860E 00
2985.	3.350	.670E 00
2993.	3.341	.442E 00
3000.	3.333	.750E 00
3010.	3.322	.267E 01
3020.	3.311	.400E 01
3030.	3.300	.930E 00
3037.	3.293	.505E 00
3050.	3.279	.900E 00
3060.	3.268	.114E 01
3075.	3.252	.135E 01
3086.	3.240	.140E 01
3095.	3.231	.137E 01
3100.	3.226	.131E 01
3110.	3.215	.110E 01
3125.	3.200	.740E 00
3150.	3.175	.262E 00
3160.	3.164	.150E 00
3175.	3.150	.680E-01
3200.	3.125	.100E-01
4082.	2.450	.143E-01
4132.	2.420	.312E-01
4153.	2.408	.545E-01
4172.	2.397	.901E-01
4186.	2.389	.124E 00
4195.	2.384	.183E 00
4203.	2.379	.249E 00
4209.	2.376	.305E 00
4227.	2.366	.422E 00
4294.	2.329	.305E 00
4354.	2.297	.249E 00
4390.	2.278	.183E 00
4435.	2.255	.124E 00
4456.	2.244	.901E-01
4496.	2.224	.545E-01
4498.	2.223	.312E-01
4552.	2.197	.143E-01

Absorption Coefficients for C_2H_4

1/CM	MICRON	K(300°) (atm^{-1} cm^{-1})
813.	12.300	.828E+00
819.	12.200	.969E+00
826.	12.100	.142E+01
833.	12.000	.289E+01
840.	11.900	.517E+01
847.	11.800	.899E+01
854.	11.700	.138E+02
862.	11.600	.208E+02
869.	11.500	.293E+02
877.	11.400	.404E+02
884.	11.300	.460E+02
892.	11.200	.549E+02
900.	11.100	.612E+02
909.	11.000	.657E+02
917.	10.900	.702E+02
925.	10.800	.854E+02
934.	10.700	.109E+03
943.	10.600	.261E+03
946.	10.563	.731E+03
952.	10.500	.226E+03
955.	10.468	.182E+03
961.	10.400	.101E+03
970.	10.300	.872E+02
980.	10.200	.778E+02
990.	10.100	.717E+02
1000.	10.000	.633E+02
1010.	9.900	.552E+02
1020.	9.800	.430E+02
1030.	9.700	.279E+02
1041.	9.600	.172E+02
1052.	9.500	.114E+02
1063.	9.400	.782E+01
1075.	9.300	.406E+01
1086.	9.200	.255E+01
1098.	9.100	.176E+01
1111.	9.000	.828E+00
1123.	8.900	.567E+00
1136.	8.800	.393E+00
1149.	8.700	.329E+00
2939.	3.402	.352E+01
3022.	3.308	.184E+02
3108.	3.217	.303E+02
3158.	3.166	.184E+02
3187.	3.137	.352E+01

Absorption Coefficients for PAN

1/CM	MICRON	K(300°) (atm^{-1} cm^{-1})
757.	13.200	.683E+00
763.	13.100	.131E+01
769.	13.002	.228E+01
775.	12.900	.416E+01
781.	12.800	.117E+02
787.	12.700	.448E+02
793.	12.600	.790E+02
800.	12.500	.296E+02
806.	12.400	.106E+02
811.	12.330	.965E+01
819.	12.200	.124E+02
826.	12.100	.990E+01
833.	12.000	.868E+01
840.	11.900	.496E+01
847.	11.800	.826E+00
1111.	9.000	.630E+00
1123.	8.900	.119E+01
1136.	8.800	.777E+01
1149.	8.700	.462E+02
1165.	8.580	.138E+03
1176.	8.500	.428E+02
1190.	8.400	.138E+01
1204.	8.300	.119E+01
1250.	8.000	.239E+01
1265.	7.900	.144E+02
1283.	7.790	.978E+02
1298.	7.700	.546E+02
1315.	7.600	.153E+02
1333.	7.500	.113E+02

C_6H_6 - BENZENE

1/CM	MICRON	K(300° K) (atm^{-1} cm^{-1})
1007.	9.923	.923E+00
1013.	9.867	.471E+01
1018.	9.821	.150E+02
1023.	9.773	.226E+02
1029.	9.712	.183E+02
1035.	9.658	.464E+02
1036.	9.648	.590E+02
1038.	9.629	.464E+02
1040.	9.610	.150E+02
1042.	9.588	.905E+01
1046.	9.559	.150E+02
1049.	9.524	.188E+02
1053.	9.490	.150E+02
1059.	9.437	.471E+01
1064.	9.397	.923E+00
3011.	3.321	.923E+00
3033.	3.300	.471E+01
3037.	3.292	.150E+02
3042.	3.287	.464E+02
3058.	3.270	.170E+03
3124.	3.201	.464E+02
3139.	3.185	.150E+02
3147.	3.177	.471E+01
3150.	3.174	.923E+00

O_3 - OZONE

1/CM	MICRON	K(300° K) (atm^{-1} cm^{-1})
1006.	9.940	.235E+01
1010.	9.900	.345E+01
1017.	9.830	.500E+01
1024.	9.770	.615E+01
1028.	9.722	.915E+01
1036.	9.650	.585E+01
1043.	9.590	.405E+01
1049.	9.530	.790E+01
1054.	9.490	.950E+01
1057.	9.460	.865E+01
1063.	9.400	.405E+01

REFERENCES

1. Study of Critical Environmental Problems (SCEP), MIT Press, 1970.

2. Study of Man's Impact on Climate (SMIC), MIT Press, 1971.

3. C. B. Ludwig, R. Bartle and M. Griggs, "Study of Air Pollutant Detection by Remote Sensors," NASA CR-1380, July 1969.

4. T. C. Chamberlain, J. Geology 7, 575, 667, 751 (1899).

5. E. Robinson and R. C. Robbins, "Sources, Abundance, and Fate of Gaseous Atmospheric Pollutants" SRI (1968); Supplement (June 1969).

6. R. Revelle, Report of the Environmental Pollution Panel, President's Science Advisory Committee, White House (Nov. 1965).

7. S. Manabe, R. T. Wetherald, J. Atmos. Sci. 24, 241 (1967).

8. F. Moller, J. Geophys. Res. 68, 3877 (1963).

9. R. A. McCormick and J. A. Ludwig, Science 156, 1358 (1967).

10. G. S. Callendar, Tellus 10, 243 (1958).

11. J. F. S. Chin, H. T. Ellis, B. G. Mendonca, R. F. Pueschel, and H. J. Simpson, NOAA Tech. Mem. ERL APCL-13 (July 1971).

12. M. U. Migeotte, Phys. Rev. 75, 1108 (1949).

13. W. Benesch, M. Migeotte and L. Neven, JOSA 43, 1119 (1953).

14. S. L. Locke and G. Herzberg, Can. J. Phys. 31, 504 (1953).

15. S. H. Shaw, Astrophys. J. 128, 428 (1958).

16. R. C. Robbins, K. M. Borg and E. Robinson, J. Air Poll. Contr. Assoc. 18, 106 (1968).

17. E. Robinson and R. C. Robbins, Antarct. J. 3, 194 (1968); J. Geophys. Res. 74, 1968 (1969).

18. J. Pressman and P. Warneck, J. Atmos. Sci. 27, 155 (1970).

19. W. Seiler and C. Junge, J. Geophys. Res. 75, 2217 (1970).

20. C. Junge, W. Seiler and P. Warneck, J. Geophys. Res. 76, 2866 (1971).

21. D. F. Wilson, J. W. Swinnerton and R. A. Lamontagne, Science 168, 1577 (1970).

22. K. Westberg and N. Cohen, Science 171, 1013 (1971).

23. J. W. Swinnerton, R. A. Lamontagne and V. J. Linnenbom, Science 172, 943 (1971).

24. L. S. Jaffe, J. Air Poll. Contr. Assoc. 18, 534 (1968).

25. R. E. Inman, R. B. Ingersoll and E. A. Levy, Science 172, 1229 (1971).

26. P. B. Hays and J. J. Olivero, Planet Space Sci. 18, 1729 (1970).

27. H. Levy II, Science 173, 141 (1971).

28. B. Weinstock, H. Niki, Science 176, 290 (1972).

29. C. M. Stevens, L. Krout, D. Walling, A. Venters, E. Engelkemeir, and L. E. Ross, "The Isotopic Composition of Atmospheric Carbon Monoxide" presented at "Sources, Sinks and Concentrations of Carbon Monoxide and Methane in the Earth's Environment", Joint Meeting of the Am. Geoph. U. and Am. Met. Soc., St. Petersburg Beach, Florida (Aug. 14-17, 1972). (Also submitted to Earth and Planetary Science Letters.)

30. E. R. Stephens, "The Formation, Reactions and Properties of PAN in Photochemical Air Pollution" in Advances in Environmental Science, J. Pitts and R. Metcalf, eds., John Wiley & Sons, Inc. (1969).

31. J. M. Heuss and W. A. Glasson, Environ. Sci. Technol. 2, 1109 (1968).

32. J. P. Lodge, Jr. and J. B. Pate, Science 153, 408 (1966).

33. H. L. Hamilton, J. J. B. Worth and L. A. Ripperton, U. S. Army Research Office, Contract No. DA-HC19-67-C-0029 (May 1968).

34. D. G. Murcray, T. G. Kyle, F. H. Murcray, and W. J. Williams, JOSA 59, 1131 (1969).

35. C. E. Junge, Air Chemistry and Radioactivity, Academic Press, N. Y. (1963).

36. D. H. Ehhalt, J. Air Poll. Contr. Assoc. 17, 518 (1967).

37. A. E. Bainbridge and L. E. Heidt, Tellus 18, 221 (1966).

38. T. G. Scholz, D. H. Ehhalt, L. E. Heidt, and E. A. Martell, J. Geophys. Res. 75, 3049 (1970).

39. J. C. McConnell, M. B. McElroy, and S. C. Wofsy, Nature 233, 187 (1971).

40. E. R. Stephens, E. F. Darley and F. R. Burleson, "Sources and Reactivity of Light Hydrocarbons in Ambient Air," Reprint No. 35-67, 32nd Midyear Meeting of the American Petroleum Institute, Los Angeles, Calif. (May 16, 1967).

41. Study of Critical Environmental Problems (SCEP), MIT Press, p. 100, 1970.

42. H. Harrison, Science 170, 734 (1970).

43. A. Ferri, Astron. & Aeron. 10, No. 7, p. 37 (1972).

44. M. Griggs, "Atmospheric Ozone," Chapter 4 in The Middle Ultraviolet A.E.S. Green, ed., John Wiley & Sons, Inc. (1966).

45. H. Johnston, Science 173, 517 (1971).

46. M. T. Ellis and R. F. Pueschel, Science 172, 845 (1971).

47. G. M. Hidy and J. R. Brock, Proc. Second International Clean Air Congress, ed. H. M. Englund and W. T. Beery, Academic Press, New York, p. 1088, (1971).

48. R. A. McCormick and J. H. Ludwig, Science 156, 1358 (1967).

49. G. D. Robinson, "Long-Term Effects of Air Pollution," Center for the Environment and Man, Inc., Hartford, Rept. No. CEM 4029-400 (1970).

50. R. J. Charlson and M. J. Pilat, J. Appl. Meteor. 8, 1001 (1969).

51. M. A. Atwater, Science 170, 64 (1970).

52. J. M. Mitchell, Jr., J. Appl. Meteor. 10, 703 (1971).

53. L. Elterman, Atmospheric Attenuation Model, 1964, in the Ultraviolet, Visible, and Infrared Regions for Altitudes to 50 km, Report AFCRL-64-740, AFCRL, Bedford, Mass. (1964).

54. G. N. Plass and G. W. Kattawar, Appl. Optics 9, 1122 (1970).

55. J. S. Curcio, G. L. Knestrick and T. H. Cosden, Atmospheric Scattering in the Visible and Infrared, NRL Rpt. 5567, U.S. Naval Research Laboratory, Washington, D.C. (1961).

56. J. V. Dave and P. M. Furukawa, Meteorol. Monograph, Vol. 7 (1966).

57. L. Elterman, "UV, Visible and IR Attenuation for Altitudes to 50 km, 1968", AFCRL-68-0153 (April 1968).

58. H. C. Van de Hulst, *Light Scattering by Small Particles*, John Wiley & Sons, Inc., New York (1957).

59. D. Deirmendjian, Appl. Optics 3, 187 (1964).

60. R. A. Toth and C. B. Farmer, Paper No. 71-1109, Joint Conference on Sensing of Environmental Pollutants, Palo Alto, California (Nov. 8-10, 1971).

61. "Monitoring of Air Pollution by Satellites," NASA, CR112137 (April 1972).

62. *Handbook of Geophysics and Space Environments*, ed. S. L. Valley, McGraw-Hill Book Co. (1965).

63. M. Gutnick, "Aids for Computing Stratospheric Moisture," GRD Research Notes No. 50. AFCRL 203 (1961).

64. W. A. Hovis, Jr., Appl. Optics 5, 245 (1966).

65. K. Ya. Kondratiev, G. A. Nicolsky, I. Ya. Badinov, and S. D. Andreev, Appl. Optics 6, 197 (1967).

66. H. J. Mastenbrook, J. Atmos. Sci. 25, 299 (1968).

67. F. Saiedy, D. T. Hilleary and W. A. Morgan, Appl. Opt. 4, 495 (1965).

68. J. M. Russell III, "The Measurement of Atmospheric Ozone Using Satellite Infrared Observations in the 9.6 m Band," Univ. of Michigan, 03635-1-T (July 1970).

69. J. M. Russell III, J. Atmos. Sci. 29, 376 (1972).

70. J. C. Gille, J. Geophys. Res. 73, 1863 (1968); Bull. Amer. Meteor. Soc. 49, 903 (1968).

71. T. B. McKee, B. I. Whitman, J. J. Lambiotte, NASA TND-5068 (1969).

72. F. B. House and G. Ohring, NASA CR-1419 (1969).

73. J. C. Gille and F. B. House, J. Atm. Sci. 28, 1427 (1971).

74. A. Javan, "Stimulated Raman Effect," p. 284, Quantum Electronics and Coherent Light, ed. P. A. Miler, Academic Press (1964).

75. H. Kildal and R. L. Byer, IEEE 59, 1644 (1971).

76. A. E. Siegman, An Introduction to Lasers and Masers, McGraw-Hill Book Co. (1971).

77. C. E. Junge, J. Meteorol. 12, 13 (1955).

78. M. Corn, Air Pollution I (Ed. A. C. Stern), Academic Press, N.Y. (1968).

79. K. Bullrich, Advances in Geophysics, 10, 99 (1964).

80. C. W. Chagnon and C. E. Junge, J. Meteorol. 18, 746 (1961).

81. J. M. Waldram, Q. J. Roy, Meteorol. Soc. 71, 319 (1965).

82. F. Volz, Ann. Meteorol. 8, 34 (1957).

83. A. J. Blanco and R. G. McIntyre, Atmos. Environ. 6, 57 (1972).

84. F. E. Volz, J. Geophys. Res. 77, 1017 (1972); also Appl. Opt. 11, 755 (1972).

85. G. V. Rosenberg, Soviet Physics Uspekhi 3, 346 (1960).

86. Z. Sekera, Icarus 6, 348 (1967).

87. G. N. Plass and G. W. Kattawar, Appl. Opt. 9, 1122 (1970).

88. K. L. Coulson, General Electric Report R64 SD74 (1964).

89. J. W. Hovenier, J. Atmos. Sci. 26, 488 (1969).

90. A. McLellan, "Satellite Remote Sensing of Large Scale Local Atmospheric Pollution," Proc. 2nd Int. Clean Air Congress, ed. H. M. Englund and W. T. Beery, Academic Press, New York, p. 570 (1971).

91. T. A. Hariharan, Pure Appl. Geophys. 77, 151 (1969).

92. K. L. Coulson, G. M. B. Bouricius and E. L. Gray, General Electric Report R65 SD64 (1965).

93. S. Chandrasekhar, Radiative Transfer, Oxford University Press, London (1950).

94. J. V. Dave, Appl. Opt. 9, 2673 (1970).

95. T. A. Hariharan, J. Sci. Instr. 2, (Ser 2), 1135 (1969).

96. S. Q. Duntley, JOSA 38, 179 (1948).

97. "Determination of Aerosol Content in the Atmosphere from ERTS-A Data", Science Applications, Inc. Report No. SAI 72-39-LJ (March 1972).

98. E. V. Ashburn and R. G. Weldon, JOSA 46, 583 (1956).

99. M. Griggs, J. Appl. Meteorol. 7, 1012 (1968).

100. G. L. Clarke, G. C. Ewing, and C. J. Lorenzen, Science 167, 1119 (1970).

101. G. V. Rosenberg, Bull. (Izv.) Acad. Sci. USSR Atm. and Oceanic Phys. 3, No. 7 (1967).

102. E. Raschke, Beitr. Phys. Atmos. 45, 1 (1972).

103. M. Griggs and W. Marggraf, Final Report, AFCRL-68-0003, (1967).

104. R. D. Rawcliffe, G. E. Meloy, R. M. Friedman and E. M. Rogers, J. Geophys. Res. 68, 6419 (1963).

105. D. E. Miller and K. M. Stewart, Proc. Roy. Soc. A288, 540 (1965).

106. J. Pepin, "The Use of Extinction from High Altitude Balloons as a Probe of the Atmospheric Aerosols", ONR Contract Rept. No. AF-31, University of Minnesota (October 1969).

107. J. T. Houghton and G. E. Hunt, Quart. J. R. Meteor. Soc. 97 (1971).

108. A. E. S. Green and M. Griggs, Appl. Opt. 2, 56 (1963).

109. "Climatic Impact Assessment Program," Proc. Survey Conf., ed. A. E. Barrington, DOT-TSC-OST-72-13 (1972).

110. C. R. Gray, H. L. Malchow, D. C. Merritt and R. E. Var, "Aerosol Monitoring by Satellite Horizon Scanning," Paper No. 71-1111, Joint Conference on Sensing of Environmental Pollutants, Palo Alto, California (Nov. 8-10, 1971).

111. G. I. Marchuk, G. A. Mikhailov, M. A. Nazaralier and R. A. Darbimian, "The Resolution of Direct and Some Inverse Problems of Atmospheric Optics by the Monte-Carlo Method," Academy of Sciences, Novosibirsk (1968).

112. E. E. Uthe and W. B. Johnson, "Lidar Observations of the Lower Tropospheric Aerosol Structure During BOMEX", SRI Project 7929 (Jan. 1971).

113. R. T. H. Collis, Appl. Opt. 9, 1785 (1970).

114. A. C. Holland and G. Gagne, Appl. Opt. 9, 1113 (1970).

115. J. A. Reagan and B. M. Herman, Paper No. 71-1057, Joint Conference on Sensing of Environmental Pollutants, Palo Alto, California (Nov. 8-10, 1971).

116. W. E. Evans, "Remote Probing of High Cloud Cover via Satellite-Borne Radar", Stanford Research Institute, Final Report NASA-49 (27) (Aug. 1968).

117. J. Strong, Appl. Opt. 6, 179 (1967).

118. A. R. Barringer and J. P. Schock, Proc. 4th Symposium Rem. Sens. of Environ., at U. Michigan, p. 779 (1966).

119. L. L. Acton, E. R. Bartle, C. B. Ludwig and M. L. Streiff, "Development of Optical Correlation Methods", Report No. GDC-ERR-1486, General Dynamics/Convair (December 1970).

120. E. D. Nelson, M. L. Fredman, JOSA 60, 1664 (1970).

121. J. A. Decker, Jr., Appl. Opt. 10, 510 (1971).

122. J. H. Davies, Anal. Chem. 42, 101A (1970).

123. R. H. Kummler, R. N. Grenda, T. Baurer, and M. H. Bortner, J. H. Davies, and J. MacDowall, presented 50th Ann. Meeting Am. Geoph. Union, Washington, D.C. (April 25, 1969).

124. M. M. Millan, S. J. Townsend and J. Davies, "Study of the Barringer Refractor Plate Correlation Spectrometer as a Remote Sensing Instrument," Toronto, UTIAS Report, No. 146 (August 1970).

125. G. S. Newcomb and M. M. Millan, IEEE Trans. Geosci. Electronics GE-8, 149 (1970).

126. J. H. Davies and A. J. Moffat, Proc. 2nd Int. Clean Air Congress, ed. H. M. Englund and W. T. Berry, Academic Press, New York, p. 522 (1971).

127. C. R. McCreight and C. L. Tien, Paper No. 71-1061, Joint Conference on Sensing of Environmental Pollutants, Palo Alto, California (Nov. 8-10, 1971).

128. "Development of a Prototype Remote Sensor for Air Pollution Detection", Progress Report, GDC-DBE70-002 (May 1970).

129. K. F. Luft, Z. Techn. Phys. 24, 97 (1943).

130. A. H. Pfund, Sci. 90, 326 (1939); Bull. Johns Hopk. Hos. 67, 61 (1940).

131. H. Schmick, U. S. Patent No. 1, 758, 088.

132. N. Wright and L. W. Herscher, JOSA 36, 195 (1946).

133. W. G. Fastie and A. H. Pfund, JOSA 37, 762 (1947).

134. L. E. Maley, ISA J. 5, 85 (1958).

135. E. R. Bartle, S. Kaye and E. A. Meckstroth, J. Spacecraft and Rockets 9, 836 (1972).

136. S. D. Smith and C. R. Pidgeon, Proc. XII Intern. Astrophys. Symp. Liege, p. 336 (June 24, 1963).

137. J. J. Barnett, M. J. Cross, R. S. Harwood, J. T. Houghton, C. G. Morgan, G. E. Peckham, C. D. Rodgers, S. D. Smith, and E. J. Williamson, Quart. J. Roy. Met. 98, 17 (1972).

138. R. Goody, JOSA 58, 900 (1968).

139. C. B. Ludwig, L. L. Acton, M. Griggs, G. D. Hall and W. Malkmus, Paper No. 71-1107, Joint Conference on Sensing of Environmental Pollutants, Palo Alto, California (Nov. 8-10, 1971).

140. "Development of the Gas Filter Correlation Instrument for Air Pollution Detection," General Dynamics, Report No. GDCA-HAB-73-011 (Aug. 1972).

141. L. W. Chaney, S. R. Drayson, and C. Young, Appl. Optics 6, 347 (1967).

142. R. A. Hanel and L. W. Chaney, Proc. 17th Intern. Astron. Congress, Madrid, Dunod, Paris, Vol. 2 (1966).

143. R. A. Hanel, B. Schlachman, F. D. Clark, C. H. Prokesh, J. B. Taylor, W. M. Wilson, and L. Chaney, Appl. Optics 9, 1767 (1970).

144. R. A. Hanel, B. Schlachman, D. Rogers, and D. Vanous, Appl. Optics, 10, 1376 (1971).

145. R. B. Blackman and J. W. Tukey, "The Measurement of Power Spectra, Dover Publ. Inc., New York (1958).

146. R. A. Hanel and B. J. Conrath, Nature 228, 143 (1970); B. J. Conrath, R. A. Hanel, V. G. Kunde, and C. Prabhakara, J. Geophys. Res. 75, 5831 (1970).

147. R. N. Grenda, M. H. Bortner, P. J. LeBel, J. H. Davies, and R. Dick, Paper No. 71-1120, Joint Conference on Sensing of Environmental Pollutants, Palo Alto, California (Nov. 8-10, 1971).

148. J. Connes and P. Connes, J. Opt. Soc. Am. 56, 896 (1966).

149. R. Beer, Appl. Opt. 6, 209 (1967).

150. R. Beer and D. Marjaniemi, Appl. Opt. 5, 1191 (1966).

151. P. Connes, Proc. Conf. New Methods of Instrumental Spectroscopy, Centre National de Recherche Scientifique, Paris (1967).

152. M. Cuisenier and J. Pinard, ibid.

153. R. A. Schindler, Appl. Optics 9, 301 (1970).

154. R. A. Schindler, Paper No. 71-1108, Joint Conference on Sensing of Environmental Pollutants, Palo Alto, California (Nov. 8-10, 1971).

155. R. T. Menzies, Appl. Opt. 10, 1532 (1971).

156. R. T. Menzies and M. S. Shumate, Paper No. 71-1083, Joint Conference on Sensing of Environmental Pollutants, Palo Alto, California (Nov. 8-10, 1971).

157. M. C. Johnson, Proc. Second International Clean Air Congress, ed. H. M. Englund and W. T. Beery, Academic Press, New York, p. 490 (1971).

158. I. M. Pikus, H. W. Goldstein and T. R. Riethof, Paper 71-1112, Joint Conference on Sensing of Environmental Pollutants, Palo Alto, California (Nov. 8-10, 1971).

159. R. S. Reynolds, "Space Qualified CO_2 Laser," Final Report, Contract No. NAS12-2021, GTE Sylvania Inc., Mountain View, Calif. (July 1971).

160. W. P. Kolb, "Research Directed Toward Perfecting a Design for a Space Qualified He-Ne Laser," Final Report Contract No. NAS12-579, Hughes-Electron Dynamics Div., Torrance, Calif. (January 1970).

161. D. C. Forster, F. E. Goodwin, and W. B. Bridges. IEEE J. Quant. Electron, Vol. QE-8, 263 (1972).

162. W. S. Benedict, R. Herman, G. E. Moore, and S. Silverman, Astrophys, J. 135, 277 (1962).

163. D. M. Gates, R. F. Calfee, D. W. Hansen, and W. S. Benedict, "Line Parameters and Computed Spectra for Water Vapor Bands at 2.7 Microns," NBS Monograph 71 (1964).

164. W. S. Benedict and R. F. Calfee, "Line Parameters for the 1.9 and 6.3 Micron Water Vapor Bands," ESSA Professional Paper 2 (1967).

165. M. Migeotte, L. Neven, and J. Swensson, "The Solar Spectrum from 2.8 to 23.7 Microns," Liege, Belgium (1956).

166. J. H. Shaw, R. M. Chapman, J. N. Howard, and M. L. Oxholm, Astrophys. J. 113, 45 (1951).

167. O. C. Mohler, A. K. Pierce, R. R. McMath, and L. Goldberg, "Photometric Atlas of the Near Infrared Solar Spectrum", University of Michigan Press (1950).

168. J. N. Howard and J. H. Shaw, Phys. Rev. 87, 679 (1952).

169. S. S. Penner, Quantitative Molecular Spectroscopy and Gas Emissivities, Addison-Wesley Publishing Co., (1959).

170. C. P. Courtoy, Annales de la Societe Scientifique de Bruxelles 73, 5 (1959).

171. R. W. Boese, J. H. Miller, E. C. Y. Inn, and L. P. Giver, J. Quant. Spectry. Radiative Transfer 8, 1001 (1968).

172. D. E. Burch, J. D. Pembrook, and D. A. Gryvnak, "Absorption and Emission by SO_2 Between 1050 and 1400 cm^{-1} (9.5-7.1 μm)", Aeronutronic Publ. No. U-4947 (July 1971).

173. J. H. Shaw, M. L. Oxholm, and H. H. Claassen, Astrophys. J. 116, 77 (1952).

174. G. Abe, F. Myers, T. K. McCubbin, and S. R. Polo, J. Mol. Spectry. 38, 552 (1971).

175. P. L. Hanst, Appl. Spectry. 24, 161 (1970).

176. L. L. Abels and J. H. Shaw, J. Mol. Spectry. 20, 11 (1966).

177. E. K. Plyler, E. D. Tidwell, and A. G. Maki, J. Res. NBS 68A, 79 (1964).

178. G. D. Yale, D. L. Ford, and J. H. Shaw, Appl. Opt. 7, 695 (1968).

179. E. D. Tidwell, E. K. Plyler, and W. S. Benedict, J. Opt. Soc. Am. 50, 1243 (1960).

180. R. M. Goody, Atmospheric Radiation. I. Theoretical Basis, Oxford University Press, London (1964).

181. J. S. Garing, H. H. Nielsen, and K. N. Rao, J. Mol. Spectry. 3, 496 (1959).

182. W. L. France and D. Williams, J. Opt. Soc. Am. 56, 70 (1966).

183. W. S. Benedict, E. K. Plyler, and E. D. Tidwell, J. Chem. Phys. 32, 32 (1960).

184. W. S. Benedict, E. K. Plyler, and E. D. Tidwell, J. Res. NBS 61, 123 (1958).

185. G. Herzberg, Molecular Spectra and Molecular Structure: II. Infrared and Raman Spectra of Polyatomic Molecules, D. Van Nostrand Company, Inc., Princeton, New Jersey (1945).

186. H. H. Nielsen, Phys. Rev. 46, 117 (1934).

187. R. Penndorf, "Research on Aerosol Scattering in the Infrared. Scientific Report No. 2. Mie Scattering in the Forward Area," Technical Report RAD-TR-60-10 (February, 1960).

188. R. J. Charlson, N. C. Ahlquist, M. Selvidge, and P. B. MacCready, Jr., J. Air Poll. Contr. Assoc. 19, 937 (1969).

189. R. A. McCormick and D. M. Baulch, J. Air Poll. Contr. Assoc. 12, 492 (1962).

190. M. Griggs, J. Air Poll. Contr. Assoc. 22, 356 (1972).

191. F. F. Hall, Appl. Opt. 7, 891 (1968).

192. F. R. Valovcin, Appl. Meteor. 7, 817 (1968).

193. "Infrared Satellite Backgrounds", Boeing Report AFCRL-1069 (I) (Sept. 1961).

194. J. E. Hansen and J. B. Pollack, J. Atmos. Sci. 27, 265 (1970).

195. G. N. Plass, J. Opt. Soc. Am. 48, 690 (1958); D. E. Burch, J. N. Howard, and D. Williams, J. Opt. Soc. Am. 46, 334 (1956).

196. W. Malkmus and A. Thomson, J. Quant. Spectry. Radiative Transfer 2, 70 (1962).

197. A. Thomson, in "Proceedings of Specialist Conference on Molecular Radiation" (NASA TMX-53711) pp. 137-163 (Oct. 6/7, 1967).

198. D. E. Burch, E. B. Singleton, and D. Williams, Applied Optics 1, 359 (1962).

199. R. H. Pierson, A. N. Fletcher, and E. St. Clair Gantze, Anal. Chem. 28, 1218 (1956).

200. C. D. Walshaw, Quart. J. Roy. Met. Soc. 83, 315 (1957).

201. P. A. Leighton, *Photochemistry of Air Pollution*, Academic Press, New York, 1961.

☆U.S. GOVERNMENT PRINTING OFFICE: 1973-739-155/68

NATIONAL AERONAUTICS AND SPACE ADMINISTRATION
WASHINGTON, D.C. 20546

OFFICIAL BUSINESS
PENALTY FOR PRIVATE USE $300

SPECIAL FOURTH-CLASS RATE
BOOK

POSTAGE AND FEES PAID
NATIONAL AERONAUTICS AND
SPACE ADMINISTRATION
451

U.S.MAIL

POSTMASTER : If Undeliverable (Section 158
Postal Manual) Do Not Return

> *"The aeronautical and space activities of the United States shall be conducted so as to contribute . . . to the expansion of human knowledge of phenomena in the atmosphere and space. The Administration shall provide for the widest practicable and appropriate dissemination of information concerning its activities and the results thereof."*
>
> —NATIONAL AERONAUTICS AND SPACE ACT OF 1958

NASA SCIENTIFIC AND TECHNICAL PUBLICATIONS

TECHNICAL REPORTS: Scientific and technical information considered important, complete, and a lasting contribution to existing knowledge.

TECHNICAL NOTES: Information less broad in scope but nevertheless of importance as a contribution to existing knowledge.

TECHNICAL MEMORANDUMS: Information receiving limited distribution because of preliminary data, security classification, or other reasons. Also includes conference proceedings with either limited or unlimited distribution.

CONTRACTOR REPORTS: Scientific and technical information generated under a NASA contract or grant and considered an important contribution to existing knowledge.

TECHNICAL TRANSLATIONS: Information published in a foreign language considered to merit NASA distribution in English.

SPECIAL PUBLICATIONS: Information derived from or of value to NASA activities. Publications include final reports of major projects, monographs, data compilations, handbooks, sourcebooks, and special bibliographies.

TECHNOLOGY UTILIZATION PUBLICATIONS: Information on technology used by NASA that may be of particular interest in commercial and other non-aerospace applications. Publications include Tech Briefs, Technology Utilization Reports and Technology Surveys.

Details on the availability of these publications may be obtained from:

SCIENTIFIC AND TECHNICAL INFORMATION OFFICE

NATIONAL AERONAUTICS AND SPACE ADMINISTRATION

Washington, D.C. 20546